IMPROVED DESIGN OF 6/4 FLUX-SWITCHING PERMANENT MAGNET MACHINE WITH SINGLE AND DOUBLE-LAYER WINDING

By

Mingda Liu

A dissertation submitted in partial fulfillment of

the Requirements for the Degree of

Doctor of Philosophy

(Electrical and Computer Engineering)

UNIVERSITY OF WISCONSIN-MADISON

2020

Date of final oral examination: May 6th, 2020

The dissertation is approved by the following members of the Final Oral Committee:

Sarlioglu, Bulent, Associate Professor, Electrical and Computer Engineering

Jahns, Thomas, Professor, Electrical and Computer Engineering

Nellis, Gregory, Professor, Mechanical Engineering

Blasko, Vladimir, Senior Fellow, United Technology Research Center

Abstract

Permanent magnet (PM) electric machines have been widely used in many applications because of the high power density and efficiency. Several topologies of PM machine have been proposed and investigated, and each topology has its own features and advantages. Flux-switching permanent magnet (FSPM) machine has been widely investigated in the past few decades because of many unique properties such as robust rotor structure and easy thermal management. Low-pole FSPM machine such as 6/4 FSPM machine is attractive for high-speed applications because of the low fundamental frequency, which is beneficial to reduce iron loss and inverter switching loss. However, the existing double-layer concentrated winding dual-stator 6/4 FSPM machine has potential issues such as large second-order harmonic and low winding factor. The purpose of this research is to further investigate the design of the 6/4 FSPM machine and to make it a competitive candidate for real-world applications. The proposed dual-stator 6/4 FSPM machine with single-layer winding is shown to be able to increase the winding factor from 0.5 to 1 and to achieve high efficiency. Analytical model and finite element analysis (FEA) models are established to compare the performance of the proposed and the existing 6/4 FSPM machine.

Having both permanent magnet and armature winding in the stator allows the FSPM machine to be easily cooled by a water jacket which locates outside the stator. One the other hand, the temperature-sensitive permanent magnets are in the stator assembly and located close to the major heat sources. Therefore, careful thermal analysis on the FSPM machine is needed to guarantee the machine sanity. Lumped-parameter thermal network (LPTN) model and thermal FEA model are built to estimate the machine steady-state and transient thermal performance. It is shown that the winding layout and the use of winding encapsulation play an important role in the thermal performance of the FSPM machine.

Windage loss and housing eddy current loss is more prominent in the FSPM machine compared to the surface PM machine and interior PM machine due to the salient rotor pole and stator-mounted permanent magnet. This research investigates the windage and housing loss of the FSPM machine and proposes modified machine structures to mitigate the windage loss and housing loss. Prototype 6/4 FSPM motors are built and tested on the dynamometer test bench. Good agreement is found between the measured data and the machine performance predicted by the analytical calculation and FEA simulation.

Acknowledgments

This Ph.D. thesis contains the results of my research work at the University of Wisconsin-Madison during the past few years. Being a Ph.D. student in UW-Madison has been an inspiring, challenging, yet very enjoyable experience. It is impossible for me to go this far without the support of others. I truly appreciate all the generous helps provided by the faculties and staff from UW-Madison and by my friends and families.

First, I would like to express my sincere gratitude to my advisor Professor Bulent Sarlioglu for his insightful guidance and continued support. He has always been willing to help and always been helpful. His enthusiasm for engineering and pursuit of excellence has been the motivation to push me forward. During the past few years, I benefited a lot from his experience and knowledge, which is valuable not only in the technical aspect but also in daily life. The time management, critical thinking, and multi-tasking capability that I developed are beneficial for the rest of my life.

Besides my advisor, I would like to extend my thanks to all the WEMPEC faculty and staff members, Prof. Thomas Jahns, Prof. Robert Lorenz, Prof. Giri Venkataramanan, Prof. Daniel Ludois, Prof. Eric Severson, James Sember, Kathy Young, Kyle Hanson, and Helene Demont. They have been very kind and helpful to me and all WEMPEC students. My thanks also go to Prof. Gregory Nellis. He is the co-PI of the project that I was working on. He has always been very efficient and can see problems and suggest solutions quickly. I also would like to express my gratitude to Dr. Vladimir Blasko from United Technologies Research Center (UTRC) for serving as my Ph.D. exam committee members, who is also the co-PI of my project.

I also would like to thank David Farnia for his professional technical support for JMAG software and practical suggestions for prototype motor fabrication. My appreciation is also expressed to Aaron William, Matt Marion, and Ryan Halverson from Arnold Magnetics

Technologies for their support of prototype motor manufacturing. My thanks also extend to Jagadeesh Tangudu from United Technologies Research Center for the collaboration on my project. I would like to thank the National Science Foundation (NSF) for financially supporting my research via the Grant Opportunities for Academic Liaison with Industry (GOALI) project. I would like to thank all the WEMPEC sponsors for providing the research software, the informative Friday seminars, and of course, the financial support.

I would like to express my special thanks to all the former and current WEMPEC students for making my life in Madison wonderful. They have shown great solidarity and fraternity as a community. I was able to learn so much from them and benefit from their diversity and inspiring personality. I am honored to be able to work with them.

Finally, I would like to give my greatest gratitude to my parents, my other family members for their unconditional love and support.

Table of Content

Abstract i

Acknowledgments iii

Table of Content v

List of Figures x

List of Tables xxi

Introduction 1

Research motivation and overview 1

Major contributions 3

Organization of chapters 4

Chapter 1 State-of-the-Art Literature Review 7

1.1. High-speed machine and stator mounted pm machines 7

1.1.1. High-speed electric machine 8

1.1.2. Stator-mounted PM machine 10

1.2. Flux-switching machines topologies in literature 17

1.2.1. FSPM machine operation principle 17

1.2.2. Stator slot/rotor pole combination of FSPM machine 20

1.2.3. FSPM machine with unconventional topologies 25

1.3. Low-pole FSPM machine design 42

1.3.1. FSPM machine for high-speed application 42

1.3.2. Low-pole FSPM machine 46

1.3.3. Dual-stator 6/4 FSPM machine 49

1.4. Multi-physics design for FSPM machine 55
1.4.1. Thermal analysis 56
1.4.2. Structural and mechanical tolerance analysis 59
1.4.3. Windage loss 64
1.5. Summary 66
Chapter 2 Analytical Modeling of Dual-Stator 6/4 FSPM Machine 68
2.1. Fundamentals of dual-stator 6/4 FSPM machine 68
2.1.1. Second-order harmonic in flux-linkage and the cancellation 68
2.1.2. Gap between two stators 73
2.2. Winding configuration of 6/4 FSPM machine 76
2.2.1. Back EMF vector graph and winding factor of FSPM machine 76
2.2.2. Winding factor of 6/4 FSPM machine 78
2.2.3. Single-layer Circumferential winding and Toroidal winding layout 79
2.3. Design parameters of the dual-stator 6/4 FSPM machine 83
2.3.1. Sizing equation of 6/4 FSPM machine 84
2.3.2. Machine design parameters 85
2.4. Harmonic analysis of single-layer 6/4 FSPM machine 93
2.4.1. No load air gap flux density of 6/4 FSPM machine 94
2.4.2. Stator winding MMF of 6/4 FSPM machine 99
2.5. Summary 101
Chapter 3 Comparison between Single-Layer and Double-layer Winding Design 103
3.1. Optimization of single-layer dual-stator 6/4 FSPM machine 103
3.1.1. Stator optimization 104
3.1.2. Rotor optimization 106
3.1.3. Comparison of 2D results v.s. 3D results 108
3.1.4. Machine geometry parameters 110

3.2. Torque production capability comparison 112
3.2.1. Open-circuit characteristics 113
3.2.2. Loaded machine characteristics 115
3.3. Loss distribution and efficiency comparison 117
3.3.1. Copper loss 117
3.3.2. Stator and rotor iron loss 118
3.3.3. Magnet loss 121
3.3.4. Housing loss 122
3.3.5. Comparison of efficiency and power factor 123
3.4. Permanent magnet demagnetization in 6/4 FSPM machine 124
3.4.1. Permanent magnet loss and temperature distribution 126
3.4.2. Permanent magnet demagnetization analysis 128
3.5. Summary 131
Chapter 4 Cooling Design and Thermal Analysis of 6/4 FSPM Machine 133
4.1. Design of water jacket integrated housing 133
4.1.1. Spiral channel water jacket 134
4.1.2. Axial channel water jacket 138
4.1.3. Choice of winding encapsulation material 139
4.2. Steady state thermal analysis of dual-stator 6/4 FSPM machine 141
4.2.1. Lumped parameter thermal network model 142
4.2.2. Thermal network modeling of 6/4 FSPM machine 144
4.2.3. Thermal performance evaluation for 6/4 FSPM machine 154
4.3. Machine transient thermal behavior 160
4.3.1. Thermal finite element analysis 160
4.3.2. 6/4 FSPM machine transient thermal behavior 164
4.4. Summary 167

Chapter 5 Special Design Consideration in FSPM Machine 169

5.1. Housing loss 170

5.1.1. Magnet iron bridge 174

5.1.2. Housing cavities 175

5.2. Windage loss 177

5.2.1. Machine sizing and windage loss reduction rotor structure 178

5.2.2. Windage loss estimation and structural analysis 180

5.2.3. Electromagnetic properties of windage loss reduction structure 188

5.2.4. Windage reduction structure and rotor heat transfer 192

5.3. Summary 194

Chapter 6 Experiment Verification 196

6.1. Prototype motor fabrication 196

6.1.1. Double-layer concentrated winding 6/4 FSPM machine prototype 197

6.1.2. Single-layer toroidal winding 6/4 FSPM machine prototype 201

6.2. Prototype motor test setup 205

6.2.1. Test equipment and configurations 205

6.2.2. Switching current ripple and choose of output filter 208

6.3. Electromagnetic performance tests 211

6.3.1. Prototype motors parameters 211

6.3.2. Open circuit test 213

6.3.3. Loaded test 218

6.4. Thermal testing of dual-stator 6/4 FSPM machine 225

6.4.1. Steady state thermal testing and comparison 226

6.4.2. Transient thermal testing 229

6.5. Summary 230

Chapter 7 Conclusion and Future Work 231

7.1. Research conclusions 231

7.2. Research contributions 234

7.3. Remaining work 237

Chapter 8 Reference 239

Annex 248

List of Figures

Figure 1.1-1. Definition of tip speed of a rotating item 8

Figure 1.1-2. Section view of (a) Interior permanent magnet machine (b) Surface permanent magnet machine 9

Figure 1.1-3. Three-phase 12 slot 8 pole DSPM machine (a) Section view (b) Flux linkage waveform. [20]-[22] 11

Figure 1.1-4. Special stator core shape for increased magnet volume (a) Hexagon shape stator (b) Square shape stator [24][25] 11

Figure 1.1-5. Flux reversal permanent magnet machine (a) 6/8 topology (b) Back EMF waveform [26]-[28] 12

Figure 1.1-6. Novel flux reversal permanent magnet machine topologies for reducing flux leakage (a) Inset magnet structure (b) Consequent pole structure [29][30] 13

Figure 1.1-7. Single-phase FSPM alternator [31] 14

Figure 1.1-8. Three-phase FSPM machine (a) Section view (b) Flux-linkage and back EMF waveform [33] 15

Figure 1.2-1. Geometry of conventional 12/10 FSPM machine (a) 3D isometric view (b) Section view [117] 17

Figure 1.2-2. Permanent magnet flux path in 12/10 FSPM machine with different rotor positions (a) Minimum flux linkage position (b) First zero flux linkage position (c) Maximum flux linkage position (d) Second zero flux linkage position (e) Flux linkage waveform. [45] 18

Figure 1.2-3. 12/10 FSPM airgap flux density waveform and harmonic components [46] 19

Figure 1.2-4. Variation of back EMF amplitude as a function of rotor pole number [48] 21

Figure 1.2-5. Illustration of magnetic force (I_d = 0) of (a) 6/5 FSPM. (b) 6/7 FSPM. (c) 12/11 FSPM. (d) 12/13 FSPM. [50] 22

Figure 1.2-6. Torque-current characteristic of 12-slot FSPM machine [48] 23

Figure 1.2-7. Sound power level of loaded configuration for 12-slot FSPM machine with different number of rotor poles at 400 rpm. [51] 24

Figure 1.2-8. Topologies of FSPM machine with high number of phase (a) Five-phase FSPM machine (20/18). (b) Nine-phase FSPM machine (36/34). [55] 25

Figure 1.2-9. (a) C-core FSPM machine (b) E-core FSPM machine [57] 26

Figure 1.2-10. Back EMF waveform of (a) C-core FSPM (b) E-core FSPM machine with different number of rotor poles [57] 26

Figure 1.2-11. Torque output characteristics of C-core and E-core FSPM machine [57] 27

Figure 1.2-12. Structure of multi-tooth FSPM machine (a) Cross-section view (b) Stator and rotor prototype [58] 27

Figure 1.2-13. Torque output of multi-tooth FSPM machine and conventional 12/10 FSPM machine [58] 28

Figure 1.2-14. Torque-current curve of multi-tooth FSPM machine [58] 29

Figure 1.2-15. FSPM machine with modified magnet placement (a) Sandwiched FSPM (b) V-shape sandwiched FSPM [62] 29

Figure 1.2-16. Output torque comparison of sandwiched FSPM machine and conventional 12/10 FSPM machine [61] 30

Figure 1.2-17. Structure of adjustable flux FSPM machine with (a) All flux adjustor (b) Alternate flux adjustor [63] 30

Figure 1.2-18. Torque-speed curve of adjustable flux FSPM machine [63] 31

Figure 1.2-19. Memory FSPM machine with two types of permanent magnets [66] 32

Figure 1.2-20. Torque-speed curve of hybrid magnet memory FSPM machine [73] 32

Figure 1.2-21. Hybrid excited flux-switching machine with parallel field (a) Stator structure (b) Rotor structure [74] 33

Figure 1.2-22. Flux path of permanent magnet and DC coil in the case of (a) Flux intensifying (b) Flux weakening [77] 34

Figure 1.2-23. (a) Back EMF waveform (b) Output torque of parallel field hybrid excited flux switching machine [77] 35

Figure 1.2-24. Other hybrid excitation flux-switching machine topologies [76] [78] 35

Figure 1.2-25. DC excited flux-switching machine (a) Section view (b) Flux path [80] 36

Figure 1.2-26. Output torque comparison of the DC-excited flux-switching machine [78] 36

Figure 1.2-27. Modular rotor FSPM machine (a) Section view (b) Prototype rotor [81] 37

Figure 1.2-28. DC excited partitioned stator FSPM machine (a) Section view (b) Prototype assembly [82] 38

Figure 1.2-29. Partitioned stator FSPM machine (a) Section view (b) Magnetic flux path [83] .. 38

Figure 1.2-30. Novel FSPM machine with combined modified structure (a) Partitioned stator memory FSPM machine with hybrid excitation [84] (b) Partitioned stator FSPM machine with hybrid excitation [85] 39

Figure 1.2-31. Configuration of linear flux-switching permanent magnet motor [89]..... 40

Figure 1.2-32. Linear FSPM machine with assistance teeth for detent force reduction [87] 40

Figure 1.2-33. Axial field flux-switching permanent magnet machine (a) Dual-stator structure (b) Dual-rotor structure 41

Figure 1.3-1. Field weakening characteristics comparison between IPM and FSPM machine (a) Torque-speed curve (b) Power-speed curve [106]..... 43

Figure 1.3-2.Proximity effect in the stator slot of FSPM machine (a) Current density distribution (b) Conductor loss with different number of strands [107] 44

Figure 1.3-3. Eddy current loss density distribution in magnet with different number of segmentations (a) 2 segments (b) 6 segments (c) 10 segments [109]..... 45

Figure 1.3-4. 6-slot 8-pole hybrid excited FSPM machine for EV applications (a) Section view (b) Flux line with both PM and excitation field [112] 46

Figure 1.3-5. Axial laminated 6/7 FSPM machine (a) Section view (b) Prototype rotor (b) Prototype stator [110] 47

Figure 1.3-6. Performance comparison of the axial laminated 6/7 FSPM machine (a) Output torque (b) Torque-speed curve (c) Power-speed curve [110] 48

Figure 1.3-7. 6-slot 4-pole FSPM machine (a) Section view (b) Back EMF waveform [113] 48

Figure 1.3-8. 6/4 FSPM machine with skewed rotor (a) Back EMF (b) Cogging torque [113]... 49

Figure 1.3-9. Flux linkage of 6/4 FSPM machine (a) Waveform of flux linkage in the three-phase coils (b) Harmonic components of phase A [114]..... 50

Figure 1.3-10. Back EMF 6/4 FSPM machine (a) Waveform of back EMF in the three-phase coils (b) Harmonic components of phase A [114] 50

Figure 1.3-11. Dual-stator 6/4 FSPM machine (a) 3D structure (b) Front stator section view (c) Rear stator section view [114] 51

Figure 1.3-12. Flux linkage of dual-stator 6/4 FSPM machine (a) Flux linkage waveform (b) Harmonic component in flux linkage 52

Figure 1.3-13. Cogging torque comparison between the dual-stator and single stator 6/4 FSPM machine [113] 53

Figure 1.3-14. Alternative topologies of dual-stator 6/4 FSPM machine (a) Topology-I (b) Topology-III [117]..... 53

Figure 1.3-15. Step skewed rotor for torque ripple reduction (a) Two-step skew (b) Four-step skew [115] 55

Figure 1.3-16. Output torque and torque ripple level of step skew rotor with different span angle (a) Two-step skew (b) Four-step skew [115] 55

Figure 1.4-1. Temperature measured for a nine-phase FSPM machine (a) Winding temperature measurement (b) Frame temperature measurement (c) Temperature variation of winding (d) Temperature variation of frame [125] 57

Figure 1.4-2. 12/10 FSPM machine with water jacket cooling (a) Section view of the machine (b) Lumped-parameter themal network model [127] 58

Figure 1.4-3. Thermal analysis of 12/10 FSPM machine (a) Correlation between convective coefficient and rotor speed (b) Machine temperature distribution from FEA [127] 58

Figure 1.4-4. Eigen mode shape of 12/10 FSPM machine stator (a) 2^{nd} Mode (b) 3^{rd} Mode (c) 4^{th} Mode (d) 5^{th} Mode [131] 60

Figure 1.4-5. Back EMF under the influence of rotor pole offset angle deviation [115] 61

Figure 1.4-6. Rotor magnetic force map with rotor pole offset angle deviation [115] 62

Figure 1.4-7. Rotor eccentricity (a) Perfectly centered rotor (b) Rotor with static eccentricity (c) Rotor with dynamic eccentricity [115] 62

Figure 1.4-8. Torque output waveform of dual-stator 6/4 FSPM machine with (a) Rotor static eccentricity (b) Rotor dynamic eccentricity [115] 63

Figure 1.4-9. Rotor magnetic force map for (a) Rotor static eccentricity (b) Rotor dynamic eccentricity [115] 63

Figure 1.4-10. Windage loss modeling for cylindrical rotor [132] 64

Figure 1.4-11. Windage loss study for a 60 kW SRM machine (a) Rotor structure (b) Windage loss from calculation and measurement [133] 64

Figure 1.4-12. Windage loss reduction structure (a) Original rotor structure (b) Rotor with ribs (c) Rotor with shrouds (d) Full cylindrical rotor [133] 65

Figure 1.4-13. Windage friction dragging torque for different types of rotor structure [134] 66

Figure 2.1-1. Classification of dual-stator 6/4 FSPM machine according to winding topology .. 69

Figure 2.1-2. Section view of a 6/4 FSPM machine with double-layer winding. 69

Figure 2.1-3. Simplified partial model of 6/4 FSPM machine with four critical rotor positions . 70

Figure 2.1-4. Flux linkage of a single stator of 6/4 FSPM machine (a) Flux linkage waveform (b) Harmonic components in the flux linkage 71

Figure 2.1-5. Section view and stator winding connection of dual-stator 6/4 FSPM machine (a) Front stator (b) Rear stator 73

Figure 2.1-6. 3D view of the dual-stator 6/4 FSPM machine 73

Figure 2.1-7. Dual-stator 6/4 FSPM machine with a stator gap length of (a) 5 mm and (b) 30 mm 74

Figure 2.1-8. Back EMF value variation versus different stator gap length 74

Figure 2.2-1. EMF vector for calculation of (a) Winding distribution factor (b) Winding pitch factor 76

Figure 2.2-2. 3-phase 12/10 FSPM machine (a) Coil side vector of phase A and (b) EMF vectors graph 77

Figure 2.2-3. Double-layer concentrated winding 6/4 FSPM machine (a) Coil side vector of phase A and (b) EMF vector graph 78

Figure 2.2-4. Single-layer concentrated winding 6/4 FSPM machine (a) Coil side vector of phase A and (b) EMF vector graph 79

Figure 2.2-5. Realization of single-layer winding 6/4 FSPM machine with (a) Single-layer overlapping winding (SLOW) and (b) Single-layer toroidal winding (SLTW) 80

Figure 2.2-6. Section views of the front stator of (a) SLOW and (b) SLTW dual-stator 6/4 FSPM machine 81

Figure 2.2-7. Geometry parameters for stator winding resistance calculation. 82

Figure 2.3-1. Stator units with winding geometry parameters of (a) Double-layer concentrated winding and (b) Single-layer toroidal winding dual-stator 6/4 FSPM machine. 86

Figure 2.3-2. Winding resistance of the DLCW and SLTW 6/4 FSPM machine considering proximity effect. 87

Figure 2.3-3. Magnetic flux path of 6/4 FSPM machine (a) 6/4 FSPM machine at d-axis position (b) d-axis flux path (c) 6/4 FSPM machine at q-axis position (b) q-axis flux path 89

Figure 2.3-4. *d*-axis and *q*-axis Inductance of DLCW and SLTW 6/4 FSPM machine at different current levels. 90

Figure 2.3-5. Slot section view for calculating slot leakage inductance (a) Single-layer winding (b) Double-layer winding 91

Figure 2.4-1. 6/4 FSPM machine stator core and permanent magnet (a) Rectangular stator model (b) Magnet MMF considering the stator saliency 94

Figure 2.4-2. 6/4 FSPM machine rotor core permeance function (a) Rectangular rotor model (b) Rotor permeance function 96

Figure 2.4-3. No-load airgap magnetic flux density distribution (a) Radial flux density distribtuion (b) Harmonic components 98

Figure 2.4-4. 6/4 FSPM machine winding MMF comparison 100

Figure 2.4-5. 6/4 FSPM machine winding function (a) DL winding and (b) SL winding 100

Figure 3.1-1. Magnetic flux density contour of DL 6/4 FSPM machine 105

Figure 3.1-2. Flux linkage of SLTW 6/4 FSPM machine with different magnet thickness and stator tooth width 106

Figure 3.1-3. Electromagnetic performance with varying rotor geometry parameters (a) Output torque (b) Torque ripple (c) Iron loss level (d) Efficiency 107

Figure 3.1-4. Comparison of 2D and 3D FEA simulation results for dual-stator 6/4 FSPM machine (a) Back EMF (b) Cogging torque 108

Figure 3.1-5. Comparison of output torque of 2D and 3D FEA simulation 109

Figure 3.1-6. Section view and geometry parameters of the dual-stator 6/4 FSPM machine (a) DL machine (b) SLTW machine 110

Figure 3.1-7. 3D view of the three dual-stator 6/4 FSPM machine under comparison (a) DLCW 6/4 FSPM machine (b) SLTW 6/4 FSPM machine 112

Figure 3.2-1. Open circuit characteristics of the three dual-stator 6/4 FSPM machines (a) Back EMF waveform (b) Back EMF harmonic components (c) Flux linkage waveform (d) Flux linkage harmonic components 113

Figure 3.2-2. Magnetic flux density distribution contour at no-load for (a) DLCW 6/4 FSPM machine and (b) SLTW 6/4 FSPM machine 114

Figure 3.2-3. Cogging torque of the DLCW and SLTW dual-stator 6/4 FSPM machines 114

Figure 3.2-4. Comparison of output torque of DLCW and SLTW 6/4 FSPM machine (a) Rated torque waveform and (b) Torque-current curve 115

Figure 3.2-5. Magnetic flux density distribution contour at rated output condition of (a) DLCW 6/4 FSPM machine and (b) SLTW 6/4 FSPM machine 116

Figure 3.3-1. Winding resistance of the DLCW and SLTW 6/4 FSPM machine considering proximity effect. 117

Figure 3.3-2. Magnetic flux line of a double-layer 6/4 FSPM machine at (a) 0° rotor position (b) 30° rotor position (c) 60° rotor position (b) 90° rotor position 119

Figure 3.3-3. Magnetic flux density variation (a) Position of the magnetic flux density probe in FEA (b) Waveform of three locations in the machine 120

Figure 3.3-4. Eddy current density in the stator-mounted permanent magnet of the dual-stator 6/4 FSPM machine..... 121

Figure 3.3-5. Magnet loss versus number of magnet segmentation 121

Figure 3.3-6. Housing loss of dual-stator 6/4 FSPM machine (a) Eddy current density and (b) Eddy current loss density 122

Figure 3.4-1. Magnet grade (from Hitach Co.) for different heat resistance level [148]..... 124

Figure 3.4-2. B-H curve of NdFeB permanent magnet from Hitach Metal Inc. (a) 41CH magnet and (b) 41SH magnet [148] 125

Figure 3.4-3. Permanent magnets in 6/4 FSPM machine (a) Loss density distribution and (b) Temperature distribution 127

Figure 3.4-4. Magnet temperature variation as a function of slot current density..... 127

Figure 3.4-5. PM magnetic field and armature reaction field in 6/4 FSPM machine..... 128

Figure 3.4-6. Magnetic flux density variation at the inner radius corner of magnet (a) With positive q-axis current and (b) with negative d-axis current..... 129

Figure 3.4-7. Demagnetization investigation: change of armature current, magnet temperature and back EMF in FEA simulation..... 130

Figure 3.4-8. Demagnetization ratio of DLCW and SLTW 6/4 FSPM machine with CH and SH grade NdFeB magent at different current density..... 130

Figure 4.1-1. Double-layer dual-stator 6/4 FSPM machine..... 133

Figure 4.1-2. Coolant channel of water jacket (a) Spiral channel (b) Axial channel. 134

Figure 4.1-3. Section view of the spiral channel water jacket and dimensional parameters. 135

Figure 4.1-4. Computational fluid dynamics simulation of spiral channel water jacket (a) Velocity stream plot (b) Temperature contour plot (c) Turbulence intensity (d) Static pressure. 137

Figure 4.1-5. Section view of the axial channel water jacket and dimensional parameters. 138

Figure 4.1-6. Computational fluid dynamics simulation of axial channel water jacket (a) Velocity stream plot (b) Temperature contour plot (c) Turbulence intensity (d) Static pressure. 140

Figure 4.2-1. Geometry parameters for (a) Rectangular conductive heat transfer model, (b) Cylindrical conductive heat transfer model. 143

Figure 4.2-2. Steady-state lumped-parameter thermal network (LPTN) model for dual-stator 6/4 FSPM machine with (a) Circumferential winding and (b) Toroidal winding 144

Figure 4.2-3. Equivalent rotor model transformation from salient rotor structure to cylindrical structure. 146

Figure 4.2-4. Characterization of air flow in the air gap region (a) Air flow velocity stream line plot (b) Rotor surface temperature 147

Figure 4.2-5. Rotor surface average heat transfer coefficient at different rotation speed 148

Figure 4.2-6. Equivalent stator slot model for heat transfer from winding to stator (a) Real slot occupation (b) Equivalent slot model. 149

Figure 4.2-7. Different types of interface gap [157] 150

Figure 4.2-8. Loss segregation as a function of current density for (a) Circumferential winding machine and (b) Toroidal winding machine. 153

Figure 4.2-9. Flow chart for determining temperature dependent copper loss. 154

Figure 4.2-10. Dual-stator 6/4 FSPM machines temperatures versus stator slot current density at (a) Stator winding (b) Stator and magnet (c) Rotor 156

Figure 4.2-11. Thermal resistance of the water jacket as a function of coolant flow rate. 157

Figure 4.2-12. Current density limit of the machines with different encapsulation thermal conductivities 158

Figure 4.2-13. Component temperature of SLTW 6/4 FSPM machine with M2 encapsulation and natural convection cooling 159

Figure 4.3-1. Defining current flow direction in coils 161

Figure 4.3-2. Thermal circuit in FEA tool 162

Figure 4.3-3. Temperature distribution of dual-stator 6/4 FSPM machine at 4800 rpm from FEA simulation. 163

Figure 4.3-4. Transient temperature rises during overloading operations for (a) DLCW 6/4 FSPM machine with M1 encapsulation and (b) SLTW 6/4 FSPM machine with M2 encapsulation. 165

Figure 4.3-5. Thermal network for short-time transient overloading 166

Figure 4.3-6. Winding temperature variation with first-order approximation 167

Figure 5.1-1. Geometry of the dual-stator 6/4 FSPM machine with single-layer toroidal winding 170

Figure 5.1-2. (a) Magnetic flux penetration into aluminum housing and the placement of B field probe (b) Magnetic flux density variation near magnet and winding slot 171

Figure 5.1-3. Housing eddy current loss density (a) at 1500 rpm (100 Hz) and (b) at 15000 rpm (1000 Hz) 172

Figure 5.1-4. Housing eddy current loss of 6/4 FSPM machine at different speed 173

Figure 5.1-5. Magnet iron bridge structure for shunting the flux leakage in the housing 174

Figure 5.1-6. Housing loss reduction and output torque variation with different magnet iron bridge thickness. 175

Figure 5.1-7. Cavity in the machine housing near permanent magnet for reducing eddy current loss. 176

Figure 5.1-8. Housing loss reduction and efficiencies with different housing slot width. 176

Figure 5.2-1. Original and modified rotor structure for windage loss (a) Original dual-stator 6/4 FSPM rotor (b) Rotor with ribs (c) Rotor with two end shrouds (d) Rotor with four end shrouds (e) Cylindrical rootor 179

Figure 5.2-2. Friction coefficient – Reynolds number empirical relation for turbulence flow .. 181

Figure 5.2-3. Air flow velocity stream line plot of dual-stator 6/4 FSPM machine at 15,000 rpm with (a) Original rotor (b) Rotor with rib (c) Rotor with two shrouds (d) Rotor with four shrouds (e) Rotor with cylindrical shape (f) Enclosed machine end cap 183

Figure 5.2-4. Comparison of empirical windage loss and CFD windage loss for dual-stator 6/4 FSPM machine..... 184

Figure 5.2-5. Amplitude of displacement of rotor under rated condition with (a) 1 mm rib and (b) Rotor with two shroud. 186

Figure 5.2-6. Von Mises stress of rotor under rated condition with (a) 1 mm rib and (b) Rotor with two shroud. 187

Figure 5.2-7. Magnetic flux density of rotor (a) Original rotor (b) Rotor with rib..... 188

Figure 5.2-8. Flux linage of dual-stator 6/4 FSPM machine with different type of rotor for windage loss reduction (a) Flux linkage waveform (b) Flux linkage harmonic component..... 189

Figure 5.2-9. Flux linkage variation for different shroud thickness 189

Figure 5.2-10. Output torque of different rotor structure..... 189

Figure 5.2-11. Convective heat transfer coefficient of the rotor surface for 6/4 FSPM machine with original rotor and with rotor shroud..... 192

Figure 5.2-12. Temperature contour of dual-stator 6/4 FSPM machine with original rotor and with shrouded rotor. 193

Figure 6.1-1. Photo of the assembled prototype DLCW 6/4 FSPM prototype motor 197

Figure 6.1-2. Stator assembly of the DLCW 6/4 FSPM machine (a) CAD drawing and (b) Actual stator assembly photo 198

Figure 6.1-3. Placement of 10 RTD temperature sensors in the DLCW 6/4 FSPM machine prototype 199

Figure 6.1-4. Rotor assembly CAD drawing 199

Figure 6.1-5. DLCW 6/4 FSPM machine housing (a) Water jacket (b) End cap. 200

Figure 6.1-6. Photo of the assembled prototype SLTW 6/4 FSPM prototype motor 201

Figure 6.1-7. Photos of the stator of the SLTW 6/4 FSPM machine (a) Stator core and (b) Stator assembly. 202

Figure 6.1-8. RTD temperature sensors placement of the SLTW 6/4 FSPM machine 203

Figure 6.1-9. Rotor assembly of the SLTW 6/4 FSPM machine (a) CAD drawing and (b) Rotor photo. 204

Figure 6.1-10. CAD drawing of the housing (a) Water jacket and (b) Front and rear end caps. 204

Figure 6.2-1. Schematics of the dynamometer test bench setup (Add temperature data logger, electric power measurement). 206

Figure 6.2-2. Photo of dynamometer test bench setup for (a) DLCW 6/4 FSPM prototype motor and (b) SLTW 6/4 FSPM prototype motor 207

Figure 6.2-3. Electric motor drive system with output filter. 209

Figure 6.2-4. Simulink model of the drive system. 209

Figure 6.2-5. Motor phase current waveforms without filter (a) Simulated (b) Measured 210

Figure 6.2-6. Motor current waveform with inductor filter 211

Figure 6.2-7. Motor phase current waveform with filter (a) LC sine-wave fileter (b) Inductor. 211

Figure 6.3-1. Measured variation of prototype motors stator winding resistance considering the ac resistance 212

Figure 6.3-2. Measured three-phase back EMF of the prototype dual-stator 6/4 FSPM machine at 4800 rpm. 214

Figure 6.3-3. Back EMF of prototype 6/4 FSPM motors at different speeds. 215

Figure 6.3-4. 3D view of the step skewed rotor for torque ripple reduction. 215

Figure 6.3-5. Cogging torque waveform for the dual-stator 6/4 FSPM machine. 216

Figure 6.3-6. Mechanical dragging powr and no-load iron loss (a) Torque and (b) Loss 217

Figure 6.3-7. Rated output torque waveform of (a) DLCW 6/4 FSPM machine and (b) SLTW 6/4 FSPM machine 218

Figure 6.3-8. Output torque characteristics of the dual-stator 6/4 FSPM machine (a) Torque-current curve (b) Output torque waveform 219

Figure 6.3-9. Torque versus current angle in dual-stator 6/4 FSPM machine 220

Figure 6.3-10. Loss comparison between measured data and simulation results 221

Figure 6.3-11. Phasor diagram of 6/4 FSPM machine with zero *d*-axis current control 222

Figure 6.3-12. *d*-axis and *q*-axis inductance variation due to iron saturation 223

Figure 6.3-13. Phase A current and voltage waveform at (a) Light load (b) Full-load 223

Figure 6.3-14. Power factor of dual-stator 6/4 FSPM machine 224

Figure 6.4-1. Data logger for temperature recording. 225

Figure 6.4-2. IR image of the dual-stator 6/4 FSPM motor at thermal steady state. 226

Figure 6.4-3. Temperature rise of different parts of the prototype motor till steady state (a) DLCW 6/4 FSPM machine, (b) SLTW 6/4 FSPM machine 227

Figure 6.4-4. Temperature rise of different parts of the prototype motor till steady state of different component inside the motor 229

List of Tables

TABLE 1-1. COMPARISON OF STATOR-MOUNTED PERMANENT MAGNET MACHINES 16

TABLE 1-2. COMPARISON OF MANUFACTURING, ASSEMBLING SIMPLICITY, AND PERFORMANCE OF DIFFERENT DUAL-STATOR 6/4 FSPM MACHINE TOPOLOGIES 54

TABLE 2-1. LOSSES AND EFFICIENCIES OF DUAL-STATOR 6/4 FSPM MACHINE WITH DIFFERENT GAP DISTANCE BETWEEN THE STATORS 75

TABLE 2-2. WINDING PARAMETERS OF 6/4 FSPM MACHINES 82

TABLE 2-3. STATIONARY COMPONENT OF NO-LOAD AIRGAP MAGNETIC FLUX DENSITY OF 6/4 FSPM MACHINE 97

TABLE 2-4. FORWARD ROTATING COMPONENT OF NO-LOAD AIRGAP MAGNETIC FLUX DENSITY OF 6/4 FSPM MACHINE 97

TABLE 2-5. BACKWARD ROTATING COMPONENT OF NO-LOAD AIRGAP MAGNETIC FLUX DENSITY OF 6/4 FSPM MACHINE 97

TABLE 3-1. MACHINE LOADED CHARACTERISTICS COMPARISON WITH DIFFERENT ROTOR BACK IRON THICKNESS 108

TABLE 3-2. COMPARISON OF 2D AND 3D FEA SIMULATION FOR DUAL-STATOR 6/4 FSPM MACHINE 109

TABLE 3-3. GEOMETRY AND MACHINE PARAMETERS OF DL AND SLTW DUAL-STATOR 6/4 FSPM MACHINES 111

TABLE 3-4. MACHINE PARAMETERS OF DL AND SLTW DUAL-STATOR 6/4 FSPM MACHINES ... 111

TABLE 3-5. OPERATING CHARACTERISTICS OF DUAL-STATOR 6/4 FSPM MACHINE 116

TABLE 3-6. LOSS AND EFFICIENCY COMPARISON OF DLCW AND SLTW DUAL-STATOR 6/4 FSPM MACHINE 123

TABLE 3-7. KNEE POINTS MAGNETIC FLUX DENSITY OF CH AND SH GRADE MAGNETS AT DIFFERENT OPERATING TEMPERATURE 126

TABLE 4-1. LOSS DISTRIBUTION IN DOUBLE-LAYER DUAL-STATOR 6/4 FSPM MACHINE AT 15000 RPM 135

TABLE 4-2. PARAMETERS OF THE SPIRAL CHANNEL WATER JACKET 136

TABLE 4-3. PARAMETERS OF THE AXIAL CHANNEL WATER JACKET 139

TABLE 4-4. SLOT ENCAPSULATION MATERIAL PROPERTIES 141

TABLE 4-5. 6/4 FSPM MACHINE PARAMETERS AND MATERIAL PROPERTIES 143

TABLE 4-6. EQUIVALENT INTERFACE GAPS FOR CONTACT THERMAL RESISTANCE 150

TABLE 4-7. THERMAL RESISTANCES FOR THE DLCW MACHINE WITH M1 ENCAPSULATION 151

TABLE 4-8. THERMAL RESISTANCES FOR THE SLTW MACHINE WITH M2 ENCAPSULATION 152

TABLE 4-9. TEMPERATURE OF 6/4 FSPM MACHINE COMPONENTS FROM FEA SIMULATION AND LPTN MODEL 164

TABLE 4-10. 6/4 FSPM MACHINE PARAMETERS AND MATERIAL PROPERTIES 164

TABLE 5-1. LOSSES AND EFFICIENCIES OF 6/4 FSPM MACHINE WITH DIFFERENT MAGNET IRON BRIDGE THICKNESS 175

TABLE 5-2. LOSSES AND EFFICIENCIES OF 6/4 FSPM MACHINE WITH OR WITHOUT SLOT NEAR MAGNET IN THE HOUSING 177

TABLE 5-3. DESGIN PARAMETERS OF 70 KW 6/4 FSPM MACHINE 178

TABLE 5-4. WINDAGE LOSS ESTIMATED WITH ANALYTICAL EQUATIONS AND CFD SIMULATION OF DIFFERENT ROTOR STRUCTURE 185

TABLE 5-5. MODAL ANALYSIS FOR DIFFERENT ROTOR STRUCTURE 187

TABLE 5-6. AVERAGE TORQUE AND TORQUE RIPPLE FOR DIFFERENT ROTOR STRUCTURES 190

TABLE 5-7. LOSSES AND EFFICIENCIES OF 70 KW DUAL-STATOR 6/4 FSPM MACHINE WITH DIFFERENT ROTOR STRUCTURES 191

TABLE 5-8. TEMPERATURE OF 6/4 FSPM MACHINE COMPONENTS FROM FEA SIMULATION AND LPTN MODEL 193

TABLE 6-1. GEOMETRY AND OPERATING PARAMETERS OF THE PROTOTYPE DUAL-STATOR 6/4 FSPM MACHINE 196

TABLE 6-2. DESCRIPTION OF PROTOTYPE MOTOR TESTING EQUIPMENT 208

TABLE 6-3. MEASURED PARAMETERS OF THE DUAL-STATOR 6/4 FSPM MACHINE 212

TABLE 6-4. COMPARISON OF OPERATING PARAMETERS BETWEEN TESTING AND FEA SIMULATION 221

TABLE 6-5 TEMPERATURE DISTRIBUTION (°C) OF THE DLCW 6/4 FSPM MACHINE AT DIFFERENT CURRENT DENSITIES 228

TABLE 6-6 TEMPERATURE DISTRIBUTION (°C) OF THE SLTW 6/4 FSPM MACHINE AT DIFFERENT CURRENT DENSITIES 228

Introduction

Research motivation and overview

Permanent magnet (PM) machines have been widely investigated in technical researches and have been used in many industrial applications because of their high efficiency and high power density. The commonly seen PM machine topologies such as interior permanent magnet (IPM) and surface permanent magnet (SPM) have the permanent magnet in the rotor, which creates a synchronized rotating magnetic field. However, having the permanent magnet in the rotor raises several issues such as rotor cooling and mechanical integrity, especially during high-speed operation. The flux-switching permanent magnet (FSPM) machine has been proposed as a stator-mounted permanent magnet machine to solve the issues as mentioned above. Among different FSPM topologies proposed in the literature, low-pole FSPM machine has a promising property of low fundamental frequency, which is a valuable benefit for high-speed operation. Conventional FSPM machines usually have a high pole count (the most seen one has 20 poles), which requires, for example, 2.5 kHz fundamental frequency to run at 15,000 rpm. Such high frequency is not only difficult to achieve with Si-based IGBT inverter for pulse-width-modulation (PWM) regulation due to the limited switching frequency but also causes high iron loss and ac copper loss in the machine. Whereas a 6/4 FSPM machine can reduce the fundamental frequency by 60% compared to the 12/10 FSPM machine.

The 6/4 FSPM machine proposed in literature employs a double-layer concentrated winding, which has the benefit of short end turns. However, it is shown that this winding topology has a winding factor of 0.5. In contrast, the high-pole FSPM machine could reach a 0.86 even 0.96 winding factor, depending on the slot/pole combination. According to the machine sizing equation, the machine with a lower winding factor needs larger size or higher electric loading to achieve the

same output power. Therefore, the first objective of this research is to investigate the winding configuration and propose a high winding factor topology for the 6/4 FSPM machine. With the same machine size and magnetic loading, the high winding factor design allows a lower electric loading, which leads to lower copper loss and higher efficiency. Comparison between the conventional 6/4 FSPM machine with double-layer winding and the proposed single-layer 6/4 FSPM machine is made to illustrate the benefits of high winding factor design, with both analytical calculation and finite element analysis (FEA) simulation.

As a relatively new machine topology compared to IPM and SPM machine, the multi-physics design of the FSPM machine, such as thermal analysis, mechanical loss analysis, and housing design, have not been thoroughly investigated in the literature. Yet those aspects are critical to ensure the good functionality of the machine. FSPM machine has the permanent magnet in the stator, which is close to the heat sink (water jacket or finned housing) and is usually claimed to have easy thermal management. On the other hand, having both armature winding and a permanent magnet in the stator and close to each other increases the risk of magnet overheating. The second objective of this research is to investigate the cooling design and the thermal analysis for the proposed FSPM machine. The steady-state and transient thermal performance are analyzed. The influence of the different winding topologies and winding encapsulation is taken into consideration. Prototype 6/4 FSPM machines with water jacket cooling have been built and tested to verify the cooling design and thermal analysis. Another issue brought by the stator mounted permanent magnet is the eddy current loss in the housing, which is not significant in the rotor-mounted PM machine. Few literatures addressed this topic while it is non-negligible for high-speed operation. This research investigated the eddy current loss in the housing and proposed possible solutions to mitigate.

The FSPM machine has a salient rotor pole, which causes considerable dragging force when rotates at high-speed. A similar salient rotor structure is used for switch reluctance machines, and windage loss reduction structures have been proposed. However, due to the different operation principles, when applying the same rotor structure in the 6/4 FSPM machine, the impact on the electromagnetic performance needs to be evaluated. In this report, the electromagnetic performance and windage loss of 6/4 FSPM machines with different rotor structures are evaluated and compared based on computational fluid dynamics simulation.

The FSPM machine, especially the low pole (6/4) FSPM machine, is a competitive candidate for high efficiency and high-speed application. The research work presented in this report deal with some of the major issues of the 6/4 FSPM machine mentioned previously and push this machine further into real applications.

Major contributions

The major contributions of this research include proposing a new winding topology for the 6/4 FSPM machine, which theoretically doubles the winding factor compared to the existing winding configuration and investigating the electromagnetic and thermal designs of the machine. The proposed single-layer 6/4 FSPM machine can achieve higher efficiency because of the lower electric loading required compared to the double-layer 6/4 FSPM machine for the same output power. The single-layer winding topology is difficult for manufacturing with circumferential winding due to the long end turn and the thick overlapping. The use of toroidal winding avoids the overlaps between the phases, which makes the manufacturing easy. The toroidal winding allows the magnet not to be surrounded by the winding. In this way, the magnet thermal management is easier. The separation of winding and magnet allows more choice of winding encapsulation material since the magnet can be inserted after the encapsulation. The benefits and problems of

using toroidal winding have discussed. Comparison between the existing 6/4 FSPM machine and the proposed single-layer 6/4 FSPM machine has been conducted.

The second contribution of this research is the cooling design and the thermal analysis of the 6/4 FSPM machine with different winding topologies. Water jackets with a spiral channel and axial channel have been designed and compared. Lumped-parameter thermal network (LPTN) model and thermal FEA model have been established for the 6/4 FSPM machines to investigate the steady-state and transient thermal behavior. Important heat transfer parameters have been derived with empirical equations and CFD simulations. The thermal performance of 6/4 FSPM machines with different winding topologies and encapsulation materials have been compared.

The stator-mounted permanent magnet and the salient rotor structure bring some special design considerations to the FSPM machine. The third contribution of this research is to investigate the housing loss and windage loss of the 6/4 FSPM machine. 3D electromagnetic FEA simulation, CFD simulation is used to evaluate the characteristics of the machine. Modified machine structures to reduce the housing and windage loss are proposed, and the impacts on the electromagnetic performance are studied.

Two prototype 6/4 FSPM motors with double-layer winding and single-layer winding, respectively, are built and tested to validate the electromagnetic and thermal performance predicted by the analytical calculation, FEA simulation, and CFD simulation. The measured results are compared with the models.

Organization of chapters

This thesis is organized as follows:

- Chapter 1 reviews state-of-the-art researches on the flux-switching permanent machine, including the operating principle, various FSPM machine topologies, and

multi-physics design on the FSPM machine. Knowledge gaps and research opportunities are pointed out at the end of the chapter.

- Chapter 2 first discusses the fundamentals of the 6/4 FSPM machine, including the origin of the second-order harmonic in the flux linkage and its cancellation with the dual-stator structure. Different winding configurations and the corresponding winding factor for the 6/4 FSPM machine are investigated. A single-layer toroidal winding 6/4 FSPM machine is proposed. The machine sizing equation and the calculation of important machine parameters are derived. The operating principle of the 6/4 FSPM machine is presented, including the harmonic analysis of the air gap magnetic flux distribution and the winding MMF.
- Chapter 3 presents the comparison study between the existing double-layer 6/4 FSPM machine and the proposed single-layer toroidal winding 6/4 FSPM machine. The single-layer machine is first optimized, then the torque output capability, losses distribution, efficiency, and resistance to demagnetization are compared.
- Chapter 4 presents the cooling design and thermal analysis of the 6/4 FSPM machine. Two types of water jackets with spiral and axial cooling channels are designed and compared, respectively. The cooling fluid flow and heat transfer characteristics are studied with computational fluid dynamics. The steady-state and transient thermal performance of the single-layer winding and double-layer winding 6/4 FSPM machine are analyzed with the lumped parameter thermal network model and thermal finite element analysis, respectively.
- Chapter 5 shows some design considerations that are unique for the FSPM machine, such as housing eddy current loss minimization and windage loss reduction. Modified machine structures are implemented to mitigate high housing loss and

windage loss. The structural and thermal performance impacts brought by the modified structures are studied and investigated.

- Chapter 6 presents the mechanical design and the manufacture of the single-layer winding and double-layer winding 6/4 FSPM prototype motor. The experimental testing setups for the two prototype motors are presented. The electromagnetic and thermal testing has been conducted on the two 6/4 FSPM prototype motors at different operating points. The measured data are compared with the results from the analytical calculation and FEA simulation.
- Chapter 7 gives the conclusion found from this research and summarized the contributions. Potential future work related to this research subject is also proposed in this chapter.

Chapter 1 State-of-the-Art Literature Review

In this chapter, an overview of the design and operating principle of the flux-switching permanent magnet (FSPM) machine is given. The state-of-the-art research relating to the FSPM machine is reviewed. The knowledge gap in the FSPM machine study and potential research opportunities are identified. This chapter begins with an introduction of the stator-mounted PM machines, which is a general category that the FSPM machine belongs to. The second section reviews the analysis methods developed for the FSPM machine in the literature, including magnetic circuit, flux modulation theory, etc. The third section presents the topologies of low-pole FSPM machine, which is suitable for high-speed application that has been proposed and studied. The multi-physics design of the FSPM machine, such as thermal analysis, structural analysis, and windage loss study, are shown in Section 4. The summary of the chapter is given at last.

1.1. High-speed machine and stator mounted pm machines

Being omnipresent in daily life and industry, electric machines are key power conversion tools in modern society, either from mechanical energy to electrical energy (generator) or the other way around (motor). The development of electric machines is a highly integrated and multi-disciplinary subject, including material science, mechanical engineering, electrical engineering, and even computer science. During the past hundred years of development, many electric machine topologies operating with AC or DC power source, with or without permanent magnet material, have been proposed and studied. Each topology has its advantages and should be chosen according to the application. The development trend of electric machines is always toward higher power density and efficiency. Thanks to the inventions and discoveries of new materials and

manufacturing technologies, more degrees of freedom is available for the machine designer to push the performance to limit.

1.1.1. High-speed electric machine

For rotary electric motors, the power is calculated as the product of output torque and rotation speed. The output torque mainly depends on the input armature current, which is limited by the cooling capability of the motor. An alternative way to increase power density is to increase the speed. For the same level of power density, the high-speed machine has the benefit of reduced size and weight. Besides, for high-speed applications such as compressor and drilling tool, another advantage of the high-speed machine is that no gearbox is needed, which further reduce the machine sizing and cost. Machine reliability is also increased because of less component [1]–[3].

The criterion of “high-speed” is commonly defined by the rotor tip speed. As shown in Figure 1.1-1, the tip speed could be calculated as the product of rotor radius in meter and the rotation speed in radians per second. A high-speed machine could be either machines with small rotor sizing and high rotating speed or very large machines at a relatively lower speed. Typically, the high-speed machine indicates a tips speed higher than 100 [m/s].

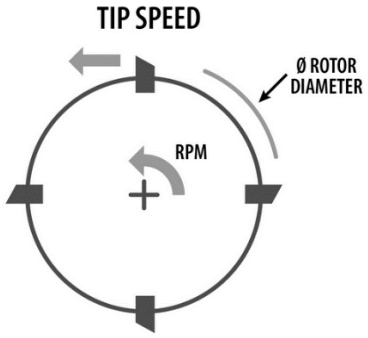

Figure 1.1-1. Definition of tip speed of a rotating item

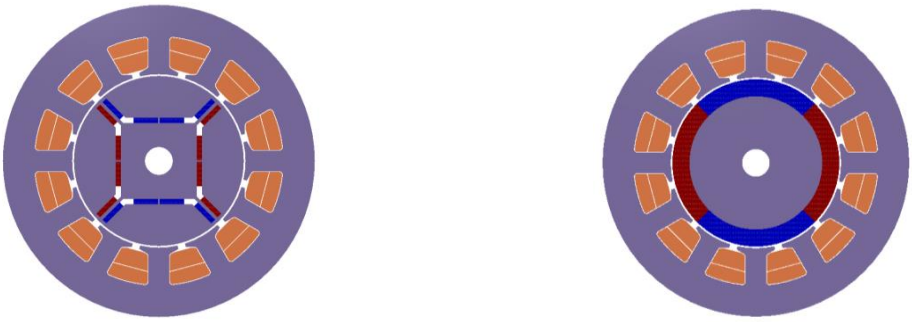

(a) (b)

Figure 1.1-2. Section view of (a) Interior permanent magnet machine (b) Surface permanent magnet machine

Nowadays, the most used and investigated machine topologies for high-speed applications are induction machine (IM) and surface permanent magnet (SPM) machine. The induction machine is a very mature machine topology, it has a very robust rotor structure and low cost. However, due to the slip frequency existing in the rotor, IM has large rotor loss compared to SPM and IPM. IM also has large copper loss because the armature current is made up of magnetizing current and torque production current. In general, the power density and efficiency of IM are inferior compared to the permanent magnet machines.

SPM machine has permanent magnets attached to the rotor surface, as shown in Figure 1.1-2. Comparing to the induction machine, the excitation field is supplied by a permanent magnet. Therefore, no magnetizing current is needed, except for field weakening or field intensifying operation. The problem with the SPM machine for high-speed applications is that at high-speed, the magnets need a large enough centrifugal force to keep attached to the rotor. The most common solution to this issue is binding the magnets to the rotor by retaining sleeves with high structural strength such as glass fiber, carbon fiber, or Titanium [4] [5]. Depending on the mass of magnet and the rotating speed, the retaining sleeve thickness varies from fractions of a millimeter to several millimeters. However, the sleeve not only introduces an extra air gap between stator and rotor,

which affects the machine performance but also causes Eddy current loss since the sleeve is usually electrically conductive [6]. Another problem with the SPM machine is rotor thermal management. It is known that the properties of permanent magnet material such as remnant flux density and coercivity depend on the operating temperature [7]–[9]. As a matter of factor, it is hard to remove heat from the machine rotor because it is usually locating in the middle of the machine. Rotor cooling technologies such as shaft-mounted fan, oil-spraying cooling, and heat pipe have been investigated [10]–[15] in the past decades. However, rotor cooling is still not as effective as stator cooling. In addition, these cooling technologies usually have a complex structure and occupy significant volume, which compromises the power density and reliability of the machine

Interior permanent magnet (IPM) is one of the most popular machine topologies because of high efficiency and high power density. IPM is widely used in electric vehicles due to its excellent traction capability. However, IPM is not widely used in high-speed applications, mainly due to the structural issue. As shown in Figure 1.1-2, The rotor of the IPM machine has cavities to avoid magnetic flux leakage between magnets. The thin bridge between cavities would sustain significant stress under high-speed conditions [16] [17]. Other electric machine topologies such as switch reluctance machine (SRM) and synchronous reluctance machine (SyRM) also have the drawback of low power density or low power factor since no permanent magnet is used in the machine.

From the discussion stated above, for high power density, the use of permanent magnet material is preferred. However, due to either structural or thermal issues, a rotor mounted permanent magnet machine topology has challenges for high-speed application.

1.1.2. Stator-mounted PM machine

As mentioned previously, the permanent magnet synchronous machine (PMSM) has advantages of high torque density and high efficiency. The permanent magnet flux rotates at the

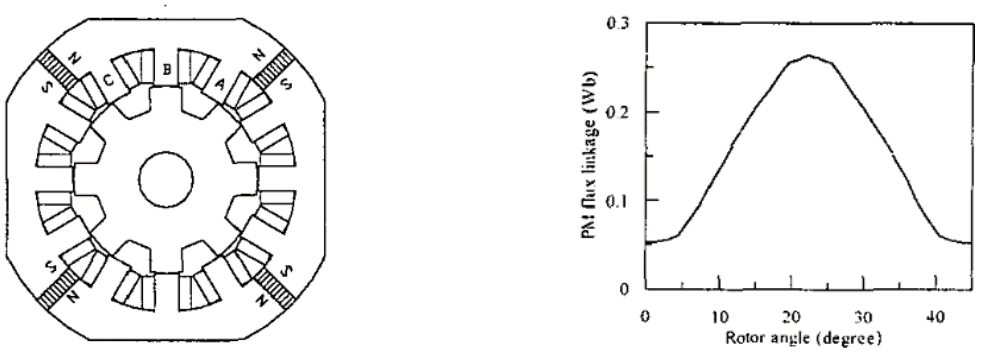

(a) (b)

Figure 1.1-3. Three-phase 12 slot 8 pole DSPM machine (a) Section view (b) Flux linkage waveform. [20]-[22]

same speed as the rotor and interacts with armature MMF to produce torque. With the development of permanent magnet material in the past few decades, rare earth permanent magnet such as NdFeB magnet can provide intensive magnetic flux density. To avoid the issues discussed for rotor-mounted PM machines in Section 1.1.1, several types of stator mounted PM machines have been proposed and investigated in the past few decades, including flux reversal permanent magnet (FRPM) machine, doubly salient permanent magnet (DSPM) machine and flux switching

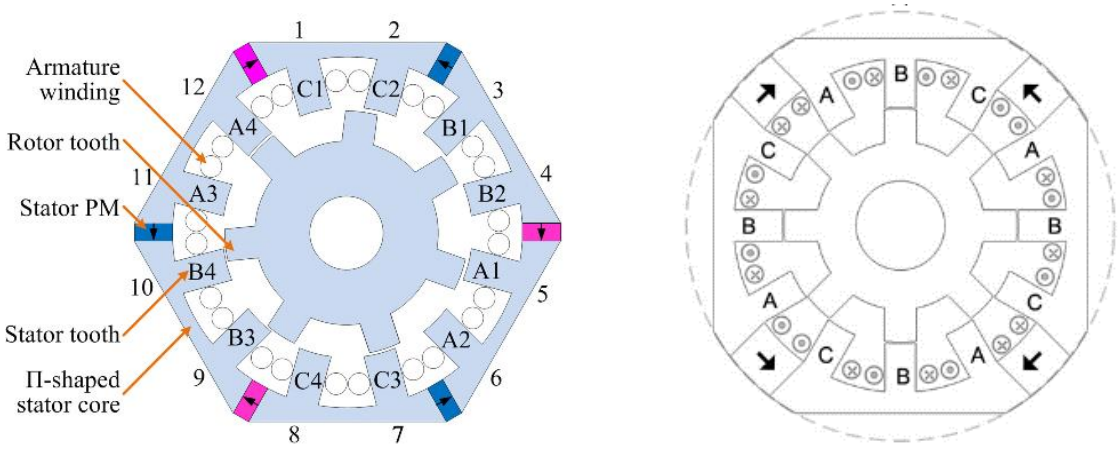

(a) (b)

Figure 1.1-4. Special stator core shape for increased magnet volume (a) Hexagon shape stator (b) Square shape stator [24][25]

permanent magnet (FSPM) machine [18] [19]. For rotor mounted PM machine, the magnet flux is rotating at the same speed as the rotor, the flux linkage for each phase is bipolar and sinusoidal. The difference is mainly with respect to the inductance and machine saliency. However, the operating principles of stator mounted PM machines are different and depend on the placement of permanent magnets.

Doubly salient permanent magnet machine has permanent magnets located at the stator yoke, magnetized circumferentially [20]–[22]. Double layer concentrated windings are used for DSPM, as shown in Figure 1.1-3. Taking the 12/8 topology as an example, it can be seen that in Figure 1.1-3, when the rotor rotates 45 degrees, the flux linkage for one phase is varying form a positive minimum to a maximum in an almost linear fashion then goes back to the minimum (trapezoidal). Because of the unipolar flux linkage, the magnetic loading of DSPM is limited. The back electromotive force (EMF) of this machine has a square waveform, which means DSPM operates with DC commutation drive, similar as brushless DC machine. Other DSPM topologies such as 4/6, 6/8 structure have been proposed and investigated as well [23] [24]. It is shown that DSPM

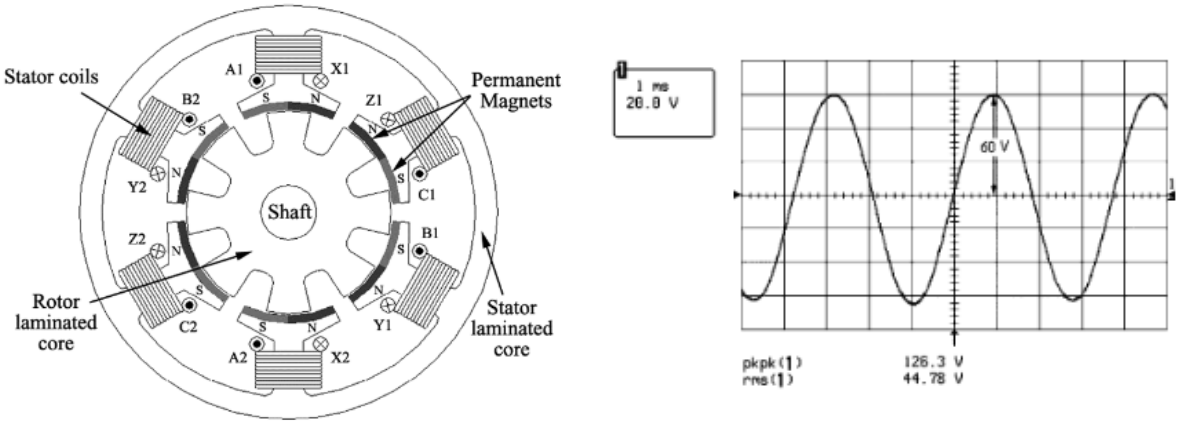

(a) (b)

Figure 1.1-5. Flux reversal permanent magnet machine (a) 6/8 topology (b) Back EMF waveform [26]-[28]

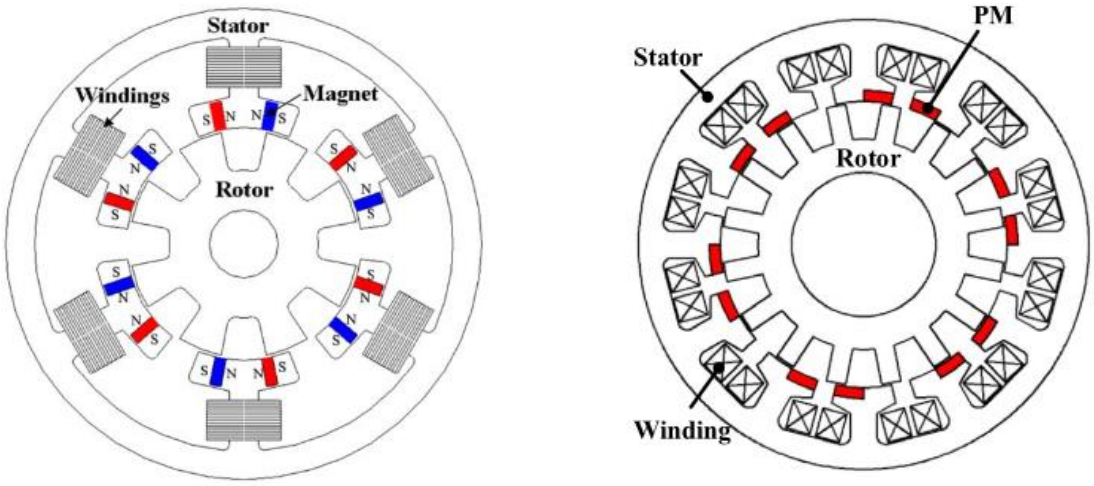

(a) (b)

Figure 1.1-6. Novel flux reversal permanent magnet machine topologies for reducing flux leakage (a) Inset magnet structure (b) Consequent pole structure [29][30]

has a good fault tolerance capability. Because the permanent magnet is in the stator back yoke, the volume of the magnet is constraint by the stator outer diameter, which limits the power density of DSPM. Special shape stator core for DSPM, as shown in Figure 1.1-4, has been proposed to increase the magnet volume without expanding the total machine volume [24] [25].

Another stator-mount PM machine topology is called flux reversal permanent magnet machine, where two slices of permanent magnet with opposite magnetizing orientation are attached to one stator tooth [26]–[28], as shown in Figure 1.1-5. The structure of the FRPM machine has some similarities from the SPM machine, where the magnets are in the air gap region. When the rotor pole sweeps from one magnet to the next one, the flux linkage in the corresponding coil changes direction. In other words, the flux linkage of the FRPM machine is bipolar. As shown in Figure 1.1-5, the back EMF of FRPM is sinusoidal, which means this machine operates with a normal AC drive. The bipolar flux linkage enables the FRPM machine to have a higher power density compared to the DSPM machine. However, since the permanent magnets are located

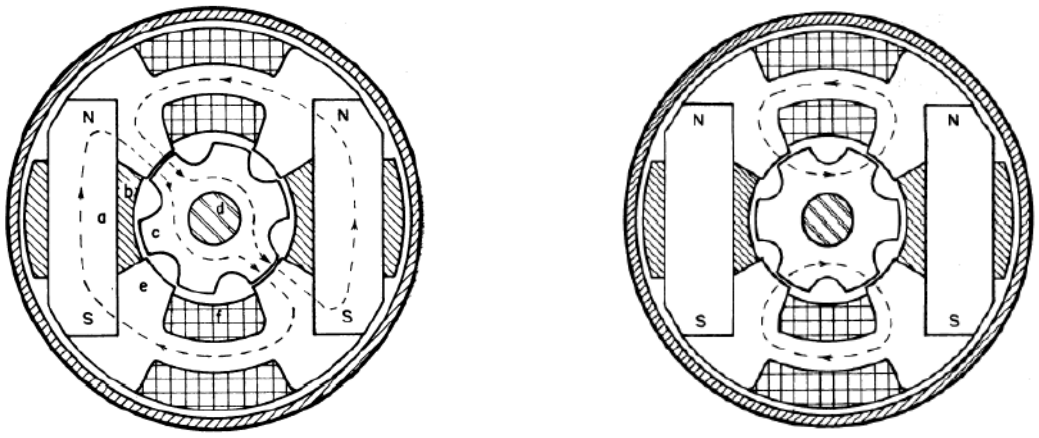

(a) (b)

Figure 1.1-7. Single-phase FSPM alternator [31]

between the stator and rotor, the equivalent air gap is large. Note that the armature MMF is in series with the magnetic flux provided by the permanent magnet, there is a risk of permanent demagnetization.

In addition, the two magnets with opposite magnetizing directions are placed next to each other. There will be flux leakage between the north and south pole, which reduces the usage of PM material. Novel FRPM topologies have been proposed to reduce the flux leakage by employing inset magnet, and consequent-pole structure [29] [30], the section views of these two topologies are given in Figure 1.1-6. Another concern about the FRPM machine is stator integrity. The permanent magnet pieces are attached to the inner surface of stator poles. It is challenging to use the retaining sleeve as for SPM machine. Although the stator-mounted permanent magnets do not have movement during normal operation, parasitic vibration and gravity could potentially disintegrate the magnets from stator pole and cause permanent damage to the machine.

The third type of stator-mounted PM machine is flux-switching permanent magnet machine. The concept of flux-switching is first brought up in 1955 for a single-phase alternator [31]. The section view of the FSPM alternator is shown in Figure 1.1-7. As the rotor pole sweeps from one

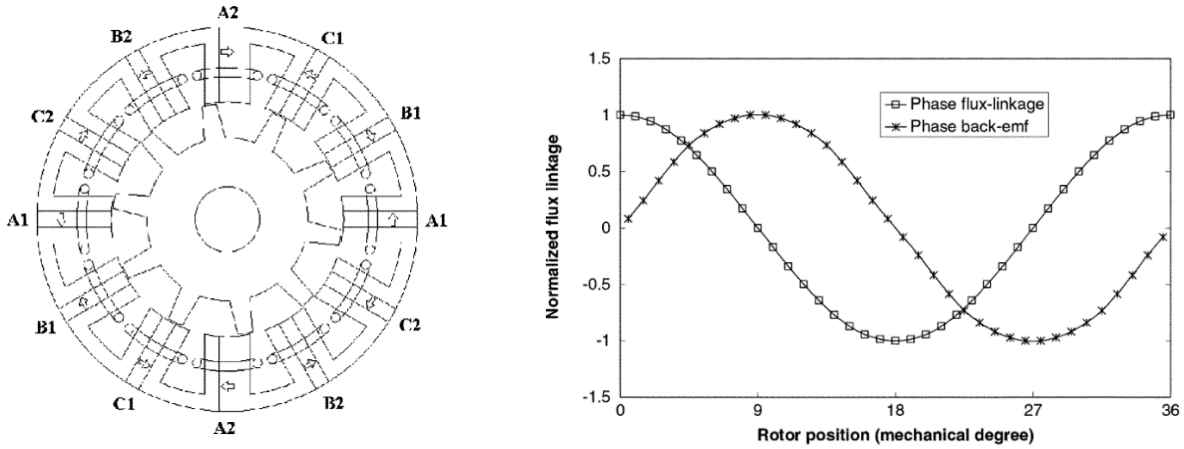

(a) (b)

Figure 1.1-8. Three-phase FSPM machine (a) Section view (b) Flux-linkage and back EMF waveform [33]

stator tooth to the next, the flux linkage across the stator winding changes direction, and in the mid-position, the net flux linkage will be zero. The FSPM machine has a bipolar flux linkage and has the permanent magnet in the stator yoke. Therefore, compared to DSPM and FRPM machine, the FSPM machine provides higher power density and less risk of permanent demagnetization since the magnetic flux source of the PM is in parallel with armature MMF. However, the FSPM machine was not very popular in the early age due to the low remnant flux of the magnet. Nowadays, with the appearance of the strong rare-earth permanent magnet, FSPM machine is becoming a widely investigated research topic [32], [33], [42]–[44], [34]–[41].

The most commonly seen 3-phase FSPM machine structure has 12 stator slots and 10 rotor poles (12/10), with the permanent magnets placed in spoke type (magnetized circumferentially) between two stator cores, as shown in Figure 1.1-8 (a). As can be seen in Figure 1.1-8 (b), the flux linkage and back EMF of 12/10 FSPM machine have a sinusoidal waveform, which make this machine suitable to operate with AC drive. The spoke type permanent magnets are placed in adjacent to the long edge of the stator teeth. The magnetic flux is concentrated to the relative short stator tooth. The flux focusing effect allows the FSPM machine has a high air gap flux density.

TABLE 1-1. COMPARISON OF STATOR-MOUNTED PERMANENT MAGNET MACHINES

Aspect/Topology	Double Salient	Flux Reversal	Flux Switching
PM Placement	In stator yokes	On stator teeth surface	Besides stator teeth
PM Volume	Low	Medium	High
Flux Linkage	Unipolar	Bipolar	Bipolar
Drive Type	Brushless DC	Brushless AC	Brushless AC
Power Density	Low to medium	Low to medium	High
Slot Area	Medium	Large	Small
Stator Assembly	Medium	Medium	Complex
Risk of Demagnetized	Low	High	Low

Because of the sandwich structure of stator iron and the permanent magnet, the stator assembly of the FSPM machine is more complicated than DSPM and FRPM machine. It often involves modular stators, which increase the difficulty in assembly and keeping tolerance. The stator slot area of the FSPM machine is smaller compared to the other stator-mounted PM machine and rotor-mounted PM machine. Therefore, the electrical loading capability is restricted. Other topologies of FSPM with different slot/pole combinations and phase numbers have been investigated by researchers as well due to the advantage of the FSPM machine mentioned previously. They will be recapitulated in the following sections.

To have a clear comparison among the three major types of stator-mounted PM machines, TABLE 1-1 summarizes a qualitative analysis of the three machine topologies [18] [19]. As can be seen, compared among the stator-mounted PM machines, despite the relative complex stator assembly, the FSPM machine has high power density due to the flux focusing effect and bipolar flux linkage and low risk of demagnetization of the permanent magnet. Comparing with SPM and IPM machines, the FSPM machine has the advantage of easy thermal management and robust rotor

structure. The advantages mentioned above make FSPM machine an interesting machine topology to investigate.

1.2. Flux-switching machines topologies in literature

1.2.1. FSPM machine operation principle

As presented in the previous section, the FSPM machine has a doubly salient structure, with permanent magnet circumferentially magnetized and placed between two U-shape stator units. Armature windings of conventional FSPM machines are wound in such a way that each coil surrounds one permanent magnet. A 3D view of a 12/10 FSPM machine is shown in Figure 1.2-1,

where the magnets with different magnetization direction and armature coil for different phases are marked with different colors. As the name of the machine suggests, as the rotor rotates, the direction of the flux linkage of the armature winding switches. It is shown in Figure 1.1-8 that the flux linkage varies in a sinusoidal way. The back EMF of an electric machine could be calculated as the derivative of flux linkage. Therefore, the back EMF of the FSPM machine also has a sinusoidal shape.

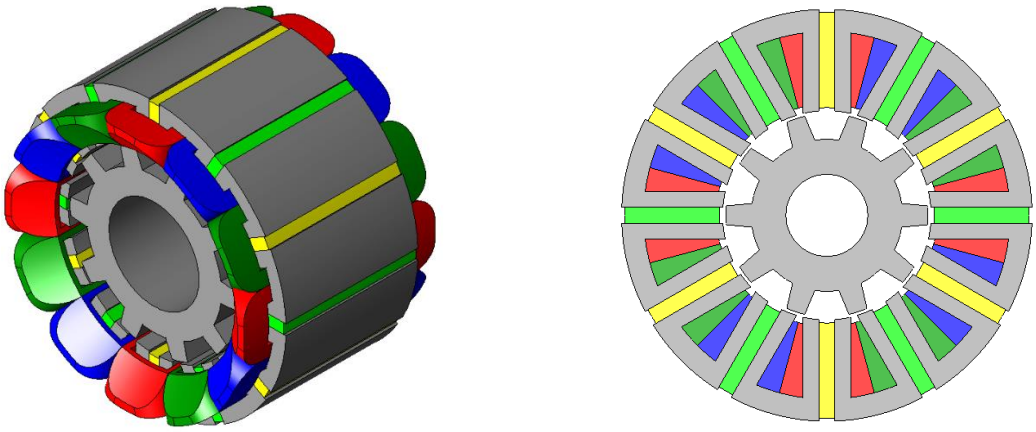

(a) (b)

Figure 1.2-1. Geometry of conventional 12/10 FSPM machine (a) 3D isometric view (b) Section view [117]

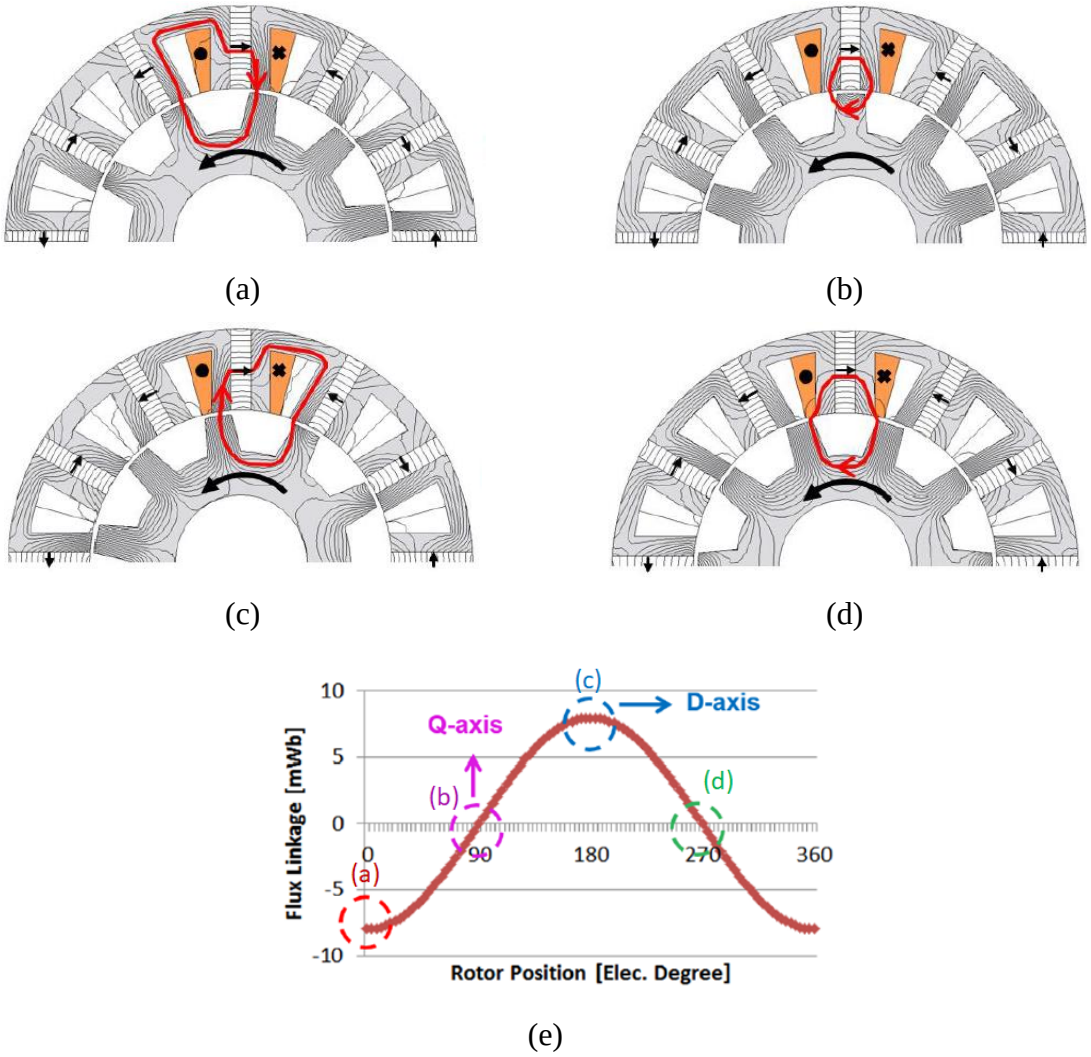

Figure 1.2-2. Permanent magnet flux path in 12/10 FSPM machine with different rotor positions (a) Minimum flux linkage position (b) First zero flux linkage position (c) Maximum flux linkage position (d) Second zero flux linkage position (e) Flux linkage waveform. [45]

To better demonstrate the operation of the FSPM machine, section views of 12/10 FSPM machine with four critical rotor positions are shown in Figure 1.2-2 (a) – (d). The flux linkage waveform with four special positions marked up is shown in Figure 1.2-2 (e).[45]. Note that the rotor positions with maximum/minimum flux linkage correspond to the d-axis position, the zero flux linkage positions are the q-axis positions. Unlike the rotor-mounted PM machine, where the d-q axis positions are stationary in the rotor reference frame, *d-q* position in the FSPM machine

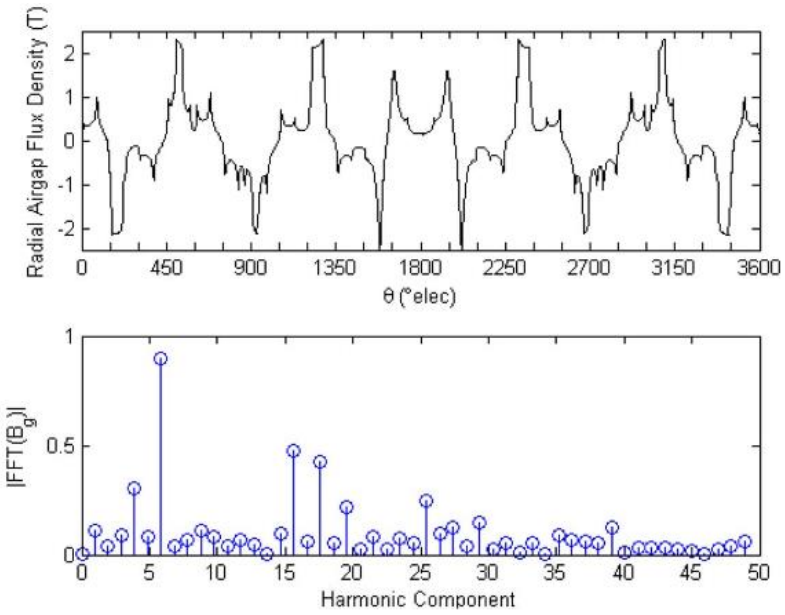

Figure 1.2-3. 12/10 FSPM airgap flux density waveform and harmonic components [46]

depends on the relative position of stator/rotor tooth. In the FSPM machine, as each rotor pole sweeps across the same stator tooth, it is one full electric cycle. Therefore, the pole pair number of FSPM machine equals the rotor pole count, i.e., the 12/10 FSPM machine is a 20-pole machine. The relation between rotor mechanical speed and fundamental frequency is given in (Equation

$$f_s = \frac{nN_r}{60} \qquad \text{(Equation 1-1)}$$

1-2), where f_s is the fundamental frequency in [Hz], n is the mechanical rotation speed in [rpm], N_r is the number of rotor pole. The FSPM machine airgap flux linkage is the result of modulation between permanent magnet MMF and airgap permeance, as shown in Figure 1.2-3. Non-negative torque is produced by matching the same harmonic components in the airgap flux linkage and armature MMF. The flux modulation is the operation principle of many electric machines, such as the doubly salient permanent magnet machine and the Vernier permanent magnet machine [46] [47]. More details about flux modulation will be presented in the analysis of FSPM machine in chapter 2.

As can be seen in Figure 1.2-2, for both *d*-axis position and *q*-axis position, the magnet flux lines pass through the permanent magnet, which has permeability close to air. In other words, the variation of permeance between *d*-axis and *q*-axis is not significant as that in the IPM machine. Therefore, the d-q inductance is almost the same for the FSPM machine. For the PM machine, the output torque could be calculated by (Equation 1-2), where L_d, L_q, I_d, I_q are the *d*-axis and *q*-axis inductance in [H] and current in [A] respectively, Ψ_{pm} is the permanent magnet flux linkage in [Wb]. The first part in (Equation 1-2) is referred to as magnetic torque. The second part is called

$$T_{out} = \frac{3}{2} N_r [\Psi_{pm} I_q + (L_d - L_q) I_d I_q] \qquad \text{(Equation 1-2)}$$

reluctance torque. Since in the FSPM machine, the difference in L_d *and* L_q is negligible. Therefore, FSPM torque is from magnetic torque, similar to the SPM machine.

1.2.2. Stator slot/rotor pole combination of FSPM machine

As mentioned in the previous section, the 12/10 is the most seen FSPM structure because of sinusoidal back EMF and symmetric radial force. Other stator slot/rotor pole combinations are possible and could be more appropriate for a specific application than 12/10 topologies such as low speed, high torque application. Many researches have been done on the investigation of optimal slot/pole combination for a different number of phases and winding types [48] [34] [49]. The stator slot number should be an even number and a multiple of the machine phase number. The number of rotor pole needs to be different from the stator slot because of the flux modulation. The stator slot number N_s and rotor pole number N_r could be determined from (Equation 1-3) and (Equation 1-4) where *m* is the number of phases, k_1 and k_2 are integers.

$$N_s = k_1 m \qquad k_1 = 1, 2\ldots \qquad \text{(Equation 1-3)}$$

$$N_r = N_s \pm k_2 \qquad k_2 = 1, 2\ldots \qquad \text{(Equation 1-4)}$$

Note that when the number of phase *m* is an odd number, k_1 needs to be an even number to have a symmetric flux linkage. Taking the example of a 12-slot FSPM machine, the variation of normalized back EMF amplitude is given in Figure 1.2-4. It can be seen that high back EMF could

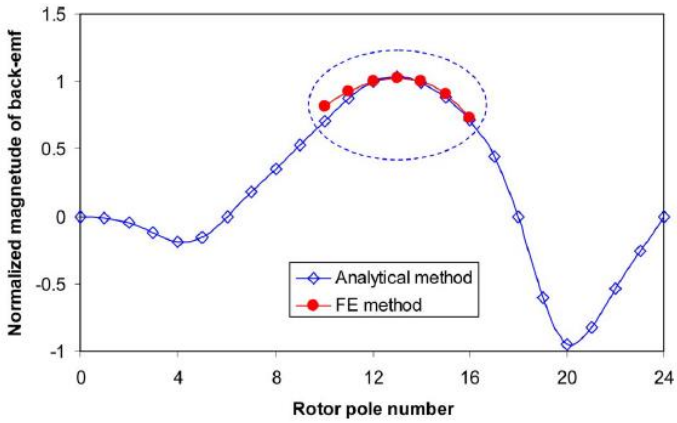

Figure 1.2-4. Variation of back EMF amplitude as a function of rotor pole number [48]

be achieved when the stator slot number and rotor pole number are close. Although the flux linkage and back EMF of 12/10 FSPM machine are sinusoidal, for a single coil, the back EMF could be asymmetric because of the permeance variation. Symmetrical phase flux-linkage could be achieved by employing two coils that have a phase shift of 180 electrical degrees. The angular difference in radians between two coils in the same phase is given by (Equation 1-5), where n_{pp} is the number of stator pole pitches between the two coils belong to the same phase. To have a 180-degree phase shift between the two coils, (Equation 1-6) needs to be satisfied, where k_3 is also an

$$\theta_{coil} = \frac{2\pi N_r n_{pp}}{N_s} \qquad \text{(Equation 1-5)}$$

$$\frac{N_r}{N_s} = \frac{2k_3 - 1}{2n_{pp}} \qquad \text{(Equation 1-6)}$$

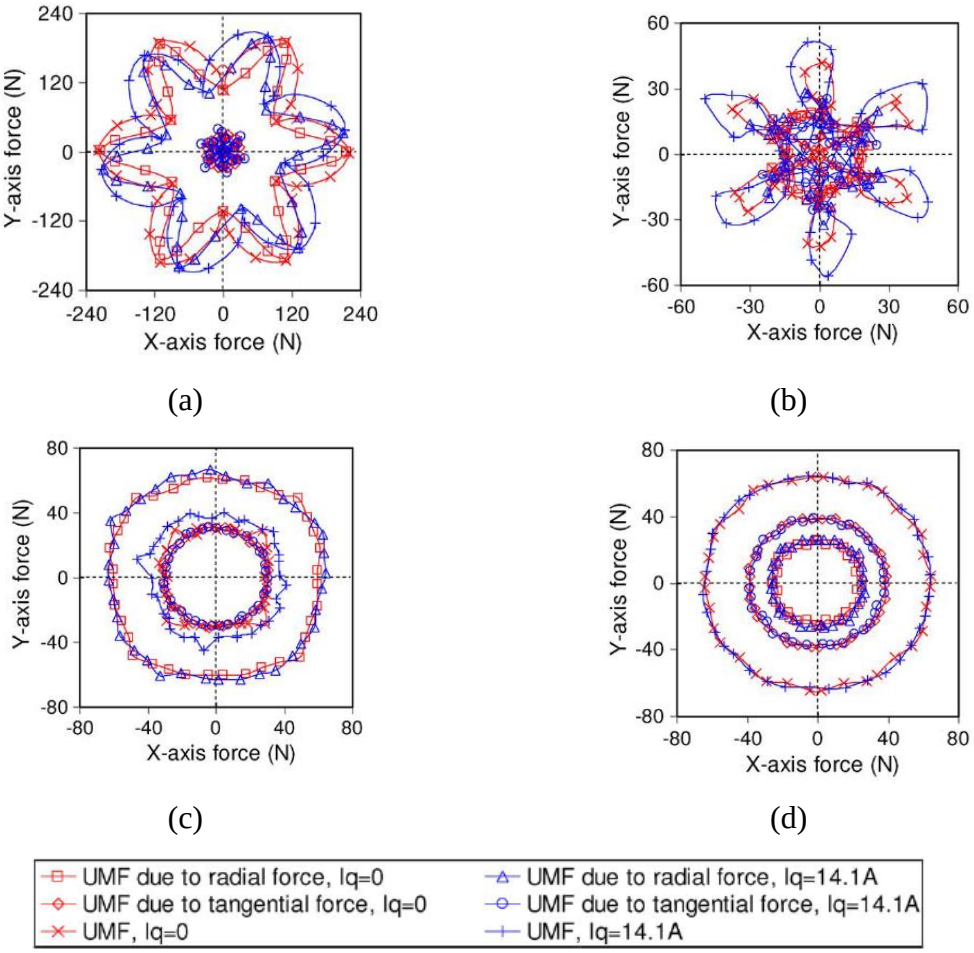

Figure 1.2-5. Illustration of magnetic force (I_d = 0) of (a) 6/5 FSPM. (b) 6/7 FSPM. (c) 12/11 FSPM. (d) 12/13 FSPM. [50]

integer. (Equation 1-5) could be rewritten as (Equation 1-7). It can be seen that in the irreducible

$$2\pi\frac{N_r}{N_s}n_{pp}=(2k_3-1)\pi \qquad \text{(Equation 1-7)}$$

fraction format, the numerator should be an odd number, and the denominator should be an even number. However, it is shown that FSPM machines with an odd number of rotor pole sustain an unbalanced magnetic force (UMF) [50], as illustrated in Figure 1.2-5. The UMF exerts extra stress on the bearing and the shaft, which reduces the reliability of the machine and causes vibration and

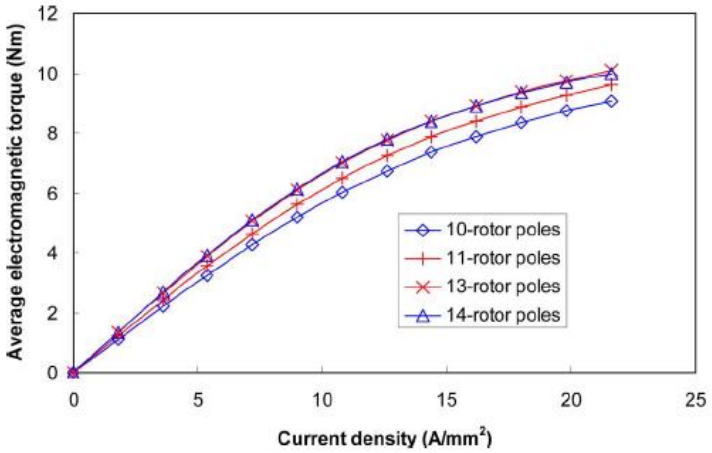

Figure 1.2-6. Torque-current characteristic of 12-slot FSPM machine [48]

noise during operation. To have an even number of rotor pole and satisfy (Equation 1-5), the number of stator slots (N_s) will be a multiple of 4.

From the parametric plot shown in Figure 1.2-4, it can be seen that for 12 slot FSPM machine, rotor with 10 to 14 rotor poles gives the highest level of back EMF. The torque-current plot, as shown in Figure 1.2-6, indicates that higher torque could be achieved with a higher number of rotor pole. Per the previous discussion, the odd rotor pole number is not preferable due to UMF. Therefore, 14 pole structure is the best choice in term of torque production. However, the FSPM machine with a large number of rotor pole requires high fundamental frequency as (Equation 1-2)indicates, which might cause a high iron loss in the machine and switching loss in the drive.

The number of rotor poles affects the vibration and acoustic noise level as well. Because of the unbalanced magnetic force, 12/11 and 12/13 FSPM structure have a higher level of vibration and noise, specifically due to the third and fifth harmonics [49]. It is shown in [51] that rotor only matters for low frequency under 500 Hz, and the first resonant frequency related to circumferential mode appears above 4 kHz. The spectrum of the sound power level of the FSPM machine with the same stator structure but different rotor pole numbers are given in Figure 1.2-7. The mode 0 and

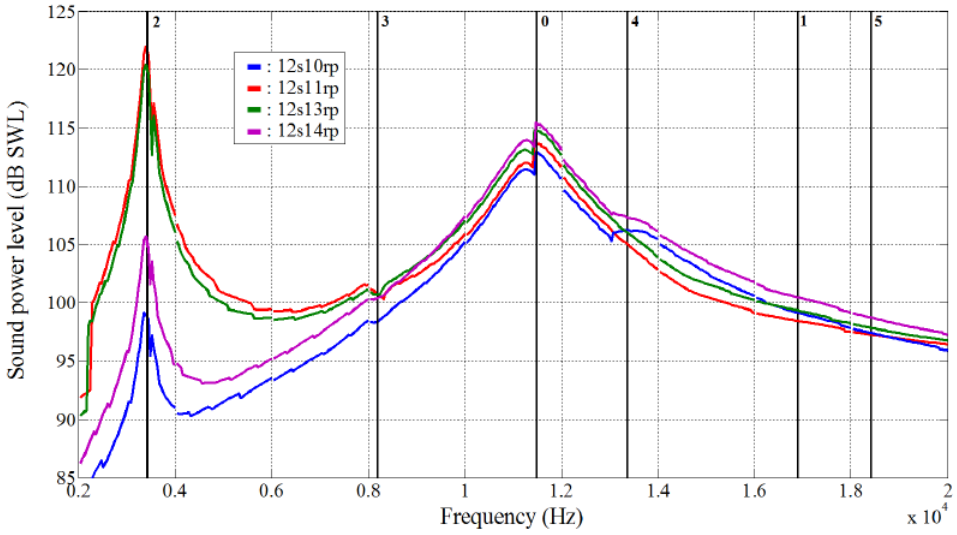

Figure 1.2-7. Sound power level of loaded configuration for 12-slot FSPM machine with different number of rotor poles at 400 rpm. [51]

mode 2 which correspond to 11490 Hz and 3414 Hz respectively have the largest sound power level. It is shown that 12/10 FSPM structure has the lowest sound power level among all 12-slot structures.

A three-phase electric machine is the most common type of AC machines. However, multi-phase (phase number > 3) machines are popular for certain applications that require a high level of reliability such as aerospace application, ship propulsion, and wind power generation [52] [53] [54]. Additional phases allow the drive to have a more flexible control strategy and better fault-tolerant capability compared to a three-phase drive. For very high power rating machines with MW level power, a higher phase number is often preferred since individual inverter power rating is decreased [55] [56], which could reduce the total cost and improve reliability as well. Figure 1.2-8 shows the section views of five-phase and nine-phase FSPM machines. It can be seen that the number of stator slots (N_s) equals the number of phase times 4, which agrees with the

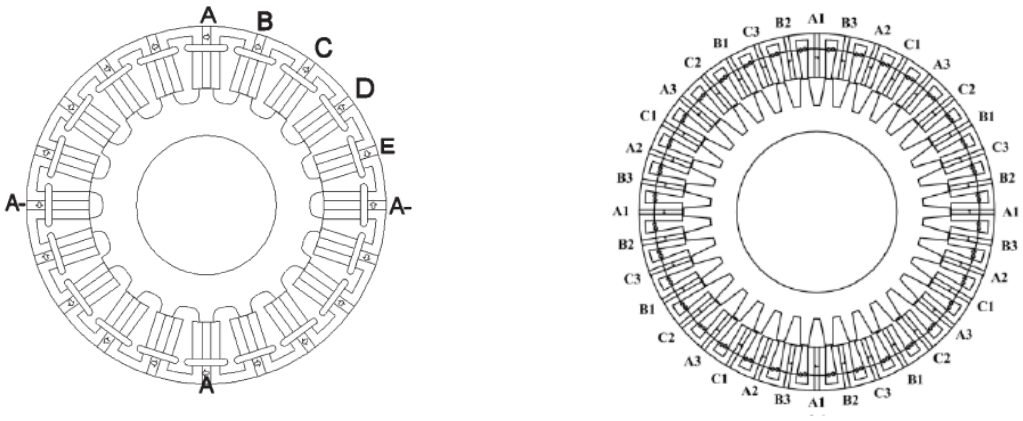

(a) (b)

Figure 1.2-8. Topologies of FSPM machine with high number of phase (a) Five-phase FSPM machine (20/18). (b) Nine-phase FSPM machine (36/34). [55]

conclusion drawn previously. The number of rotor pole is also chosen to be an even number and close to the number of stator slots for high torque production and zero UMF.

1.2.3. FSPM machine with unconventional topologies

FSPM machine has been an attractive research topic because of its unique advantages such as high power density, robust rotor structure, and easy thermal management. However, conventional FSPM machine several drawbacks, for example, high torque ripple, complex stator assembly, high fundamental frequency. Novel FSPM machine structures with either modified stator or modified rotor have been proposed to solve the aforementioned issues. The investigations of the novel FSPM structure not only allow researchers to have a deeper understanding of the operation principle of the FSPM machine but also help to make the FSPM machine more practical for industry and daily applications.

A. Modified stator structures

The FSPM machines usually have a larger permanent magnet material consumption compared to IPM and SPM because the magnets are placed in the stator. The stator-mounted magnets also restrict the winding copper and stator iron volume, which limits the electric loading

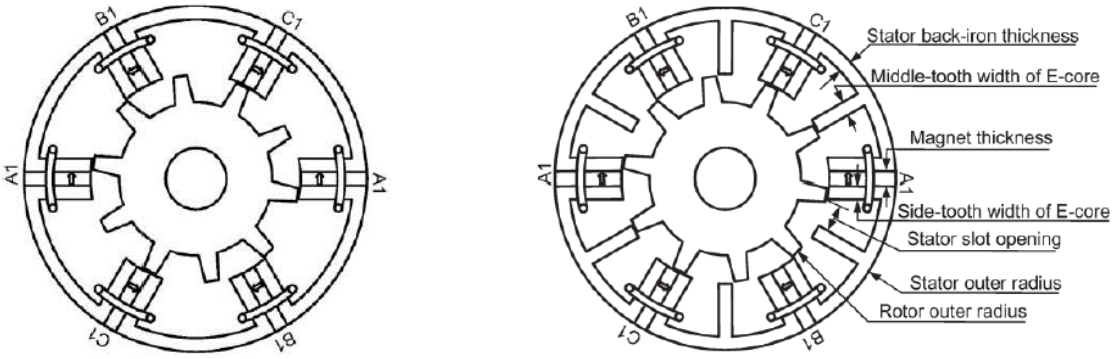

(a) (b)

Figure 1.2-9. (a) C-core FSPM machine (b) E-core FSPM machine [57]

of the machine. Special types of FSPM machine with half of the number of magnets have been proposed, where C-shape and E-shape core are used [37] [57]. The structures of the C-core and E-core FSPM are shown in Figure 1.2-9. It can be seen that the stator slot area is significantly increased compared to the 12/10 FSPM machine. According to the previous discussion, for conventional stator topologies, the number of rotor poles should be close to the number of stator slots to achieve high torque output. To investigate the optimum slot-pole combination, back EMF waveforms of C-core and E-core FSPM machine with various rotor pole number are plotted in

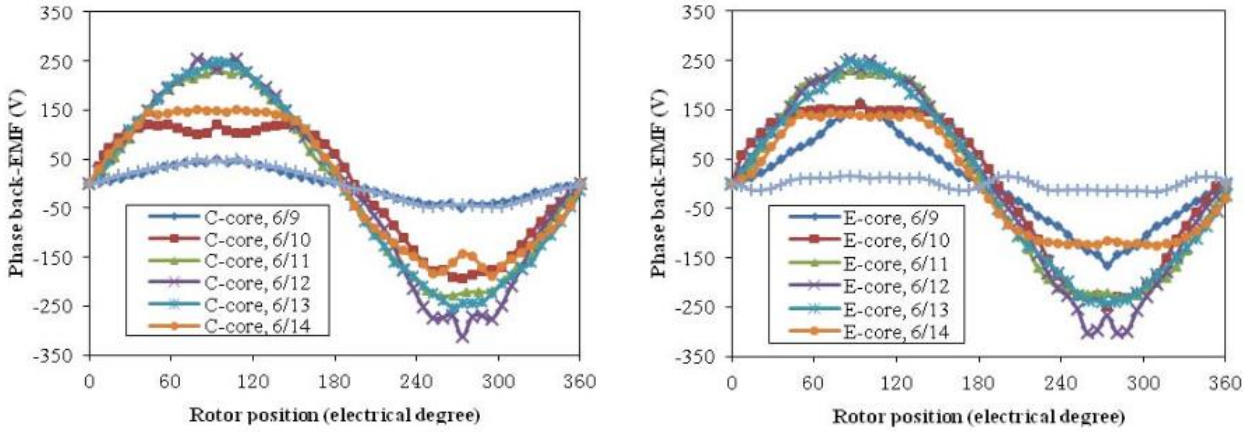

(a) (b)

Figure 1.2-10. Back EMF waveform of (a) C-core FSPM (b) E-core FSPM machine with different number of rotor poles [57]

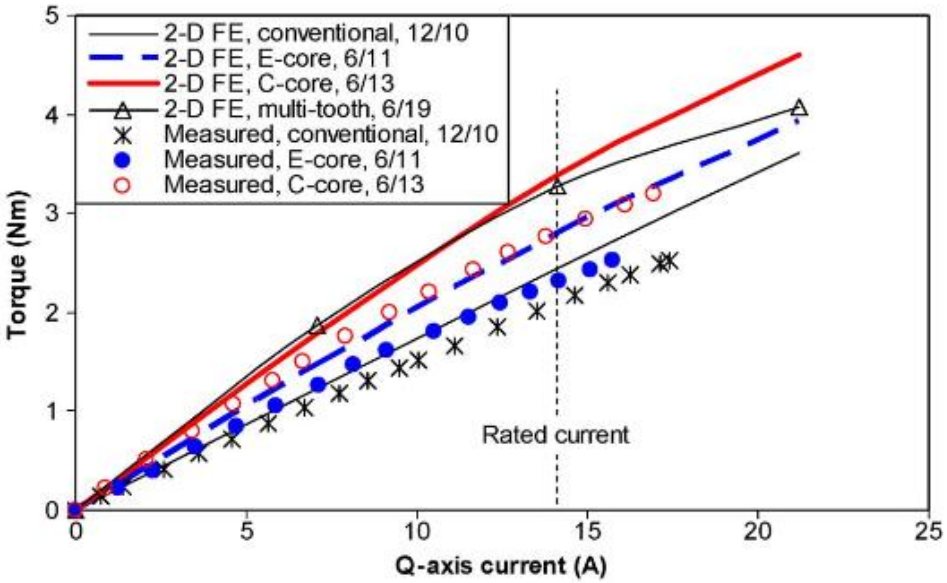

Figure 1.2-11. Torque output characteristics of C-core and E-core FSPM machine [57]

Figure 1.2-10 [57]. It can be seen that for both C-core and E-core, 11 and 13 rotor poles generate the highest amplitude of back EMF. In terms of torque production capability, as can be seen in Figure 1.2-11, the C-core 6/13 and E-core 6/11 structure can produce 35% and 15% more than conventional 12/14 FSPM machine respectively while using a reduced volume of the permanent magnet material. Note that because of the odd number of rotor poles, the C-core 6/13 and E-core

(a) (b)

Figure 1.2-12. Structure of multi-tooth FSPM machine (a) Cross-section view (b) Stator and rotor prototype [58]

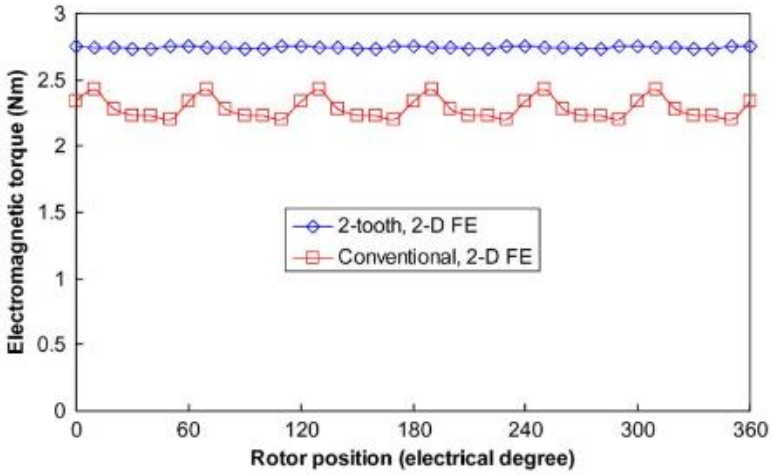

Figure 1.2-13. Torque output of multi-tooth FSPM machine and conventional 12/10 FSPM machine [58]

6/11 FSPM machines have the problem of unbalanced magnetic force. As can be seen in Figure 1.2-10, the C-core and E-core FSPM machine with even rotor pole number have significant THD in the back EMF.

Multi-tooth FSPM structure has been proposed and investigated for high-torque direct drive applications in [58]–[60]. Similar to the C-core and E-core FSPM machine, the multi-tooth FSPM structure also reduces the usage of PM material. As shown in Figure 1.2-12, one stator tooth is split into two, the slot openings between two stator teeth have been kept identical. A rotor pole number of 19 has been proved to work the best with the multi-tooth stator. As can be seen in Figure 1.2-13, the multi-tooth FSPM machine can produce 14% higher torque than the convention FSPM structure. The torque ripple of the multi-tooth structure is significantly reduced compared to the conventional FSPM machine. Figure 1.2-14 shows the torque-current characteristics of the multi-tooth and conventional FSPM machine. It can be seen that the multi-tooth FSPM machine is easier to saturate. Therefore, it has an inferior over-load capability than the conventional FSPM machine.

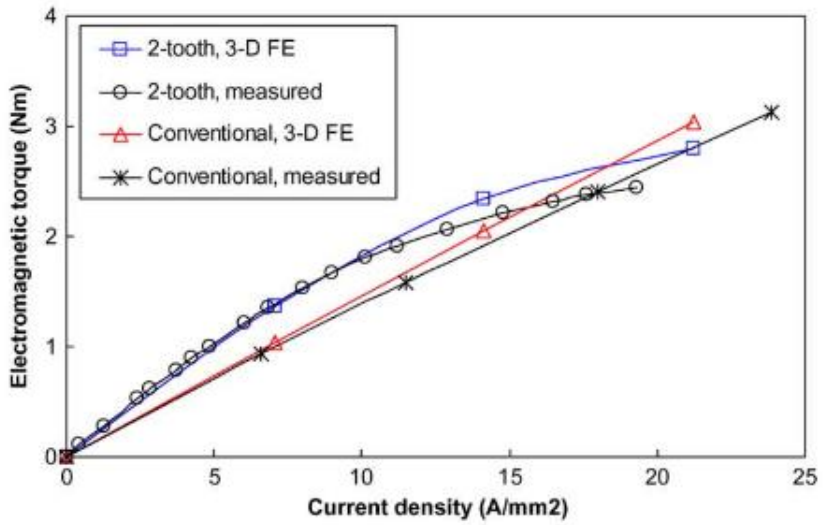

Figure 1.2-14. Torque-current curve of multi-tooth FSPM machine [58]

Sandwiched FSPM structure has been proposed to maximize the output torque density by increasing the stator slot area [61], [62]. A 3D structure of sandwiched FSPM is shown in Figure 1.2-15 (a). The back EMF and average torque of the sandwich FSPM machine are increased compared to the conventional FSPM machine, as can be seen in Figure 1.2-16. To improve the magnet usage efficiency, a V-shape sandwich FSPM machine is proposed, as shown in Figure

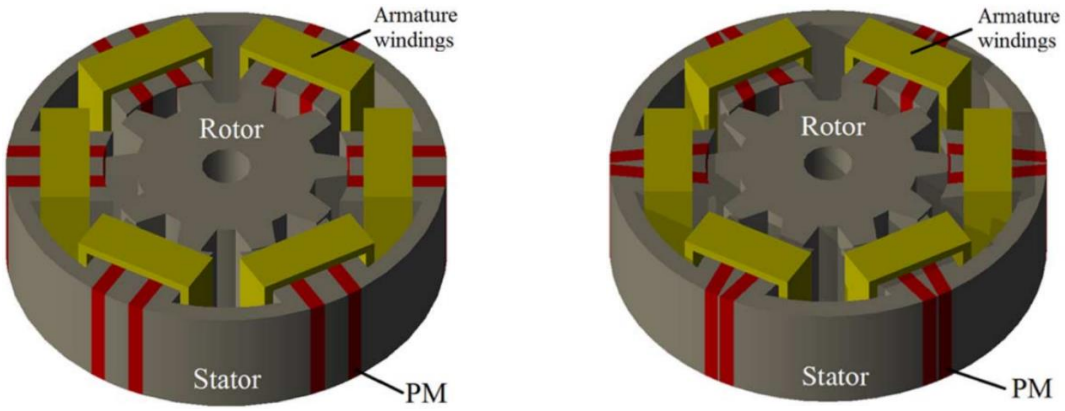

(a) (b)

Figure 1.2-15. FSPM machine with modified magnet placement (a) Sandwiched FSPM (b) V-shape sandwiched FSPM [62]

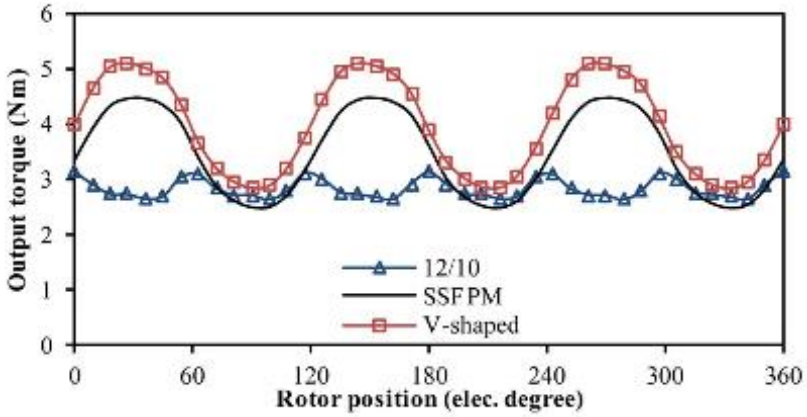

Figure 1.2-16. Output torque comparison of sandwiched FSPM machine and conventional 12/10 FSPM machine [61]

1.2-15 (b). The V-shape sandwiched FSPM machine can achieve higher torque with less magnet material usage because of the higher slot area. However, as shown in Figure 1.2-16, the torque ripple of the sandwiched FSPM machines is much higher than the conventional 12/10 FSPM machine. Torque ripple reduction structure, such as rotor skew, needs to be implemented.

Being able to adjust the permanent magnet flux density level will significantly improve the operating range of the electric machine. A mechanical PM flux adjustment structure has been proposed. In FSPM machine, the magnets are magnetized circumferentially in the stator. Inherent leakage at the outer diameter exist. A moveable ferromagnetic piece could be used to shunt the

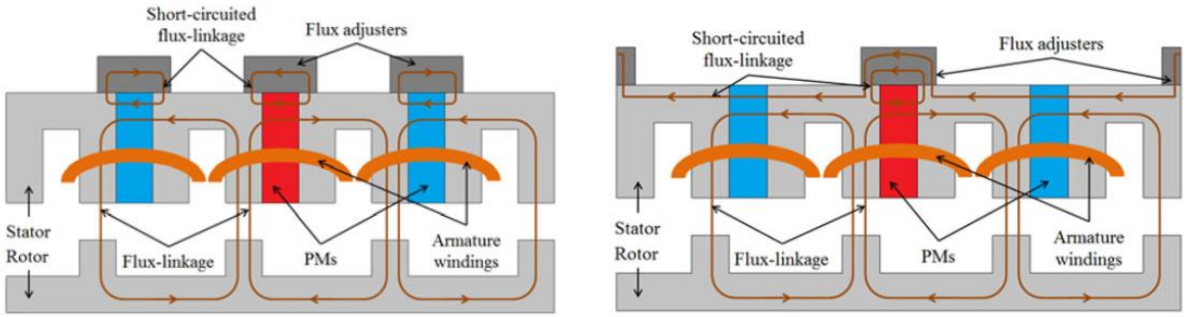

(a) (b)

Figure 1.2-17. Structure of adjustable flux FSPM machine with (a) All flux adjustor (b) Alternate flux adjustor [63]

magnet flux and reduce the counter electromotive force [63]–[65]. Larger speed range could be achieved with the same inverter voltage limit. The structure of the FSPM machine with flux adjustor is shown in Figure 1.2-17, where the flux adjustor could move axially. Note that the flux adjustor could be placed beside either all magnet or alternate magnet, depends on the desired flux adjusting range. Figure 1.2-18 shows the torque-speed curve of the FSPM machine with/without a

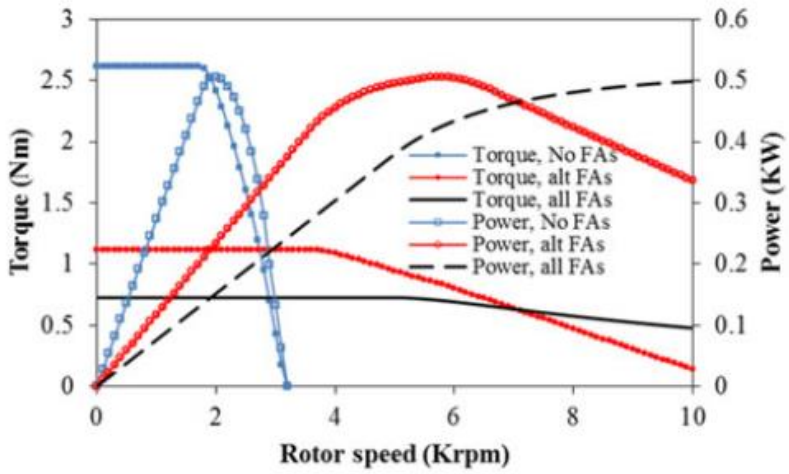

Figure 1.2-18. Torque-speed curve of adjustable flux FSPM machine [63]

flux adjustor. It can be seen that with the flux adjustor, the constant power speed range has been extended. The use of a flux adjustor introduces additional components in the stator and requires separate control of the flux adjustor position. In reference [65], the flux adjustors are placed only in two positions, either fully inserted or fully removed. Partial insertion might cause axial unbalanced torque since stator and rotor iron are axially laminated.

Electric machines with memory permanent magnet with low coercive force such as AlNiCo have been investigated for its easy flux controlling capability [66]–[72]. The magnet with low coercive force could be magnetized and demagnetized with a DC pulse, which only requires energy during the flux changing period. The low coercivity magnet flux is usually in parallel with the high

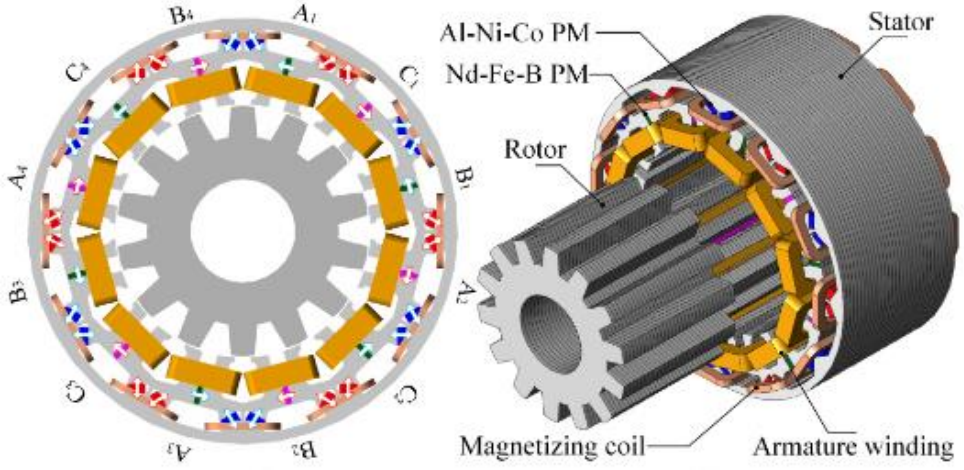

Figure 1.2-19. Memory FSPM machine with two types of permanent magnets [66]

coercivity magnet (such as NdFeB) to alleviate the risk of demagnetization. A similar concept could be used in the FSPM machine, where the two types of magnets are placed in the stator [66]–[72]. Because two types of magnets, as well as the armature coil and DC magnetizing coil, are placed together, the stator of the memory FSPM machine has a very complex structure, as shown in Figure 1.2-19. Optimizations in terms of PM grade, PM thickness, and length, torque ripple reduction have been done in [73]. With proper design optimization, the memory FSPM machine

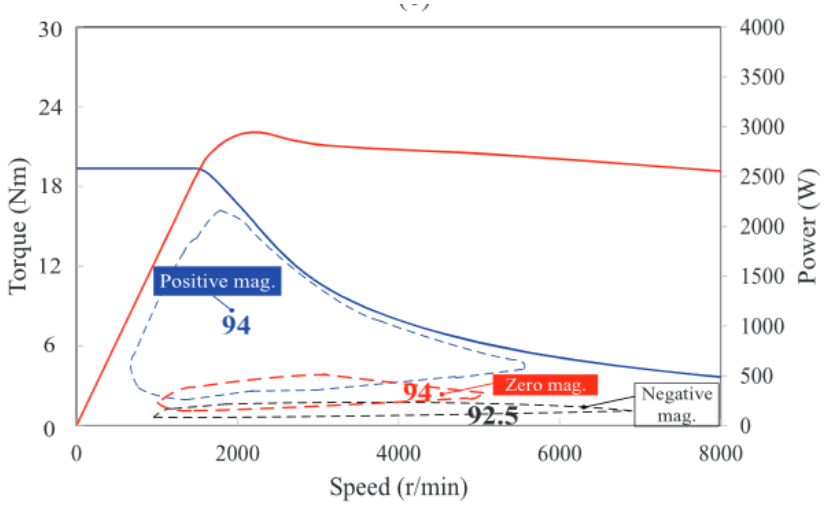

Figure 1.2-20. Torque-speed curve of hybrid magnet memory FSPM machine [73]

can achieve a similar performance as the memory IPM machine. The torque-speed curve presented in Figure 1.2-20 shows that a wide constant power speed range and high efficiency could be achieved.

B. Hybrid-excited and DC-excited flux-switching machine

Permanent magnet material is usually the most expensive part of a PM machine. One of the challenges that FSPM machine has is a large amount of PM material required. The C-core, E-core, and multi-tooth FSPM machines can reduce the PM volume by half. To further reduce or eliminate the PM usage, FSPM machines with DC field winding in the stator have been proposed and investigated. Using both field winding and permanent magnet (hybrid excitation) as excitation source has the benefit of high torque density and a wide range of flux regulation capability. A hybrid excited flux-switching machine for electric vehicle applications has been studied [74]–[76]. The permanent magnet field and the DC coil are usually placed in parallel, to reduce the risk of demagnetization.

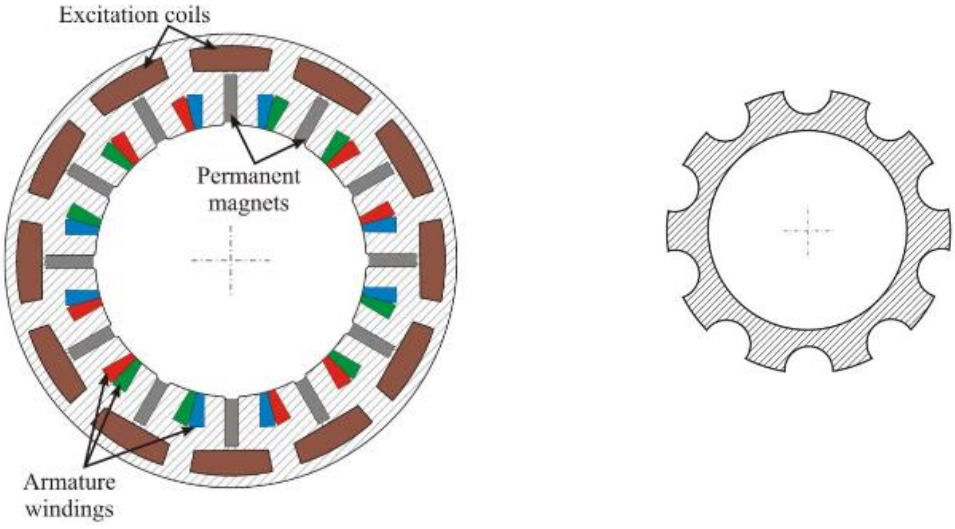

(a) (b)

Figure 1.2-21. Hybrid excited flux-switching machine with parallel field (a) Stator structure (b) Rotor structure [74]

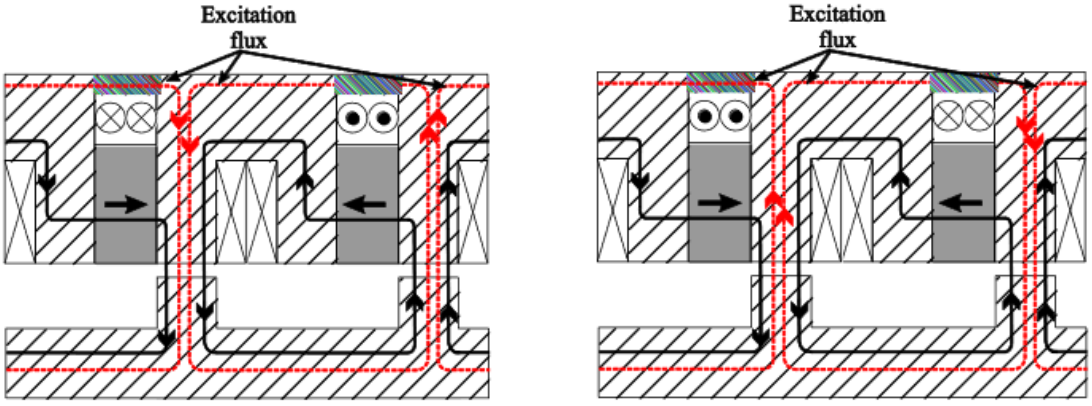

(a) (b)

Figure 1.2-22. Flux path of permanent magnet and DC coil in the case of (a) Flux intensifying (b) Flux weakening [77]

The parallel fields could be achieved by the structure shown in Figure 1.2-21 [74], [77], DC excitation coils are wound in the stator yoke. The rotor has the same shape as a conventional PM excited flux switching machine. It can be seen that the iron bridge is added to the enhanced DC field, and the stator core is no longer segmented. Having stator core as a whole piece is preferable for manufacture. The permanent magnet and DC coil flux are shown in Figure 1.2-22, where both flux weakening and flux intensifying cases are presented. The no-load flux waveforms and output torque curves at different DC current levels are shown in Figure 1.2-23. It can be seen that the DC field could effectively intensify the total flux up to 20 A/mm^2 because of the iron saturation. Note that the DC excitation current introduces extra Joule loss that needs to be dissipated as well. Other hybrid excitation topologies are possible, as shown in Figure 1.2-24, the DC excitation coils are placed in different locations in the stator, but they have similar operation principle. Note that the stator of FSPM machine already has a complex structure, the additional DC field winding further increase the manufacturing difficulty.

DC excited flux-switching machine is able to eliminate the use of permanent magnet material to further reduce the cost of the machine. Design considerations such as torque production,

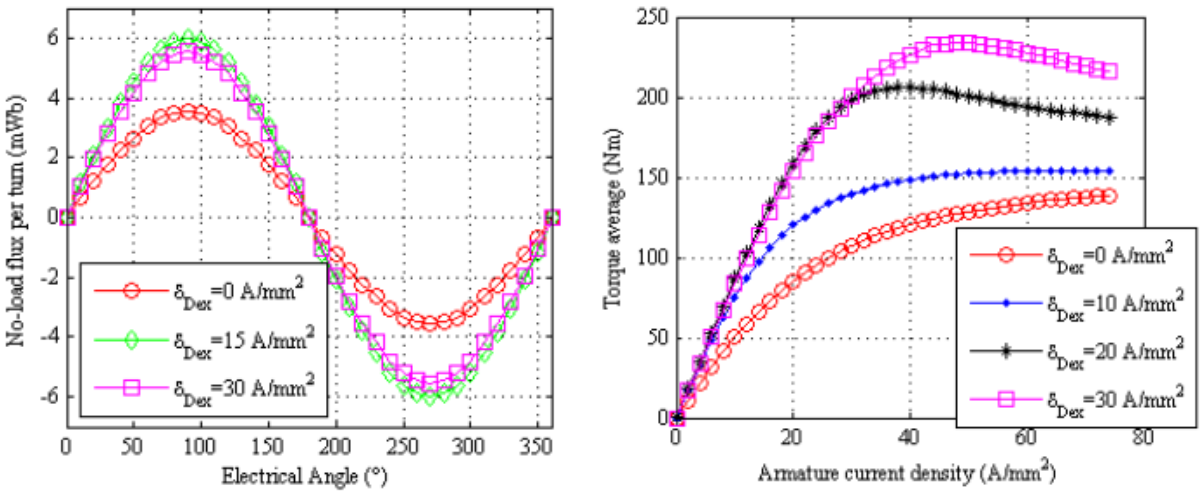

(a) (b)

Figure 1.2-23. (a) Back EMF waveform (b) Output torque of parallel field hybrid excited flux switching machine [77]

scalability, aspect ratio have been investigated [78], [79]. The cross-section view of the DC-excited flux switching machine is shown in Figure 1.2-25. With the excitation field fully provided by the DC coil, the airgap flux density could be controlled in the full range. In addition, since no permanent magnet material is used, the allowable operating temperature of the DC-excited flux-switching machine is higher than the FSPM and hybrid excited FSPM machine. However, compared to FSPM and hybrid FSPM machine, the DC-excited flux-switching machine has lower efficiency due to the copper loss in the DC coil. A comparison between the DC-excited flux-

Figure 1.2-24. Other hybrid excitation flux-switching machine topologies [76] [78]

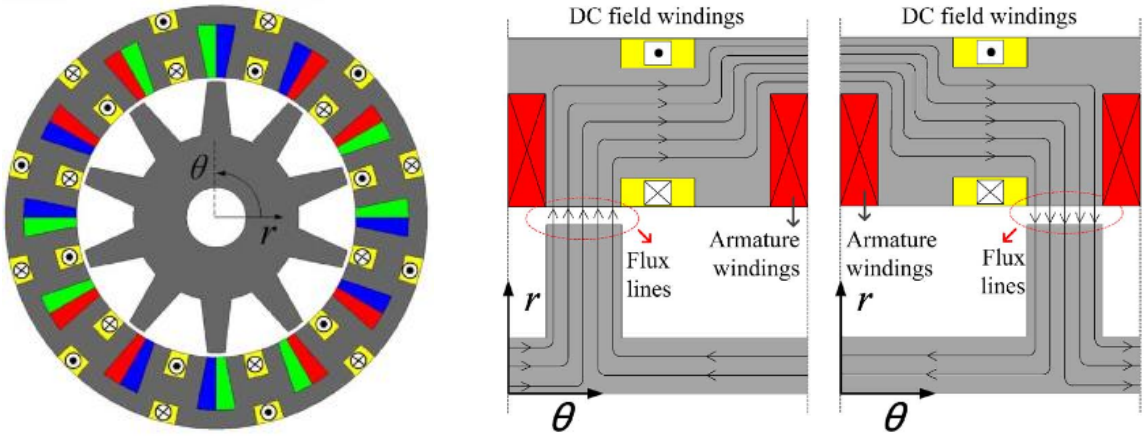

(a) (b)

Figure 1.2-25. DC excited flux-switching machine (a) Section view (b) Flux path [80]

switching machine and the flux-switching permanent magnet machine has been made in [80]. As can be seen in Figure 1.2-26 that the DC-excited flux-switching machine has similar torque density compared to FSPM machine with ferrite magnets.

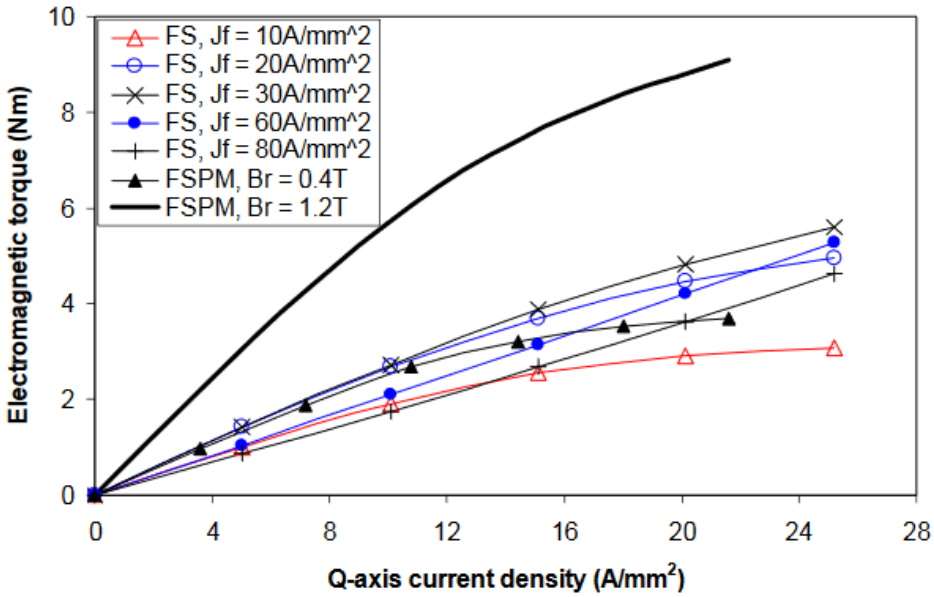

Figure 1.2-26. Output torque comparison of the DC-excited flux-switching machine [78]

C. FSPM machine with modified rotor structure

For the rotor-mounted PM machine, the rotor hysteresis loss is negligible because the rotor flux is synchronized with the rotor movement. However, in FSPM machine, the flux in the rotor is bi-directionally varying at frequency f_r that can be calculated with (Equation 1-8), where f_s is the

$$f_r = f_s \frac{N_s}{2N_r} \qquad \text{(Equation 1-8)}$$

stator frequency calculated from (Equation 1-2).

Therefore, the FSPM machine rotor iron loss is comparable to the stator iron loss. Although the FSPM machine can operate with higher rotor temperature, the excessive rotor iron loss compromises the efficiency. To reduce the rotor iron loss, a modular segmented rotor has been proposed in [81]. The structure of the modular rotor FSPM machine is shown in Figure 1.2-27. Only the rotor pole is magnetic steel, the rotor back iron is non-magnetic supporting material. The output torque of the modular rotor FSPM machine is shown to be approximately 10% less than the conventional FSPM machine, but a 13% total loss reduction can be achieved. One potential issue that the modular rotor FSPM machine has is the rotor structure strength. At high-speed conditions, the integrity of the rotor needs to be verified.

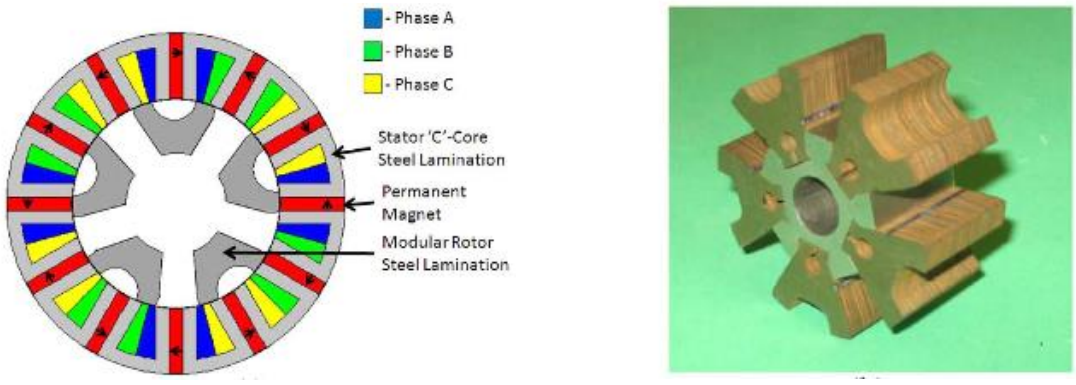

(a) (b)

Figure 1.2-27. Modular rotor FSPM machine (a) Section view (b) Prototype rotor [81]

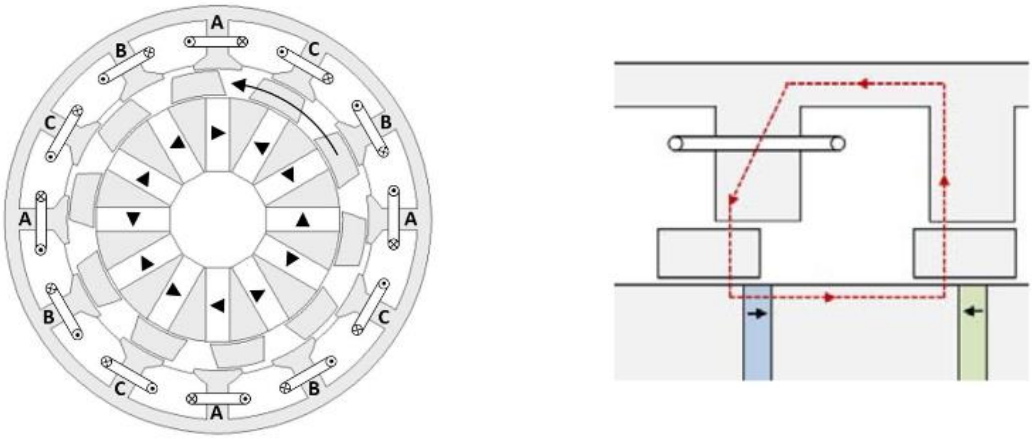

(a) (b)

Figure 1.2-28. Partitioned stator FSPM machine (a) Section view (b) Magnetic flux path [83]

The stator structure of conventional FSPM machine is complex because both armature winding and permanent magnet are in the stator. For the same reason, the stator slot area of FSPM machine is limited and the armature current is restricted. A partitioned stator FSPM machine is proposed to have armature winding and permanent magnet placed separately in the outer and inner stator respectively [82], as shown in Figure 1.2-28. The inner stator is fixed via the end cap to the

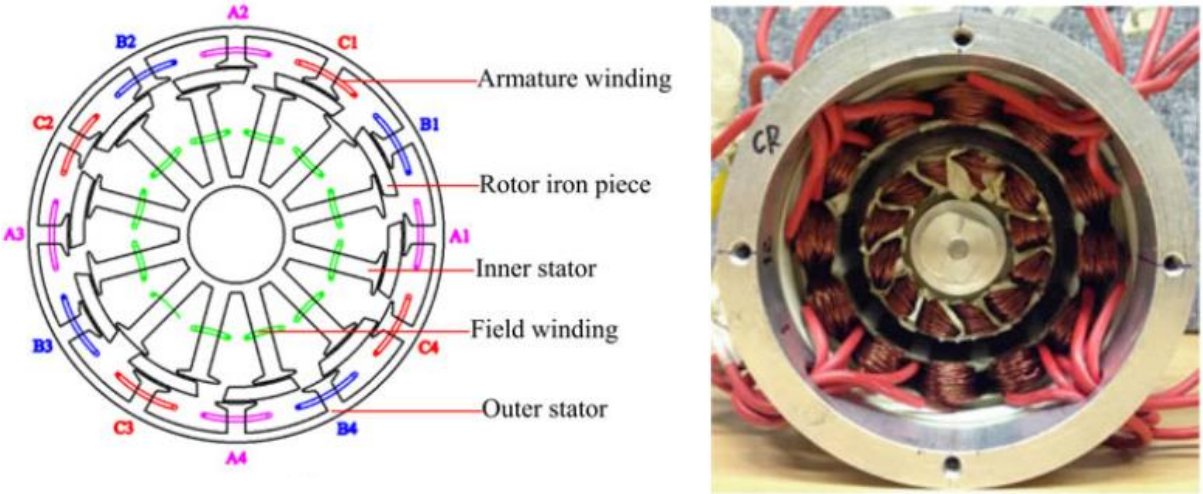

Figure 1.2-29. DC excited partitioned stator FSPM machine (a) Section view (b) Prototype assembly [82]

main housing, the rotor iron is fixed by non-magnetic structural material. By moving the permanent magnet to the inner stator, larger stator slot area could be obtained. Note that the inner stator with permanent magnets need to be properly cooled to maintain the performance. The permanent magnet in the inner stator could be replaced by DC field coil to form a DC-excited FSPM machine [83], as shown in Figure 1.2-29. The partitioned stator FSPM machine with a

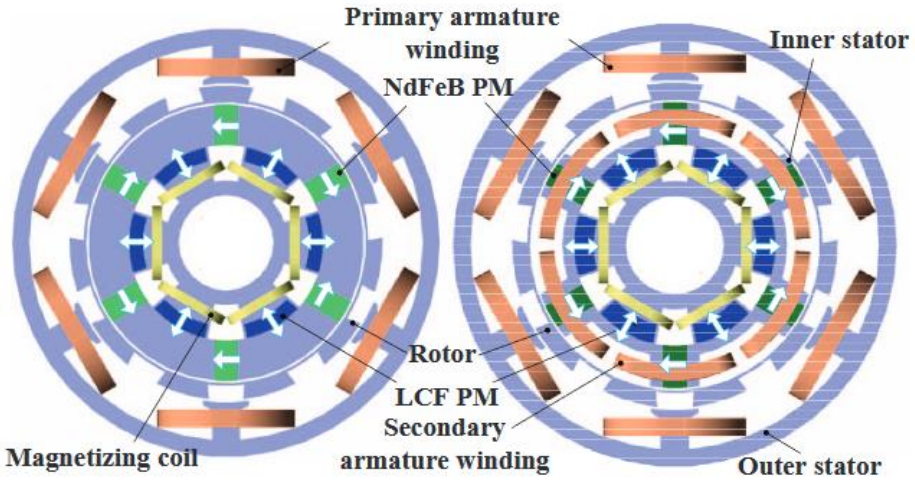

(a)

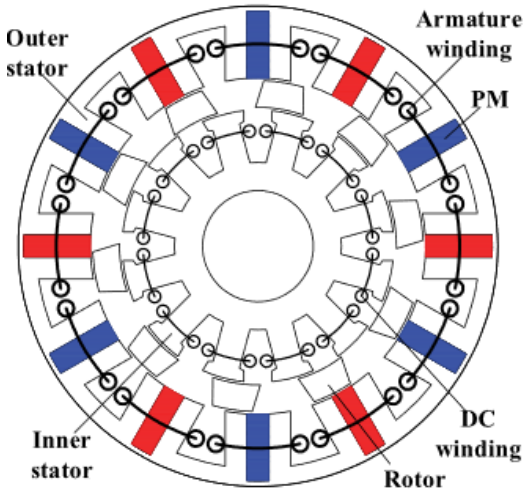

(b)

Figure 1.2-30. Novel FSPM machine with combined modified structure (a) Partitioned stator memory FSPM machine with hybrid excitation [84] (b) Partitioned stator FSPM machine with hybrid excitation [85]

different number of rotor poles and winding types have been investigated [82]. Similar to conventional FSPM machine, 14 rotor pole machine has the highest output torque but requires highest fundament frequency.

The previously mentioned modified structures and topologies could be integrated as needed. A hybrid excited FSPM machine with a partitioned stator is investigated in [84]. By putting the DC excitation coil in the inner stator, the permanent magnet flux and the DC coil flux are in series. High torque density and wide speed range could be achieved without having a limited stator slot area. A partitioned stator memory FSPM machine with hybrid excitation has been proposed in [85]. The use of a low coercive magnet allows changing the magnetic flux level efficiently. These combined modified structures have challenges in manufacturing because of the complex geometry, as shown in Figure 1.2-30. Proper thermal management is needed to keep the operation reliable.

D. Linear FSPM machine

Linear machine has been used in industrial automation and railway traction [86], direct linear drive has the benefits of higher dynamic performance and improved reliability by eliminating the

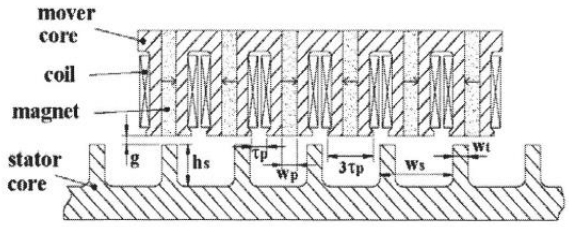

Figure 1.2-31. Configuration of linear flux-switching permanent magnet motor [89]

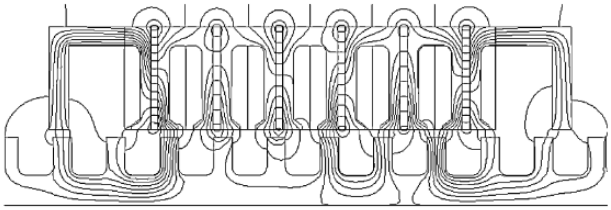

Figure 1.2-32. Linear FSPM machine with assistance teeth for detent force reduction [87]

transmission from rotary motion to linear motion [87]. The operation principle of the flux-switching machine could also be applied to linear machines [87], [88]. Another benefit of using the flux-switching topology in a linear machine is that the long-distance railway could be made of low-cost steel. The rotor in the conventional radial flux FSPM machine now is acting as the stator, as shown in Figure 1.2-31. Detent force in the linear FSPM machine has been studied in [89], [90], where the detent force has been segregated into components that originated from the end effect and slotting effect. Rotor with assistant teeth has been proposed to reduce the detent force, as shown in Figure 1.2-32. Some of the new topologies such as double-sided linear FSPM machine, multi-tooth FSPM linear machine, modular linear FSPM machine for rail transit application, and hybrid excited linear FSPM machine are also proposed by the researchers [91]–[96].

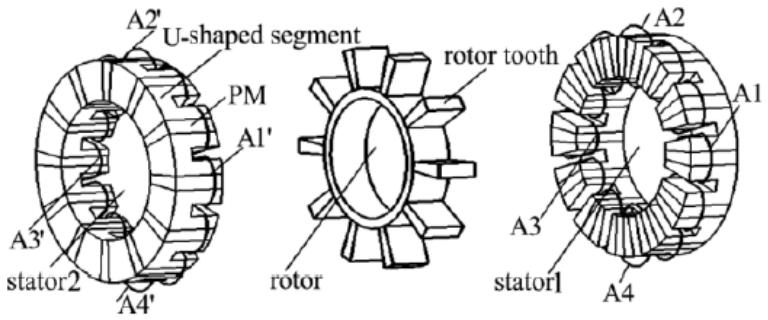

(a)

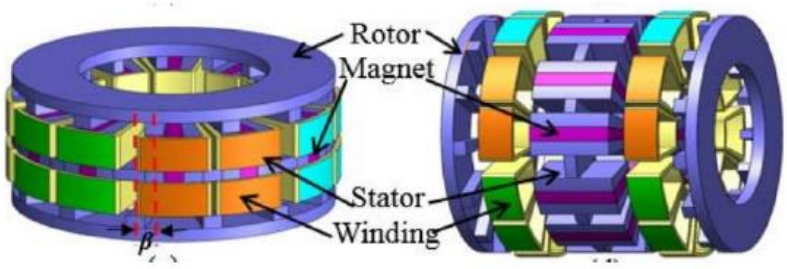

(b)

Figure 1.2-33. Axial field flux-switching permanent magnet machine (a) Dual-stator structure (b) Dual-rotor structure

E. Axial flux FSPM machine

Axial flux machines are widely used in applications where short stack length, disk-shaped machines are preferred. The operating and design principle for the radial flux FSPM machine could be easily applied to the axial flux machine [97]–[103]. Different axial flux FSPM machine structures have been proposed by researchers. Figure 1.2-33 shows the structures of dual-stator axial flux FSPM machine and dual-rotor axial flux FSPM machine [104]. The use of the dual structure allows the balancing of magnetic pulling force generated between the stator and rotor.

1.3. Low-pole FSPM machine design

1.3.1. FSPM machine for high-speed application

As mentioned in the previous sections, the flux-switching permanent magnet machine has the benefits of having a robust rotor structure and no magnet in the rotor. Because of these two advantages, the FSPM machine is usually claimed to be more suitable for the high-speed application, compared to rotor-mounted permanent magnet machines where rotor cooling and magnet retaining are issues in high-speed condition. Comparisons between FSPM machine and IPM, SPM machine for high-speed applications have been done. It is shown that the FSPM machine has similar or even better performance than IPM machines in terms of flux weakening capability and torque density when the appropriate split ratio is designed [105]. Various IPM machines (radially magnetized PM, spoke-type PM, and V-shape PM) are compared with the FSPM machine by using both NdFeB and ferrite magnets to quantify the differences in torque production, active material cost, and demagnetization behavior [106]. The radially magnetized IPM machine has the best demagnetization withstand capability. The spoke-type IPM machine is found to have the best torque per active material mass property, but its PMs are most vulnerable to demagnetization. V-shaped IPM machine has only partial demagnetization behavior at a nominal load. If ferrite magnets are used, the spoke-type IPM machine and the FSPM machine

have partial demagnetization behavior. For the FSPM machine, the risk of highest demagnetization happens at the tips of magnets near the airgap. The torque-speed and power-speed curves comparison between the IPM and FSPM machine are shown in Figure 1.3-1.

FSPM machine does not have the previously mentioned magnet heating issue since the magnets are located in the stator. However, FSPM machine has its own challenges for high-speed operation. The fundamental frequency of FSPM machine could be calculated by (Equation 1-1), which indicates that the machine pole pair number equals to the rotor pole number. Taking the most commonly seen 12/10 structure as an example, it is equivalent to a 20-pole machine from the control perspective. With such a large pole number, the required fundamental frequency will be very high for high-speed operation. The high fundamental frequency will cause a large iron loss in the stator as well as in the rotor. In IPM and SPM machine, rotor flux is synchronized with the

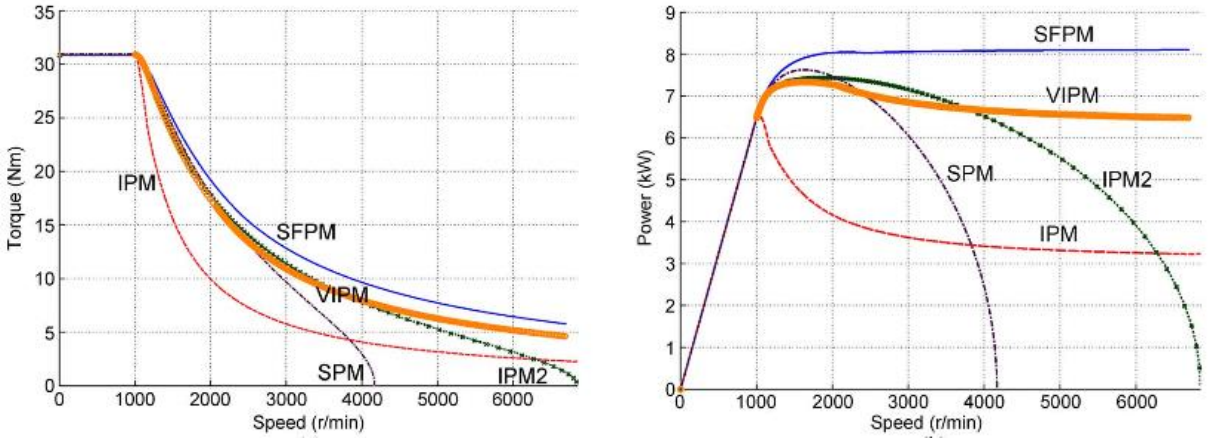

(a) (b)

Figure 1.3-1. Field weakening characteristics comparison between IPM and FSPM machine (a) Torque-speed curve (b) Power-speed curve [106]

rotor rotation. The rotor loss is caused by the Eddy current induced by flux space harmonics due to slot opening and time harmonics due to the current ripple. For the FSPM machine, the rotor flux

is varying at frequency f_r, which could be calculated by (Equation 1-9), where n is the rotor rotation

$$f_r = \frac{nN_s}{120} \qquad \text{(Equation 1-9)}$$

speed in rpm, N_s is the stator slot number.

Besides the high iron loss, the high fundamental frequency also causes additional copper loss in the armature winding. The high frequency would increase the winding resistance due to skin effect and proximity effect. Skin effect can be mitigated by using multi-strands wires, at kilo Hertz level, AWG#16 wire has a radius smaller than the skin depth. Proximity effect in high-frequency FSPM machine has been studied in [107], where 2D FEA simulation and analytical calculation have been done to predict the current distribution in the stator slot, for different numbers of strands. The slot current density is shown in Figure 1.3-2 (a), the area close to the slot opening is the most influenced part. The conductor loss shown in Figure 1.3-2 (b) shows that the proximity loss can also be reduced by employing multiple strands of wire.

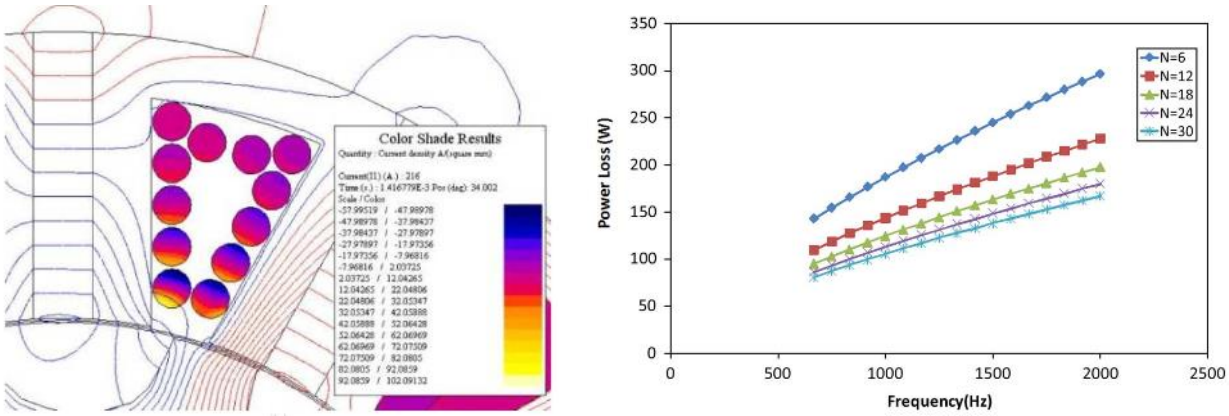

(a) (b)

Figure 1.3-2.Proximity effect in the stator slot of FSPM machine (a) Current density distributio (b) Conductor loss with different number of strands [107]

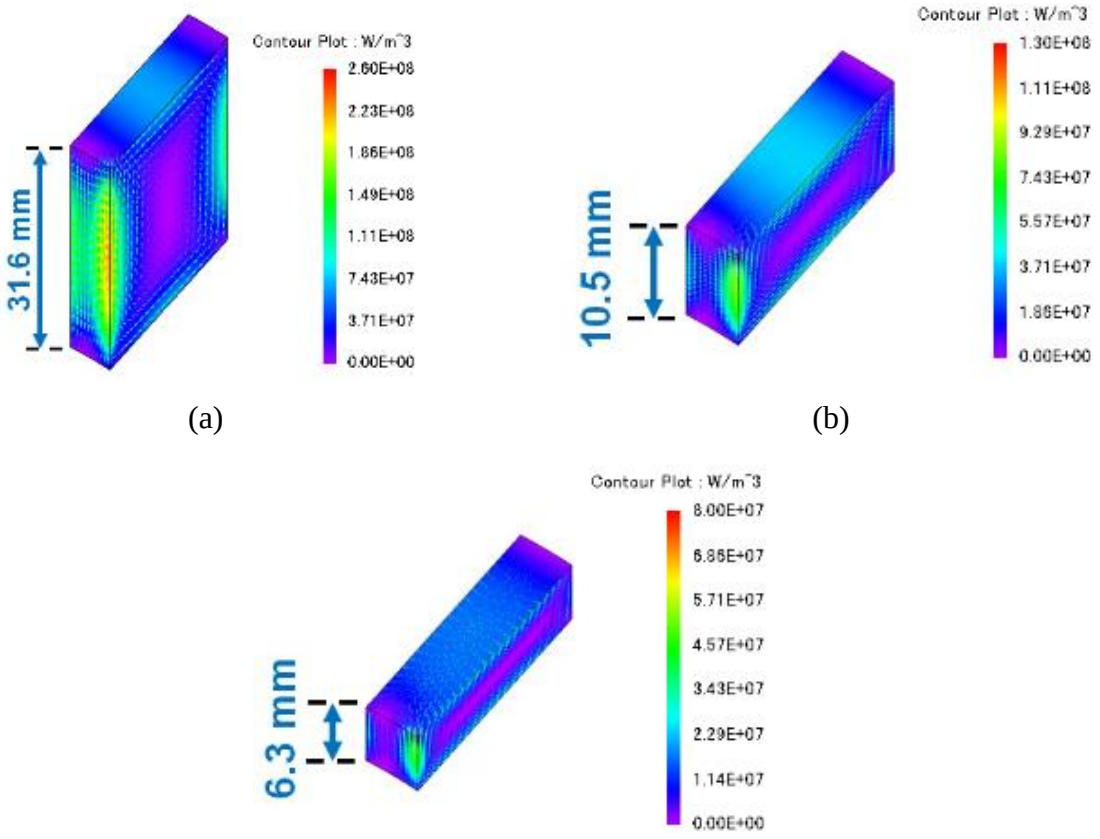

Figure 1.3-3. Eddy current loss density distribution in magnet with different number of segmentations (a) 2 segments (b) 6 segments (c) 10 segments [109]

The magnet eddy current loss in the FSPM machine is also an important subject since the magnet flux variations near the airgap is severe and prone to induce large magnet losses. Plus, the magnets are usually sensitive to the temperature variation. An effective method proposed in [108] shows that cutting a small portion of the magnet at two radial ends reduces the generated magnet eddy current loss. In addition, segmentation of the magnets is also proven to be effective for loss reduction. Both the radial segmentation and the axial segmentation show promising results in reducing the magnet eddy current loss [108], [109]. The magnet eddy current loss density with a different number of magnet segmentation is shown in Figure 1.3-3.

1.3.2. Low-pole FSPM machine

Many FSPM machine topologies have been reviewed in the previous sections. For the three-phase FSPM machine, most of them are variations based on the 12/10 structure. A high number of rotor poles, such as 12/14 structure, is shown to have good torque production capability. High pole structure is suitable for low-speed, high-torque applications but requires high fundamental frequency at high-speed. Since the 12/10 FSPM machine is the most commonly investigated structure, the machine with a rotor pole number higher than ten is considered as high-pole topology, and machine with a rotor number less than ten as low-pole topology.

High-pole FSP M machine requires high fundamental frequency at high-speed. As shown in the previous section, the high fundamental frequency will lead to a significant loss in the machine and compromise the efficiency. For the 12/10 FSPM machine, the fundamental frequency is 2.5 kHz for a speed of 15,000 rpm, which is challenging for a drive with Si-based inverter. Therefore, the low-pole FSPM machine is a better candidate for high-speed applications. Compared to the 12/10 FSPM structure and high-pole structure, the low-pole FSPM machine is much less

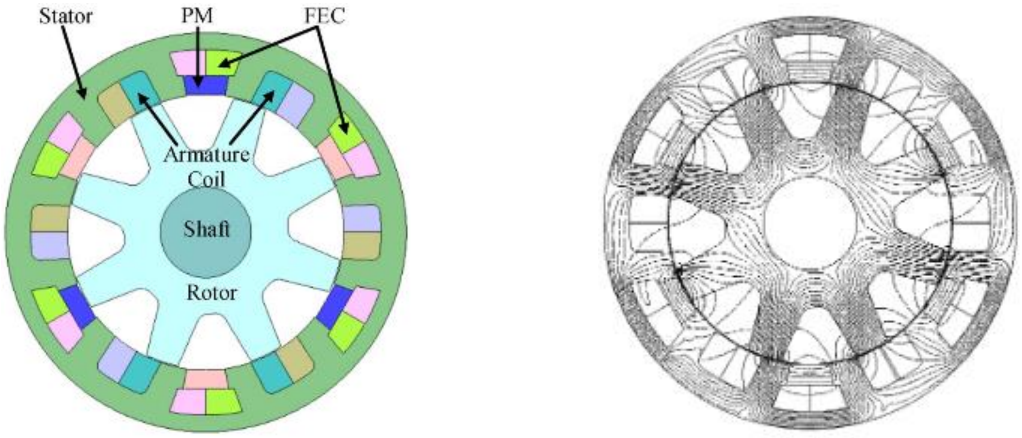

(a) (b)

Figure 1.3-4. 6-slot 8-pole hybrid excited FSPM machine for EV applications (a) Section view (b) Flux line with both PM and excitation field [112]

investigated in the literature. Considering the three-phase FSPM machine, the number of slots has to be an even multiple of the phase number, as shown in section 1.2. Therefore, the minimum slot number is 6. With either a single layer or double layer winding, the 6-slot stator FSPM machine has been studied with 4,5,7,8 rotor poles [110]–[112]. The 6-slot FSPM machines have either asymmetric back EMF or unbalanced magnetic force on the rotor due to the odd number of rotor poles. A section view of a 6-slot 8-pole hybrid excited FSPM machine for electric vehicle application is shown in Figure 1.3-4. It is shown in [112] that this machine is a good candidate for the targeted application.

An axially laminated 6/7 FSPM machine is presented in [110], [111]. It is shown that compared to the conventional lamination direction, axial lamination allows the FSPM machine to better utilized the PM flux and have a lower iron loss. The structure of the 6/7 axial laminated

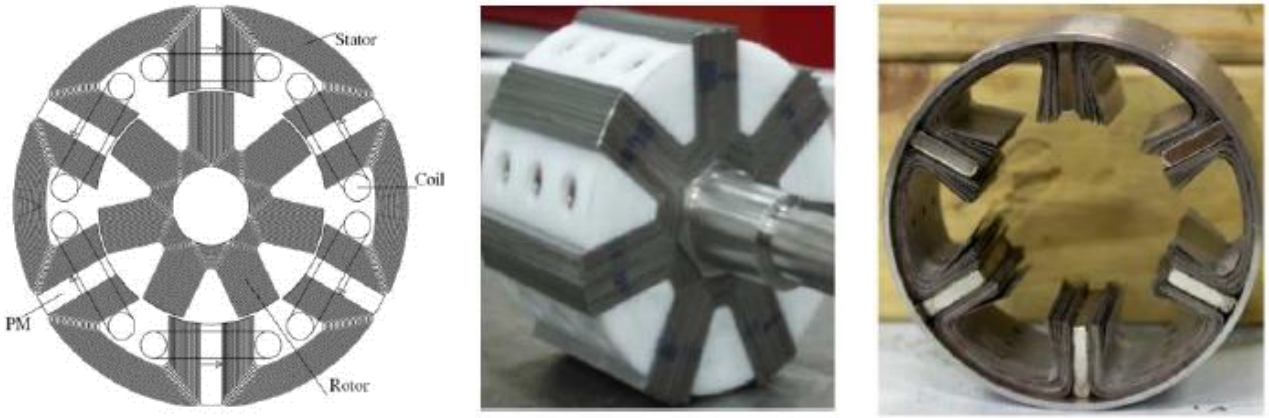

(a) (b) (c)

Figure 1.3-5. Axial laminated 6/7 FSPM machine (a) Section view (b) Prototype rotor (b) Prototype stator [110]

FSPM machine, as well as the prototype stator/rotor parts, are shown in Figure 1.3-5. Comparison studies show that the 6/7 structure produces the highest average torque with low torque ripple. Axial laminated FSPM machine is shown to have a wider constant power speed range compared

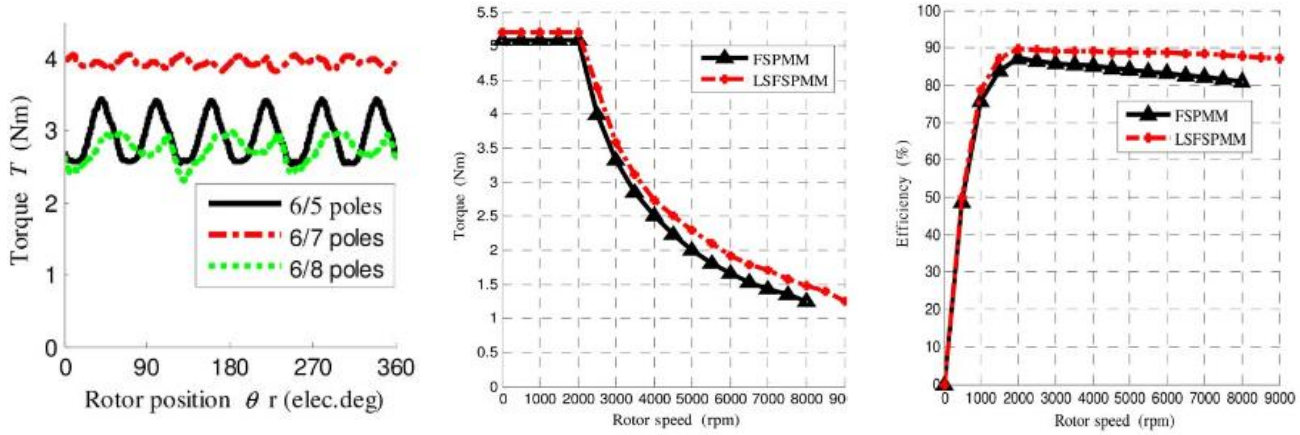

(a) (b) (c)

Figure 1.3-6. Performance comparison of the axial laminated 6/7 FSPM machine (a) Output torque (b) Torque-speed curve (c) Power-speed curve [110]

to conventional FSPM machine, as illustrated in Figure 1.3-6. However, because of the odd number of rotor poles, there is an unbalanced magnetic force exerted on the shaft.

6-slot 4-pole FSPM machine has been investigated in [113], it is shown that there are large second harmonics in the flux linkage and back EMF, as shown in Figure 1.3-7. The skewed rotor has been used to reduce the harmonic components. However, the torque ripple is significant even

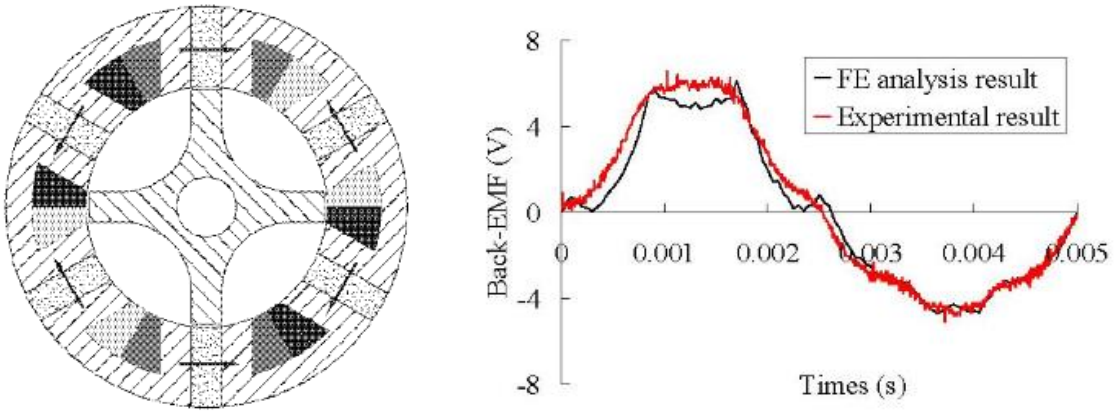

(a) (b)

Figure 1.3-7. 6-slot 4-pole FSPM machine (a) Section view (b) Back EMF waveform [113]

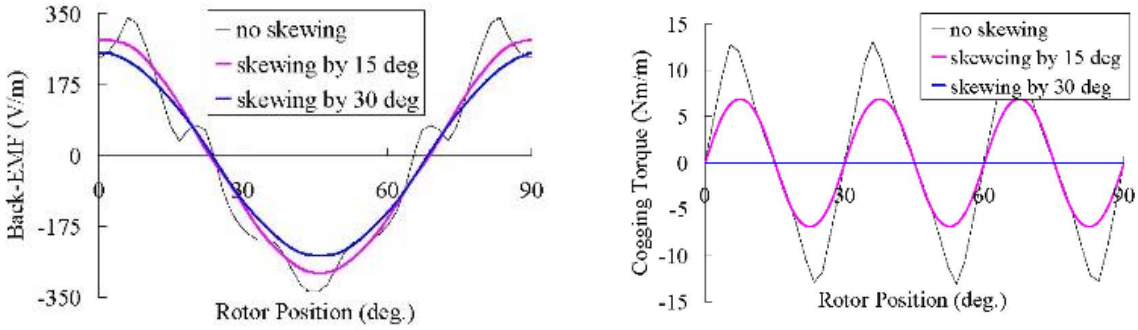

(a) (b)

Figure 1.3-8. 6/4 FSPM machine with skewed rotor (a) Back EMF (b) Cogging torque [113]

with the skewed rotor. Figure 1.3-8 shows the back EMF and cogging torque comparison between the un-skewed rotor and skewed rotor. As can be seen, the torque ripple is still very high, which indicates that the harmonics are not canceled to enough level.

1.3.3. Dual-stator 6/4 FSPM machine

As previously discussed, low-pole FSPM is appropriate for high-speed applications because it inherits the advantage of FSPM machines such as robust rotor structure and easy thermal management while avoiding the drawback of the high fundamental frequency. However, as shown in the previous section, the low-pole FSPM machines either suffer from an unbalanced magnetic force or have large harmonics in the flux linkage. In reference [114], it is shown that there is significant second-order harmonic in the flux linkage as well as the back EMF for the 6/4 FSPM machine, as shown in Figure 1.3-9 and Figure 1.3-10. The second harmonic is generated because as the rotor sweeps one full pitch, it aligns sequentially with the stator tooth, slot opening, stator tooth, and permanent magnet. The permanent magnet has a similar permeability as the slot opening. Therefore, the permeance will experience two periods, while the flux linkage only has one period

$$\lambda_{1,2} = \sum_{h=1,3,5...}^{\infty} A_h \cos(h\theta_e + \theta_h) + \sum_{h=2,4,6...}^{\infty} A_h \cos(h\theta_e + \theta_h) \qquad \text{(Equation 1-10)}$$

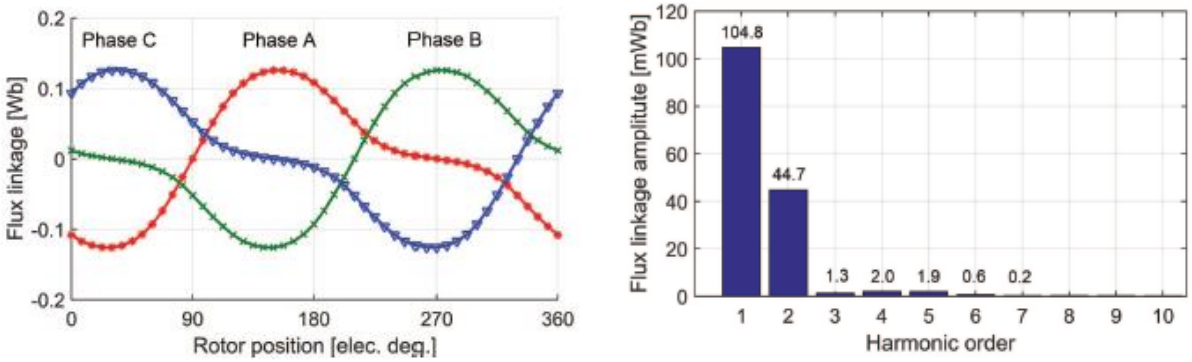

(a) (b)

Figure 1.3-9. Flux linkage of 6/4 FSPM machine (a) Waveform of flux linkage in the three-phase coils (b) Harmonic components of phase A [114]

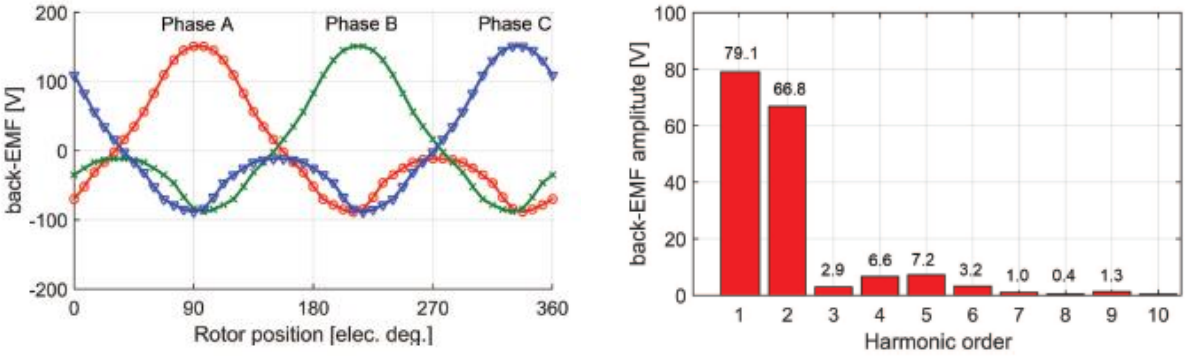

(a) (b)

Figure 1.3-10. Back EMF 6/4 FSPM machine (a) Waveform of back EMF in the three-phase coils (b) Harmonic components of phase A [114]

change. The flux linkage of one phase can be expressed by (Equation 1-10), A_h and θ_h are the amplitude and phase angle of the h^{th} harmonic, respectively. θ_e is the rotor position in electric degree. The second harmonic does not exist in the 12/10 FSPM structure because there are four coils for one phase, the two coils placed opposite to each other has a phase shift of 180 electrical degree, which cancel the second harmonic internally. Although the 6/4 FSPM machine also has two coils for one phase, there is no phase shift for between the flux linkage of the two coils. To

achieve similar harmonics cancellation occurs in the 12/10 FSPM machine, a dual-stator 6/4 FSPM machine has been proposed and investigated [109], [115]–[119].

The structure of the proposed dual-stator 6/4 FSPM machine is shown in Figure 1.3-11 (a). Two 6/4 FSPM machine stators are placed axially next to each other. The two stators are separated by a certain distance to accommodate the end turn. The section views of the front and rear stator

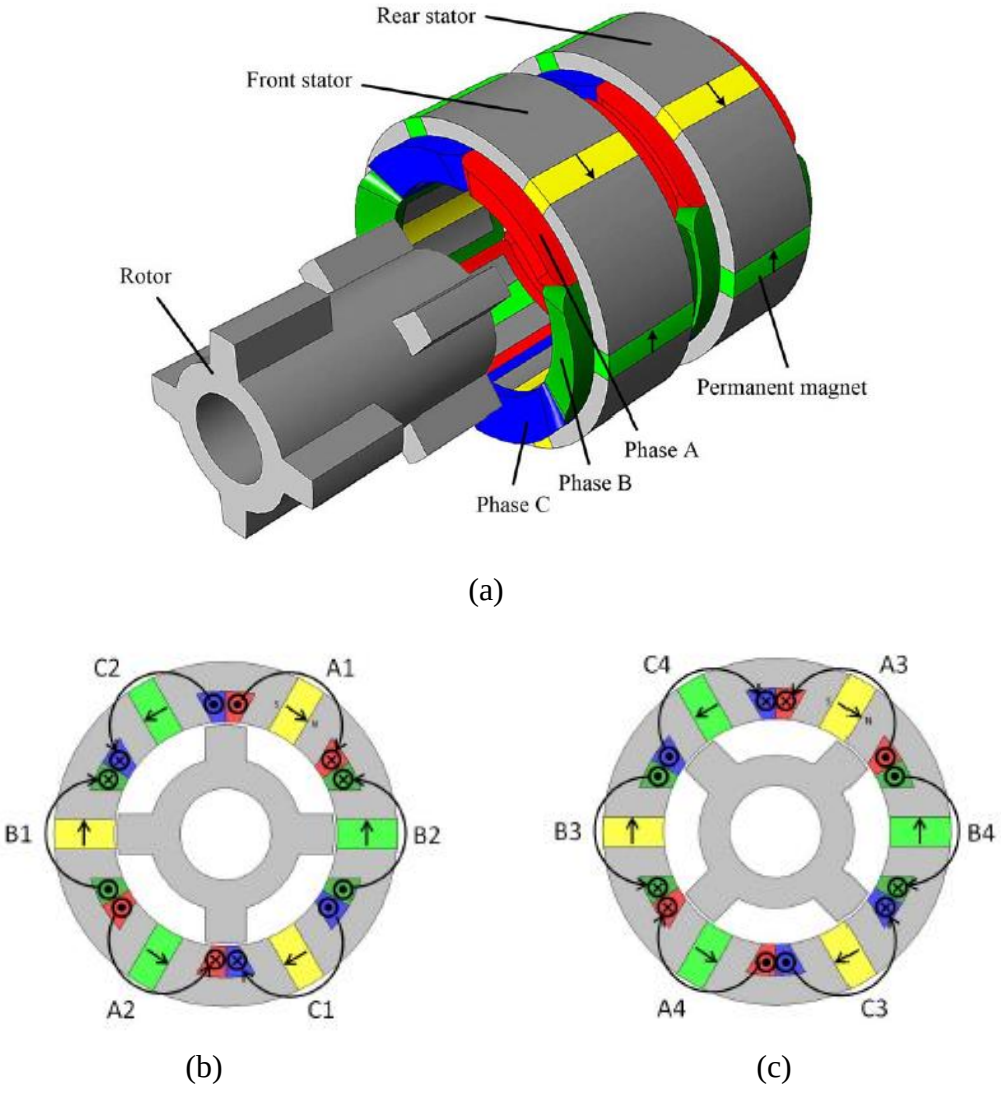

Figure 1.3-11. Dual-stator 6/4 FSPM machine (a) 3D structure (b) Front stator section view (c) Rear stator section view [114]

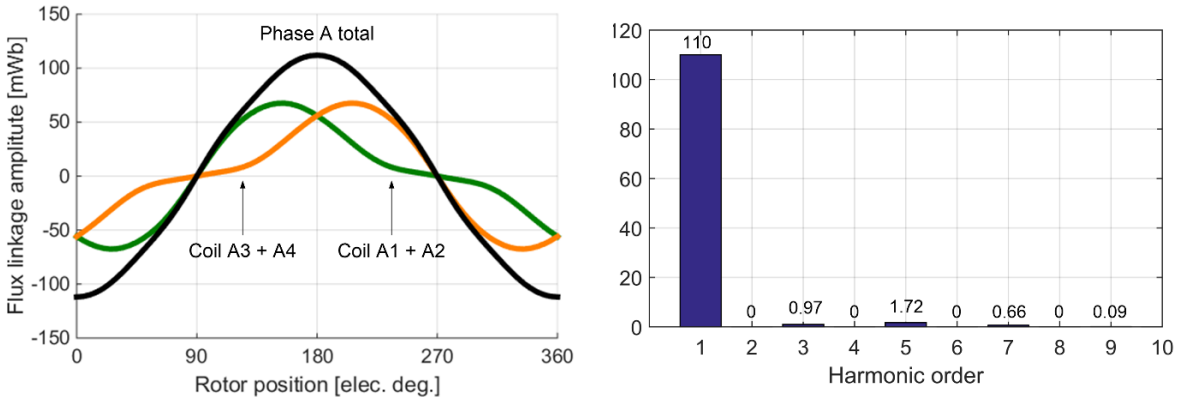

(a) (b)

Figure 1.3-12. Flux linkage of dual-stator 6/4 FSPM machine (a) Flux linkage waveform (b) Harmonic component in flux linkage

are shown in Figure 1.3-11 (a) (b), as can be seen, the winding direction in the two stators are opposite to create a 180-degree phase difference. Two rotors with a 45-degree shift are put together to work with the two stators. There are four coils for each phase, similar to the 12/10 FSPM machine. The second-order harmonic is canceled internally. The total flux linkage of one phase has a sinusoidal shape, as shown in Figure 1.3-12 (a). Similar to (Equation 1-10), the flux linkage of the other two coil can be expressed by (Equation 1-11). The total flux linkage can be calculated as (Equation 1-12), which has a sinusoidal shape.

$$\lambda_{3,4} = \sum_{h=1,3,5...}^{\infty} A_h \cos(h\theta_e + \theta_h) - \sum_{h=2,4,6...}^{\infty} A_h \cos(h\theta_e + \theta_h) \quad \text{(Equation 1-11)}$$

$$\lambda_{total} = \sum_{h=1,3,5...}^{\infty} 2A_h \cos(h\theta_e + \theta_h) \quad \text{(Equation 1-12)}$$

It is shown in the previous section that the conventional 6/4 FSPM machine has a significant cogging torque even with a skewed rotor because the second harmonics is not fully canceled. With the dual-stator structure, the even-order harmonics, including the second-order harmonic, are canceled, as shown in Figure 1.3-12 (b). Without addition torque ripple reduction optimization

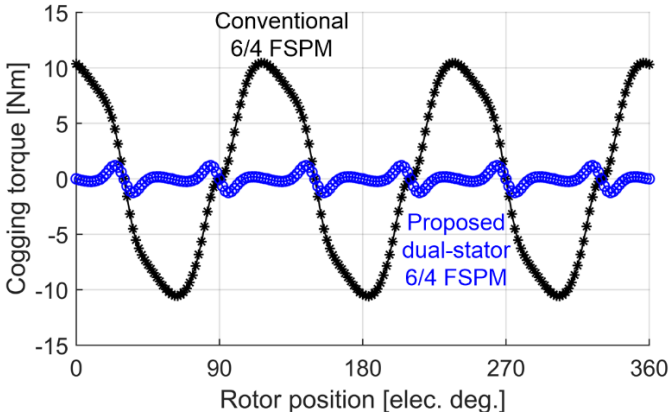

Figure 1.3-13. Cogging torque comparison between the dual-stator and single stator 6/4 FSPM machine [113]

such as tooth tip notching and rotor skewing, the dual-stator 6/4 FSPM machine achieves a cogging torque reduction of more than 70% compared to the single stator 6/4 FSPM machine, as can be seen in Figure 1.3-13. The even harmonics cancellation is achieved by the 180-degree phase shift between the two coil pairs in one phase. Therefore, besides the topology shown in Figure 1.3-11 (a), other even harmonic cancellation topologies are available.

Figure 1.3-14 shows the other two dual-stator structures proposed in [117], the structure shown in Figure 1.3-11 (a) is referred to as Topology-II. Topology-I has one single-coil crossing

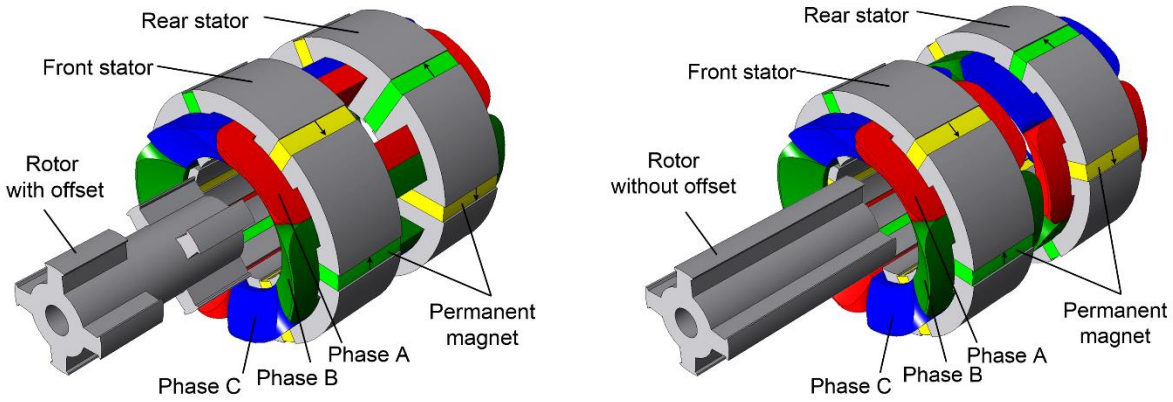

(a) (b)

Figure 1.3-14. Alternative topologies of dual-stator 6/4 FSPM machine (a) Topology-I (b) Topology-III [117]

TABLE 1-2. COMPARISON OF MANUFACTURING, ASSEMBLING SIMPLICITY, AND PERFORMANCE OF DIFFERENT DUAL-STATOR 6/4 FSPM MACHINE TOPOLOGIES

Characteristics	Topology-I	Topology-II	Topology-III
Rotor assembling simplicity	Simple	Simple	Most simple
Winding assembling	Less simple	Simple	Simple
Stator alignment simplicity	Simple	Simple	Less simple
Modular design capability	Good	Excellent	Excellent
Machine compactness	Most compact	Less compact	Less compact
Material consumption	Lowest	Higher	Highest
Torque density	High	Highest	Higher

two stators, which can reduce 50% of the end turn and decrease the stator winding resistance. The 180-degree phase shift is achieved by placing the magnets oppositely in the two stators. The rotor is twisted in the same way as in Topology-II. Although no end turn exists between the two stators, the axial gap is still required to prevent magnetic flux leakage. The rotor of Topology-I and Topology-II has three sections, which increase the manufacturing cost because three types of lamination are needed. Topology-III has a straight rotor tooth and requires only one type of rotor lamination. The two stators are twisted 45 degrees instead. A qualitative comparison of the three topologies is given in TABLE 1-2 [117].

FSPM machines usually have large torque ripples due to the double saliency structure, which true for the dual-stator 6/4 FSPM machine as well. Several torque ripple reduction techniques can be found in literature, including rotor pole shaping [120], tooth notching [121], axial pairing of rotor teeth [27], and rotor step skewing [32], [122]. The rotor step skew is the simplest and the most cost-effective method compared to the other techniques. The torque ripple reduction of the dual-stator 6/4 FSPM machine has been investigated in [115], where two-step skew and four-step skew with different span angles are studied. The torque ripple reduction study is based on the Topology-I introduced previously because of the compact design. The structures of the step

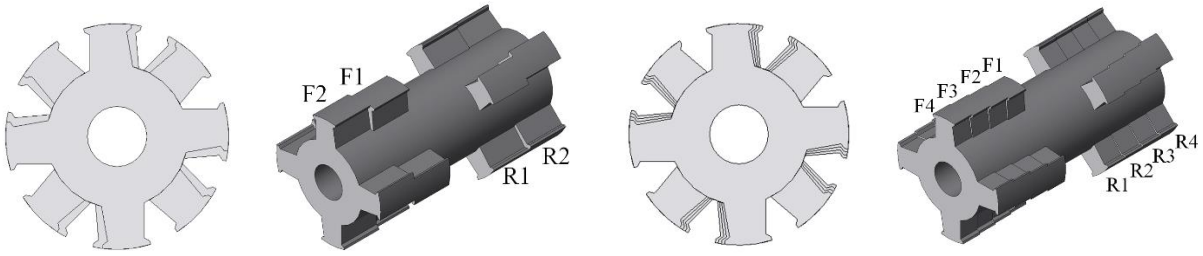

(a) (b)

Figure 1.3-15. Step skewed rotor for torque ripple reduction (a) Two-step skew (b) Four-step skew [115]

skewed rotor are shown in Figure 1.3-15. The average output torque and torque ripple of different span angles are presented in Figure 1.3-16. The two-step skew rotor with a span angle of 5 degrees is able to provide a 62.5% torque ripple reduction and maintain 98% of the average torque.

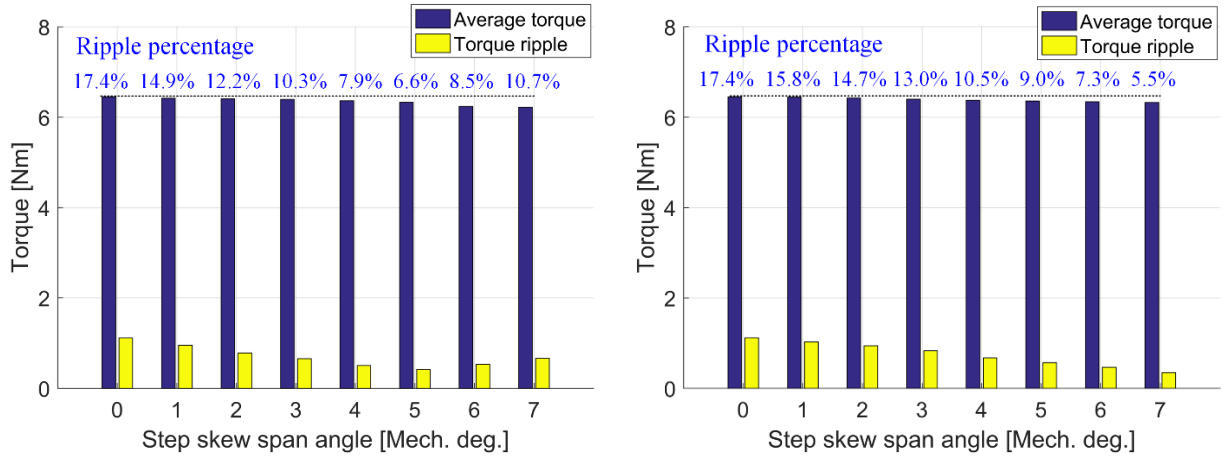

(a) (b)

Figure 1.3-16. Output torque and torque ripple level of step skew rotor with different span angle (a) Two-step skew (b) Four-step skew [115]

1.4. Multi-physics design for FSPM machine

The electrical machine design has always been a multi-physics area that involves electrical and mechanical engineering. Mechanical design includes thermal management, structural analysis, and mechanical loss characterization. Most of the components in an electrical machine have

temperature-dependent properties. Therefore, the electromagnetic and thermal performance of the electric machine is cross-coupled. The structural analysis is essential since it ensures the normal function of the electric machine. This section reviews the former work that has been done on the thermal analysis, structural analysis, and windage loss characterization.

1.4.1. Thermal analysis

The first part of the thermal analysis of electric machine includes machine loss (heat source) and heat rejection system characterization. The machine loss information comes from the electromagnetic analysis and is mapped into the thermal analysis. Shaft-mounted fan and water jacket are the commonly used cooling technologies for electric machines. Many research papers have addressed the thermal analysis of the FSPM machine [42], [123], [124]. Most of the existing papers employ lumped-parameter thermal network (LPTN), finite element analysis (FEA) and computational fluid dynamics (CFD) for estimating the thermal performance.

The loss and thermal analysis of a nine-phase FSPM machine have been presented in [125]. The heat transfer characteristics inside and between the machine parts have been described. The thermal finite element analysis model is built to estimate the temperature distribution. The winding and housing temperatures are measured, as shown in Figure 1.4-1, to compare with the temperature predicted in the model. It can be seen that the FEA model correctly estimates the temperature of the machine. In this paper, the convective heat transfer is modeled with analytical-empirical equations (Equation 1-13) and (Equation 1-14) given in [126], where ρ_f and c_f are the density

$$h = \frac{\rho_f \, c_f \, D \, v}{4L}[1 - e^{-m}] \qquad \text{(Equation 1-13)}$$

$$m = \frac{0.1448 \, L^{0.946}}{D^{1.16}}\left[\frac{\lambda_f}{\rho_f \, c_f \, v}\right]^{0.124} \qquad \text{(Equation 1-14)}$$

(kg/m3) and the specific heat capacity (J/kg-K) of the fluid respectively. D is the hydraulic

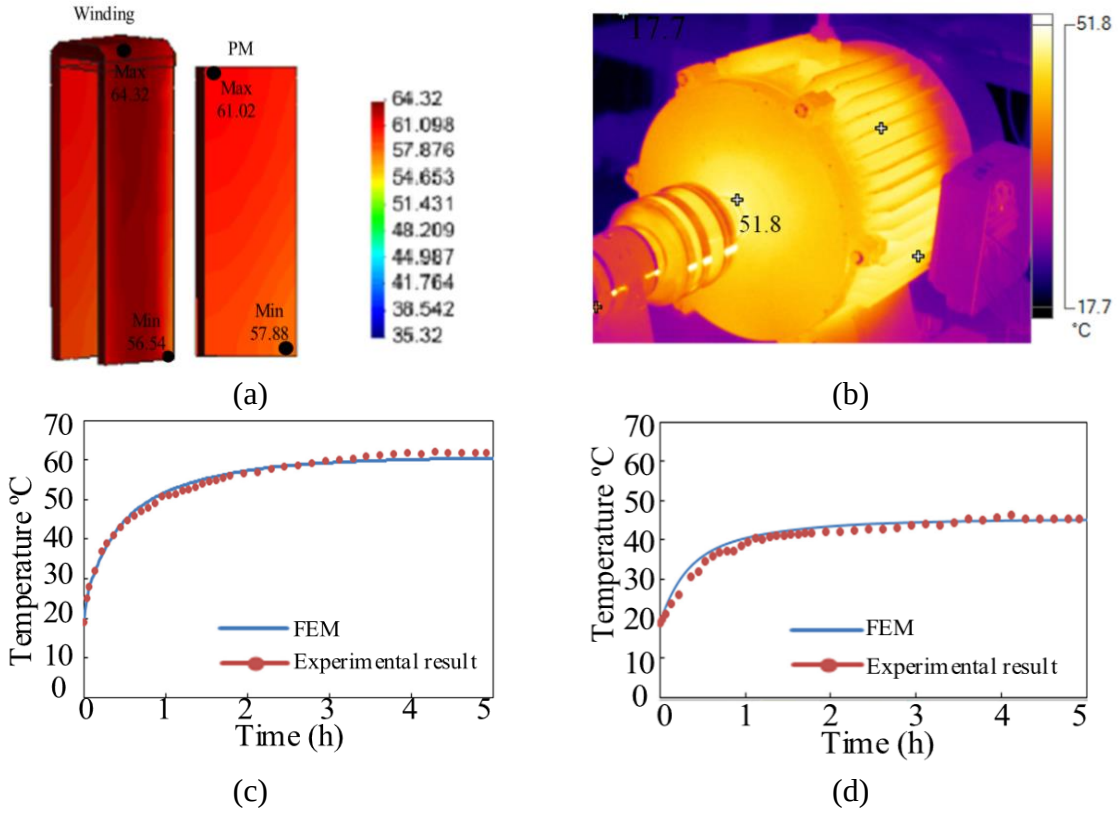

Figure 1.4-1. Temperature measured for a nine-phase FSPM machine (a) Winding temperature measurement (b) Frame temperature measurement (c) Temperature variation of winding (d) Temperature variation of frame [125]

diameter (m), *v* is the velocity (m/s) of the fluid, *L* is the axial length (m) of the cooling surface. However, in this analysis, fan cooling is employed, which might not adequate for the high power density FSPM machine. The performance of the fan cooling system is coupled with the rotation speed of the machine. In addition, the permanent magnet is usually the most temperature-sensitive component, but the temperature is not monitored here.

Thermal analysis of a 12/10 FSPM machine with water jacket cooling has been shown in [127], where the anisotropic thermal conductivity of the lamination steel and thermal contact resistance are discussed. The directional heat transfer in the winding is considered, which allows the accurate modeling of the end winding heat transfer. Both LPTN and FEA models are used to characterize the thermal performance of the machine. Figure 1.4-2 shows the geometry of the

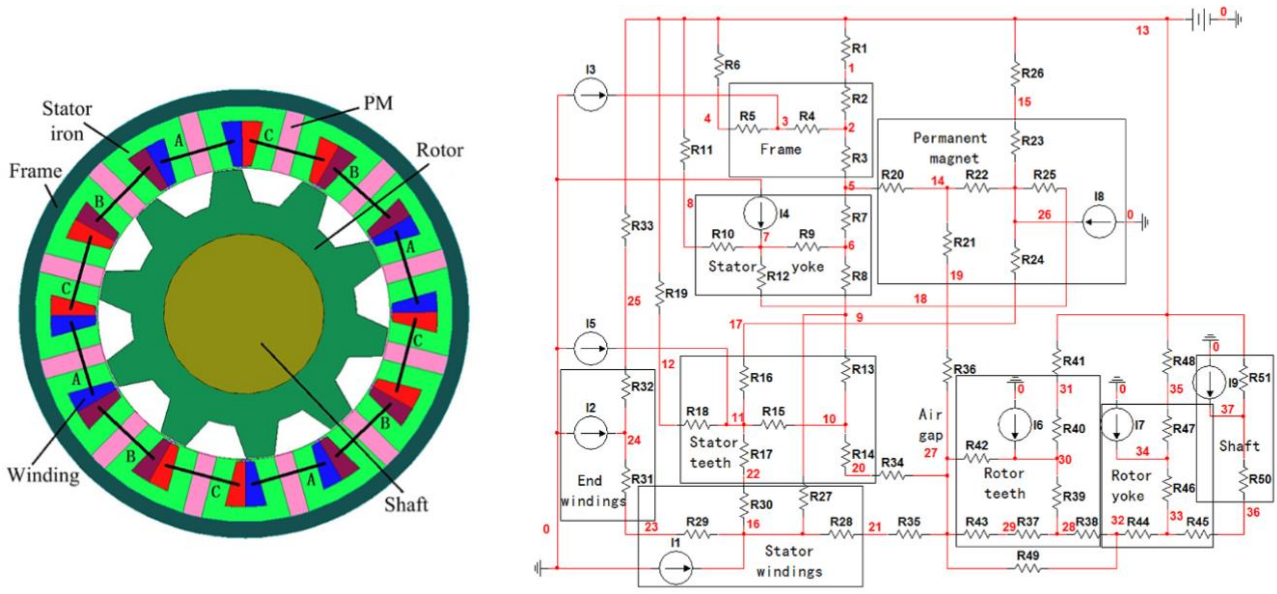

(a) (b)

Figure 1.4-2. 12/10 FSPM machine with water jacket cooling (a) Section view of the machine (b) Lumped-parameter themal network model [127]

machine as well as the thermal network model. In this paper, the convective heat transfer coefficient for the air gap, and the rotor/stator are derived from CFD simulation. As a result, the correlation curve between the heat transfer coefficient of the stator/rotor surface and the rotor speed

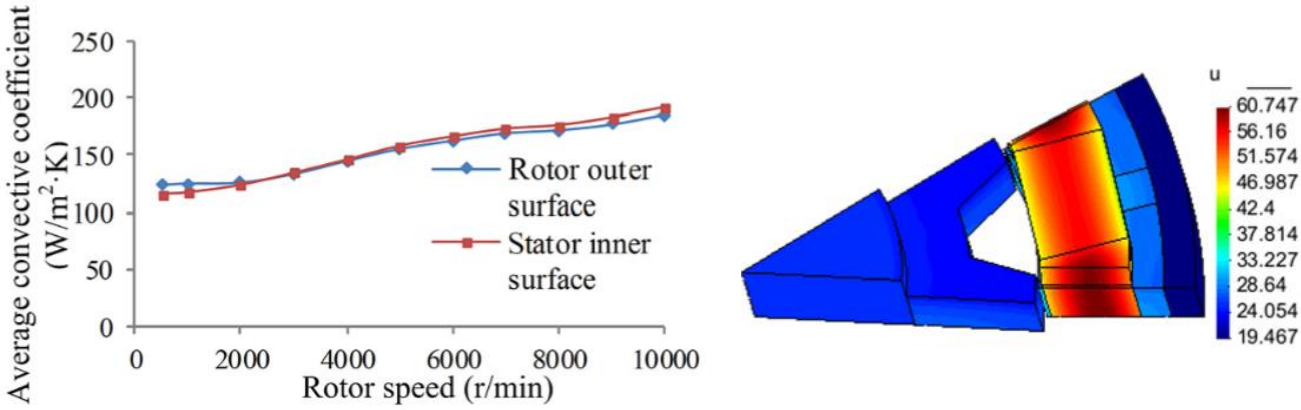

(a) (b)

Figure 1.4-3. Thermal analysis of 12/10 FSPM machine (a) Correlation between convective coefficient and rotor speed (b) Machine temperature distribution from FEA [127]

is given in Figure 1.4-3 (a). The temperature distribution from thermal FEA simulation is shown in Figure 1.4-3 (b). This paper gives a relatively complete thermal analysis, starting from the loss analysis, to the different heat transfer coefficient, until the temperature estimation with LTPN and FEA model. It is shown that with water jacket cooling, the machine temperature, especially the magnet temperature, could be well controlled. However, this paper focuses on the machine component modeling, and the description of the heat rejection system itself is missing.

1.4.2. Structural and mechanical tolerance analysis

The structural analysis for the electric machine is critical to ensure the mechanical integrity of the machine and helps to predict the noise level when operating. In addition, during the manufacturing of the machine, the actual size of the parts could be deviated from the designed size due to tooling tolerance. It is important to investigate how the machine performs in the worst scenario. It is a cost-performance trade-off since small tolerance tooling is usually expensive.

A. Structural analysis

Many references could be found discussing the structural analysis of electric machines [128]–[130]. The vibration in the electric machine is mainly due to the radial magnetic force, which causes the stator deformation. The vibration and noise are amplified when the excitation frequency

$$f_{m(=0)} = \frac{1}{2\pi R_m}\sqrt{\frac{E_s}{\rho_s \Delta}} \qquad \text{(Equation 1-15)}$$

$$f_{m(=1)} = f_{m(=0)}\sqrt{\frac{2}{1+i^2\frac{\Delta_m}{\Delta}}} \qquad \text{(Equation 1-16)}$$

$$f_{m(\geq 2)} = \frac{f_{m(=0)} im(m^2-1)}{\sqrt{(m^2+1)+i^2(m^2-1)(4m^2+m^2\frac{\Delta_m}{\Delta}+3)}} \qquad \text{(Equation 1-17)}$$

(a) (b) (c) (d)

Figure 1.4-4. Eigen mode shape of 12/10 FSPM machine stator (a) 2nd Mode (b) 3rd Mode (c) 4th Mode (d) 5th Mode [131]

or its harmonics is close to the mode frequency and causes resonance. Some formula have been developed to estimate the mode frequencies [129], as given in (Equation 1-15) - (Equation 1-17), where *m* is mode number, Δ is the mass addition factor of displacement, *Es* and ρs are the modulus of elasticity and density of the material respectively. However, it is pointed out in [131] that the above equations are valid for the single-piece stator, which is not the case for the FSPM machine. To incorporate the segmented stator iron and the sandwiched permanent magnet, the values of the *Es* and ρs used in (Equation 1-15) - (Equation 1-17) need to be adjusted with (Equation 1-18) and (Equation 1-19) [131], where η_{steel} is the volume percentage of the steel in the stator. The second

$$E_{s,FSPM} = \eta_{steel} E_{steel} + (1-\eta_{steel}) E_{magnet} \quad \text{(Equation 1-18)}$$

$$\rho_{s,FSPM} = \eta_{steel} \rho_{steel} + (1-\eta_{steel}) \rho_{magnet} \quad \text{(Equation 1-19)}$$

mode to the fifth mode shapes of a 12/10 FSPM machine are given in Figure 1.4-4. Note that depending on the sizing and material of the machine, the mode frequencies of the machine are different. To avoid resonance, the machine should be designed in such a way that the excitation frequency is away from the natural frequency.

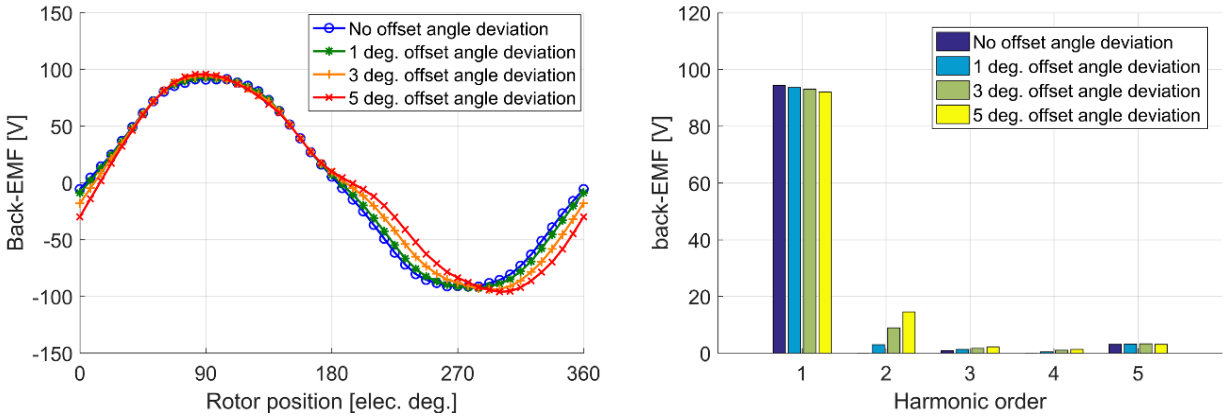

(a) (b)

Figure 1.4-5. Back EMF under the influence of rotor pole offset angle deviation [115]

B. Mechanical tolerance analysis

As mentioned previously, the imperfection of manufacturing not only compromise the performance of the electric machine but also increase the risk of malfunction. As the rotating component of the machine, the rotor required a careful tolerance analysis. In reference [115], three rotor mechanical tolerances have been investigated, i.e. rotor pole offset angle deviation, rotor static eccentricity, and rotor dynamic eccentricity. The dual-stator 6/4 FSPM machine has a salient pole rotor with 90° between adjacent rotor poles. The two rotor sets have a 45° shift angle to realize the even harmonics cancellation. However, there is a possibility that the required 45° shift angle is not respected. Reference [115] has investigated the angle deviations from 1° to 5°. The change of the back EMF waveform and the harmonics components are given in Figure 1.4-5. The fundamental component of the back EMF reduces while the harmonics increase, as the deviation angle becomes larger. The rotor magnetic force and the torque output under different deviation angle is shown in Figure 1.4-6. It can be seen that rotor pole offset angle deviation has small

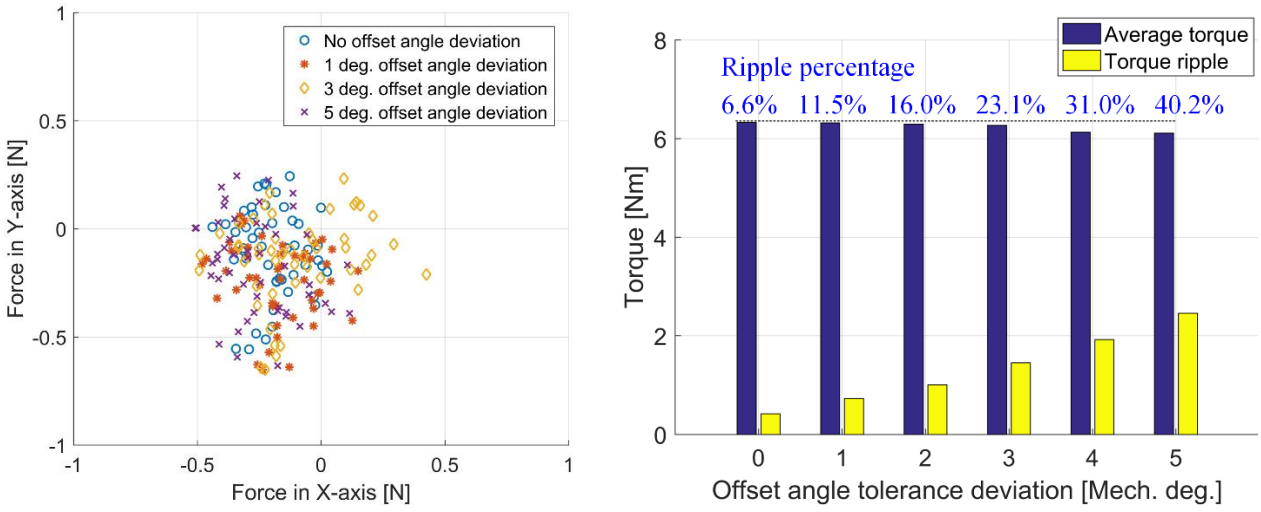

(a) (b)

Figure 1.4-6. Rotor magnetic force map with rotor pole offset angle deviation [115]

influence on the rotor magnetic radial force but has a significant impact on the average torque and torque ripple. The rotor static and dynamic eccentricity are defined as shown in Figure 1.4-7.

Both cases of eccentricity are studied with deviation range from 0.1 mm to 0.3 mm. The torque output waveforms of the dual-stator 6/4 FSPM machine with either a static or dynamic eccentricity are shown in Figure 1.4-8 (a) and Figure 1.4-8 (b), respectively. As can be seen, the

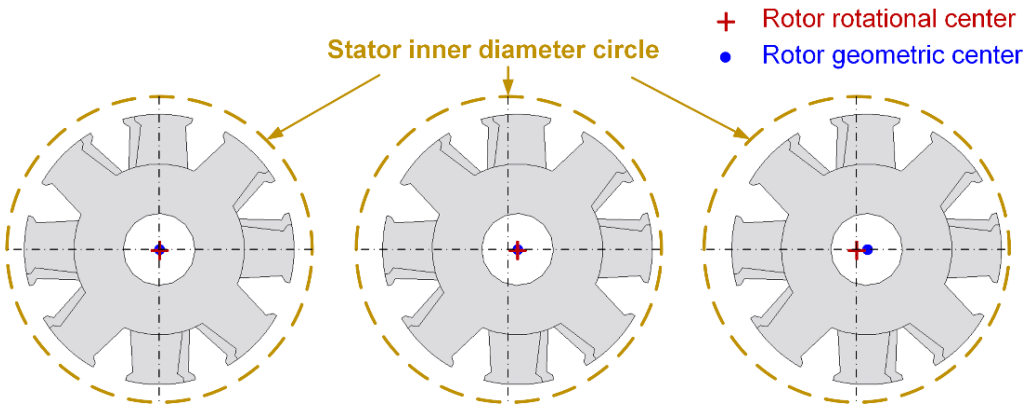

(a) (b) (c)

Figure 1.4-7. Rotor eccentricity (a) Perfectly centered rotor (b) Rotor with static eccentricity (c) Rotor with dynamic eccentricity [115]

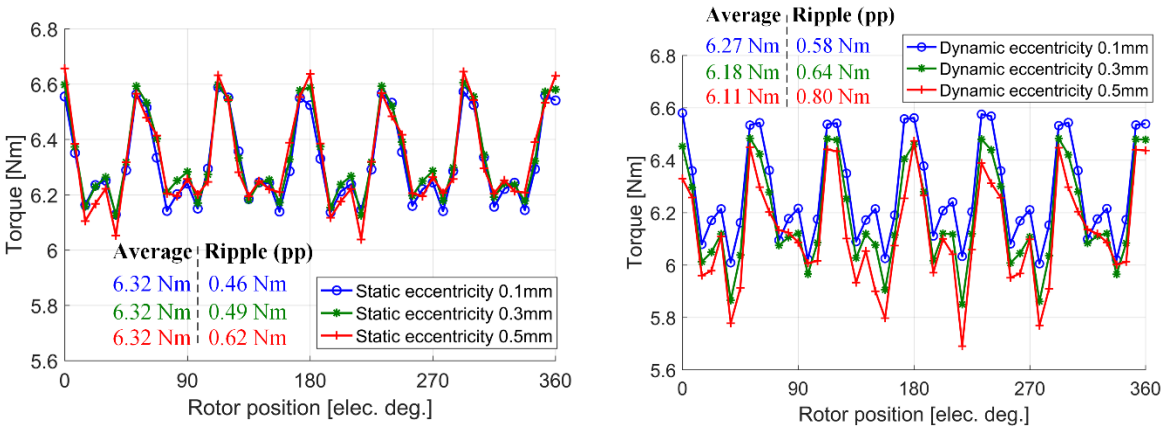

(a) (b)

Figure 1.4-8. Torque output waveform of dual-stator 6/4 FSPM machine with (a) Rotor static eccentricity (b) Rotor dynamic eccentricity [115]

torque output is hardly influenced by the rotor static eccentricity. However, larger rotor dynamic eccentricity causes a decrease in the average torque and an increase of torque ripple.

The magnetic force maps for rotor with static and dynamic eccentricity are given in Figure 1.4-9. It can be seen that for static eccentricity, the rotor magnetic force exists only in the direction

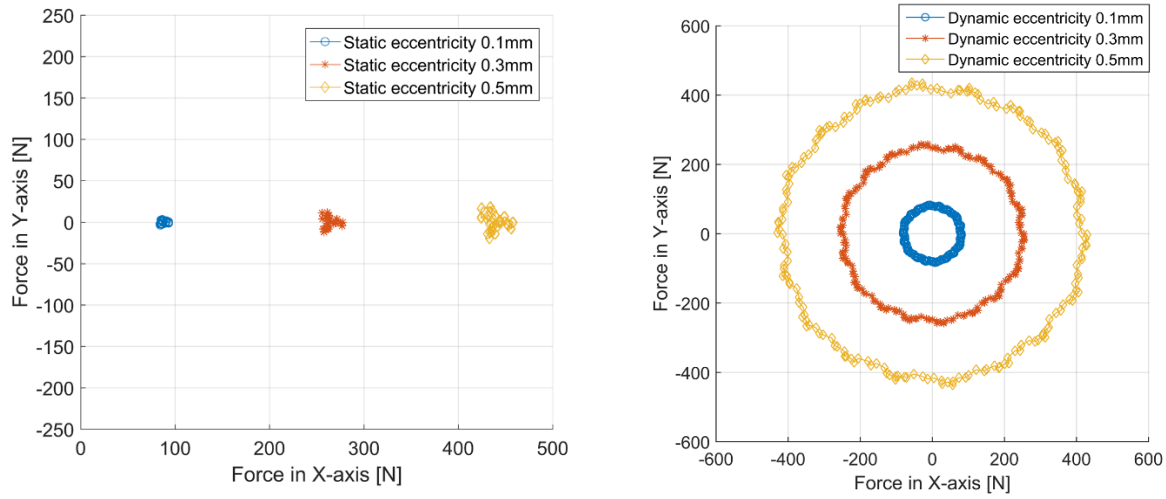

(a) (b)

Figure 1.4-9. Rotor magnetic force map for (a) Rotor static eccentricity (b) Rotor dynamic eccentricity [115]

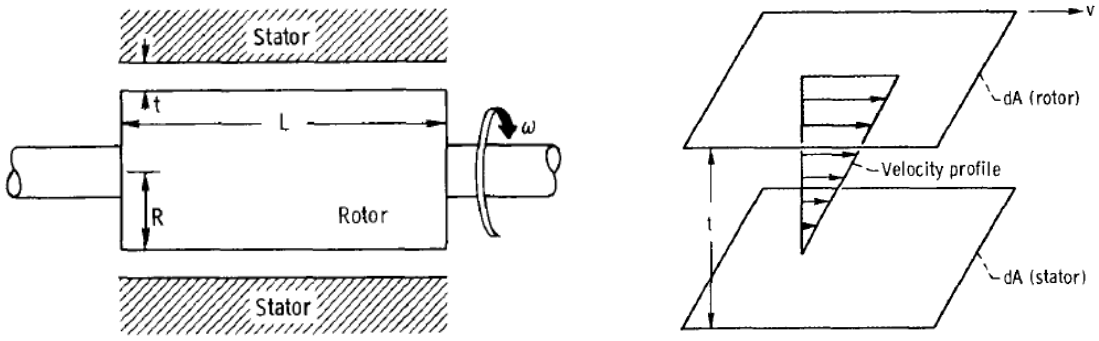

(a) (b)

Figure 1.4-10. Windage loss modeling for cylindrical rotor [132]

of deviation and is proportional to the deviation distance. The rotor magnetic force exists in every direction of the plane and is also proportional to the deviation distance.

1.4.3. Windage loss

Switch reluctance machine (SRM) and FSPM machine have been claimed suitable for high-speed applications because of the simple and robust rotor structure. However, the salient rotor pole causes non-negligible windage loss. An analytical model has been established to estimate the windage loss in [132]. For cylindrical rotor, as shown in Figure 1.4-10, the windage loss assuming laminar flow could be calculated with (Equation 1-20), where the friction coefficient (*Cd*) is

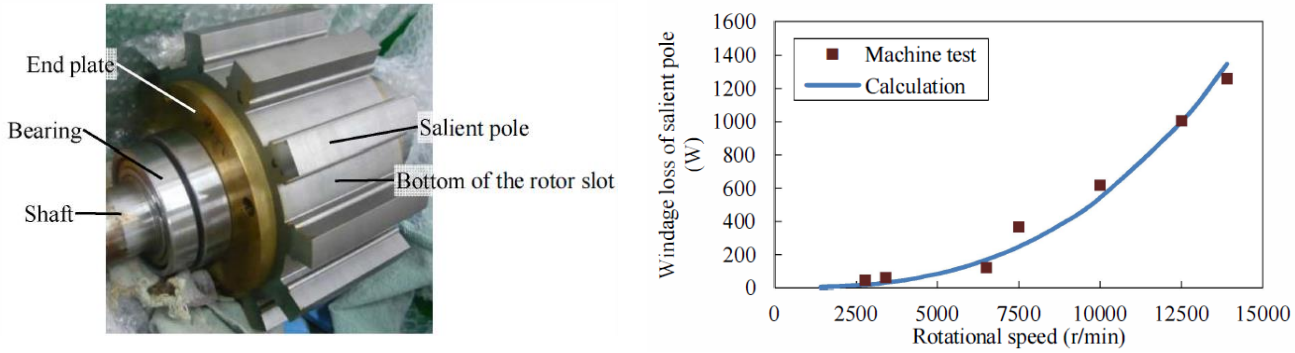

(a) (b)

Figure 1.4-11. Windage loss study for a 60 kW SRM machine (a) Rotor structure (b) Windage loss from calculation and measurement [133]

$$P_{wind} = \pi C_d \rho R^4 \omega^3 L \quad \text{(Equation 1-20)}$$

$$\mathrm{Re} = \frac{r\omega\rho t}{\mu} \quad \text{(Equation 1-21)}$$

$$\frac{1}{\sqrt{C_d}} = 2.04 + 1.768 \ln(\mathrm{Re}\sqrt{C_d}) \quad \text{(Equation 1-22)}$$

$$K_{salient} = 8.5\frac{H}{R} + 2.2 \quad \text{(Equation 1-23)}$$

defined as 2/*Re*. *Re* is the Reynold number and is calculated with (Equation 1-21). For the case of salient rotor pole with turbulent flow, the friction coefficient can be derived from (Equation 1-22). The windage loss needs to be corrected with a correction factor given by (Equation 1-23). The analytical-empirical equations have been used in many papers to estimate the windage loss. In reference [133], the windage loss of a 60 kW switch reluctance machine with 13 900 rpm is studied. The rotor geometry is shown in Figure 1.4-11(a), together with the calculated and measured mechanical loss shown in Figure 1.4-11 (b).

Windage loss reduction structures have been discussed for SRM and FSPM in many papers [133]–[136]. Essentially three types of rotor structure modifications have been proposed – ribs between rotor poles, shroud at the end of the rotor, and total cylindrical rotor, as shown in Figure 1.4-12. The dragging torque due to the windage friction of rotors with OD of 176.4 mm is given

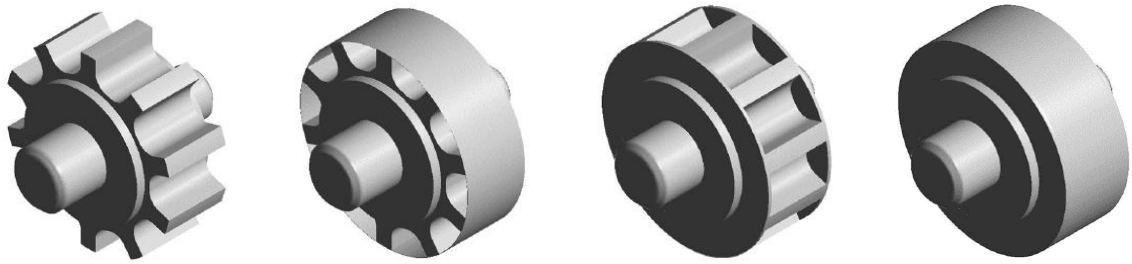

(a) (b) (c) (d)

Figure 1.4-12. Windage loss reduction structure (a) Original rotor structure (b) Rotor with ribs (c) Rotor with shrouds (d) Full cylindrical rotor [133]

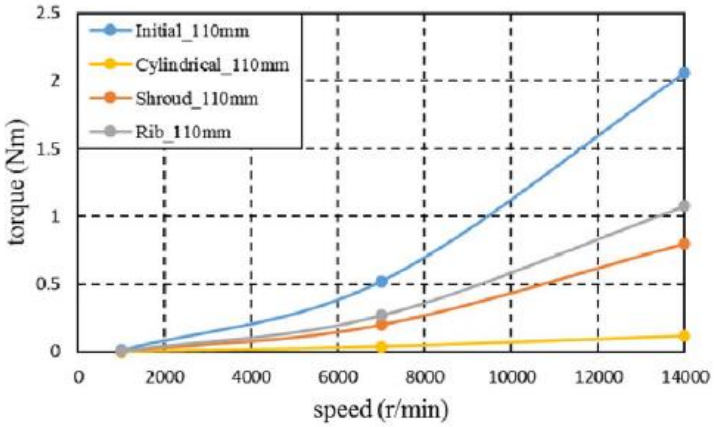

Figure 1.4-13. Windage friction dragging torque for different types of rotor structure [134]

in Figure 1.4-13. As can be seen, the cylindrical rotor has the most significant reduction of windage drag, and the shrouded rotor and rib rotor have similar performance. However, the influence on the electromagnetic performance needs to be further investigated to verify that the overall efficiency is improved. In addition, for the dual-stator 6/4 FSPM machine, the rotor structure is different from the conventional salient pole rotor. Therefore, further investigation of the windage loss is needed.

1.5. Summary

This chapter presents the state-of-the-art literature review on the research work about the flux switching permanent magnet machine. The main advantage of the FSPM machine is having both the permanent magnet and the armature winding in the stator, which allows a simple and robust rotor. Because of the use of the permanent magnet, the FSPM machine has higher power density compared to other machine topologies with robust rotor such as switch reluctance machine, synchronous reluctance machine, and induction machine. Therefore, the FSPM machine is a promising candidate for high power density and high-speed applications. In this chapter, the operation principle of the FSPM machine has been explained. Previous work on the design,

slot/pole combination study, optimization of the FSPM machine, and many creative FSPM topologies for improving the machine performance has been presented.

The most seen FSPM machine topology has 12 stator slots and 10 rotor poles, which acts as a 20-pole machine. Such high pole count is against the previously advertised high-speed application. The high fundamental frequency leads to a large amount of iron loss other AC machine losses. It is shown that the low-pole FSPM (dual-stator 6/4 FSPM) machine requires only a 40% fundamental frequency than the conventional 12/10 FSPM machine. However, the dual-stator 6/4 FSPM machine only has a maximum winding factor of 0.5, which limits the electric loading of the machine. It is worthwhile investigating the winding topology for the low-pole FSPM machine to improve the winding factor.

The multi-physics design for the FSPM machine is briefly reviewed. Having the permanent magnet and armature winding both in the stator makes the machine thermal management easier. On the other hand, it also requires a more effective cooling system than rotor-mount PM machines under full load and overload conditions. Previous work on the thermal analysis of the 12/10 FSPM machine is a good guideline for conducting thermal analysis for the low-pole FSPM machine. Because of the salient rotor structure, the windage loss is not negligible for high-speed FSPM machine. Researches on windage loss reduction for switch reluctance machine have proposed some rotor structure to reduce windage loss. It is worthwhile investigating the impacts and benefits of the modified rotor structure on the low-pole FSPM machine.

As a summary, this research continues the previous work on the investigation of low-pole FSPM machine with a focus on the 6/4 topology. The objective is to further improve the performance of the machine and to investigate the multi-physics design. The following chapters are dedicated to addressing those research topics individually.

Chapter 2 Analytical Modeling of Dual-Stator 6/4 FSPM Machine

As shown in the previous chapter, the 6/4 FSPM machine operates with 60% less fundamental frequency compared to the commonly seen 12/10 FSPM machine at the same speed. The reduced fundamental frequency brings the benefits of lower iron loss and ac copper loss. In addition, with the same current switching ripple level, the inverter's switching frequency can be reduced for lower fundamental frequency. Therefore, switching loss in the motor drive is also reduced. However, the conventional 6/4 FSPM machine has considerable second-order harmonic in the flux linkage and back EMF, which makes it impossible to operate with sinusoidal three-phase ac drive. The origin of the large second-order harmonic and its cancellation are discussed in this chapter. In addition, the winding factor of the 6/4 FSPM machine is investigated. High winding factor design for the 6/4 FSPM machine is identified.

2.1. Fundamentals of dual-stator 6/4 FSPM machine

Several topologies of the 6/4 FSPM machine have been investigated in this research, which can be classified into different groups according to the winding topology. To clarify the focus of this research, a figure of the classification of different dual-stator 6/4 FSPM machine is plotted, as shown in Figure 2.1-1. The three topologies on the right with no middle end turn (NMET) are the main investigation target of this thesis.

2.1.1. Second-order harmonic in flux-linkage and the cancellation

FSPM machine places the circumferentially magnetized permanent magnet in a spoke-type fashion on the stator. It does not rely on the rotor-mounted magnet to generate the alternating flux linkage synchronized to the rotor rotation. The section view of a 6/4 FSPM machine with double-

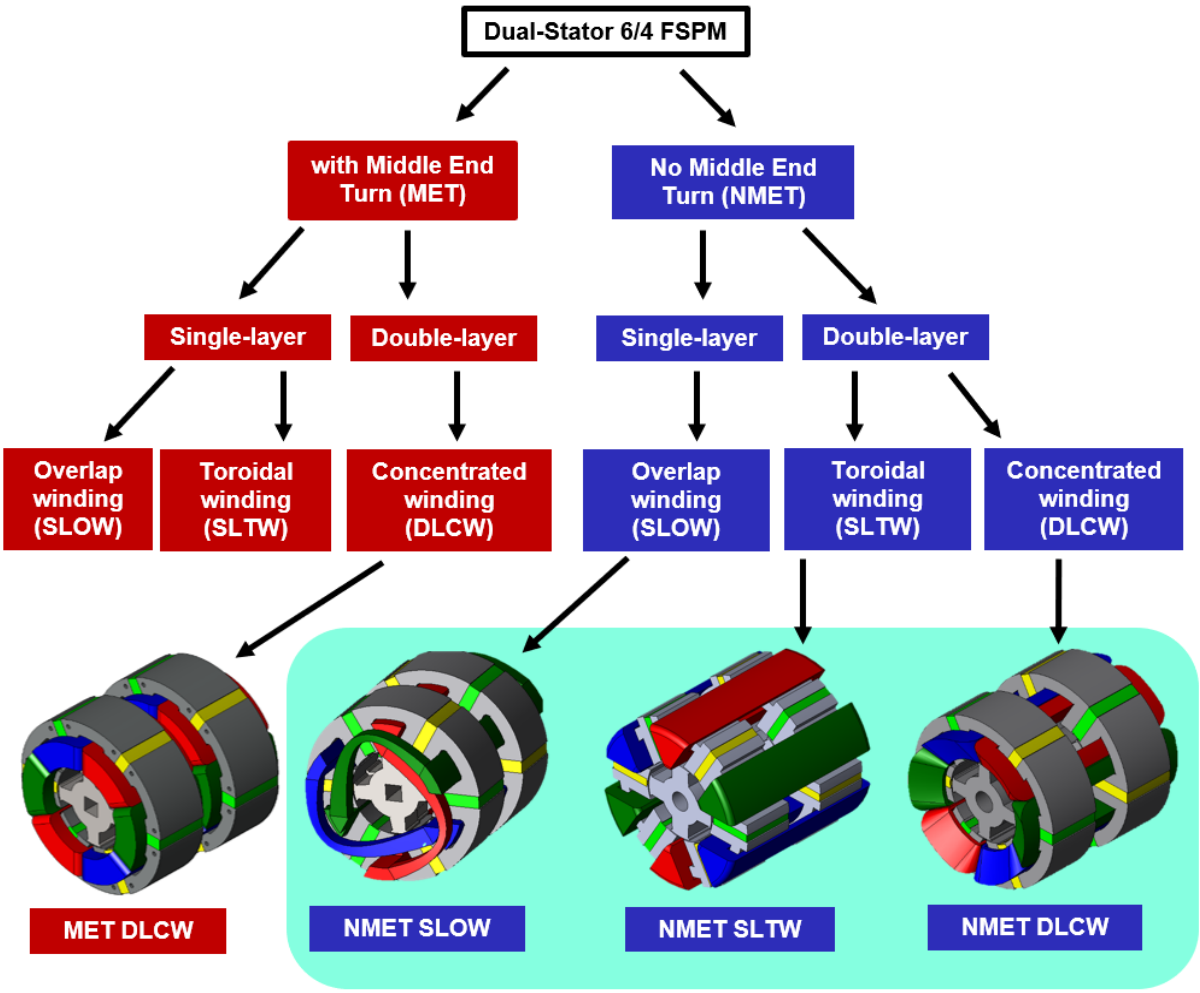

Figure 2.1-1. Classification of dual-stator 6/4 FSPM machine according to winding topology

layer winding is shown in Figure 2.1-2. As the rotor rotates, the flux linkage across the coil is varying and induces back electromotive force (EMF) at the terminals of the motor phase cables. To better illustrate the operation of the 6/4 FSPM machine, a simplified rectangular partial model of the 6/4 FSPM machine is established and shown in Figure 2.1-3. As can

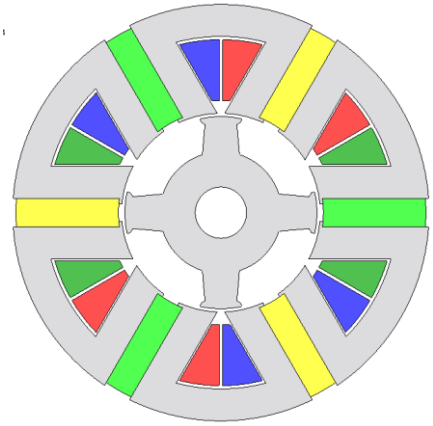

Figure 2.1-2. Section view of a 6/4 FSPM machine with double-layer winding.

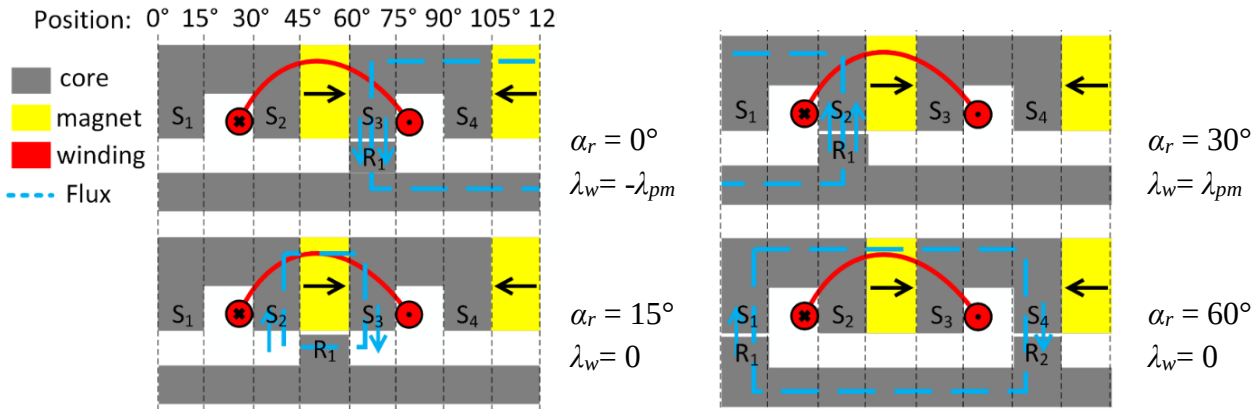

Figure 2.1-3. Simplified partial model of 6/4 FSPM machine with four critical rotor positions

be seen, the magnets on the stator are magnetized circumferentially. Arrows on the magnets indicate the direction of magnetization. The rotor is set moving from the right to the left, and four critical rotor positions are shown consecutively (from $\alpha_r = 0$ to $\alpha_r = 60$, where α_r is the rotor rotation angle). Note that each stator unit consists of one U-shape stator core and one adjacent permanent magnet. Therefore, the partial model shown in Figure 2.1-3 is one-third of the whole stator and has a mechanical angle span of 120°. The rotor is not a multiple of three, and the number of rotor pole shown in the figure is changing.

The rotor poles are placed 90° away from each other since there are four rotor poles in the 6/4 FSPM machine. For simplicity, the stator tooth width, rotor pole width, slot opening, and the magnet thickness are assumed to be the same. The angular positions of each segment of the stator and the rotor are marked in Figure 2.1-3. At the first position ($\alpha_r = 0°$), where the rotor pole R_1 is aligned with stator tooth S_3, the magnetic flux is passing from the stator tooth to the rotor pole through the air gap. When defining the positive flux linkage direction as from the rotor towards the stator, the flux linkage of the winding reaches its minimum at $\alpha_r = 0°$, noted as $-\lambda_{pm}$. In the second position where the rotor pole is aligned with the magnet between S_2 and S_3, the flux path is closed between the two coil sides of the winding. Therefore, no net flux linkage passes through

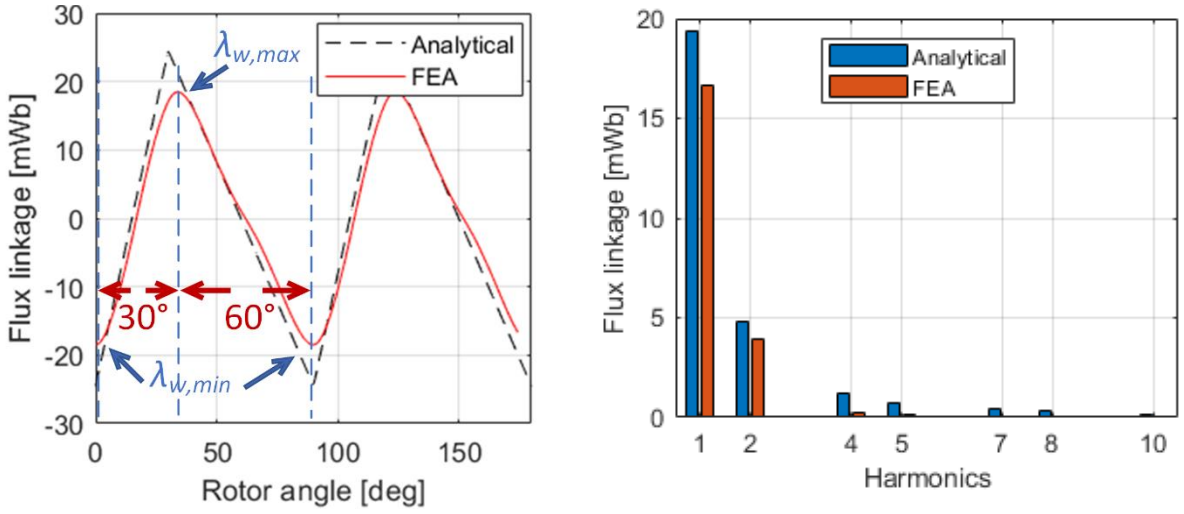

(a) (b)

Figure 2.1-4. Flux linkage of a single stator of 6/4 FSPM machine (a) Flux linkage waveform (b) Harmonic components in the flux linkage

the winding at α_r = 15°. As the rotor pole R_1 is aligned with S_2 at α_r = 30°, the flux is passing from the rotor pole to the stator tooth. According to the direction defined previously, the flux linkage of the winding is now at maximum, i.e. λ_{pm}. At the fourth position, the rotor pole R_1 and R_2 are aligned with the two stator teeth S_1 and S_4. As can be seen in Figure 2.1-3, the flux path is closed outside the winding. Therefore, the flux linkage through the winding is zero at α_r = 15°. It can be seen that the flux linkage through the coil is changing periodically from λ_{pm} to $-\lambda_{pm}$. However, the flux linkage changes from $-\lambda_{pm}$ to zero then to λ_{pm} with an angle step of 15°, but changes from λ_{pm} to zero then back to $-\lambda_{pm}$ with an angle step of 30°. Therefore, the flux linkage variation is asymmetric.

The winding flux linkage of the 6/4 FSPM machine can be approximated by a piecewise function, as shown in Figure 2.1-4 (a). With fast Fourier transformation, the harmonic components of the flux linkage can be calculated and are shown in Figure 2.1-4 (b). As can be seen, the fundamental and second-order harmonic are dominant. Therefore, the flux linkage in the winding λ_w can be sufficiently approximated as (Equation 2-1), where λ_1 and λ_2 are the magnitudes of the

$$\lambda_w = \lambda_1 \cos(\omega_e t) + \lambda_2 \cos(2\omega_e t) \quad \text{(Equation 2-1)}$$

fundamental and second-order harmonic components of the flux linkage (Wb), ω_e is the electrical angular speed (rad/s). The flux linkage waveform and the harmonic components from FEA simulation are also shown in Figure 2.1-4. As can be seen, the fundamental and second-order harmonic components are dominant. The difference in the amplitude comes from the simplification of the machine model.

When the rotor pole initial angle is shifted 45° mechanically, a 180° electrical phase shift is added to the flux linkage, and the new flux linkage λ_{w2} can be expressed as (Equation 2-2). The

$$\begin{aligned} \lambda_{w2} &= \lambda_1 \cos(\omega_e t + 180°) + \lambda_2 \cos[2(\omega_e t + 180°)] \\ &= -\lambda_1 \cos(\omega_e t) + \lambda_2 \cos(2\omega_e t) \end{aligned} \quad \text{(Equation 2-2)}$$

$$\lambda_{w2}' = \lambda_1 \cos(\omega_e t) - \lambda_2 \cos(2\omega_e t) \quad \text{(Equation 2-3)}$$

goal is to cancel the second harmonic and keep the fundamental component. As can be observed from (Equation 2-2), when the magnetizing direction of the magnet is inversed, the new winding flux linkage λ_{w2}' would become (Equation 2-3). When the two stators share the same sets of winding, the total flux linkage can be calculated as the sum of (Equation 2-1) and (Equation 2-3), which only contains the fundamental component.

Note that due to the symmetry of the machine, the flux linkage in the two coils in the same phase of the 6/4 FSPM machine is identical. However, for 12/10 FSPM machine and other FSPM machine with a stator slot number larger than 12, the number of coils per phase is larger or equals to four, and there are more than two pairs of coils for one phase that can cancel the second-order

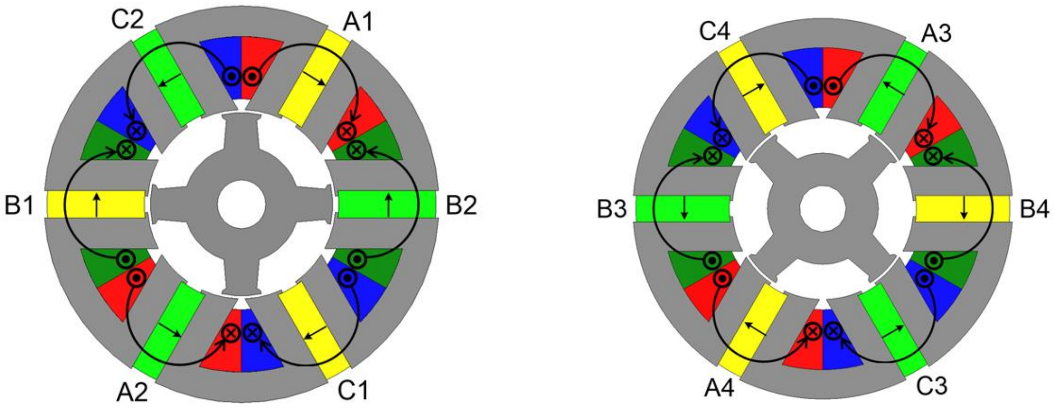

(a) (b)

Figure 2.1-5. Section view and stator winding connection of dual-stator 6/4 FSPM machine (a) Front stator (b) Rear stator

harmonic. Therefore, second-order harmonic exists in the flux linkage of each coil of all FSPM machines, but it can be canceled internally in FSPM machines with a large number of stator slot.

2.1.2. Gap between two stators

The second-order harmonic in the flux linkage can be canceled with the use of a second pair of winding, which is accommodated in another stator. The magnets in the two stators have opposite magnetizing directions. Figure 2.1-5 (a) and Figure 2.1-5 (b) shows the section view of the front stator and rear stator with winding connection, respectively. When assemble the two stators together, it is necessary to keep a certain distance between the two stators. Otherwise, significant magnetic flux leakage occurs because of the opposite magnetizing direction. As shown in Figure 2.1-6, the length of the gap between the two stators is a

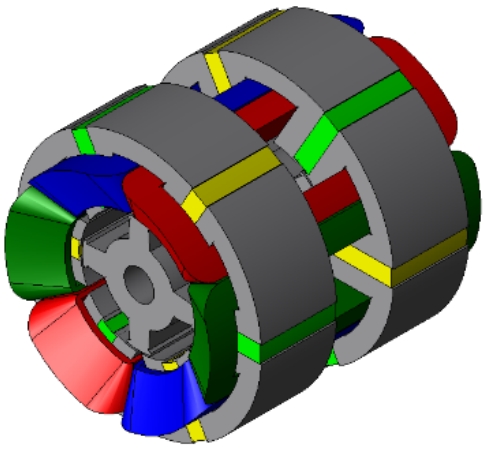

Figure 2.1-6. 3D view of the dual-stator 6/4 FSPM machine

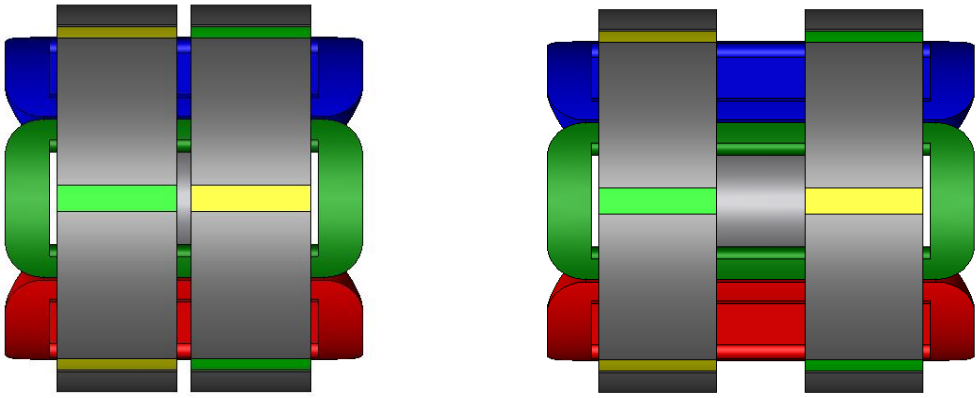

(a) (b)

Figure 2.1-7. Dual-stator 6/4 FSPM machine with a stator gap length of (a) 5 mm and (b) 30 mm

design degree of freedom. To determine an optimal gap length between the stators, a parametric study is done using 3D finite element analysis (FEA) simulation. As shown in Figure 2.1-7, two dual-stator 6/4 FSPM machines with a gap length of 5 mm and 30 mm are shown. As can be seen, shorter gap provides a more compact design which not only increases the volumetric power density, but also reduces the stator winding length which is beneficial for low copper loss. However, the magnetic flux leakage caused by the small gap length compromises the magnetic loading of the machine. Seven cases with different gap lengths are simulated in JMAG Designer at the speed of

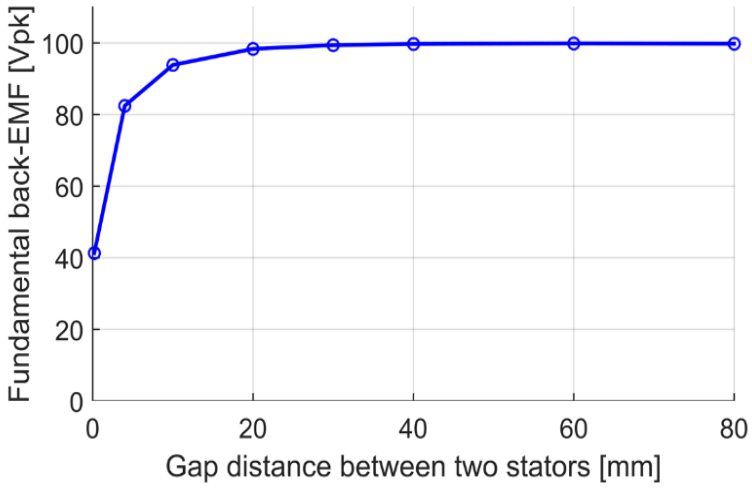

Figure 2.1-8. Back EMF value variation versus different stator gap length

TABLE 2-1. LOSSES AND EFFICIENCIES OF DUAL-STATOR 6/4 FSPM MACHINE WITH DIFFERENT GAP DISTANCE BETWEEN THE STATORS

[mm]	P_{out} [W]	P_{Cu} [W]	P_{stator} [W]	P_r [W]	P_{mag} [W]	*Eff* [%]	[kW/L]
0	5543.1	246.8	97.5	47.4	45.2	91.6	5.22
5	7561.5	255.7	121.9	58.0	48.3	92.9	6.70
10	8943.8	266.1	144.5	69.2	56.2	93.4	7.48
15	9020.6	276.5	147.8	72.9	57.9	93.2	7.15
20	9103.0	286.8	146.9	74.5	57.3	93.2	6.86
25	9159.2	298.1	146.1	76.1	57.4	93.1	6.57
30	9189.2	307.6	148.4	77.0	57.3	92.9	6.29
35	9196.6	320.4	148.5	77.9	57.1	92.8	6.02

15000 rpm. The no-load back EMF of the machines with different gap lengths are given in Figure 2.1-8. It can be seen that as the back EMF value increases with the gap length. At a length of 30 mm, the back EMF achieves 99.5% of the value when the two stators are infinitely separated. The stator/rotor iron loss is also influenced by the gap distance as well as the output power. Note that when reducing the gap length between the two stators, only reduction of back EMF amplitude is observed and no waveform distortion. There is no magnetic material between the two stators. Therefore, machine inductance is not affected.

TABLE 2-1 shows the losses of different machine components and the efficiencies of the dual-stator 6/4 FSPM machine with different gap distances between the stators. As can be seen from the table, the machine has a relatively high efficiency with a small gap distance due to the reduced copper/iron losses. However, the output power is reduced because of the flux leakage between the axially adjacent magnets. From TABLE 2-1, the dual-stator 6/4 FSPM machine with a gap of 10 mm can achieve 97% of the power of the machine with infinitely separated stators. Note that the purpose of this project is to investigate the realization of dual-stator 6/4 FSPM machine, but not investigating the engineering trade-off between performance and cost. Therefore, a 30 mm stator gap is chosen. The back EMF of the 30 mm gap design is very close to the infinitely separated case without having too much waste on the volume.

2.2. Winding configuration of 6/4 FSPM machine

2.2.1. Back EMF vector graph and winding factor of FSPM machine

Winding factor is an important machine design parameter that reflects the useful winding MMF. For a generic winding topology, the winding factor (k_w) mainly consists of two parts, distribution factor (k_d) and pitch factor (k_p). With distributed winding, there are multiple slots contributed for one magnetic pole, as shown in Figure 2.2-1 (a). The total EMF generated by the

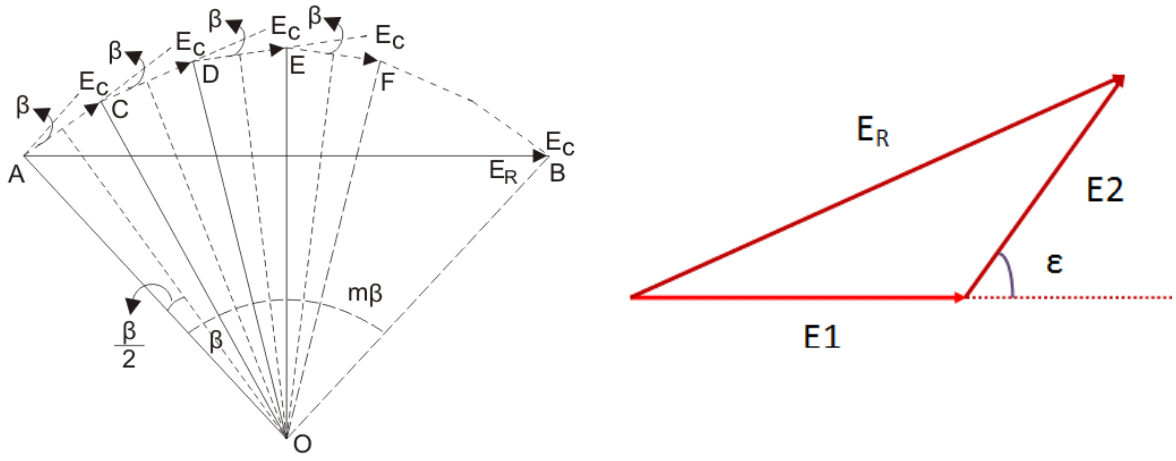

(a) (b)

Figure 2.2-1. EMF vector for calculation of (a) Winding distribution factor (b) Winding pitch factor

coils is the vector sum of the individual EMF vector, which is smaller than the arithmetic sum. The distribution factor is defined as the ratio between those two numbers, shown as (Equation 2-4).

$$k_d = \frac{\sin(m\beta/2)}{m\sin(\beta/2)} \qquad \text{(Equation 2-4)}$$

$$k_p = \cos(\frac{\varepsilon}{2}) \qquad \text{(Equation 2-5)}$$

Similarly, as shown in Figure 2.2-1 (b), when the distance two coil side of one magnetic pole is

smaller than 180°, the vector sum of the two individual EMF vector is smaller than the arithmetic sum, whose ratio defines the pitch factor, as shown (Equation 2-5).

However, as mentioned previously, FSPM machines cannot employ distributed winding due to the stator-mounted permanent magnet. Therefore, the calculation of the winding factor of the FSPM machine is done by using the EMF vector. Taking the example of the most commonly seen 12/10 FSPM machine, the coil side vectors for phase A are shown in Figure 2.2-2 (a). The EMF

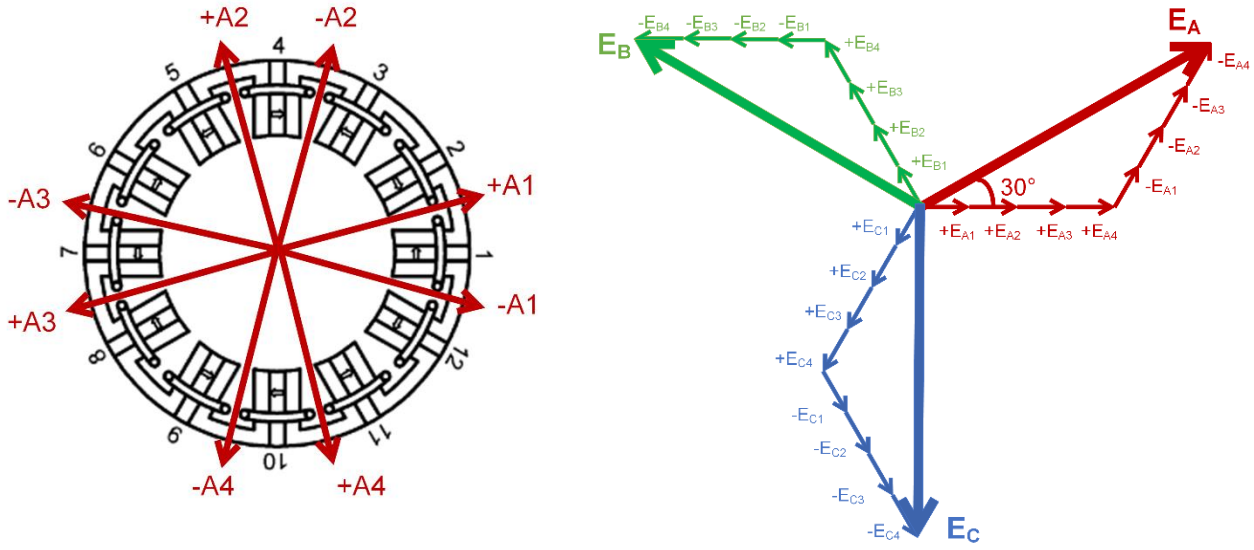

(a) (b)

Figure 2.2-2. 3-phase 12/10 FSPM machine (a) Coil side vector of phase A and (b) EMF vectors graph

vector of each coil side can be calculated as (Equation 2-6) [137], where P_r is the rotor pole number,

$$\overrightarrow{E_{xi}} = e^{jp_r\theta_{xi}} \qquad \text{(Equation 2-6)}$$

x is the phase notation (A, B, or C), i is the coil side number (1, 2, 3, or 4), θ_{xi} is the mechanical angular position of the corresponding coil side. Without loss of generality, θ_{A1} is assigned to be 0°. The EMF phase vector graph for the 3 phase 12/10 FSPM machine can be drawn as Figure 2.2-2 (b). As can be seen, each phase contains eight individual EMF vectors. However, the EMF vectors

are not co-linear, which makes their vector sum shorter than their arithmetic sum. By definition, the winding factor is the ratio between the two sums, as shown in (Equation 2-7). For the 12/10

$$k_w = \frac{|\sum_{i=1}^{N_s/3} \overrightarrow{E_{xi}}|}{\sum_{i=1}^{N_s/3} |\overrightarrow{E_{xi}}|} \qquad \text{(Equation 2-7)}$$

FSPM machine, the winding factor equals to $\cos\left(\frac{\pi}{6}\right)$=0.86. Higher number of stator slot is beneficial for increasing the winding factor of FSPM machine. Special winding layout can even achieve unity winding factor as shown in the following section.

2.2.2. Winding factor of 6/4 FSPM machine

The EMF vector method can also be applied to the 6/4 FSPM machine. Start with the conventional double-layer concentrated winding (DLCW) 6/4 FSPM machine. The coil vectors graph and the EMF vector graph are shown in Figure 2.2-3 (a) and Figure 2.2-3 (b), respectively. From the EMF vector graph, the winding factor of the DLCW 6/4 FSPM machine can be calculated

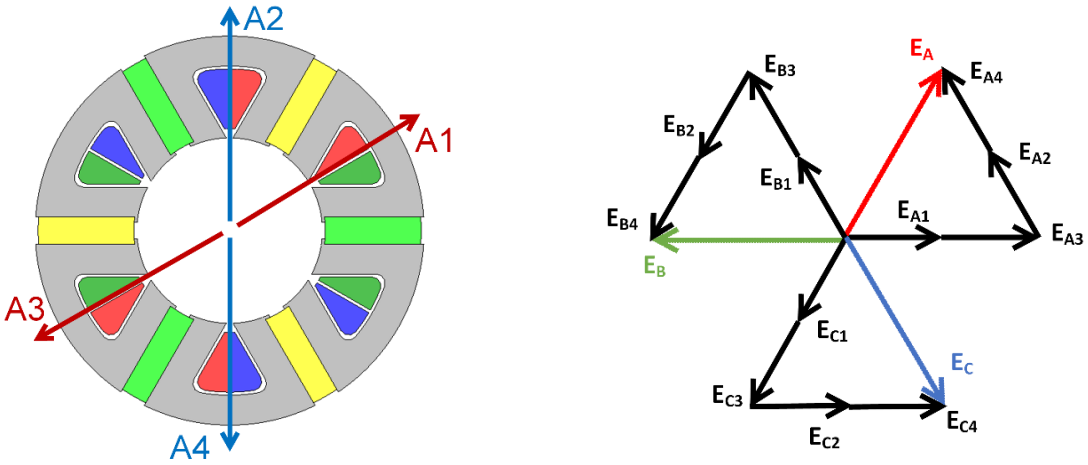

(a) (b)

Figure 2.2-3. Double-layer concentrated winding 6/4 FSPM machine (a) Coil side vector of phase A and (b) EMF vector graph

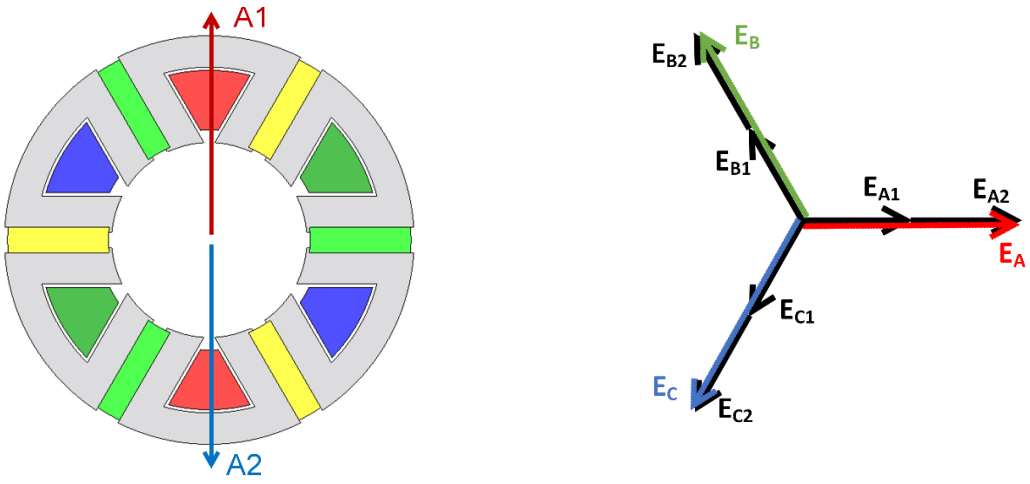

(a) (b)

Figure 2.2-4. Single-layer concentrated winding 6/4 FSPM machine (a) Coil side vector of phase A and (b) EMF vector graph

with (Equation 2-7) as $\cos\left(\frac{\pi}{3}\right)$ = 0.5. The winding factor of the DLCW 6/4 FSPM machine is 42% less than the winding factor of the 12/10 FSPM machine and left plenty of room for improvement. Keeping the 6/4 topology, instead of using a double-layer winding, single-layer winding can be applied, as shown in Figure 2.2-4 (a). In single-layer winding 6/4 FSPM machine, there are only two coil sides for each phase, which are place 180° away from each other. The corresponding EMF vector graph is shown in Figure 2.2-4 (b). As can be seen, the EMF vectors in the same phase are co-linear. Therefore, the amplitude of the total EMF for one phase is equal to the arithmetic sum of the individual vectors. According to (Equation 2-7), the winding factor of the single-layer 6/4 FSPM machine is 1. Compared to the DLCW winding, the use of single-layer winding can double the winding factor.

2.2.3. Single-layer Circumferential winding and Toroidal winding layout

Figure 2.2-4 (a) shows the section view of the single-layer winding 6/4 FSPM machine without specifying the actual winding layout. Unlike the DLCW 6/4 FSPM machine, where the

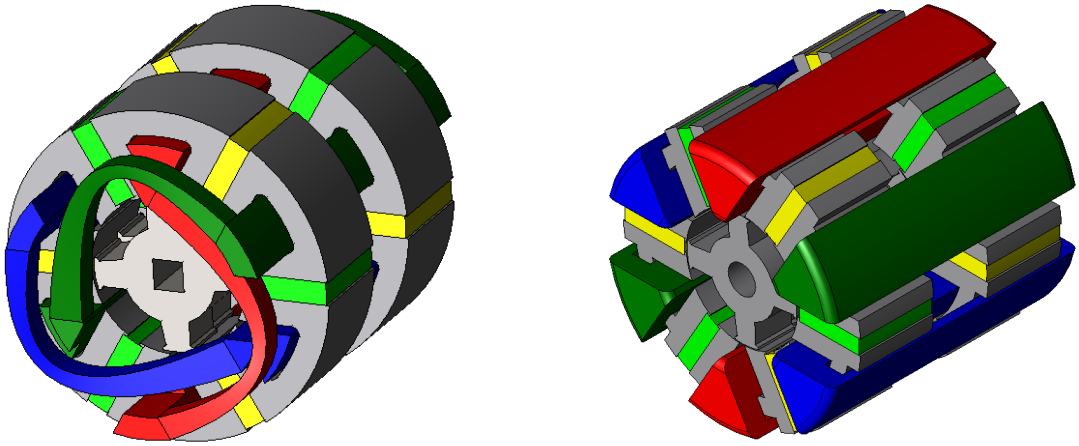

(a) (b)

Figure 2.2-5. Realization of single-layer winding 6/4 FSPM machine with (a) Single-layer overlapping winding (SLOW) and (b) Single-layer toroidal winding (SLTW)

two coil sides are very close to each other and can be easily connected with a concentrated coil, the two coil sides of the single-layer winding 6/4 FSPM machine locates 180° away. The straightforward way of realization is using circumferential winding, as shown in Figure 2.2-5 (a). The two coil sides are connected through end windings that travel across half of the entire stator circumference. The other possible winding topology is single-layer toroidal winding (SLTW), as shown in Figure 2.2-5 (b). The returning coil comes back from the outside of the stator back iron. In order to provide a structural support for the returning coil, the stator core is designed to be an H-shape. The section views of the front stator of the two winding topologies are shown in Figure 2.2-6 (a) and Figure 2.2-6 (b), respectively. The two single-layer winding layouts have differences in several aspects, which will be discussed in the following part.

A. Manufacturing complexity

As can be seen clearly in Figure 2.2-5 (a), the end winding of the overlapping winding has 180^{o} span angle and covers half of the entire stator circumference. For random wound winding, such large span angle makes the winding mechanically unstable due to gravity, if not properly

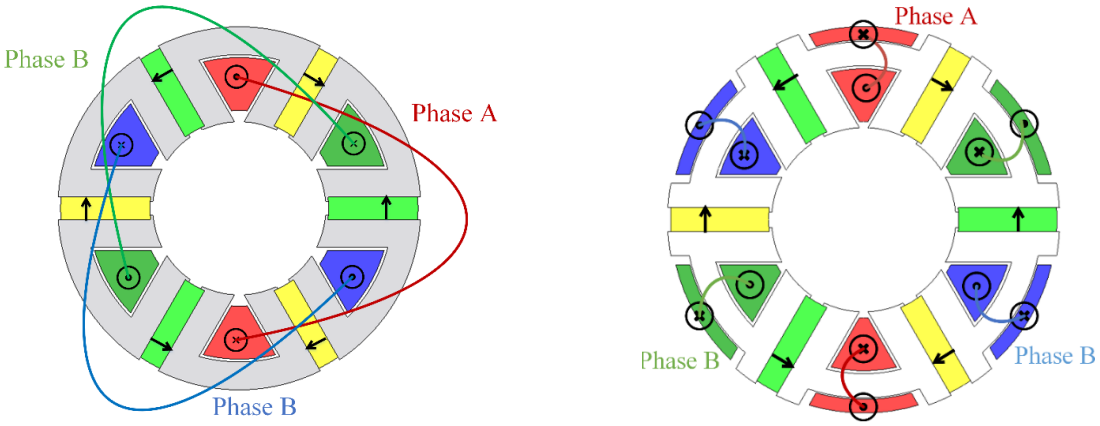

(a) (b)

Figure 2.2-6. Section views of the front stator of (a) SLOW and (b) SLTW dual-stator 6/4 FSPM machine

bound or fixed. The winding overlaps occur at three positions, which are close to the coil's entering and leaving location. Therefore, an extra axial volume is needed to accommodate the bent coil. Whereas for the toroidal winding, as shown in Figure 2.2-5 (b), no overlapping occurs between the coils, and phase-phase insulation is not needed. The toroidal winding also makes the machine has a more modular design, as shown in Figure 2.2-6. The individual stator unit is not linked by the stator winding, which potentially allows higher slot filling factor and easier manufacturing.

B. Stator winding length

The winding resistance is proportional to the length of the winding coil. The two machines have the same stack length, and the end winding length determines which topology has a larger winding resistance. The SLOW 6/4 FSPM machine has an end turn that travel across half of the stator circumference, while the returning coil of the SLTW topology is acting like an end turn. The total length of a coil (l_c) can be calculated as (Equation 2-8), where l_{stack} is the stack length, a and

$$l_C = n(2l_{stack} + 4a + 2b) \qquad \text{(Equation 2-8)}$$

b are the axial and planar length of the end winding, respectively. n is the number of coils per

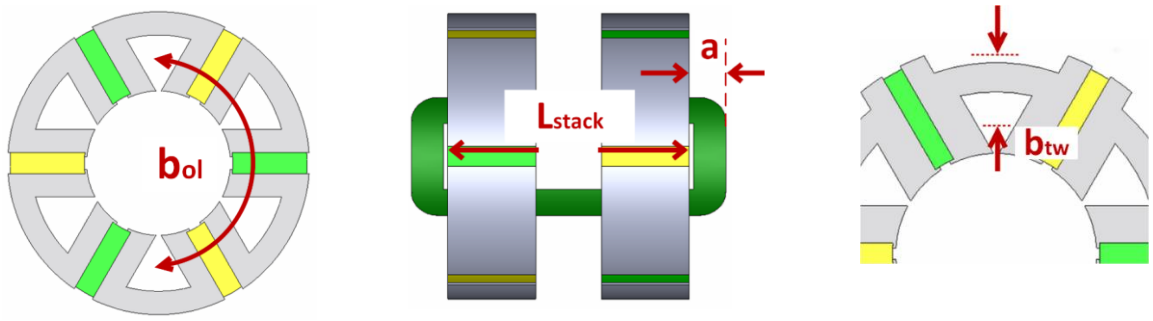

(a) (b) (c)

Figure 2.2-7. Geometry parameters for stator winding resistance calculation.

TABLE 2-2. WINDING PARAMETERS OF 6/4 FSPM MACHINES

	D_{os} [mm]	l_{stack} [mm]	a [mm]	b [mm]	l_C [mm]	Rs [Ω]
SLOW	130	110	15	152	584	31.9
SLTW	130	110	15	18	632	34.7 (+8%)

phase. The *a* and *b* for the two winding layouts are shown in Figure 2.2-7. A comparison of coil length is given in TABLE 2-2. As can be seen, with the given machine outer diameter and stack length, the total coil of the two machines are similar with a difference of 8%.

C. Cooling and thermal management

FSPM machine is usually claimed to have easy thermal management because of both armature windings and permanent magnets located in the stator. Compared to rotor-mounted permanent magnet machine such as IPM and SPM machine, the temperature-sensitive magnet us easier to be cooled by a water jacket integrated housing or housing with fins. On the other hand, having permanent magnets and armature windings both in the stator requires cautious machine thermal analysis. For the double-layer FSPM machine, the magnets are surrounded by the end winding. If not properly cooled, the overheating issue could be severe. Things get worse for the single-layer FSPM machine with overlapping winding because of the larger end winding.

For the single-layer toroidal winding FSPM machine, as can be seen in Figure 2.2-5 (b), the armature windings and the magnets are well separated in space. The magnets are away from the hot windings and are only in contact with the stator core, which has lower temperature than the magnets. The toroidal topology allows one coil side of the winding has a close contact with the housing. With proper encapsulation of high thermal conductivity epoxy, the thermal resistance between the windings and the water jacket will be significantly lower compared to the overlapping winding topology and double-layer winding configuration. Detailed cooling design and thermal analysis are done in Chapter 5. The stator winding of electric machine is usually encapsulated with epoxy to improve the thermal performance since air is a terrible conductor for heat. Different encapsulation materials have various curing temperature, which ranges from room temperature up to hundreds degree Celsius. The curing temperature of certain encapsulation material might exceed the temperature limit of the permanent magnet and cannot be applied to the double-layer winding FSPM machine. Therefore, the separation of armature winding and the permanent magnet in the single-layer toroidal winding FSPM machine allows a wider choice of encapsulation material and can potentially improve the thermal performance of the machine.

The two realizations of the single-layer winding topologies have difference in several aspects, the comparisons shown above suggest that the toroidal winding is a more reasonable approach than the overlapping winding. In the following part of this paper, the analysis, simulation, and comparison will be done with the toroidal winding for the single-layer winding topology.

2.3. Design parameters of the dual-stator 6/4 FSPM machine

In the previous section, it is shown that the single-layer winding 6/4 FSPM machine can achieve twice winding factor than the conventional double-layer winding 6/4 FSPM machine. The single-layer toroidal winding further increases the manufacturing feasibility and thermal performance. The machine design parameters and the sizing equations of the 6/4 FSPM machines

are presented in this section, to analytically evaluate the benefits of the single-layer winding 6/4 FSPM machine.

2.3.1. Sizing equation of 6/4 FSPM machine

The sizing equation is a commonly used design tool to preliminarily determine the volume of the machine required for a specific power level. Assuming that the stator tooth width, stator slot opening width, and the magnet thickness are identical. The flux linkage per coil can be modeled as (Equation 2-9) where N_C is the number of turns per coil, B_t is the magnetic flux density (T) in

$$\lambda_C = N_C D_{is} L \int_{\theta_0}^{\theta_0+\theta_s} B_t(\theta) d\theta \qquad \text{(Equation 2-9)}$$

the stator tooth, D_{is} is the stator inner diameter (m), l_{stack} is the machine stack length (m), θ_s is the angular span (rad) of one stator tooth, and N_s is the number of stator slot. Assuming that the magnetic flux density is uniform in the stator tooth, the back EMF per coil can be calculated as (Equation 2-10) The total back EMF per phase can be derived as (Equation 2-11) where B_{t1} is the

$$e_C = \frac{d\lambda_C}{d\theta}\frac{d\theta}{dt} = \frac{\omega_r N_C D_{is} \pi L}{4N_s}\frac{dB_t}{d\theta} \qquad \text{(Equation 2-10)}$$

$$= \frac{\omega_r N_C D_{is} \pi L}{4N_s}\left(\frac{2B_{t1}}{\pi/N_r}\right) = \frac{N_r}{2N_s} N_C D_{is} L B_{t1} \omega_r$$

$$E_{rms} = \frac{N_s}{3\sqrt{2}} k_w e_C = \frac{1}{6\sqrt{2}} k_w N_r N_C D_{is} L B_{t1} \omega_r \qquad \text{(Equation 2-11)}$$

amplitude of the fundamental component of the stator tooth flux density (T).

The armature current (I_{rms}) can be expressed as a function of the current density ($K_{s,rms}$) at the stator inner surface, as shown in (Equation 2-12) As a three-phase machine, the output power

$$I_{rms} = \frac{K_{s,rms}\pi D_{is}}{N_s N_C} \quad \text{(Equation 2-12)}$$

$$P_{out} = 3E_{rms}I_{rms} = \frac{\pi}{2\sqrt{2}}\frac{N_r}{N_s}k_w D_{is}^2 L B_{t1} K_{s,rms}\omega_r \quad \text{(Equation 2-13)}$$

of the 6/4 FSPM machine can be expressed as (Equation 2-13). As can be seen, with a defined machine stator diameter and stack length, the output power of the 6/4 FSPM machine is proportional to the product of the winding factor, magnetic loading, and electric loading. Therefore, less magnetic or electric loading is needed for machine with higher winding factor for the same power level, which leads to lower copper loss and iron loss. Detailed losses and efficiency comparison are shown in Chapter 3.

2.3.2. Machine design parameters

In order to have a direct comparison between the single-layer and double-layer winding 6/4 FSPM machine, and to illustrate the pros and cons of the single-layer winding design, the single-layer dual-stator 6/4 FSPM machine is designed to have the same sizing, i.e. outer diameter and stack length as the double-layer FSPM machine shown in [138]. Machine design parameters such as stator resistance and winding inductance are calculated and compared in this section.

A. Stator resistance

Copper loss is one of the major losses in electrical machines and is related directly to the winding resistance. Although the winding layout is different in the single-layer toroidal winding (SLTW) than in the double-layer concentrated winding (DLCW), the calculation of winding resistance is similar. The DC winding resistance per phase can be calculated with (Equation 2-14)

$$R_s = \frac{n\rho_{Cu}N_C^2 l_C N_{layer}}{k_{Cu}A_S} \quad \text{(Equation 2-14)}$$

where n is the number of coils per phase, ρ_{Cu} is the resistivity (Ω-m) of copper, N_c is the number of turns per coil, N_{layer} is the number of winding layer per slot, k_{Cu} is the slot filling factor, and A_s is slot area (m^2). l_C is the wire length per turn (m) and can be calculated with (Equation 2-15) where

$$l_C = 2l_{stack} + 4a + 2b \qquad \text{(Equation 2-15)}$$

a and b are the axial length and radial and circumferential length (m) of the end winding. Detailed stator units of the DLCW and SLTW dual-stator 6/4 FSPM machine with winding geometry parameters are shown in Figure 2.3-1 (a) and Figure 2.3-1 (b), respectively. The end turn

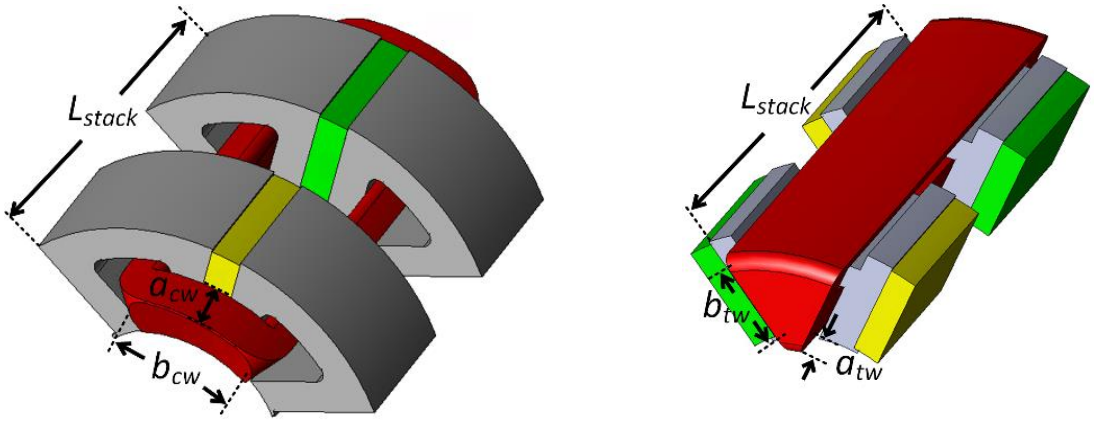

(a) (b)

Figure 2.3-1. Stator units with winding geometry parameters of (a) Double-layer concentrated winding and (b) Single-layer toroidal winding dual-stator 6/4 FSPM machine.

parameters a and b are noted with subscripts of "*cw*" and "*tw*" in Figure 2.3-1 to distinguish the two winding topologies.

AC winding resistance due to skin effect and proximity effect is not negligible when operating at elevated frequency. The skin depth (δ) characterizes the conductor current distribution under the influence of skin effect. The current density in a conductor decreases exponentially starting from the surface of the conductor, and is governed by (Equation 2-16), where J_s is the

$$J = J_s e^{-d/\delta} \qquad \text{(Equation 2-16)}$$

current density (A/mm^2) at the surface of the conductor, *d* is the depth (m) toward the center of the conductor. For a 6/4 FSPM machine running at 15000 rpm and wound with copper wire, the skin depth is 2.1 mm. Such skin depth is larger than the radius of the AWG #6 wire. Therefore, the influence of the skin effect is minimal according to (Equation 2-16). The ac winding resistance due to the proximity effect is analyzed in [139] and can be modeled with (Equation 2-17) where

$$R_{ac} = \frac{\pi \sigma l_C r_C^4 \mu_0^2 \omega_e^2 N_s N_C^3}{12 w_{si}^2} \qquad \text{(Equation 2-17)}$$

r_C and σ are the radius (m) and the electrical conductivity (S/m) of the wire, ω_e is the frequency (rad/s) of the current, w_{si} is the width (m) of the slot. The dc winding resistance of the machines under comparison and the total winding resistances of the two machines considering ac effect are calculated and compared with the measured resistance in Figure 2.3-2. As can be seen, the single-layer winding has more than 40% less resistance of the double-layer winding when the armature

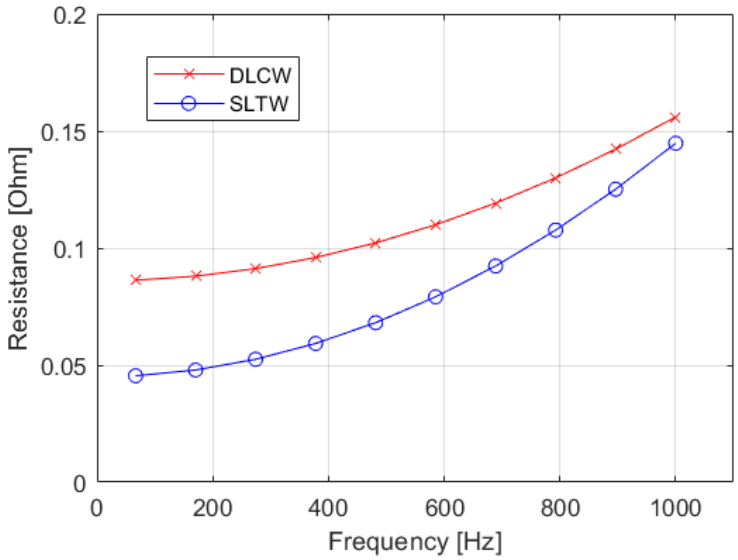

Figure 2.3-2. Winding resistance of the DLCW and SLTW 6/4 FSPM machine considering proximity effect.

current frequency is below 400 Hz. The winding resistances of the two topologies get close when the current frequency increases due to the ac winding resistance. The proximity effect can be mitigated by twisting the strands of wire in the same turn. The characterization of the twisted coil is complex and is not conducted here. The winding resistance used in the copper loss calculation will be calibrated with the measured value.

B. Machine inductance

The inductance plays an important role in the control, field weakening operation, and dynamic performance of the machine [140]. The total winding inductance consists of the magnetizing inductance and the leakage inductance. The magnetizing inductance is usually calculated using the winding function for commonly seen machines such as induction machine, SPM, and IPM machine [141]. However, as the FSPM machine has the permanent magnet in the stator, the inductance cannot be calculated directly from the winding function. In reference [142], a two-position method is proposed to calculate the inductance of a 12/10 FSPM machine. This method calculates the *d*-axis and *q*-axis inductance at two special rotor positions, instead of using Park transformation to derive the *dq* inductance from the position varying inductance in the stator reference frame. The two-position inductance calculation method is proposed for the 12/10 FSPM machine but can be easily applied on the 6/4 FSPM machine.

The magnetic flux path for the 6/4 FSPM machine in the *d*-axis aligned position is shown in Figure 2.3-3 (a). Due to symmetry, only half of the machine is shown. A simplified rectangular model is shown in Figure 2.3-3 (b) with machine geometry parameters. With the assumption that the permeability of stator and rotor iron is much larger than the permeability of air and permanent magnet, Ampere's law applied to the flux loop shown in Figure 2.3-3 (b) can be written as (Equation 2-18) where H_m and H_g are the magnetic field strength in the magnet and the air gap, respectively, N_c is the number of turns, and I is the current amplitude in the coil. The magnetic

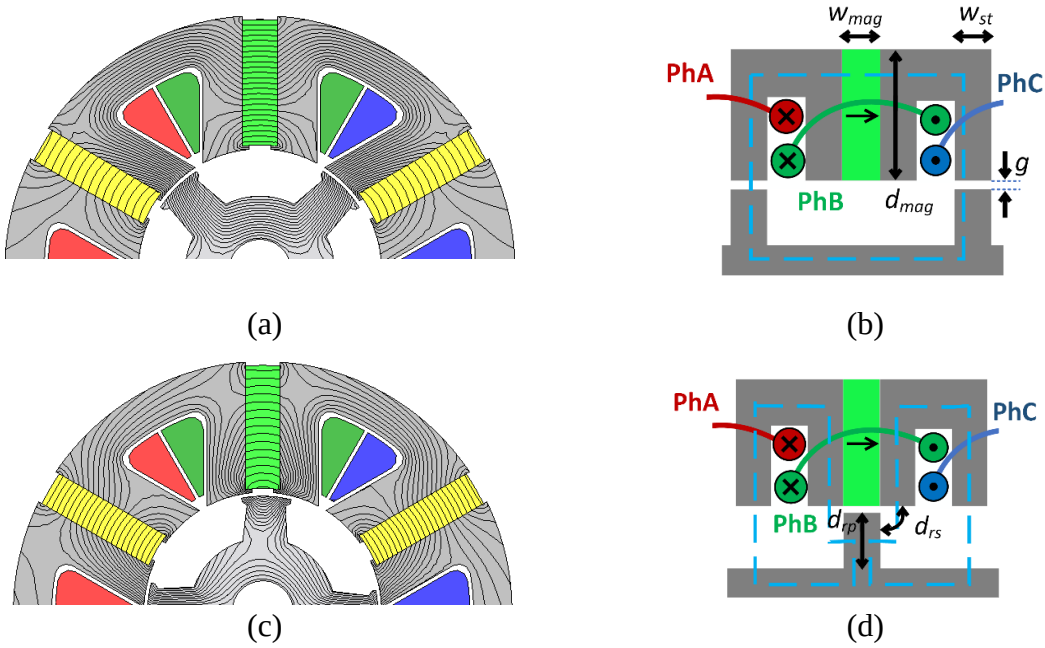

Figure 2.3-3. Magnetic flux path of 6/4 FSPM machine (a) 6/4 FSPM machine at d-axis position (b) d-axis flux path (c) 6/4 FSPM machine at q-axis position (b) q-axis flux path

$$H_m w_{mag} + 2H_g g = N_C I \qquad \text{(Equation 2-18)}$$

$$B_m = B_r + \mu_0 H_m \qquad \text{(Equation 2-19)}$$

flux in the magnet can be written as (Equation 2-19) where B_m is the magnetic flux in the magnet, B_r is the remnant flux of the magnet. By solving the magnetic flux loop in Figure 2.3-3 (b), the *d*-axis magnetizing inductance of the FSPM machine could be calculated with (Equation 2-20). Apparently, the *d*-axis inductance depends not only on the geometry of the machine, but also on the characteristics of the permanent magnet and the current amplitude, which can be observed in Figure 2.3-4. The magnetic flux path for the *q*-axis aligned position and the simplified model are shown in Figure 2.3-3 (c) and Figure 2.3-3 (d), respectively. The flux path does not pass through the magnet, and the q-axis inductance can be calculated by (Equation 2-21). Geometry parameters in equation (Equation 2-20) and (Equation 2-21) can be found in Figure 2.3-3. The magnetic flux

$$L_d = \frac{\partial \lambda_d}{\partial i} = \frac{\mu_0 N_C^2 w_{st} l_{stack}}{2g + w_{mag} w_{st} / d_{mag}} \quad \text{(Equation 2-20)}$$

$$L_q = \frac{\partial \lambda_q}{\partial i} = \frac{\mu_0 N_C^2 l_{stack} (w_{st} + d_{rp})/2}{g + d_{rp} + d_{rs}} \quad \text{(Equation 2-21)}$$

path does not change much in the SLTW machine when assuming the iron permeability is much larger than the magnet and air. Therefore, the same equations can be used for calculating the inductance of the SLTW machine.

Note that equations (Equation 2-20) and (Equation 2-21) calculate the inductance assuming the iron is not saturated. In order to take the iron saturation into account, the inductances of the 6/4 FSPM machine are obtained by FEA simulation for different armature current levels. The *dq*-axis flux linkage is first derived with the Park transformation. Then the *dq*-axis inductance is calculated. Figure 2.3-4 shows the *d* and *q*-axis inductances of the two machines at different currents. As can be seen, the *d*-axis inductance decreases faster than the *q*-axis inductance because the permanent magnet flux makes the *d*-axis path more saturated than the *q*-axis path.

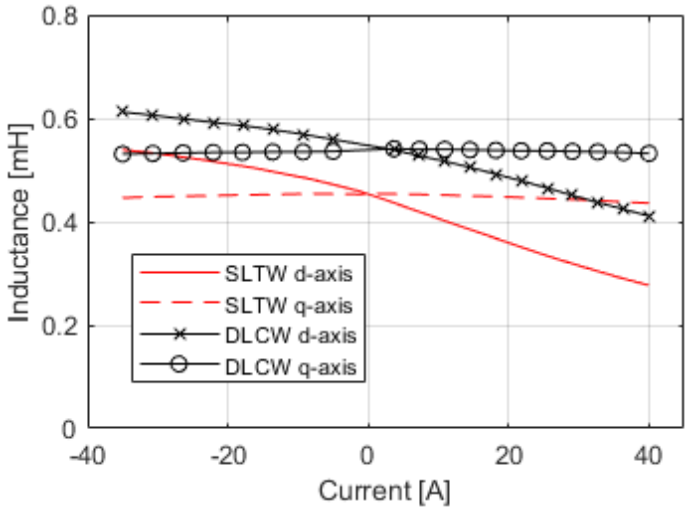

Figure 2.3-4. *d*-axis and *q*-axis Inductance of DLCW and SLTW 6/4 FSPM machine at different current levels.

C. Leakage inductance

Although the permeability of the stator/rotor core is much higher than air, leakage flux exists in the slot and the ending windings. The leakage inductance calculation for the FSPM machine is identical as for the FSCW SPM machine illustrated in [141]. The leakage inductance mainly consists of slot leakage inductance and end winding leakage inductance. There are many types of slot geometry for different types of machines and windings. The most commonly seen ones have rectangular shape or semi-round shape [143], [144]. As the 6/4 FSPM machine has a small number of slots, the slot shape is of a trapezoidal shape, as shown in Figure 2.3-5 for the single-layer

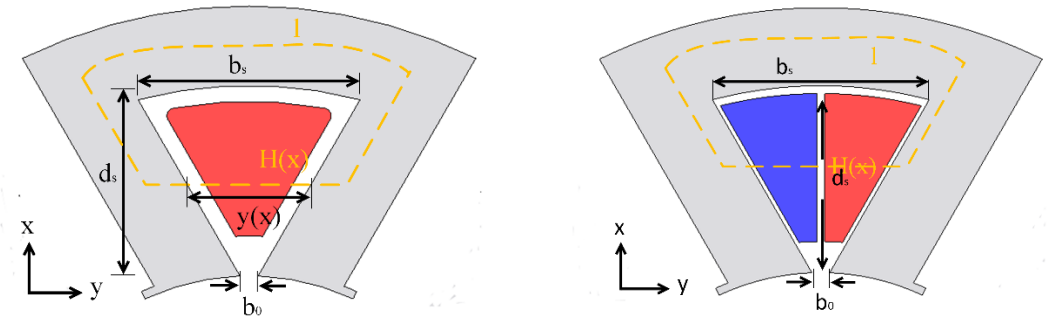

Figure 2.3-5. Slot section view for calculating slot leakage inductance (a) Single-layer winding (b) Double-layer winding

winding and double-layer winding, respectively. Unlike the calculation for magnetizing inductance, the slot leakage and end winding inductance of FSPM machine could be calculated similarly to the fractional slot concentrated winding SPM machine.

For the loop shown in Figure 2.3-5, according to Ampere's law we have $\oint H_y dl = n(x)I$, where *n(x)* is the number of turns surrounded by the integration loop. The permeability of the stator core is much larger than the air permeability, it is reasonable to assume that the surrounded coil MMF can be approximated by the MMF drop in the slot. By assuming the H field is constant along

the y-direction. We can write the loop integration as (Equation 2-22). The differential flux linkage

$$H(x)y(x) = n(x)I \quad \text{(Equation 2-22)}$$

$$d\lambda = n(x)d\Phi = \mu_0 n_s^2 I(\frac{n(x)}{n_s})^2 \frac{l_e}{y(x)} dx \quad \text{(Equation 2-23)}$$

$$y(x) = b_0 + \frac{b_s - b_0}{d_s} x \quad \text{(Equation 2-24)}$$

$$\frac{n(x)}{n_s} = \frac{2b_0 d_s x + (b_s - b_0)x^2}{(b_0 + b_s)d_s^2} \quad \text{(Equation 2-25)}$$

of the coil at position *x* can then be written as (Equation 2-23), where *y(x)* and $\frac{n(x)}{n_s}$ are functions of position in the *x*-direction and could be expressed by (Equation 2-24) and (Equation 2-25), respectively.

The differential slot leakage inductance could be calculated as (Equation 2-26). By taking the integration over the slot height (x-direction), the slot leakage inductance per slot for the single-layer winding shown in Figure 2.3-5 (a) could be expressed as (Equation 2-27), where β is the ratio

$$dL = \frac{d\lambda}{I} = \mu_0 n_s^2 (\frac{n(x)}{n_s})^2 \frac{l_e}{y(x)} dx \quad \text{(Equation 2-26)}$$

$$L_{slot} = n_s^2 l_e \mu_0 \frac{d_s}{b_s} \left[\frac{\beta^2 - \frac{\beta^4}{4} - log_e \beta - \frac{3}{4}}{(1-\beta)(1-\beta^2)^2} \right] \quad \text{(Equation 2-27)}$$

between b_0 and b_s. The slot leakage inductance per phase could be calculated by multiplying the per slot inductance by the number of slots per phase. The derivation for the slot-leakage inductance

for the double-layer winding is the same as for the single-layer winding, as each coil side takes half of the slot area. Note that there is mutual-slot leakage inductance for the double-layer winding, who has the same value as the self-slot leakage inductance.

For the double-layer FSPM machine, the end winding leakage inductance is small because of the short end turns. Apparently, it is similar for the single-layer toroidal winding. The end winding leakage inductance calculation is given in [140] based on the formula used for calculating the inductance of parallel transmission lines with image theory. The end winding leakage inductance per phase could be calculated with (Equation 2-28). l_{end} is the length of end winding, which is calculated by (Equation 2-29), where a and b are the axial and radial/circumferential

$$L_{ew} = N_t^2 \frac{S}{m} k_w^2 (2l_{end}) 1.2\mu_0 \quad \text{(Equation 2-28)}$$

$$l_{end} = 4a + 2b \quad \text{(Equation 2-29)}$$

length of the end winding respectively.

2.4. Harmonic analysis of single-layer 6/4 FSPM machine

The rotating PM magnetic field in SPM and IPM machine are generated from the rotating magnets. However, the FSPM machine has the permanent magnets in the stator and is stationary. The rotating permanent magnet magnetic field is generated from the modulation of the salient stator and rotor core. Therefore, the FSPM machine can be classified into the category of flux modulation machine, together with Vernier machine, doubly salient PM machine, and magnetic gear, where the machine torque is contributed from several harmonic components. The calculation of the open circuit air gap flux density of the 6/4 FSPM machine and the stator winding MMF of the double-layer winding and single-layer winding 6/4 FSPM machine are derived in this section.

2.4.1. No load air gap flux density of 6/4 FSPM machine

The no-load air gap magnetic flux is generated from the permanent magnets. As mentioned previously, the magnets of the FSPM machine is in the stator and are not rotating with the rotor. The rotating air gap magnetic flux is from the modulation of the stator core and the rotor core. The permanent magnet MMF distribution is first analyzed. The To simplify the analysis, the 6/4 FSPM stator assembly is presented in a rectangular model, as shown in Figure 2.4-1 (a). Note that the magnets in the stator are magnetized in the circumferential direction, and due to the flux focusing

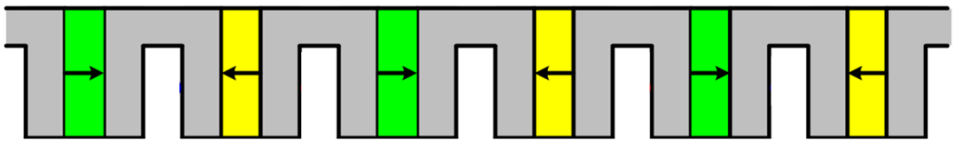

(a)

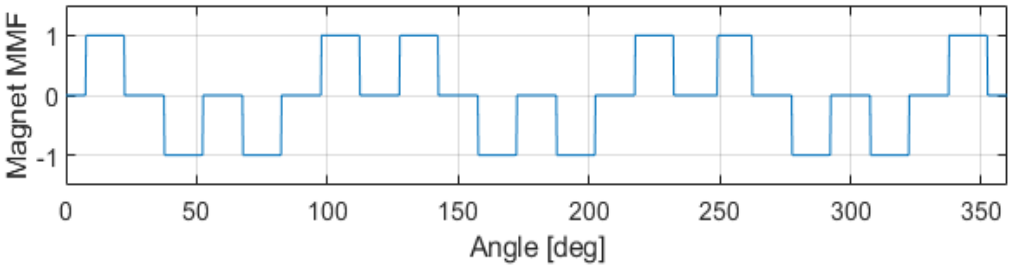

(b)

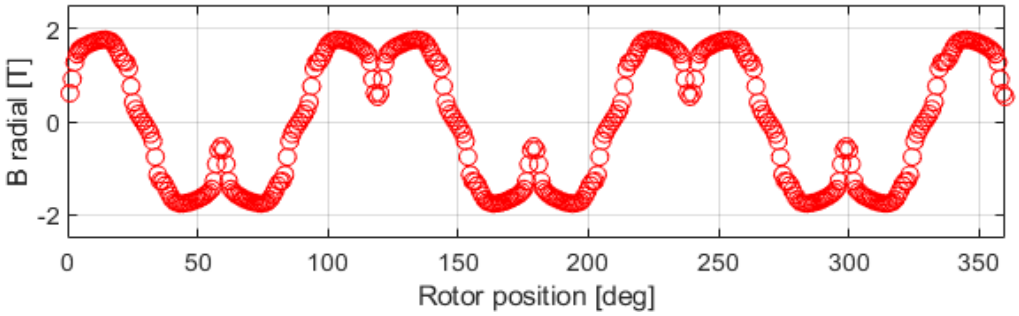

(c)

Figure 2.4-1. 6/4 FSPM machine stator core and permanent magnet (a) Rectangular stator model (b) Magnet MMF considering the stator saliency

effect, the magnetic flux direction in the stator tooth is radial, as indicated in Figure 2.4-1 (a). The magnets are sandwiched between two stator cores. It is assumed that the width of the magnet is the same as the stator tooth and the stator slot. The magnet has similar permeability as air, therefore, the magnet MMF view from the air gap need to consider the stator saliency, as shown in Figure 2.4-1 (b). To verify the previous statement, the rotor of the 6/4 FSPM machine is replaced with a full cylindrical rotor and the radial magnetic flux density is measured. As can be seen in Figure 2.4-1 (c), the shape of the radial magnetic flux density viewed from the air gap is similar to the piecewise function of the stator magnet MMF. With Fourier decomposition, the stator magnet MMF of a generic FSPM machine can be written as (Equation 2-30), where F_{PM0} is the amplitude

$$F_{PM}(\theta) = \frac{4F_{PM0}}{\pi} \sum_{n=1,3,5}^{\infty} \frac{1}{n} \left[\cos\left(\frac{n\pi}{8}\right) - \cos\left(\frac{3n\pi}{8}\right) \right] \cos\left(\frac{nN_S}{2}\theta\right) \qquad \text{(Equation 2-30)}$$

of the stator magnet MMF, N_S is the stator slot number. For the 6/4 FSPM machine, the stator magnet MMF can be written as (Equation 2-31). The period of the magnet MMF variation is 1/3

$$F_{6/4PM}(\theta) = \frac{4F_{PM0}}{\pi} \sum_{n=1,3,5}^{\infty} \frac{1}{n} \left[\cos\left(\frac{n\pi}{8}\right) - \cos\left(\frac{3n\pi}{8}\right) \right] \cos(3n\theta) \qquad \text{(Equation 2-31)}$$

of the mechanical period, because there are six magnets in the stator.

To get the actual air gap flux density, the rotor saliency needs to be considered as well. Similar to the stator, the rotor of 6/4 FSPM machine in also presented in a rectangular model, as shown in Figure 2.4-2 (a). For simplicity, the rotor tooth width is set to be the same as the stator tooth width. The rotor permeance function is a piecewise function, as shown in Figure 2.4-2 (b), where the permeance is high when the rotor tooth presents. Note that the rotor is rotating at a speed of Ωr (rad/s). Therefore, the Fourier decomposition of the rotor permeance of a generic FSPM

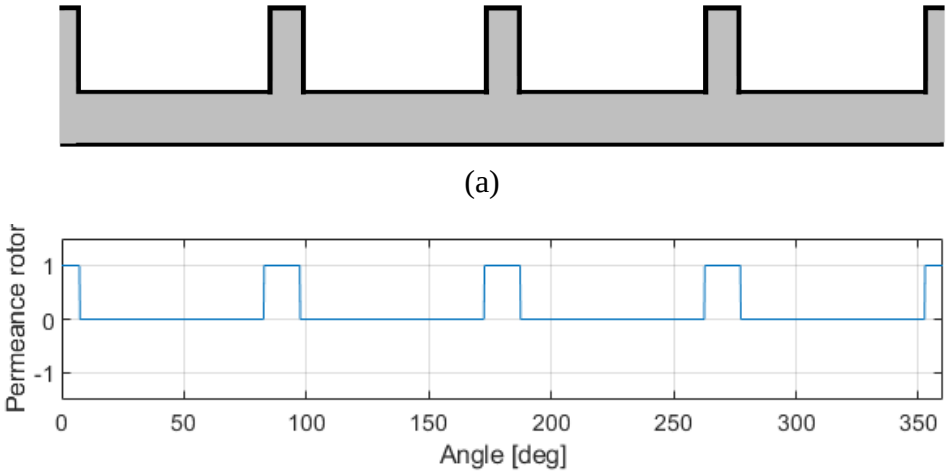

(a)

(b)

Figure 2.4-2. 6/4 FSPM machine rotor core permeance function (a) Rectangular rotor model (b) Rotor permeance function

machine and the 6/4 FSPM machine can be written as (Equation 2-32) and (Equation 2-33),

$$P_r(\theta,t) = P_{r,0} + \frac{2P_{r,1}}{\pi}\sum_{k=1}^{\infty}\frac{1}{k}\sin\left(\frac{kN_r\pi}{4N_S}\right)\cos\left[kN_r(\theta-\omega_r t)\right] \qquad \text{(Equation 2-32)}$$

$$P_{r,\ 6/4}(\theta,t) = P_{r,0} + \frac{2P_{r,1}}{\pi}\sum_{k=1}^{\infty}\frac{1}{k}\sin\left(\frac{k\pi}{6}\right)\cos\left[4k(\theta-\omega_r t)\right] \qquad \text{(Equation 2-33)}$$

respectively. As can be seen, the period of the rotor permeance variation is 1/4 of the mechanical period because of the number of rotor poles.

The no load air gap magnetic flux density can be calculated as the product of the magnet MMF considering the stator saliency and the rotor permeance as (Equation 2-34), where $A_n = \cos\left(\frac{n\pi}{8}\right) - \cos\left(\frac{3n\pi}{8}\right)$, and $B_n = \sin\left(\frac{kN_r\pi}{4N_S}\right)$. As can be seen, the no-load air gap magnetic flux density mainly consists of three components: a stationary component with a pole pair

$$B_{ag}(\theta,t) = F_{PM}(\theta)P_r(\theta,t)$$
$$= \frac{4F_{PM0}P_{r,0}}{\pi}\sum_{n=1,3,5}^{\infty}\frac{1}{n}A_n\cos\left(\frac{nN_S}{2}\theta\right)$$
$$+\sum_{n=1,3,5}^{\infty}\sum_{k=1,3,5}^{\infty}\frac{1}{2nk}A_nB_n\cos\left[\left(\frac{nN_S}{2}+kN_r\right)\theta-kN_r\omega_r t\right] \quad \text{(Equation 2-34)}$$
$$+\cos\left[\left(\frac{nN_S}{2}-kN_r\right)\theta+kN_r\omega_r t\right]$$

TABLE 2-3. STATIONARY COMPONENT OF NO-LOAD AIRGAP MAGNETIC FLUX DENSITY OF 6/4 FSPM MACHINE

n	Pole pair	Speed	Amplitude, $F_{PM0}P_{r,0}$
1	3	0	0.69
3	9	0	0.55
5	15	0	0.33

TABLE 2-4. FORWARD ROTATING COMPONENT OF NO-LOAD AIRGAP MAGNETIC FLUX DENSITY OF 6/4 FSPM MACHINE

n	*k*	Pole pair	Speed, ω_r	Amplitude, $F_{PM0}P_{r,1}$
1	1	7	-4/7	0.110
3	1	13	-4/13	0.089
1	2	11	-8/11	0.095
3	2	17	-8/17	0.076
1	3	15	-12/15	0.073

TABLE 2-5. BACKWARD ROTATING COMPONENT OF NO-LOAD AIRGAP MAGNETIC FLUX DENSITY OF 6/4 FSPM MACHINE

n	*k*	Pole pair	Speed, ω_r	Amplitude, $F_{PM0}P_{r,1}$
3	1	5	4/5	0.088
3	2	1	8	0.076

number of $\frac{nN_S}{2}$, two moving components rotating forward and backward. The pole pair number, rotating speed, and the amplitude of the three harmonic components of the no-load magnetic flux density of the 6/4 FSPM machine are shown in TABLE 2-3, TABLE 2-4, and TABLE 2-5, respectively. Note that the numbers are normalized with respect to the base value shown in the first row. As can be seen, the 6/4 FSPM machine has abundant harmonics of air gap magnetic flux that can interact with the harmonic components of the stator winding MMF which have the same pole pair number and rotating speed to produce torque. The no-load air gap magnetic flux density of the 6/4 FSPM machine is simulated with FEA tool. The air gap flux density waveform and its harmonic components are shown in Figure 2.4-3 (a) and Figure 2.4-3 (b), respectively. As can be seen, the relative amplitude among the different harmonic components from the FEA simulation match well with the analytical calculation. Note that the double-layer winding and the single-layer winding layout does not change the stator iron and the magnets placement and the no-load air gap magnetic flux distribution for the 6/4 FSPM machine.

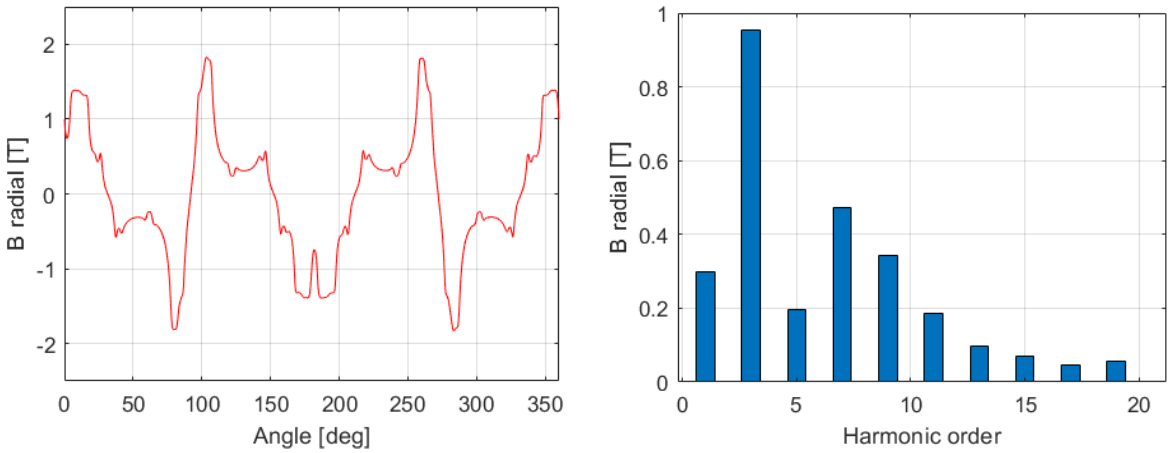

(a) (b)

Figure 2.4-3. No-load airgap magnetic flux density distribution (a) Radial flux density distribtuion (b) Harmonic components

2.4.2. Stator winding MMF of 6/4 FSPM machine

In section 2.2, 6/4 FSPM machine with double-layer (DL) winding and single-layer (SL) winding are presented. While the stator iron and the magnet placement of the two winding topologies are identical (despite the change of stator lamination to accommodate the return coil of the toroidal winding), the winding configuration are different, which cause variation in the stator winding MMF. The stator winding MMF interacts with the airgap magnetic flux to produce torque. Both DL and SL 6/4 FSPM machine are 3-phase ac machine supplied with balanced sinusoidal current, as given in (Equation 2-35). The winding MMF can be calculated as (Equation 2-36),

$$\begin{cases} i_A(t) = I_S \sin(N_r \omega_r t) \\ i_B(t) = I_S \sin\left(N_r \omega_r t - \frac{2\pi}{3}\right) \\ i_C(t) = I_S \sin\left(N_r \omega_r t + \frac{2\pi}{3}\right) \end{cases} \quad \text{(Equation 2-35)}$$

$$F_{ABC}(\theta,t) = N_A(\theta) i_A(t) + N_B(\theta) i_B(t) + N_C(\theta) i_C(t) \quad \text{(Equation 2-36)}$$

where $N_X(\theta)$ and $i_X(t)$ are the winding function and the armature current of phase X (X = A, B, and C). The winding function of the DL and SL winding 6/4 FSPM machine can be derived from the winding layout, as shown in Figure 2.4-5 (a) and Figure 2.4-5 (b), respectively. The normalized winding function are plotted under the corresponding winding layout. Nc is number of turns per coil. As can be seen in (Equation 2-36), the winding MMF is varying in both space and time. To illustrate the shape of the winding MMF, the instant when phase A current reaches maximum (I_S) is chosen without the loss of generality. At this instant, the B and C phase current is at $-I_S/2$. The winding MMF of DL and SL 6/4 FSPM machine at this instant is shown in Figure 2.4-4. As can be seen, the DL and SL 6/4 FSPM machine have the same shape of winding MMF with a phase

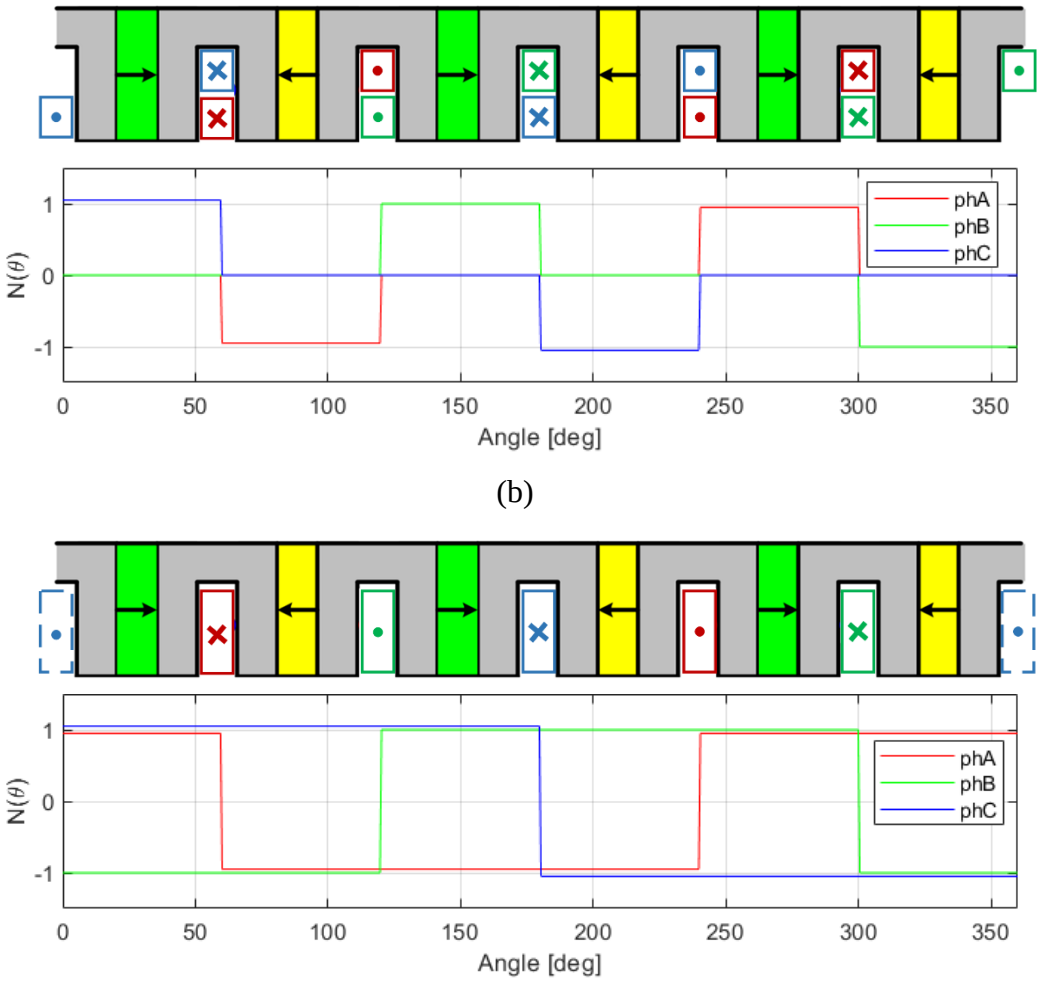

Figure 2.4-5. 6/4 FSPM machine winding function (a) DL winding and (b) SL winding

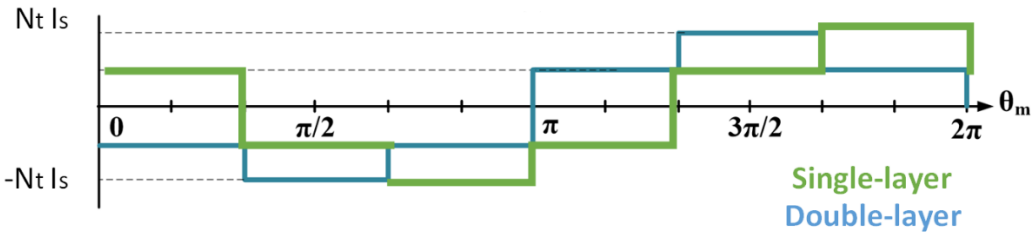

Figure 2.4-4. 6/4 FSPM machine winding MMF comparison

difference of π/3. Note that the amplitude of the MMF is the number of turns per coil times the amplitude of the armature current. Assuming that the slot area and the slot filling factor of the two

winding layouts are identical, SL 6/4 FSPM machine should have twice number of turns per coil as the DL 6/4 FSPM machine. Therefore, the winding MMF of the SL 6/4 FSPM machine is doubled compared to the DL 6/4 FSPM machine. The number of turns per coil of the two machine is chosen according to the requirement of back EMF, power rating, and inductance value. The design and comparison of the DL and SL winding 6/4 FSPM machine are shown in Chapter 3.

2.5. Summary

In this chapter, the fundamentals of 6/4 FSPM machine, including the origin of the second-order harmonic in the flux linkage, the second-order harmonic cancelation with the dual-stator structure, double-layer and single-layer stator winding topology, winding factor, and machine sizing equation are discussed. It is shown that the second-order harmonic of the flux linkage is due to the placement of the permanent magnet which induce the asymmetric of flux linkage variation. The second-order harmonic can be canceled by a second set of stator winding, which exist inherently for FSPM machine with stator slot number larger than 12. For the 6/4 FSPM machine, another stator set is needed to accommodate the harmonic cancelling winding. Certain mechanical gap between the two stators are necessary to avoid the flux leakage since the magnetizing direction of the magnets in the two stators are opposite. Larger gap is beneficial to avoid leakage, but also increase the total volume of the machine. High aspect ratio design can reduce the percentage of the gap volume.

The winding factor of FSPM machine is calculated by EMF vector method. It is shown that 6/4 FSPM machine with double-layer concentrated winding (DLCW) has a winding factor of 0.5, while the single-layer winding can achieve a winding factor of 1. The two realizations of single-layer winding have been discussed. The single-layer toroidal winding (SLTW) has the advantage of easy manufacturing and good thermal performance. The sizing equation derived for 6/4 FSPM

machine illustrates the relation among the power of the machine and the machine volumetric sizing, winding factor, electric loading, and magnetic loading. It is shown that for the same machine volume and power, high winding factor design requires lower electric loading or magnetic loading, which are beneficial for reducing the copper loss and iron loss. Basic machine design parameters such as stator winding resistance and winding inductance are derived analytically. It is shown that for the size of the machines discussed in this report, the toroidal winding and the circumferential winding have the similar coil length. Low aspect ratio design decreases the total coil length for the SLTW machine design for the same power. The calculated values will be compared to the measured values from the experimental testing.

The torque production mechanism of the 6/4 FSPM machine has been investigated based on harmonic analysis on the air gap magnetic flux density distribution and the armature winding MMF. It is shown that several harmonics contribute to the production of average torque. The double-layer winding and basic single-layer winding designs have the same stator core structure and magnet placement. Therefore, the no-load airgap magnetic flux distribution is identical. It is shown that with the same number of turns per coil, the winding MMF of the DL and SL winding is the same. If the number of turns per slot is kept identical, the SL winding design has twice winding MMF than the DL winding design.

Chapter 3 Comparison between Single-Layer and Double-layer Winding Design

In the previous chapter, dual-stator 6/4 FSPM machine with single-layer winding has been proposed. It is shown that the single-layer winding has a higher winding factor which allows the machine to produce the same amount of torque with less electric loading. With the same number of turns per slot area, the single-layer winding also has a higher inductance, which is beneficial for field weakening operation. The single-layer configuration could be realized with either overlapping winding and toroidal winding topology, as shown in Figure 2.2-5 (a), and Figure 2.2-5 (b), respectively. However, the overlapping winding topology has certain mechanical issues such as complicated winding process, end turn insulation, and magnet overheating. On the other hand, toroidal winding topology has the advantages of convenient manufacturing, easy cooling and is not surrounding the permanent magnets. Therefore, in this chapter, the single-layer toroidal winding (SLTW) dual-stator 6/4 FSPM machine is evaluated and compared with the double-layer (DL) dual-stator 6/4 FSPM machine.

3.1. Optimization of single-layer dual-stator 6/4 FSPM machine

Before comparing the baseline 6/4 FSPM machine with double-layer winding, the single-layer machine needs to be optimized in terms of the geometry parameters. Because of the single-layer winding layout, the magnetic loading of the machine is inherently higher than the double-layer winding. Therefore, the two most significantly impacted parameters would be the stator tooth and the magnet width due to the change in the iron saturation. In addition, the rotor pole width should be modified accordingly to the stator design. Note that the stator inner diameter (D_{is}) is presented in the machine sizing equation as shown in the previous chapter. Therefore, in the single-

layer machine design, the inner stator diameter is kept the same as the double-layer machine. Since the outer radius of the two designs are also the same, the split ratio is not changed. Another geometry variable is the axial gap between the front and rear stator. Because the radial length of the magnet is kept the same, the axial distance needed to minimize the magnetic flux leakage is kept identical.

Due to the nonlinear magnetic properties of the machine, analytical optimization is difficult to realize. Therefore, in this report, the optimization is realized by the parametric study using 2D FEA. The geometry of the dual-stator FSPM machine is not uniform axially, which requires 3D FEA simulation. However, it is noticed that the whole machine performance could be simulated by the combination of the front and rear part. 2D FEA simulations are run for the front part and rear part of the machine separately, and the sum of the flux linkage, back EMF, and torque from the two parts is that of the whole machine. 3D FEA is very time consuming and does not provide extra information for optimizing the geometric parameters. After determining the optimized machine geometry, the simulation results from 2D FEA will be compared with 3D FEA to justify the previous statement.

3.1.1. Stator optimization

The stator geometry optimization is a trade-off study between the magnetic loading and electric loading. As can be seen in the previous chapter, the winding factor of the single-layer machine is doubled compared to the double-layer machine, which is beneficial for high magnetic loading. On the other hand, the saturation in the stator/rotor iron would be more severe in the single-layer machine. The magnetic flux density contour of the double-layer 6/4 FSPM machine is shown in Figure 3.1-1. As can be seen, the saturation occurs mostly in the stator teeth, while the stator back iron is not as saturated. Therefore, to simplify the optimization, the thickness of stator

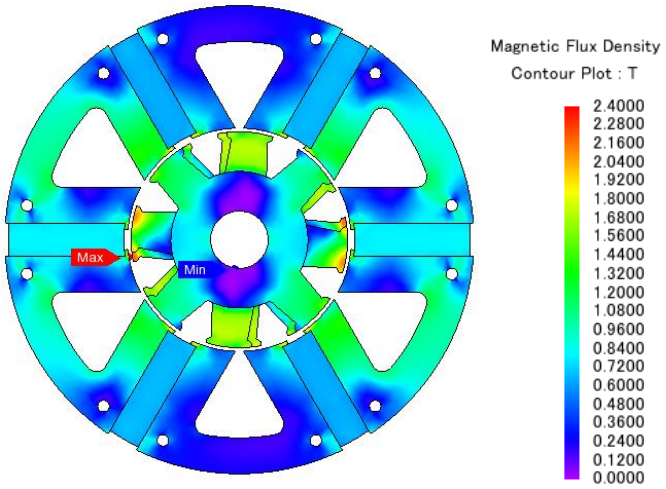

Figure 3.1-1. Magnetic flux density contour of DL 6/4 FSPM machine

back iron in the single-layer machine is kept the same as the double-layer machine. As mentioned previously, the stator outer diameter and the split ratio are also kept identical as the double-layer machine. Due to the higher saturation, it is intuitive to say that the stator tooth width should be larger in the single-layer machine. Starting from 7 mm, the stator teeth width (d_{teeth}) is varied up to 12 mm with a step of 0.5 mm. The width of the permanent magnet needs to be studied together with the stator teeth width, since they are competing for the space. The magnet width (d_{mag}) is studied in the range of 7.5mm to 9.5mm, with a step of 0.5mm. Note that the stator teeth will be in interference with each other if larger tooth width is used. Therefore, for different magnet width, the variation range of stator teeth is different.

The fundamental component of the magnetic flux linkage of the single-layer machine with different stator teeth width and magnet thickness is used as the metric to determine the optimized stator geometry. The flux linkage variation for different machine geometries are plotted in Figure 3.1-2. It can be seen that as the stator teeth width increase, the flux linkage increases. As the stator teeth and the magnet are competing for space, geometries with thinner magnet allow thicker stator teeth and tend to have higher flux linkage. The highest flux linkage within the permission of

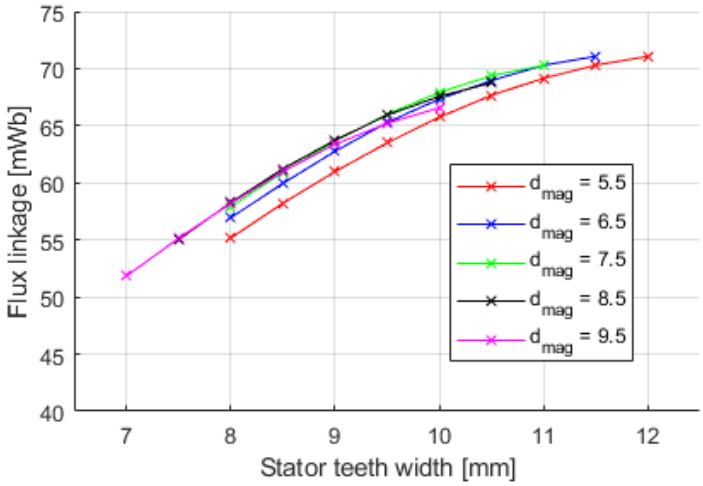

Figure 3.1-2. Flux linkage of SLTW 6/4 FSPM machine with different magnet thickness and stator tooth width

geometry sizing is achieved with a magnet thickness of 6.5 mm and a stator teeth width of 11.5 mm. The chosen stator geometry will be used in the optimization of the rotor parameter as shown in the next part.

3.1.2. Rotor optimization

After fixing the geometry of stator, the rotor geometry needs to be optimized as well. The main parameters are the width of rotor back iron (d_{rb}) and the rotor pole width (d_{rp}). Starting from having the width of the rotor back iron equals to the width of stator back iron, and the rotor pole width equals to the stator tooth width, twelve cases for each parameter with a step of 0.5 mm are studied. The rotor geometry has a major impact on the torque production, including the average torque and the torque ripple. As shown in Figure 3.1-3 (a), the average torque increases as the rotor pole width increases. However, the torque ripple becomes unacceptable with the thick rotor pole. As can be seen in Figure 3.1-3 (b), the torque ripple is minimum with a rotor pole width of 11 mm. Comparing the 11 mm pole-width and the 15 mm pole-width, the difference of average torque is 5.7% and the difference in torque ripple is 77.4%.

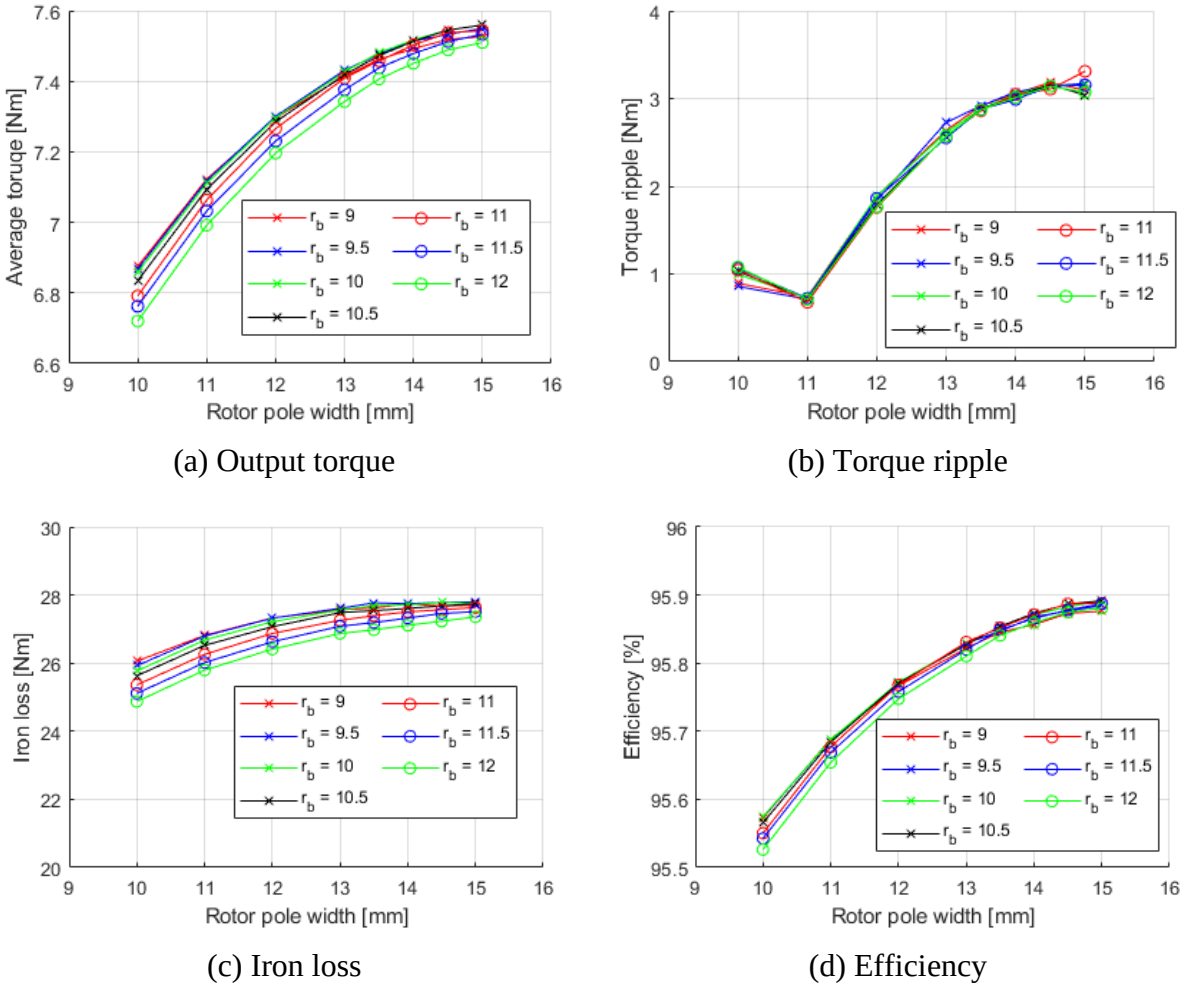

(a) Output torque (b) Torque ripple

(c) Iron loss (d) Efficiency

Figure 3.1-3. Electromagnetic performance with varying rotor geometry parameters (a) Output torque (b) Torque ripple (c) Iron loss level (d) Efficiency

The iron volume also influences the magnetic flux density and therefore the iron loss level. The iron loss for different cases are shown in Figure 3.1-3(c). It can be seen that smaller rotor pole width and thicker rotor back iron has lower iron loss. As the stator geometry is unchanged for all the cases studied here, the copper loss is identical. The overall efficiency shares the same trend as the output torque and the iron loss and is shown in Figure 3.1-3(d). As can be seen, the difference in efficiency is very small, within 0.5%. In order to determine what thickness of the rotor back iron should be chosen, some machine characteristics are listed in TABLE 3-1. Note that the pole

TABLE 3-1. MACHINE LOADED CHARACTERISTICS COMPARISON WITH DIFFERENT ROTOR BACK IRON THICKNESS

d_{rb} [mm]	$T_{average}$ [Nm]	T_{ripple} [Nm]	Ripple/Average [%]	Piron [W]	Efficiency [%]
9	7.12	0.74	10.38	26.81	95.69
9.5	7.12	0.71	10.00	26.79	95.69
10	7.11	0.73	10.25	26.68	95.69
10.5	7.09	0.72	10.14	26.52	95.68
11	7.06	0.68	9.59	26.26	95.68
11.5	7.03	0.72	10.26	26.02	95.67
12	6.99	0.71	10.15	25.80	95.65

width is fixed at 11 mm. As can be seen, all the candidates have very close efficiency. However, with a back-iron thickness of 11 mm. The torque ripple is minimal. Therefore, the 11 mm back-iron and 11 mm rotor pole width are chosen.

3.1.3. Comparison of 2D results v.s. 3D results

The optimization has been done with 2D FEA simulations as presented previously. For conventional radial flux machine, the 2D simulation is able to generate an accurate enough result. However, the dual-stator 6/4 FSPM machine involves flux coupling between the two stators. It is

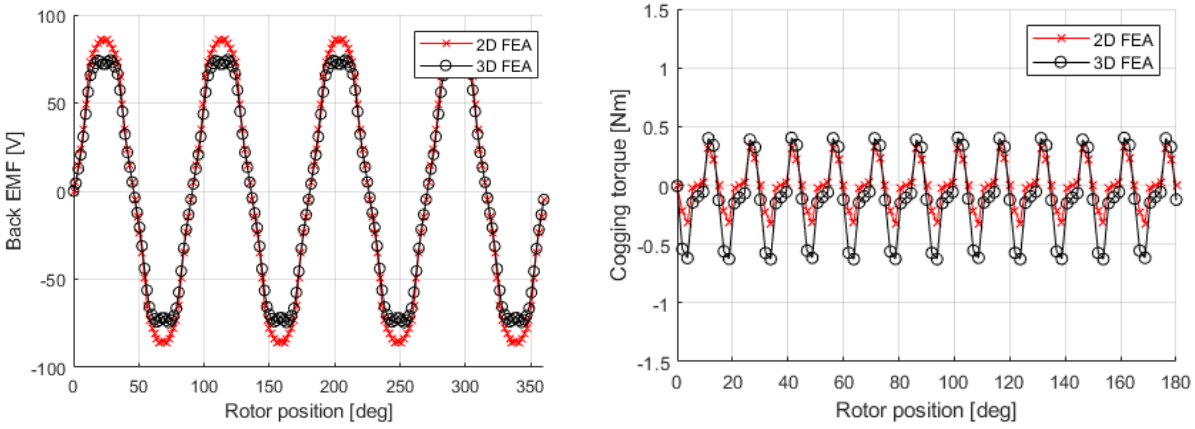

(a) (b)

Figure 3.1-4. Comparison of 2D and 3D FEA simulation results for dual-stator 6/4 FSPM machine (a) Back EMF (b) Cogging torque

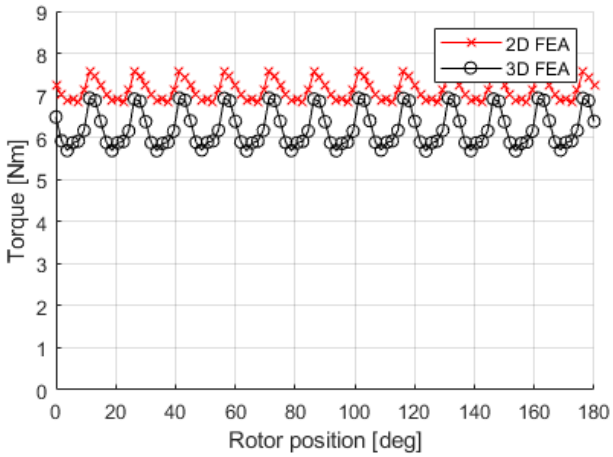

Figure 3.1-5. Comparison of output torque of 2D and 3D FEA simulation

worthwhile compare the simulation results from 2D and 3D analysis to justify the use of 2D FEA for optimization. Under no-load condition, the back EMF and the cogging torque waveforms from the 2D and 3D simulations are shown in Figure 3.1-4. It can be seen that the waveforms from 2D simulation coincide well with those from 3D FEA. The waveform of the output torque at rated condition is shown in Figure 3.1-5. As can be seen, the torque ripple period from 2D and 3D simulation match well. The average output torque from 2D FEA simulation is higher than the 3D simulation result. A quantitative comparison between the 2D and 3D simulation is summarized in TABLE 3-2. As can be seen, except for the torque ripple prediction, the differences between 2D and 3D FEA are around 10%, which is acceptable for the parametric study for the optimization. However, to evaluate the performance of the dual-stator 6/4 FSPM machine, 3D FEA is needed.

TABLE 3-2. COMPARISON OF 2D AND 3D FEA SIMULATION FOR DUAL-STATOR 6/4 FSPM MACHINE

	Back EMF [Vpk]	T_{avg} [Nm]	T_{rip} [Nm]	P_{iron} [W]	Efficiency [%]
2D FEA	85.0	7.1	0.72	26.4	95.7
3D FEA	74.6	6.2	1.25	23.5	95.2
Error [%]	12.2	12.6	42.4	10.8	0.48

3.1.4. Machine geometry parameters

The double-layer concentrated winding (DLCW) dual-stator 6/4 FSPM machine presented in [138] is used as the baseline for the comparison. This machine has been optimized in [118] [115] to have high average output torque and low torque ripple. The geometer parameter of the DLCW 6/4 FSPM machine is given in TABLE 3-3. The corresponding variables can be found in the section view of the machine shown in Figure 3.1-6 (a). The DLCW machine has a U-shape stator unit, while for the SLTW machine, because of the use of toroidal winding, the stator unit has an H-shape to accommodate the returning coil of the winding. The outer diameter of the SLTW machine is kept identical as the DL machine. Therefore, because of the H-shape stator lamination, the active stator outer diameter of the SLTW machine is smaller than the DLCW machine. The geometry parameters of the SLTW machine have been optimized in the previous part. In order to have a good comparison, the back EMF of the DLCW and the SLTW machine is set to be the same. As

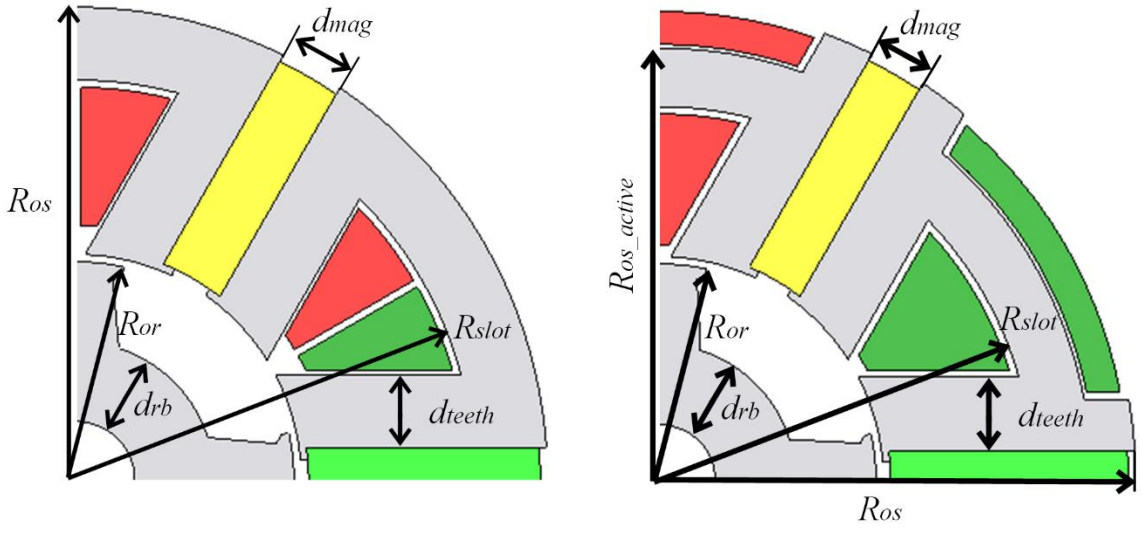

(a) (b)

Figure 3.1-6. Section view and geometry parameters of the dual-stator 6/4 FSPM machine (a) DL machine (b) SLTW machine

TABLE 3-3. GEOMETRY AND MACHINE PARAMETERS OF DL AND SLTW DUAL-STATOR 6/4 FSPM MACHINES

Variable	Symbol [unit]	DLCW	SLTW
Stator outer radius	R_{os} [mm]	65	65
Rotor outer radius	R_{or} [mm]	30	30
Air gap	g [mm]	1	1
Rotor back iron thickness	d_{rb} [mm]	11	11
Slot radius	R_{slot} [mm]	56	50
Stator teeth thickness	d_{teeth} [mm]	10	11.5
Slot area	A_{slot} [mm2]	369.1	231.9
Slot filling factor	k_{fill} [p.u.]	0.4	0.45-0.5
Magnet thickness	d_{mag} [mm]	9	9
Stack length	L_{stack} [mm]	80	80
Magnet volume	V_{mag} [cm^3]	0.123	0.123
Active mass	m_{active} [kg]	7.16	6.98

shown in Chapter 2, the single-layer machine is able to induce the same level of back EMF with a smaller number of turns because of the higher winding factor. The geometry parameters of the SLTW machine are shown in TABLE 3-3, where the corresponding variables are given in Figure 3.1-6 (b). The calculation for machine parameters such as stator resistance and machine inductance of the single-layer and double-layer machine are presented in Chapter 2. The equations are not

TABLE 3-4. MACHINE PARAMETERS OF DL AND SLTW DUAL-STATOR 6/4 FSPM MACHINES

Variable	Symbol [unit]	DLCW	SLTW
Turns per slot	N_{slot}	40	20
Turns per coil	N_{coil}	20	20
DC Stator resistance	R_s [mΩ]	93.4	34.7
Machine inductance	L_s [mH]	0.55	0.47

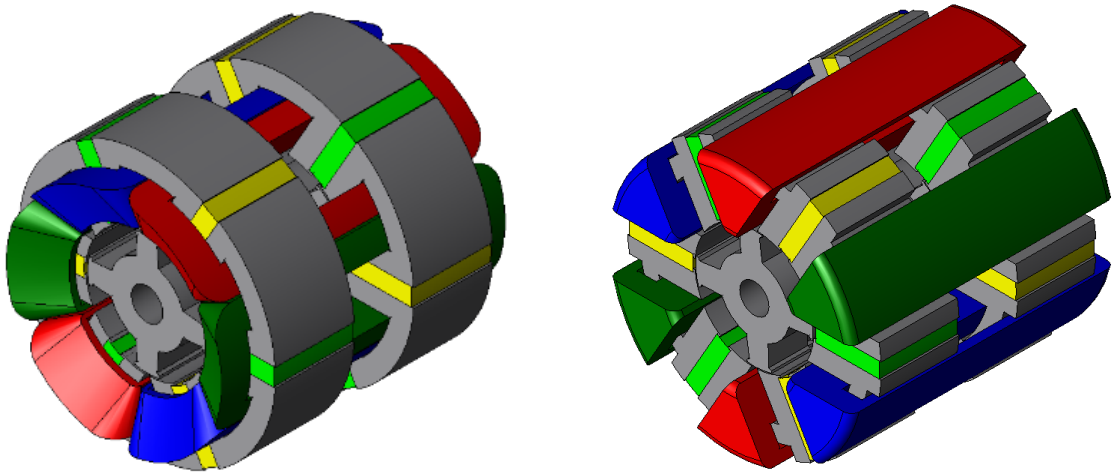

(a) (b)

Figure 3.1-7. 3D view of the three dual-stator 6/4 FSPM machine under comparison (a) DLCW 6/4 FSPM machine (b) SLTW 6/4 FSPM machine

repeated in this chapter and the numbers are given in TABLE 3-4. Note that the SLTW machine has a smaller slot area due to the H-shape stator core. But the required electric loading of the SLTW machine is less, and the SLTW does not require phase-to-phase insulation and permits a higher slot filling factor. Therefore, the reduced slot area will not increase the current density and will not cause additional cooling problem. As can be seen in TABLE 3-3 and TABLE 3-4, the SLTW machine has a more than 50% reduction in the stator resistance, because of the lower number of turns per slot. The 3D geometries of the three machines under comparison are shown in Figure 3.1-7.

3.2. Torque production capability comparison

The comparison among the two dual-stator 6/4 FSPM machines is done under the assumption that they have the same output power, similar back EMF, and the same armature current. The two machines share many identical parameters such as the machine volume, air gap length, and aspect ratio. The open-circuit characteristics and the torque production capabilities of the two machines are compared with finite element simulation.

3.2.1. Open-circuit characteristics

Because of the dual-stator structure, 3D finite element analysis is used to evaluate the machines performance. The flux linkage and back EMF waveforms and harmonic components of the two machines at 15000 rpm are shown in Figure 3.2-1. As can be seen, the DLCW and SLTW 6/4 FSPM machines have similar level of flux linkage and back EMF, which is the assumption of the comparison mentioned previously. Because of the dual-stator structure, the flux linkage and

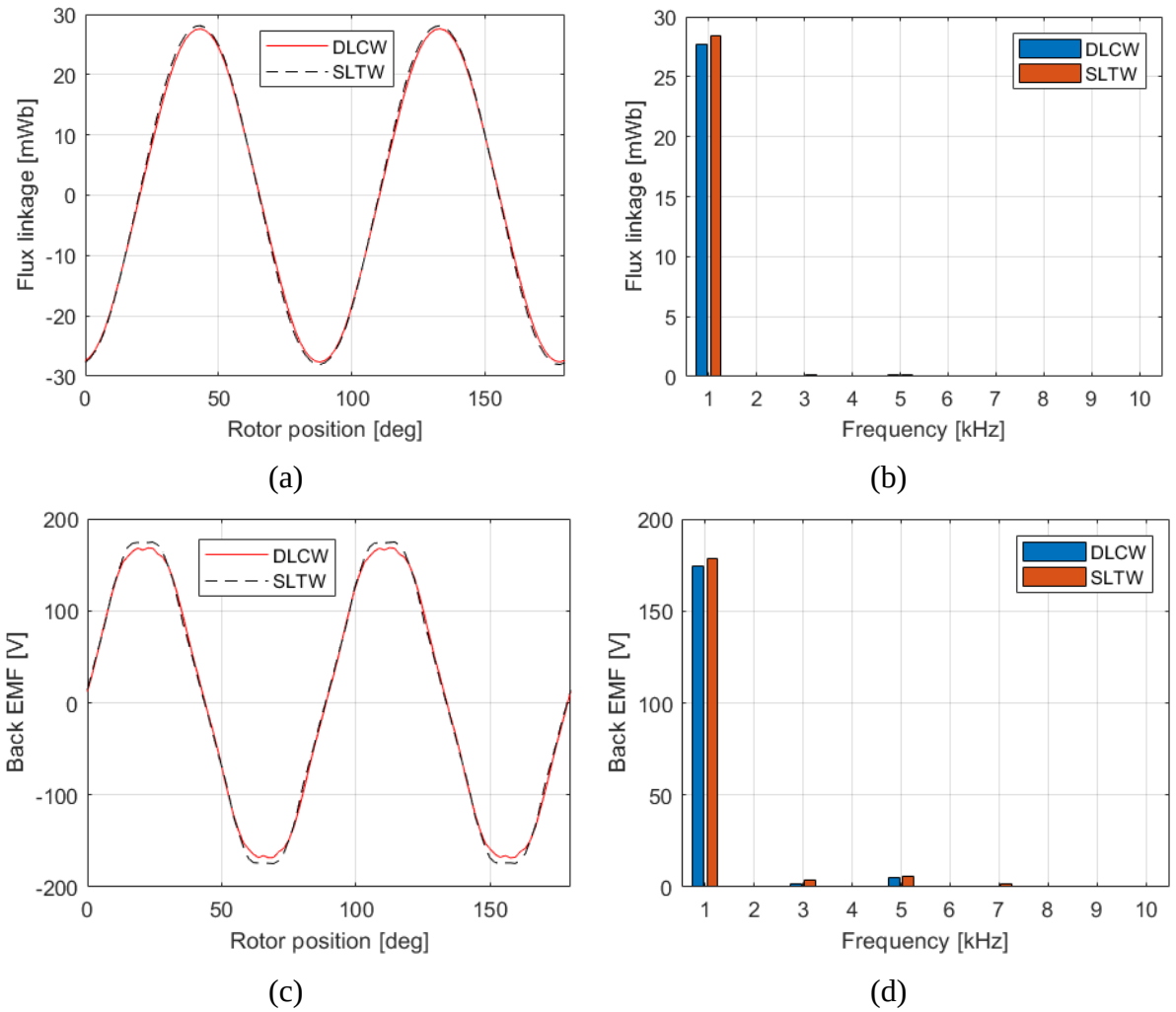

Figure 3.2-1. Open circuit characteristics of the three dual-stator 6/4 FSPM machines (a) Back EMF waveform (b) Back EMF harmonic components (c) Flux linkage waveform (d) Flux linkage harmonic components

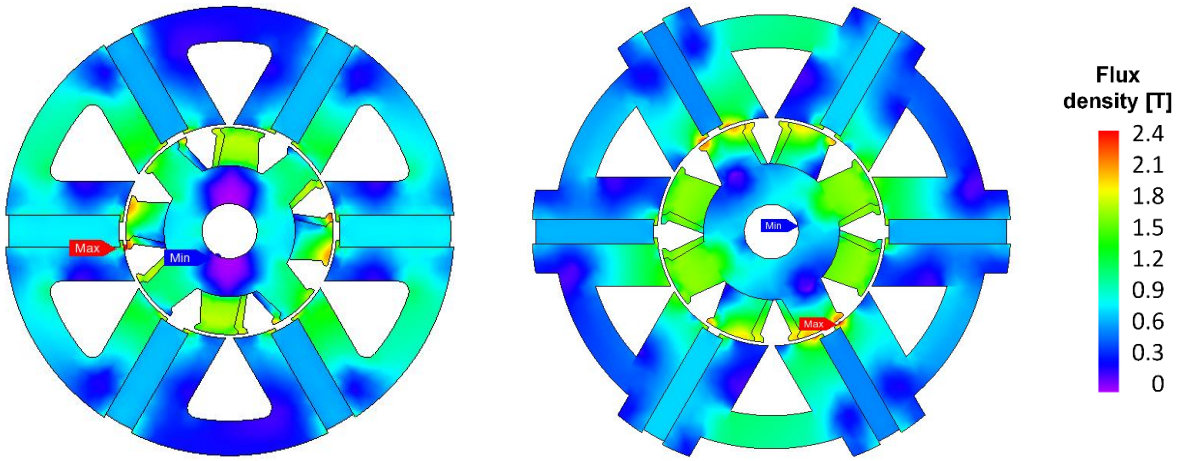

(a) (b)

Figure 3.2-2. Magnetic flux density distribution contour at no-load for (a) DLCW 6/4 FSPM machine and (b) SLTW 6/4 FSPM machine

back EMF of both machines have sinusoidal shape with low harmonic distortions. The flux density contour plots of the two machines are shown in Figure 3.2-2. As can be seen, due to the flux focusing effect of the spoke magnets, the stator and rotor tooth have higher magnetic flux density than the back iron. Because of the high air gap flux density, saturation occurs at the rotor and stator tips. The cogging torque is also simulated under the open-circuit condition. The cogging torque waveforms for the three machines are shown in Figure 3.2-3. As can be seen, the amplitude of the

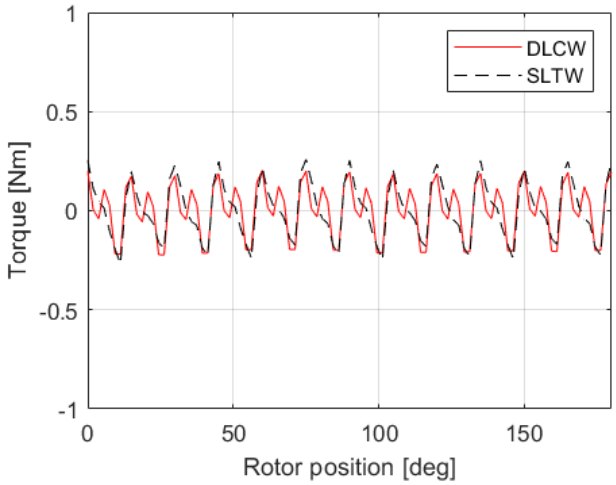

Figure 3.2-3. Cogging torque of the DLCW and SLTW dual-stator 6/4 FSPM

cogging torque of the two machines are similar. The cogging torque periodicities are identical since it depends on the machine slot/pole relation.

3.2.2. Loaded machine characteristics

The DLCW and SLTW machine are designed to have the same output power. With the same level of back EMF, as shown previously, the armature currents of the two machines are also identical. The rated output torque waveform and the torque-current relation curve are shown in Figure 3.2-4 (a) and Figure 3.2-4 (b), respectively. As can be seen, with the same rated current,

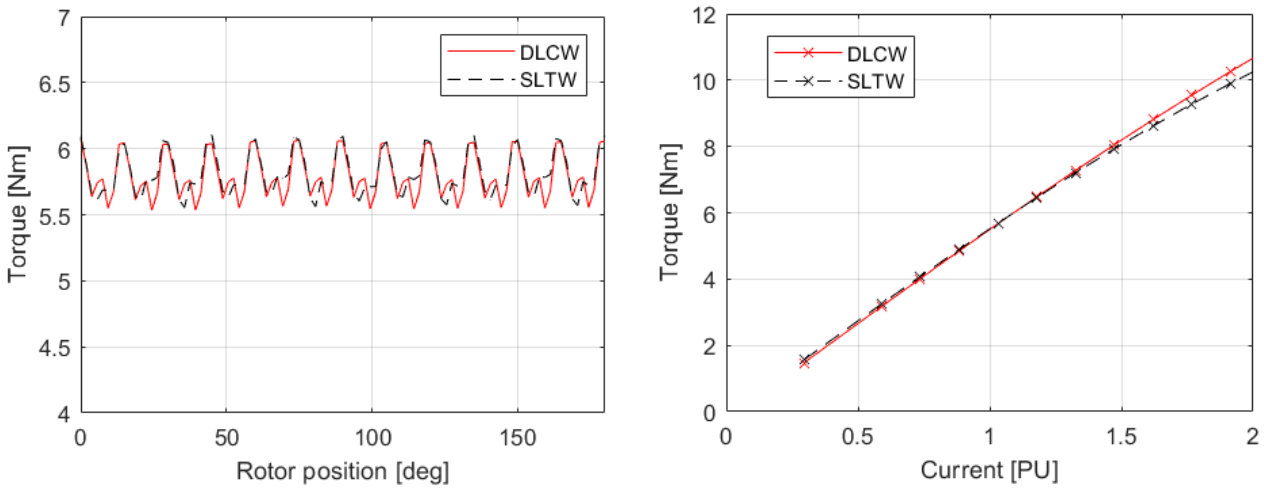

(a) (b)

Figure 3.2-4. Comparison of output torque of DLCW and SLTW 6/4 FSPM machine (a) Rated torque waveform and (b) Torque-current curve

the two machines produce similar average torque. Before the stator and rotor cores of the machine are saturated, the machine output torque should be proportional to the armature current (also *q*-axis current). The torque-current curve indicates that the DLCW machine and the SLTW machines have similar overload capability. As mentioned previously, because of the flux focusing effect of the spoke type magnet, the flux density of the stator tooth is high. Therefore, the FSPM machine

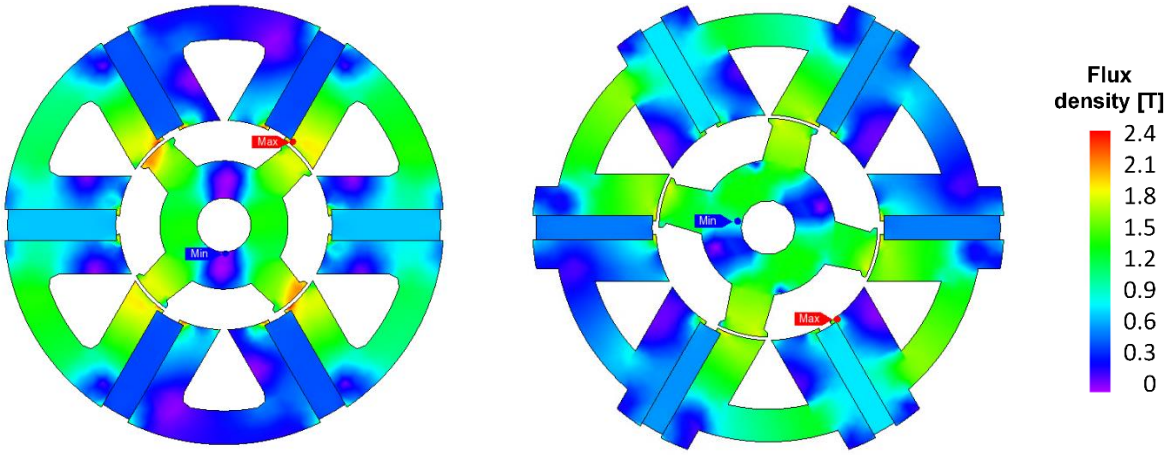

(a) (c)

Figure 3.2-5. Magnetic flux density distribution contour at rated output condition of (a) DLCW 6/4 FSPM machine and (b) SLTW 6/4 FSPM machine

inherently does not have excellent overloading capability. As can be seen in Figure 3.2-4 (b), starting from 1.5 p.u. current, the torque-current relation is no longer perfect linear.

The magnetic flux density contour plots for the two machines under rated condition are shown in Figure 3.2-5. Similar to the no load condition, the stator and rotor tooth have the higher magnetic flux density. A summary of machine performance characteristics is given in TABLE 3-5.

TABLE 3-5. OPERATING CHARACTERISTICS OF DUAL-STATOR 6/4 FSPM MACHINE

Variable	Symbol [unit]	DLCW	SLTW
Rated current	I_{rated} [Arms]	24	24
Rated speed	n_{rated} [rpm]	15000	15000
Output power	P_{out} [W]	9189.2	9157.8
Output torque	T_{out} [Nm]	5.85	5.83
Torque ripple	T_{ripple} [Nm]	0.45	0.41
Specific torque density	ξ_T [Nm/kg]	0.82	0.83
Specific power density	ξ_P [kW/kg]	1.28	1.31

The output power level of the two machines are very close. The torque production capability of the two designs are similar.

3.3. Loss distribution and efficiency comparison

The loss distribution of the machine is a very important aspect in the machine design. The losses not only affect the machine efficiency, but also influence the cooling design and the thermal performance of the machine. Efficiency of the machine is critical as well. Efficient machine is not only energy saving, but also need less cooling.

3.3.1. Copper loss

The copper loss of the machine is governed by the Joule's law, i.e. $3I^2R_s$, where I is the RMS value of stator current, R_s is the per phase stator resistance. The stator winding resistance calculation considering the ac effect has been illustrated in Chapter 2. The SLTW 6/4 FSPM machine needs less electric loading to produce the same amount of power according to the sizing equation. The less electric loading is translated to a smaller number of turns. The calculated DC stator winding resistance is shown in TABLE 3-4. The stator winding resistances versus frequency

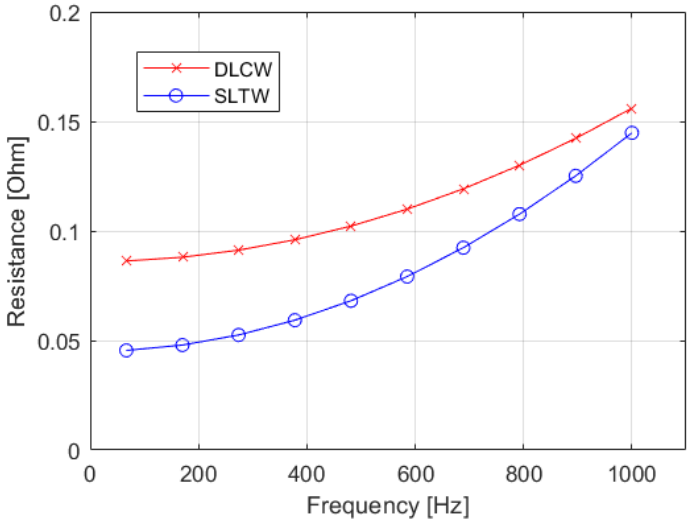

Figure 3.3-1. Winding resistance of the DLCW and SLTW 6/4 FSPM machine considering proximity effect.

are given in Figure 3.3-1. The winding resistance is also dependent on the temperature. Here the winding resistance are calculated at the temperature of 100 °C. In Chapter 4 where the thermal analysis is done, the copper loss is calibrated with the estimated winding temperature. The copper losses of the two machines are summarized in TABLE 3-6.

3.3.2. Stator and rotor iron loss

Iron loss in the stator and rotor laminations consist of mainly two parts: hysteresis loss due to the B-H loop of the electric steel and the eddy current loss due to the time varying magnetic flux. Many papers present the analytical and empirical estimation for iron loss [145]–[147]. However, because of the magnetization saturation and different machine geometry, the accuracy of analytical model is sometimes not enough. Finite element analysis (FEA) is commonly used for real time simulation. It is especially suitable for machines with specialized or 3-dimensional structure such as the 6/4 FSPM machine under investigation.

The hysteresis loss and the eddy current loss are both closely related to the frequency. Iron loss density data from the steel lamination company are often given in the form of a frequency dependent graph. Because of the flux modulation principle of the flux-switching machine, the magnetic flux is varying in the rotor reference frame, unlike the rotor mounted permanent magnet machine such as IPM and SPM machine. Therefore, determine the correct frequency is important for calculating or simulating the machine iron loss.

From the FEA simulation results, the magnetic flux line of the double-layer 6/4 FSPM machine and the single-layer 6/4 FSPM machines are shown in Figure 3.3-2. The direction of the magnetic flux is marked. There are four rotor poles for the 6/4 FSPM machine, and one electric cycle correspond to a mechanical angle of 90°, as can be observed. Therefore, the magnetic flux density variation in the stator can be calculated as $4f_m$ where f_m is the mechanical frequency derived from the mechanical rotation speed. In order to determine the rotor flux variation frequency, a red

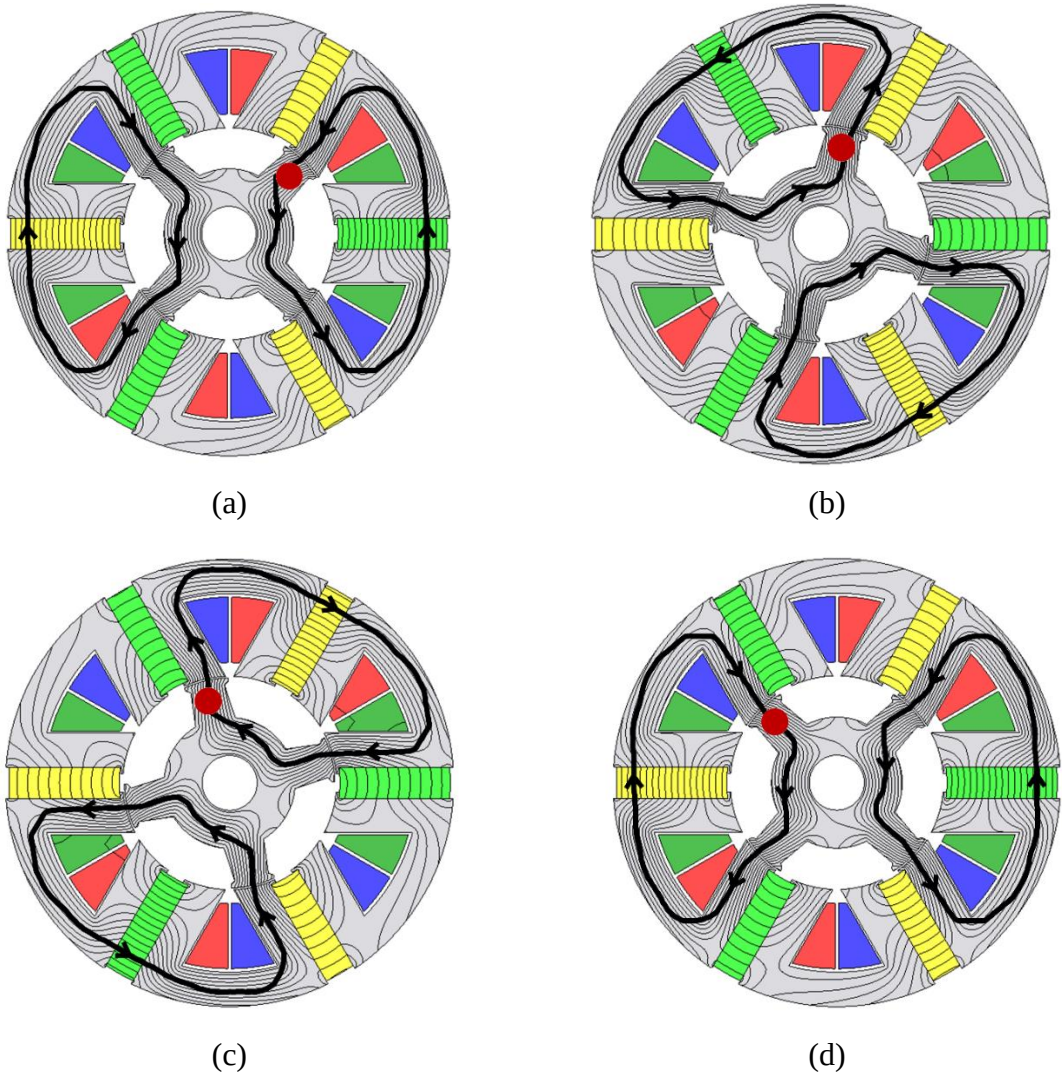

Figure 3.3-2. Magnetic flux line of a double-layer 6/4 FSPM machine at (a) 0° rotor position (b) 30° rotor position (c) 60° rotor position (b) 90° rotor position

dot is placed on one rotor tooth as reference. As can be seen in Figure 3.3-2, the magnetic flux in the rotor changes direction every time it sweeps by a permanent magnet is the stator. There are six magnets in stator. Therefore, in one mechanical rotation, the magnetic flux changes direction six times, i.e. finish three cycles. The magnetic flux variation frequency of the rotor is $3f_m$. For generic FSPM machine, the stator and rotor flux frequency calculated by (Equation 3-1) and (Equation 3-2), respectively.

$$f_{st} = \frac{nN_r}{60} \quad \text{(Equation 3-1)}$$

$$f_{st} = \frac{N_s}{2N_r}\frac{nN_r}{60} = \frac{nN_s}{120} \quad \text{(Equation 3-2)}$$

In order to verify the stator and rotor magnetic flux frequency, magnetic flux density probes are places at the stator tooth, stator back iron, and the rotor tooth. The magnetic flux density variation of three locations in the 6/4 FSPM machine are shown in Figure 3.3-3 (without loss of generality, the DLCW 6/4 FSPM machine is used as example). As can be seen, the flux frequency in the stator is four times of the mechanical frequency, and the flux frequency in the rotor is three times of the mechanical frequency. As mentioned previously, the varying magnetic flux in the rotor iron makes FSPM machine having higher iron loss than the rotor mounted PM machine. As can be seen in Figure 3.3-3, the magnetic flux variation in the stator is unipolar, which makes the B-H circulating in a smaller loop and have lower hysteresis loss.

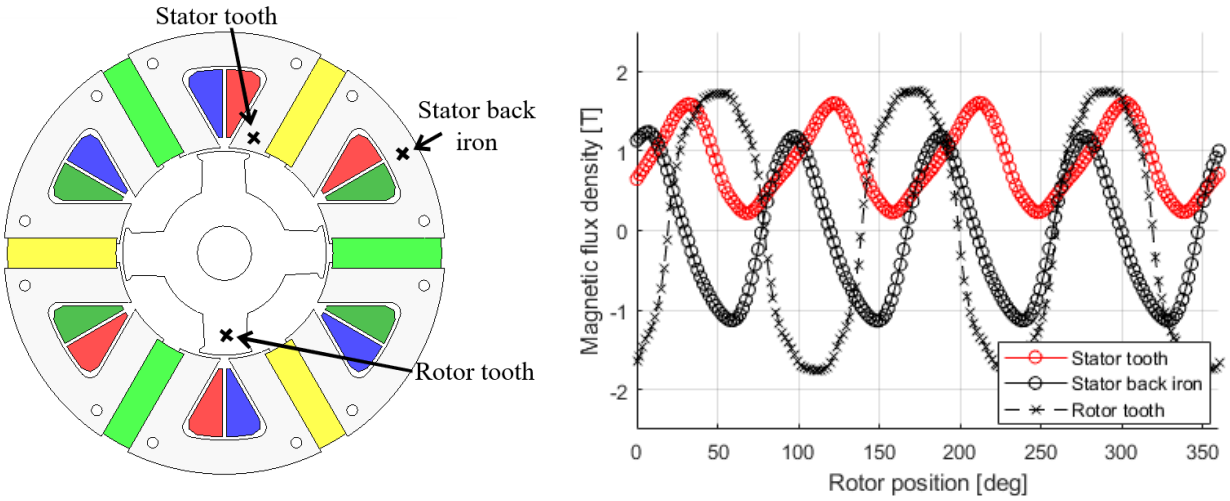

(a) (b)

Figure 3.3-3. Magnetic flux density variation (a) Position of the magnetic flux density probe in FEA (b) Waveform of three locations in the machine

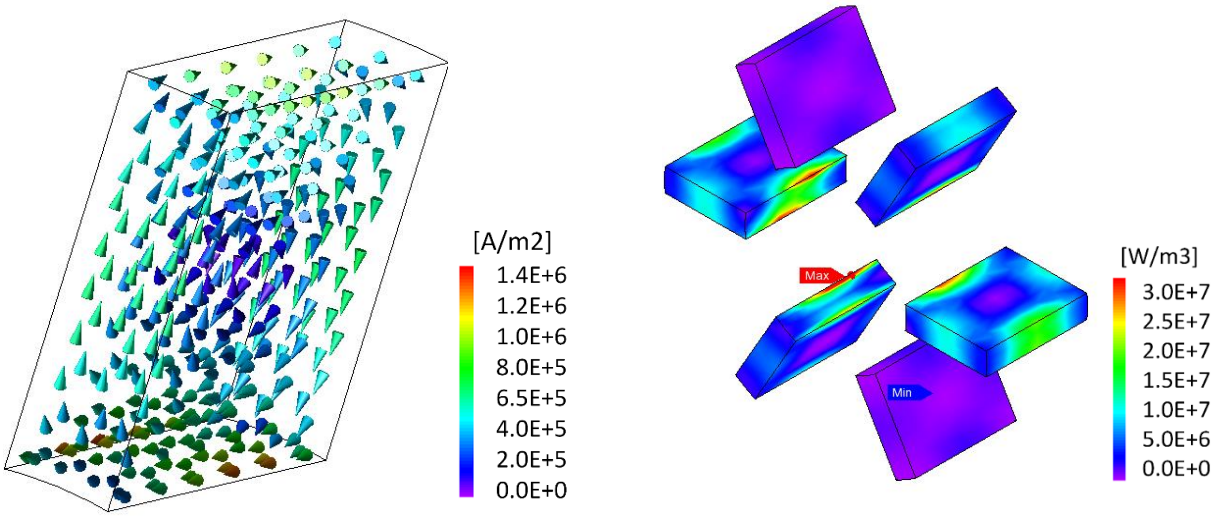

(a) (b)

Figure 3.3-4. Eddy current density in the stator-mounted permanent magnet of the dual-stator 6/4 FSPM machine

3.3.3. Magnet loss

Loss in the magnet is due to the eddy current induced by the variation of magnetic flux. As can be seen in Figure 3.3-2, the magnet flux is in the circumferential direction for the magnets. Therefore, the eddy current is circulating in the plane which is perpendicular to the circumferential direction as shown in Figure 3.3-4 (a). The eddy current has the skin effect and tends to concentrate to the surface of the magnet. Therefore, the magnet loss is concentrated at the surface of the magnets, as can be seen in Figure 3.3-4 (b). In order to reduce the magnet eddy current loss, a common practice is to use segmented magnet, similar to the lamination steel. The change of

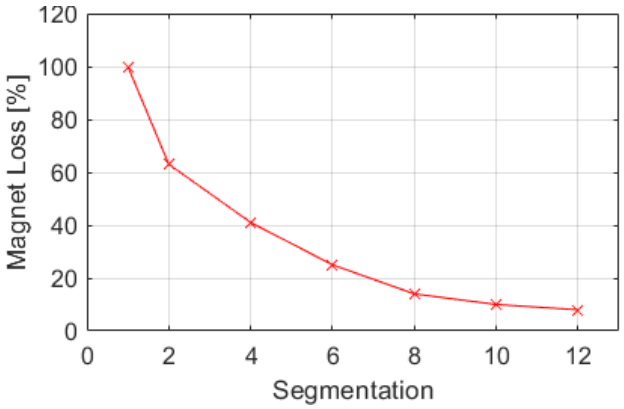

Figure 3.3-5. Magnet loss versus number of magnet segmentation

magnet loss versus the number of magnet segmentation is shown in Figure 3.3-5. As can be seen, the magnet eddy current loss reduces as the number of segmentation increases. On the other hand, a large number magnet segmentation increases the manufacturing cost of the machine. In this study, a segmentation of 8 is chosen as a trade-off between the magnet loss and cost.

3.3.4. Housing loss

The housing of the machine is usually made of non-magnetic metals such as aluminum because of the high mechanical strength and good thermal conductivity. Similar to the magnet, the metal housing also carries eddy current under a time varying magnetic field. Due to the relative complex geometry, the machine housing cannot be made of laminations. In FSPM machine, the magnets are in the stator and the housing is under a denser magnetic field compared to rotor-mounted permanent magnet machines. The eddy current density for the DLCW dual-stator 6/4 FSPM machine is shown in Figure 3.3-6 (a). As can be seen, the eddy current is mostly

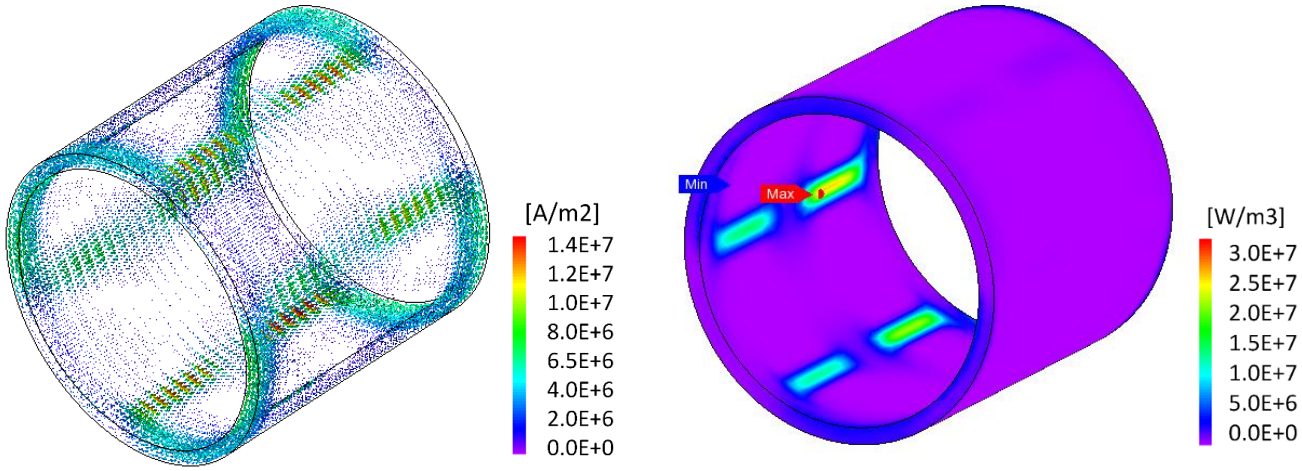

(a) (b)

Figure 3.3-6. Housing loss of dual-stator 6/4 FSPM machine (a) Eddy current density and (b) Eddy current loss density

TABLE 3-6. LOSS AND EFFICIENCY COMPARISON OF DLCW AND SLTW DUAL-STATOR 6/4 FSPM MACHINE

	@ 3000 rpm		@ 15000 rpm	
Parameters	**DLCW**	**SLTW**	**DLCW**	**SLTW**
Stator iron loss (W)	15.6	14.0	148.4	169.8
Rotor iron loss (W)	7.3	7.8	77.0	85.2
Magnet loss (W)	2.3	2.2	57.3	55.1
Copper loss (W)	221.7	102.2	307.6	260.9
Housing loss (W)	29.6	31.6	102.4	110.2
Output torque (Nm)	5.85	5.83	5.85	5.83
Output power (W)	1837.8	1831.6	9189.2	9157.8
Power factor	0.83	0.81	0.85	0.85
Efficiency (%)	86.9	92.0	92.9	93.1

concentrated in the vicinity of the permanent magnet, so as the eddy current loss density shown in Figure 3.3-6(b). The end winding region also has a higher eddy current density. Because the stator iron has a much higher magnetic permeability than the aluminum housing, the housing outside the stator iron has a very low current density. Note that the end cap of the housing also carries eddy current. However, the magnitude current in the end cap is much lower than that of the main housing and is not shown here.

The SLTW dual-stator 6/4 FSPM machine has the returning coil close to the housing. The magnetic field generated by the armature winding also have influence on the housing loss. Discussion on housing losses caused by the stator-mounted magnet and the returning coil in the toroidal winding are given in detail in Chapter 5. Housing loss reduction with stator structure modification is also presented in Chapter 5.

3.3.5. Comparison of efficiency and power factor

The evaluations of the various machine losses are presented in the previous section. The efficiencies of the DLCW and SLTW 6/4 FSPM machine are evaluated with the rated output torque

and at two speeds, 3000 rpm and 15000 rpm. The losses and the efficiencies of the two machines at the two speeds are shown in Table 3-6. At the relative low speed 3000 rpm, the copper loss is dominant among the losses. The SLTW 6/4 FSPM machine has more than 5% higher efficiency than the DLCW 6/4 FSPM machine because of the low stator winding resistance. The other losses of the two machines are similar. However, at the higher speed 15000 rpm, the copper loss is comparable to the other losses. And the advantage of low copper loss in the SLTW 6/4 FSPM machine is not as obvious as at 3000 rpm. In addition, as shown in Figure 3.3-1, at higher frequency, the total winding resistance of the SLTW is getting close to the DLCW. This is because the SLTW uses a larger wire gauge and is more sensitive to the frequency increase.

At 3000 rpm, the power factor of the SLTW 6/4 FSPM machine is lower than the DLCW machine because of lower stator winding. At 15000 rpm where the machine reactance is getting larger, the power factor of the two machines are the same.

3.4. Permanent magnet demagnetization in 6/4 FSPM machine

The torque production of the permanent magnet (PM) machine relies on the interaction between the magnetic field from the permanent magnet and the armature field. In some specific region, the magnetic flux from the armature winding is counteracting the PM field. At high load condition, the armature field could cause irreversible demagnetization of the PM if the magnetic flied strength exceed the knee point of the PM. The knee point position (characterized usually by the coercivity of the PM)

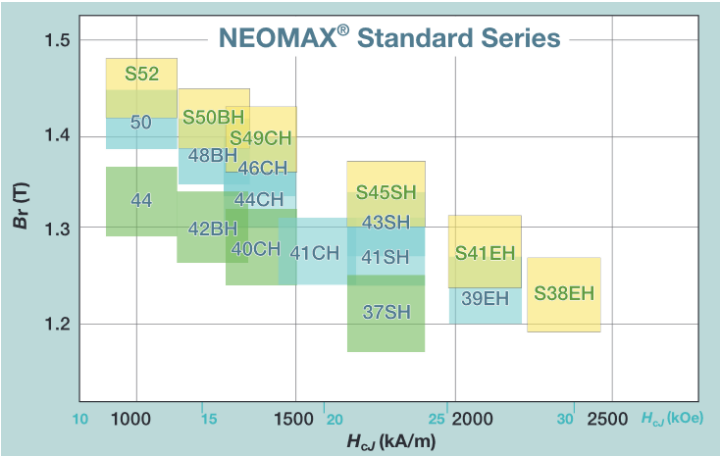

Figure 3.4-1. Magnet grade (from Hitach Co.) for different heat resistance level [148]

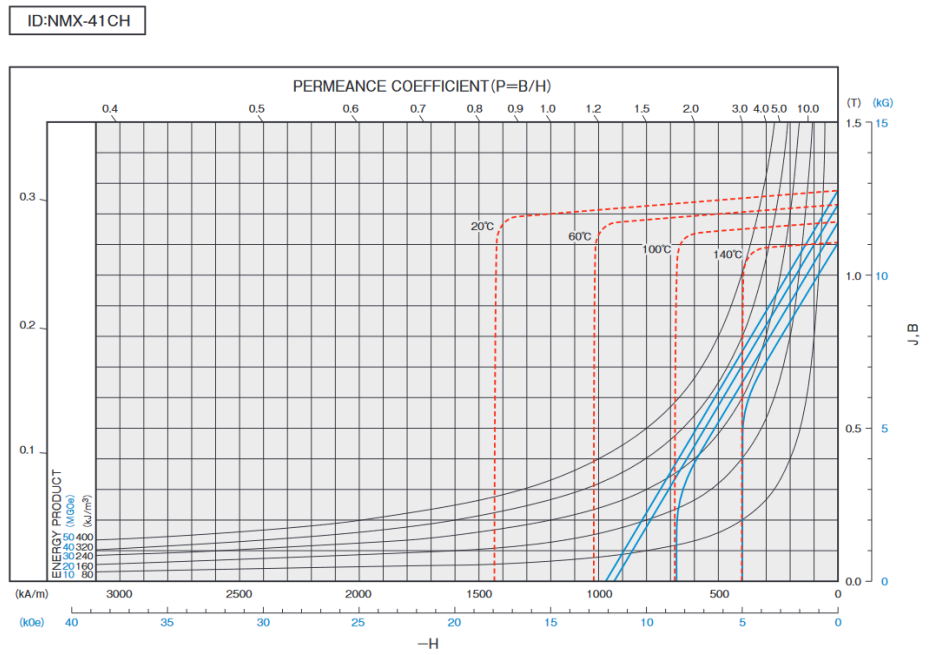

(a)

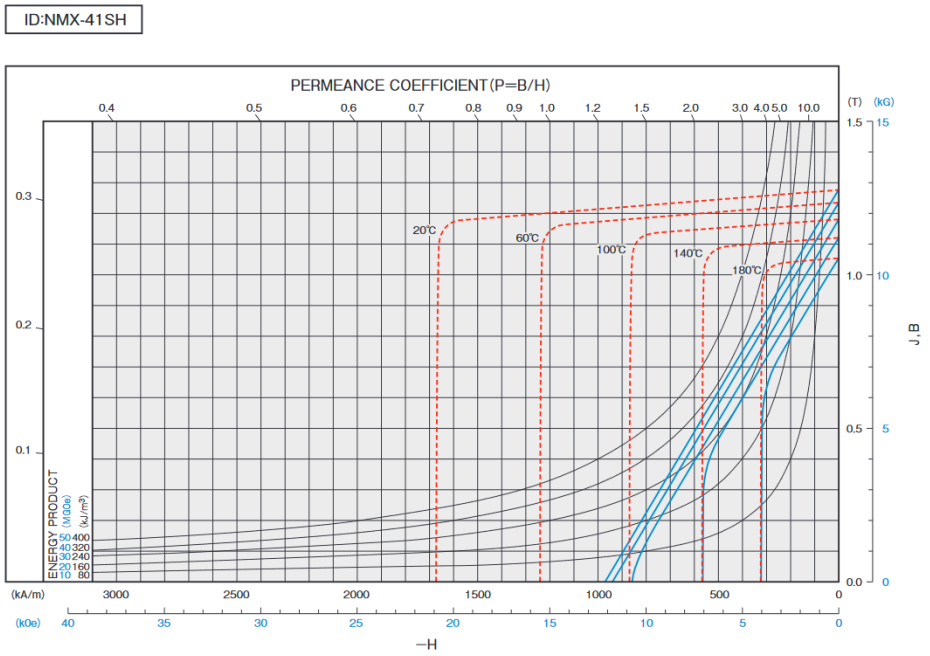

(b)

Figure 3.4-2. B-H curve of NdFeB permanent magnet from Hitach Metal Inc. (a) 41CH magnet and (b) 41SH magnet [148]

TABLE 3-7. KNEE POINTS MAGNETIC FLUX DENSITY OF CH AND SH GRADE MAGNETS AT DIFFERENT OPERATING TEMPERATURE

Grade	Temp.	20°C	60°C	100°C	140°C	180°C
CH	B_r [T]	1.28	1.24	1.18	1.10	-
	B_{knee} [T]	-0.7	-0.2	0.2	0.5	-
SH	B_r [T]	1.28	1.24	1.18	1.11	1.05
	B_{knee}[T]	< 0	< 0	0.0	0.3	0.6

depends on the magnet type, grade, and the operating temperature. For NdFeB magnet, the coercivity decreases as the temperature increase, which means the magnet is more vulnerable to demagnetization at high temperature. The PM material is grade in letter CH, SH, UH and EH, etc., as shown in Figure 3.4-1 for different heat resistance [148]. The heat resistance of the PM material is related to the Dysprosium (Dy) content. High Dysprosium content increases the temperature grade, but also reduce the remnant flux (Br) of the PM. In addition, Dy is an expensive rare-earth material and increases the cost of the machine. The B-H relation of a CH and SH grade magnet is shown in Figure 3.4-2 (a) and Figure 3.4-2 (b), respectively. When the applied magnetic field strength exceeds the knee point of the PM, irreversible demagnetization occurs and compromise the performance of the machine. The knee points magnetic flux densities of CH and SH grade magnets at different temperatures are given in TABLE 3-7. The demagnetization characteristics of the 6/4 FSPM machine is investigated in this section.

3.4.1. Permanent magnet loss and temperature distribution

As shown in Figure 3.4-2, the B-H curve of the PM material depends on the PM temperature, so does the PM material's resistivity to demagnetization. Therefore, the temperature distribution of the PM is first analyzed. The hotspot temperature of the PM has been calculated with lumped-parameter thermal network (LPTN) model in Chapter 4.2. However, precise temperature distribution is needed for the demagnetization study. Therefore, thermal finite element analysis

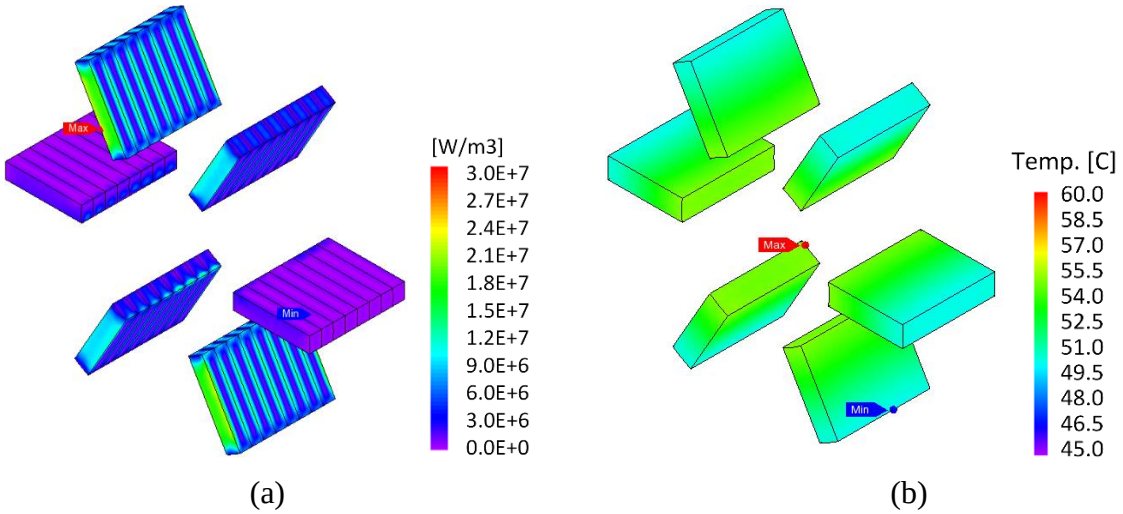

(a) (b)

Figure 3.4-3. Permanent magnets in 6/4 FSPM machine (a) Loss density distribution and (b) Temperature distribution

(FEA) shown in Chapter 4.3 is used. The machine thermal modelling and FEA configuration are described in Chapter 4.3 and is not repeated here.

The PM eddy current loss distribution contour at rated load condition at 3000 rpm from the electromagnetic FEA simulation is shown in Figure 3.4-3 (a). Note that the loss distribution shown in Figure 3.4-3 (a) is an instant loss density. The loss density change in time is much faster than the thermal transient. Therefore, average loss density could be used for the thermal simulation. The loss distribution is coupled into the thermal FEA simulation, and the magnet

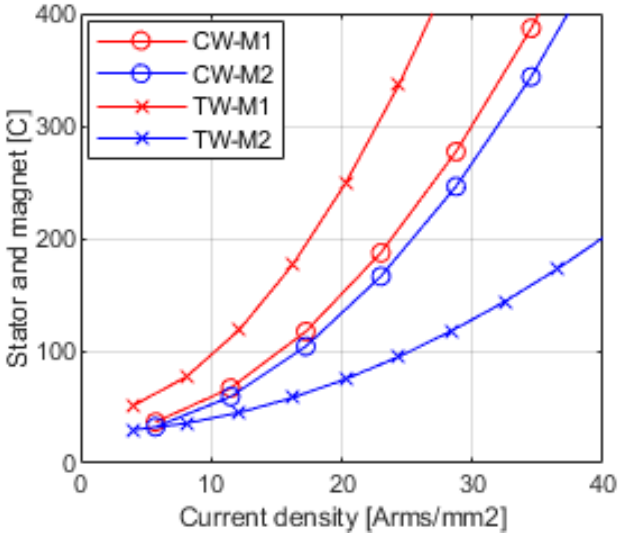

Figure 3.4-4. Magnet temperature variation as a function of slot current density

temperature distribution is shown in Figure 3.4-3 (b). As can be seen, although the magnet eddy current loss is concentrated at the outer region of the magnet, the temperature distribution in the PM is uniform with a range less than 5 ºC. The hotspot temperature will be used as the magnet temperature for the demagnetization investigation for simplicity.

Note that the PM loss and PM temperature distribution depend on the loading condition. The magnet temperature as a function of slot current density is shown in Figure 3.4-4. The temperature estimation is shown in detail in Chapter 4.2.

3.4.2. Permanent magnet demagnetization analysis

As mentioned previously, the demagnetization occurs when the armature magnetic field is counteracting the PM field and exceeding the coercivity of the PM. During the operation of FSPM machine, most of the armature reaction field is perpendicular to the PM filed. However, as shown in Figure 3.4-5, at the bottom of the PM, there are certain amount of armature field that travel in the opposite direction of the PM field. Therefore, the demagnetization of the FSPM machine will occur at the bottom of the PM material. Two magnetic flux probes are placed at the two inner radius corners of the magnet (note as P1 and P2, respectively), to monitor the magnetic flux density.

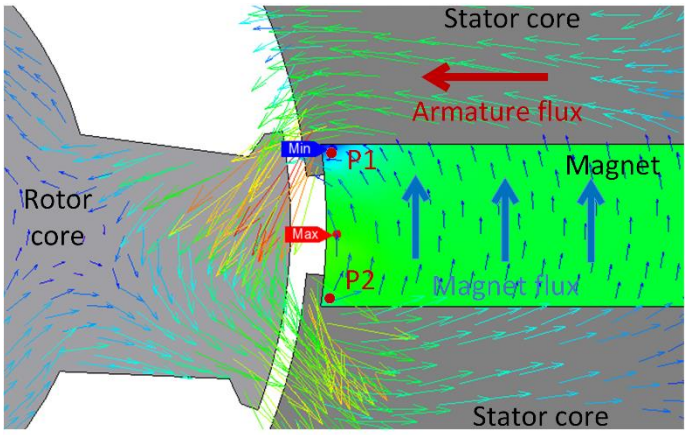

Figure 3.4-5. PM magnetic field and armature reaction field in 6/4 FSPM machine

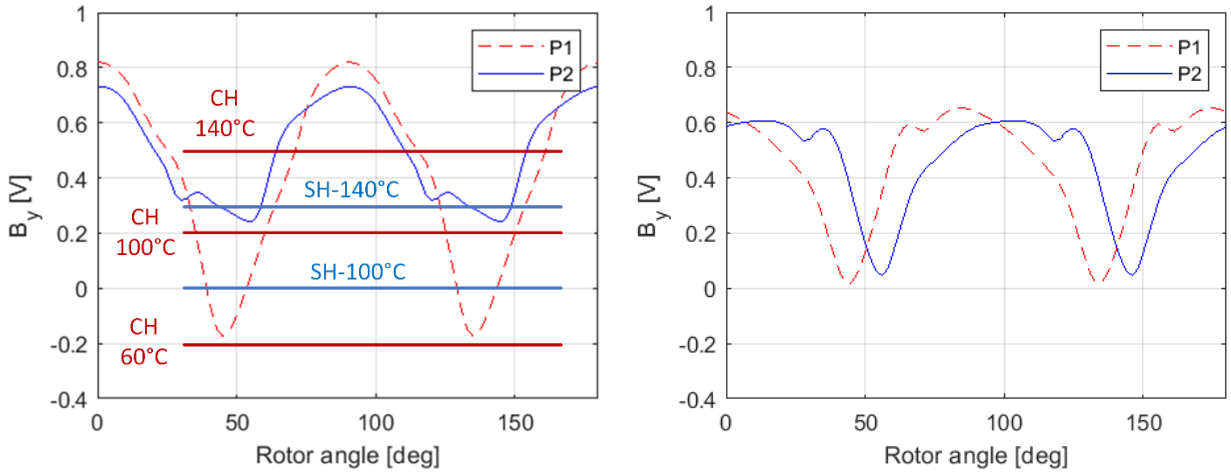

Figure 3.4-6. Magnetic flux density variation at the inner radius corner of magnet (a) With positive q-axis current and (b) with negative d-axis current

Note that the magnet shown in the figure is magnetized in the positive y-direction. Therefore, the probes at P1 and P2 are monitoring only the y-direction magnetic flux density. The variation of magnetic flux density at the two spot with only positive q-axis current applied and only with negative d-axis current applied is given in Figure 3.4-6 (a) and Figure 3.4-6 (b), respectively. As can be seen, as long as the magnet temperature is kept low enough (for example 60°C), there won't be any irreversible demagnetization occurs in the magnet. However, if the magnet temperature is high, certain amount of demagnetization would happen.

The demagnetization of the permanent magnet depends on the temperature and the armature field strength. Therefore, the demagnetization ratio needs to be evaluated for different temperatures and different current levels, whose relation is shown in Figure 3.4-4. FEA simulation is used to evaluate the demagnetization ratio of the PM at different condition. The demagnetization ratio is defined as the amount of demagnetization compared to the normal magnetization (usually referenced to the first step in the transient simulation). One full mechanical cycle of the 6/4 FPSM machine at 3000 rpm takes 0.02 second. The temperature of the magnets is assigned to 55 ºC for the first 0.005

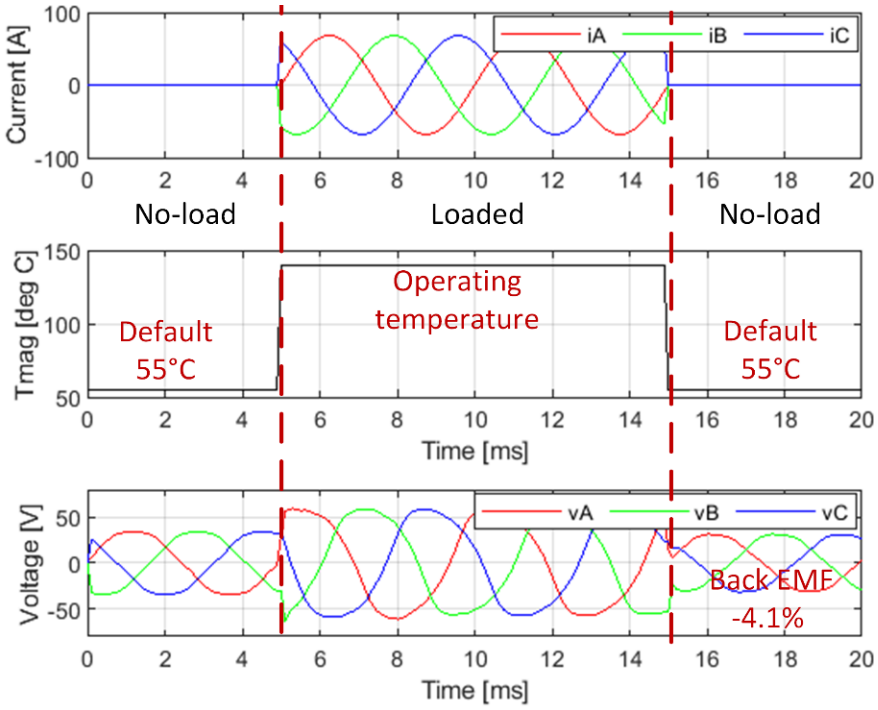

Figure 3.4-7. Demagnetization investigation: change of armature current, magnet temperature and back EMF in FEA simulation

second, then to the temperature corresponds to the current level. Certain armature current is applied starting from 5 ms and the magnet temperature is assigned to the corresponding temperature from the thermal analysis. The armature current is turn back to zero and the magnet temperature is

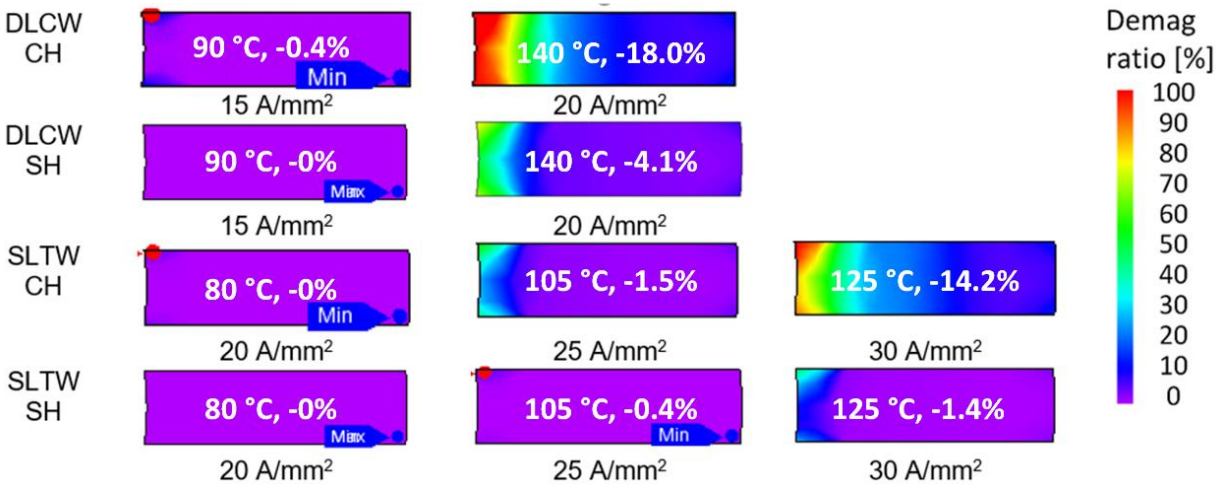

Figure 3.4-8. Demagnetization ratio of DLCW and SLTW 6/4 FSPM machine with CH and SH grade NdFeB magent at different current density

change back to the default level at 15 ms, as shown in Figure 3.4-7. The reduction of the back EMF level is another good metric for quantify how the irreversible demagnetization is besides the demagnetization ratio.

Demagnetization ratio contour plots for the DLCW and SLTW 6/4 FSPM machine with CH and SH grade PM under different slot current densities are shown in Figure 3.4-8. The percentage of back EMF reduction is also included in the figure. As can be seen, the SH grade magnet provides a much better heat resistance than the CH grade magnet and allow approximately 5 Arms/mm^2 more current density. The SLTW 6/4 FSPM machine has less demagnetization issue because the magnet temperature can be kept low even with high current density. Therefore, the SLTW 6/4 FSPM machine can use lower temperature grade PM material and have lower material cost than the DLCW 6/4 FSPM machine.

3.5. Summary

In this chapter, several aspects of the DLCW and SLTW 6/4 FSPM machines have been compared. The geometry parameters of the SLTW 6/4 FSPM machine including the stator and rotor tooth width and magnet thickness have been optimized with the help of 2D FEA simulation. Two 6/4 FSPM machines with DLCW and SLTW with the same volume and power rating are designed to conduct comparison. The no-load and loaded characteristics have been simulated with 3D FEA. Because of the higher winding factor, the electric loading of the SLTW 6/4 FSPM machine is half of the DLCW 6/4 FSPM machine. In the stator slot, no phase-phase insulation is needed for the SLTW. Therefore, higher slot filling factor can be achieved. It is shown that at the speed of 3000 rpm, the SLTW 6/4 FSPM machine has 5% higher efficiency than the DLCW 6/4 FSPM machine because of the low winding resistance. At the speed of 15000 rpm, the efficiency difference drops to 0.2% because the copper loss is no longer dominant at such speed, and the ac resistance is rising faster in the SLTW 6/4 FSPM macihne.

In FSPM machine, the direction of the armature magnetic flux is perpendicular to the PM flux for the most part. Therefore, FSPM machine is inherently not vulnerable to demagnetization. However, counteracting armature field exists at the bottom of the magnet. Therefore, demagnetization could happen at the bottom of the PM. The demagnetization is related to the PM temperature. With the same slot current density, the SLTW 6/4 FSPM machine has lower magnet temperature than the DLCW 6/4 FSPM machine. Therefore, the SLTW 6/4 FSPM machine can use lower temperature grade PM without risking the magnet of irreversible demagnetization.

Chapter 4 Cooling Design and Thermal Analysis of 6/4 FSPM Machine

The flux-switching permanent magnet (FSPM) machine has both armature windings and permanent magnets in the stator, which could be easily cooled by the heat sink in the housing. The rotor of the FSPM machine consists only lamination steels, which is relatively robust to high temperature. This structure makes the thermal management of FSPM machine easier compared to the rotor-mounted permanent magnet machine such as surface permanent magnet (SPM) and interior permanent magnet (IPM) machine. On the other hand, as shown in Figure 4.1-1, in the double-layer FSPM machine, the stator-mounted permanent magnets are surrounded by the armature winding, and the temperature sensitive magnets are very close to the source of copper loss. Therefore, the thermal analysis needs to be carefully conducted to avoid irreversible demagnetization of the permanent magnet. This chapter presents the choice and design of the cooling method for the dual-stator 6/4 FSPM machine. Thermal analysis is done to investigate the temperature distribution inside the machine.

4.1. Design of water jacket integrated housing

One commonly used cooling approach for the electric motor is a shaft mounted fan. However, at high-speed operation, this approach is not optimal because a large amount of shaft power is converted to kinetic energy in the circulating air and the output torque is compromised. In addition, the cooling performance is highly dependent to the

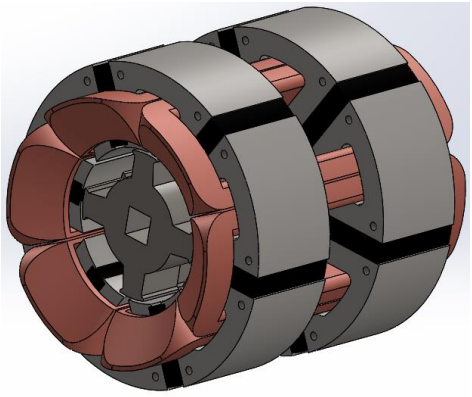

Figure 4.1-1. Double-layer dual-stator 6/4 FSPM machine.

(a) (b)

Figure 4.1-2. Coolant channel of water jacket (a) Spiral channel (b) Axial channel.

rotor speed and not well matched to the cooling requirement. In addition, for a compact motor design, the air flowing through the stator side is very limited and is not adequate to cool the winding and the magnet. As mentioned previously, for FSPM machine, both armature winding and permanent magnet are in the stator. Therefore, water jacket outside the stator is appropriate for cooling FSPM machine. The coolant channel of the water jacket could be either spiral type or axial type, as shown in Figure 4.1-2. The spiral type channel has the advantage of lower head loss than the axial channel because the coolant flow does not need to change direction. However, the locations of the inlet and outlet opening of the spiral channel need to be at the two sides of the water jacket, whereas the axial channel does not have such constraint.

4.1.1. Spiral channel water jacket

The spiral channel water jacket is used on the double-layer dual-stator 6/4 FSPM machine. The water jacket is a two-part assembly where the cooling channel grooved in the inner jacket. The outer jacket is a cylindrical sleeve and is shrink fit to the inner jacket to prevent coolant leakage. An energy balance is used to calculate the coolant flow rate required by the water jacket. It is assumed that all the heat from the machine is removed by the water jacket. The losses of the

TABLE 4-1. LOSS DISTRIBUTION IN DOUBLE-LAYER DUAL-STATOR 6/4 FSPM MACHINE AT 15000 RPM

Loss Component	Value
Copper loss [W]	307.6
Stator iron loss [W]	148.4
Rotor iron loss [W]	77.0
Magnet loss [W]	57.3
Housing loss [W]	102.4
Total loss [W]	692.7

machine at 15,000 rpm are given in TABLE 4-1. The temperature rise between the inlet and outlet of the cooling channel is set to be 1.8 °C. The necessary volume flow rate is calculated with (Equation 4-1), where P is the total power (W) need to be dissipated by the water jacket, c_{water} is

$$\dot{V} = \frac{P}{c_{water}\Delta T \rho_{water}} \qquad \text{(Equation 4-1)}$$

the specific heat capacity (J/kg-K) of water, ρ_{water} is the water density (kg/m^3), $\dot{V}$ is the volume flow rate (m^3/s), and ΔT is the temperature rise (K) from the outlet to the inlet of cooling channel. The geometry parameters of the cooling channel are labeled in Figure 4.1-3, and the corresponding

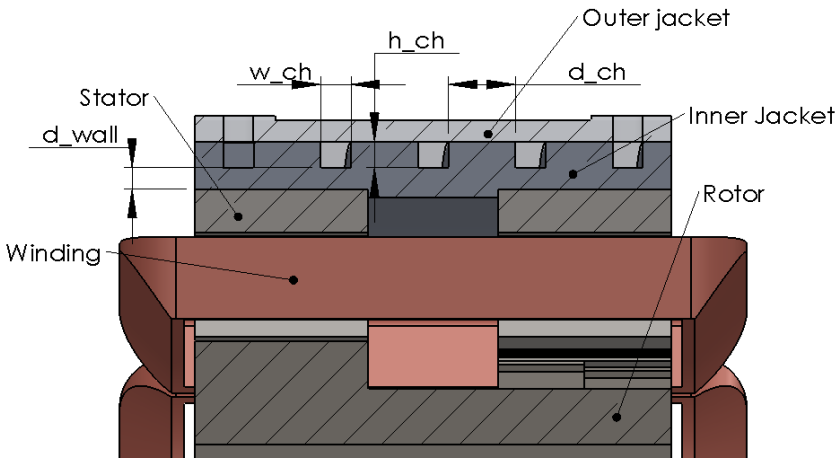

Figure 4.1-3. Section view of the spiral channel water jacket and dimensional parameters.

TABLE 4-2. PARAMETERS OF THE SPIRAL CHANNEL WATER JACKET

Parameters	Value
Cross section area, A_{ch} (mm^2)	42.0
Fluid-solid interface area (mm^2)	47903.6
Channel height, h_{ch} (mm)	6.0
Channel width, w_{ch} (mm)	7.0
Wall thickness, d_{wall} (mm)	5.0
Channel interval, d_{ch} (mm)	15.5
Total channel length, L_{ch} (mm)	1912.2
Volume flow rate, $\dot{V}$ (L/min)	3.65
Pressure drop, ΔP (mbar)	221.9
Temperature drop, ΔT (°C)	1.8
Heat transfer coefficient, $\bar{h}$ (W/m^2-K)	4619.6

values are given in TABLE 4-2 together with the coolant flow characteristics calculated with (Equation 4-1) given above.

In order to predict the behavior of the spiral channel water jacket, computational fluid dynamics (CFD) is used to simulate the fluid flow in the channel. As mentioned in the previous paragraph, all the losses are assumed to be dissipated through the cooling water. The assumption will be justified with the experiment testing. The fluid domain geometry of the spiral channel water jacket is imported to the CFD code. Energy equations are enabled to take the heat transfer between the aluminum housing and the coolant into consideration. The coolant inlet temperature and velocity are set up according to the parameters in TABLE 4-2. The velocity stream line and the temperature contour plots of the fluid in the spiral channel are shown in Figure 4.1-4. As can be seen, the fluid is smooth in the spiral coolant channel with small velocity variation. Figure 4.1-4 (b) shows that the temperature gradient between the inlet and outlet of the channel is approximately 2.2 °C, which is close to the assumption made previously. The turbulence intensity, which is defined as the ratio between the root-mean-square (RMS) of the turbulence velocity fluctuation and the mean velocity of the fluid, inside the channel is shown in Figure 4.1-4 (c). As can be seen,

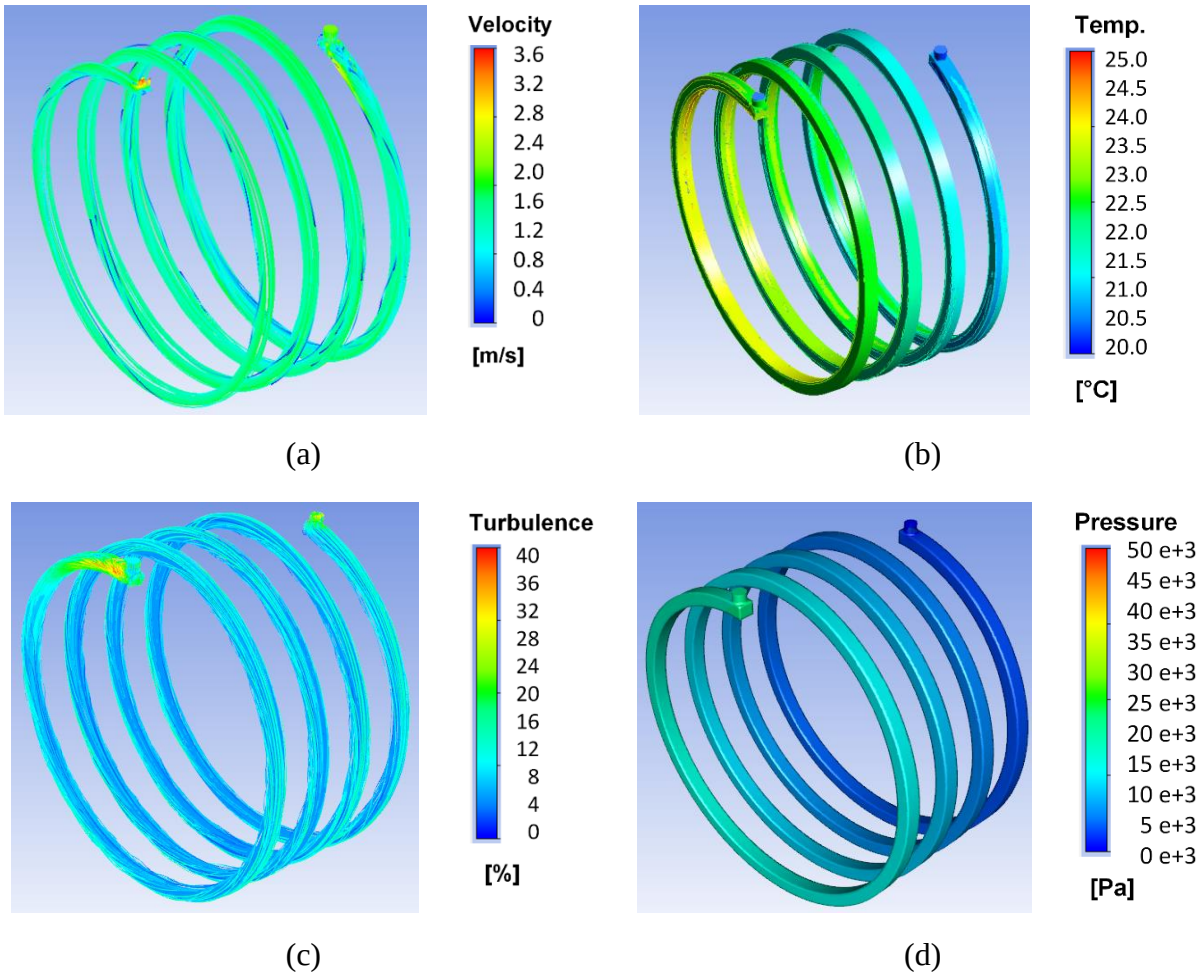

Figure 4.1-4. Computational fluid dynamics simulation of spiral channel water jacket (a) Velocity stream plot (b) Temperature contour plot (c) Turbulence intensity (d) Static pressure.

most of the turbulence occurs at the inlet and outlet of the channel. The fluid in the middle of the channel has a turbulence intensity around 16%.

The CFD simulation also gives the characteristics of the convective heat transfer between the fluid and the solid, which is used in the thermal analysis shown in the next section. The average heat transfer coefficient (W/m^2-K) can be calculated by (Equation 4-2), where $\dot{q}''$ is the heat flux

$$\bar{h} = \frac{\dot{q}''}{\int_A T_{wall} - T_{ref}} \qquad \text{(Equation 4-2)}$$

(W/m^2), A is the channel wall surface area, T_{wall} is the spot temperature on the surface of the wall, T_{ref} is the reference temperature of the media to calculate the heat transfer coefficient. The calculated average heat transfer coefficient is shown in TABLE 4-2.

4.1.2. Axial channel water jacket

The axial channel water jacket is applied to the single-layer toroidal winding dual-stator 6/4 FSPM machine. Similar to the spiral channel water jacket, the coolant channel is grooved in the inner housing with the outer housing shrink fitted. The stator consists six units placed circumferentially, the axial channel also has six groups, as can be seen in Figure 4.1-2 (b). The discontinuity between the groups of channels is due to the potential design of housing cavities to reduce the housing eddy current loss, as shown in chapter 5. As mentioned previously, the position of the inlet/outlet of the axial channel is flexible. In this study, the inlet/outlet of the channel are place at the middle of the housing without loss of generality. The flow characteristics of the axial channel can be calculated similarly to the spiral channel. The section view of the channel is shown in Figure 4.1-5, and the water jacket parameters are summarized in TABLE 4-3.

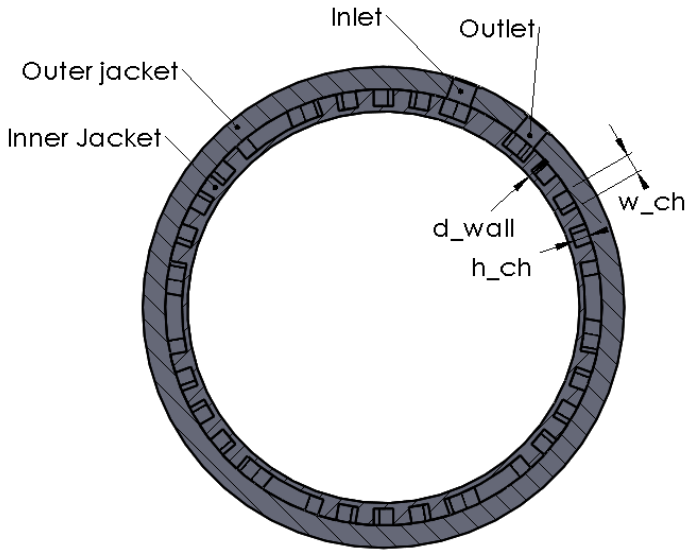

Figure 4.1-5. Section view of the axial channel water jacket and dimensional parameters.

TABLE 4-3. PARAMETERS OF THE AXIAL CHANNEL WATER JACKET

Parameters	Value
Cross section area, A_{ch} (mm^2)	42.0
Fluid-solid interface area (mm^2)	90318.1
Channel height, h_{ch} (mm)	6.0
Channel width, w_{ch} (mm)	7.0
Wall thickness, d_{wall} (mm)	3.0
Total channel length, L_{ch} (mm)	3220.6
Volume flow rate, $\dot{V}$ (L/min)	3.65
Pressure drop, ΔP (mbar)	431.4
Temperature drop, ΔT (°C)	2.6
Heat transfer coefficient, $\bar{h}$ (W/m^2-K)	3231.3

The CFD simulation results are shown in Figure 4.1-6. The temperature rise of the coolant is about 2.6 °C, which is higher than the spiral channel water jacket. The fluid in the axial channel is more turbulent than the spiral channel because the flow needs to change direction inside the channel. As can be seen in Figure 4.1-6 (c), the turbulence intensity is high at the turning corner of the channel. Compared to the spiral channel water jacket, the axial channel water jacket requires higher pumping power for the same flow rate. The heat transfer coefficient of axial channel water jacket is about 70% of the spiral channel water jacket. However, the geometry and location of the axial channel are more flexible, which is beneficial in certain cases, for example, the inlet/outlet location of the channel are constraint by the surrounding of the machine.

4.1.3. Choice of winding encapsulation material

Most of the armature windings of electric machines consist of multiple turns per coil. Although some designs use pressing tool to preform the coil and squeeze the turns together to increase the slot filling factor, majority of the machine windings have a slot filling factor from 30%

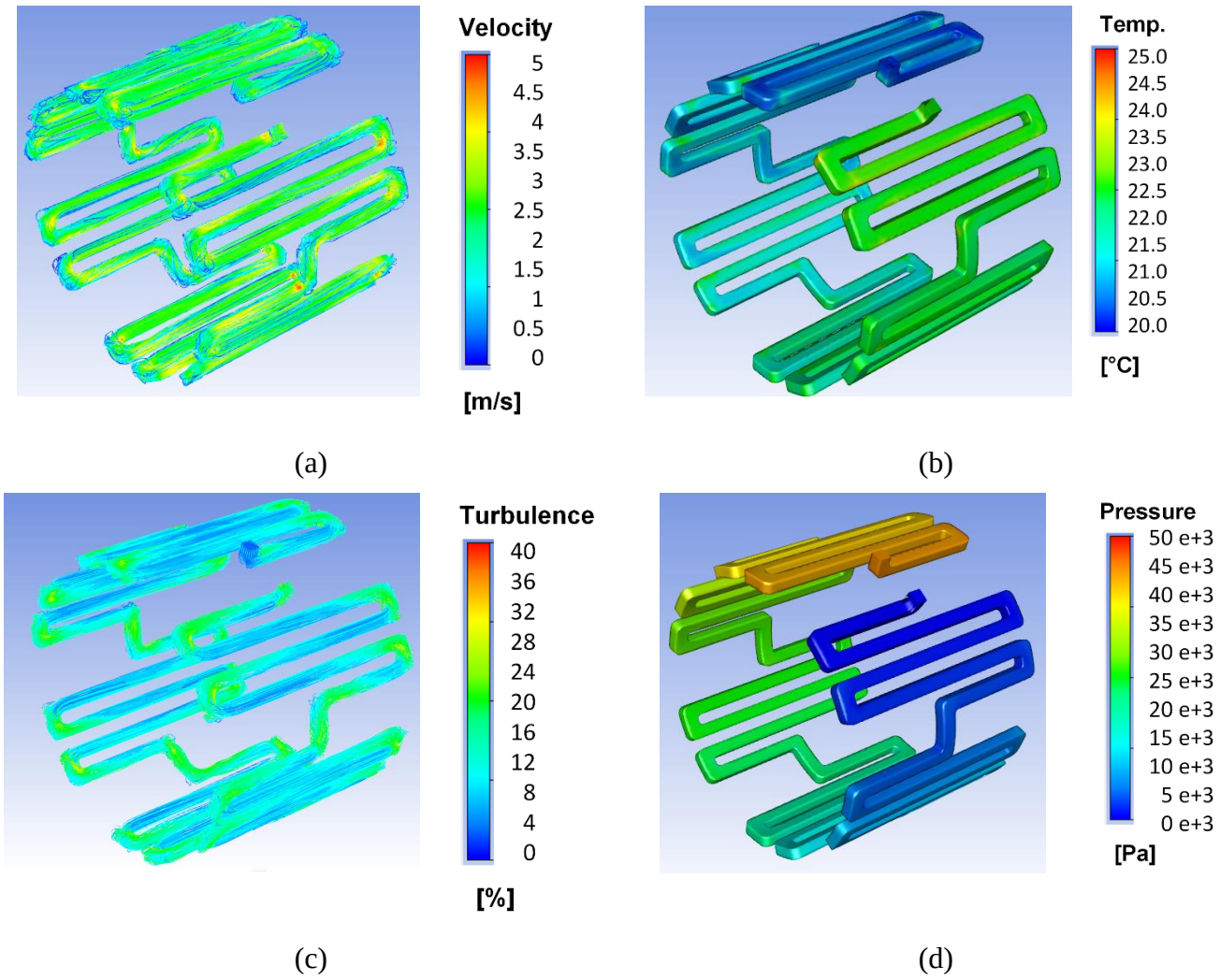

Figure 4.1-6. Computational fluid dynamics simulation of axial channel water jacket (a) Velocity stream plot (b) Temperature contour plot (c) Turbulence intensity (d) Static pressure.

- 60%. Besides the slot linear and the varnish on each turn of wire, the non-copper area of the slot is left with either air or filled with insulated encapsulation material.

Air has a low thermal conductivity of only 0.026 W/m-K. Therefore, having air in the slot provides a substantial thermal resistance between the windings and the water jacket. Filling the slot with dielectric material that is more thermally conductive than the air it displaces, i.e. winding encapsulation material, is a commonly used technique in electric machine design to improve the thermal performance [149]. A vacuum chamber is usually used to pull the air out from the slot and

TABLE 4-4. SLOT ENCAPSULATION MATERIAL PROPERTIES

Parameters	CC-1105	EFI-108
Thermal conductivity [W/m-K]	0.14	1.9
Density [kg/m3]	1246.2	2444.5
Viscosity [Pa-s]	0.9 to 1.5	2.7
Curing temperature [°C]	163	200

fully impregnate the slot with the encapsulation material. The thermal impedance between the windings and the stator core/housing mainly depends on the properties of the encapsulation material. Unfortunately, commonly used dielectric materials also tend to be thermal insulators. The thermal properties of the two encapsulation materials chosen in this paper are listed in TABLE 4-4. As can be seen, the EFI-108 epoxy mixture has a thermal conductivity of 1.9 W/m-K, which is more than 10 times higher than that of Dolph's CC-1105 polyester resin and almost 100 times higher than air. Other properties such as viscosity and curing temperature are related to the encapsulation procedure, which is not the focus of this paper. In addition to thermal performance improvement, encapsulation also helps to prevent winding damage from vibration and contamination.

4.2. Steady state thermal analysis of dual-stator 6/4 FSPM machine

As mentioned in the previous section, water jacket cooling is an effective way to reject heat from FSPM machine. Thermal analysis is necessary to verify that the temperature of the critical components is below the operation limit. The double-layer concentrated winding (DLCW) and single-layer toroidal winding (SLTW) 6/4 FSPM machines are different in structure as well as in the thermal behavior which need to be modeled and compared. The steady state thermal performance is first analyzed in this section.

4.2.1. Lumped parameter thermal network model

Lumped parameter thermal network (LPTN) is a common tool to model the thermal behavior of a system. LTPN is beneficial for its short calculation time, and the quasi-instant results which enable designers to iterate quickly. The thermal network is similar to an electrical circuit, where a heat source is analogous to a current source, heat flow to current flow, and temperature reference to voltage reference. By solving the nodal equations for the network, the temperatures of each point and the heat flow through each branch can be calculated. Results from the thermal network help the designer to find the most critical impedance in the heat dissipation path and propose a more effective cooling.

For a steady-state study, the critical component in a thermal network is the thermal resistance. Depending on the heat transfer mode, a thermal resistance can be put into three main categories: conduction, convection and radiation heat transfer. Many sources cover the derivation of these three types of thermal resistance [150][151]. Radiation is not considered here since it is negligible compared to the other mechanisms of heat transfer in most cases. However, for aerospace application where conduction and convection heat transfer do not exist, radiative heat transfer becomes non-negligible. (Equation 4-3) - (Equation 4-5) are used for calculating different types of

conduction (rectangular shape) $$R = \frac{L}{Ak}$$ (Equation 4-3)

conduction (cylindrical shape) $$R = \frac{\ln(\frac{r_1}{r_2})}{2\pi k L_a}$$ (Equation 4-4)

convection $$R = \frac{1}{hA}$$ (Equation 4-5)

thermal resistances, where k is the thermal conductivity (W/m-K) of the material, h is the heat

transfer coefficient (W/m^2-K). The geometry variables are shown in Figure 4.2-1, all lengths are in (m).

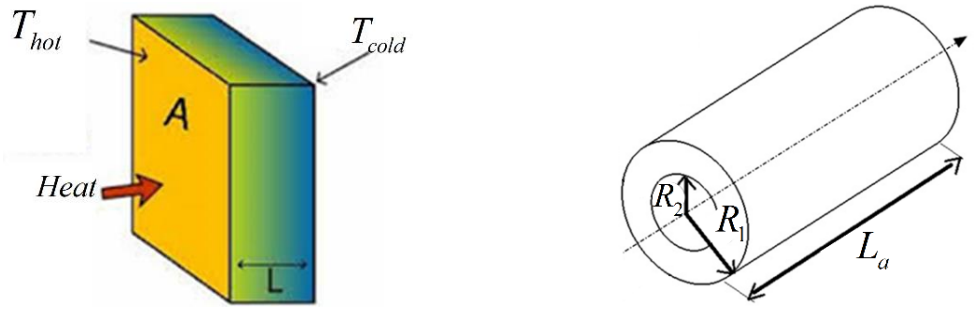

(a) (b)

Figure 4.2-1. Geometry parameters for (a) Rectangular conductive heat transfer model, (b) Cylindrical conductive heat transfer model.

TABLE 4-5. 6/4 FSPM MACHINE PARAMETERS AND MATERIAL PROPERTIES

Parameters	DLCW	SLTW
Stator outer radius (mm)	65	
Stator tooth width (mm)	10	11
Axial stack length (mm)	80	80
Magnet thickness (mm)	9	8
Airgap (mm)	1	
Stack length (mm)	80	80
Slot area (mm^2)	369.1	231.9
Permanent magnet type	NdFeB, B_r = 1.2 T, k_{mag} = 7.6 W/m-K	
Water jacket material	Aluminium, k_{alu} = 205 W/m-K	
Lamination steel	Arnon 5, thickness = 0.127mm k_{ax} = 0.7 W/m-K, k_{pl} = 22.4 W/m-K	
Winding	Copper, 8 strands of AWG#23 wire k_{Cu} = 380 W/m-K Slot fill factor = 0.4 for CW; 0.45 for TW	

4.2.2. Thermal network modeling of 6/4 FSPM machine

According to the geometry and dimensions of the DLCW and SLTW 6/4 FSPM machine, an LPTN thermal network can be generated based on the heat conduction path and losses associated with the machine components. The basic geometry and thermal parameters of the 6/4 FSPM machine are given in TABLE 4-5. Because of the symmetric geometry of the 6/4 FSPM machine, 1/12 of the whole machine is sufficient to model the thermal behavior. The symmetry boundaries in the thermal models are considered adiabatic. The LPTN steady state thermal models for the two machines are shown in Figure 4.2-2 (a) and Figure 4.2-2 (b), respectively. Since the water jacket located outside the stator is the main heat sink, machine losses are predominantly conducted in the radial direction. Therefore, the LPTN model is constructed in the X-Y plane. Note that the axial heat transfer in the coil is non-negligible due to the high thermal conductivity of

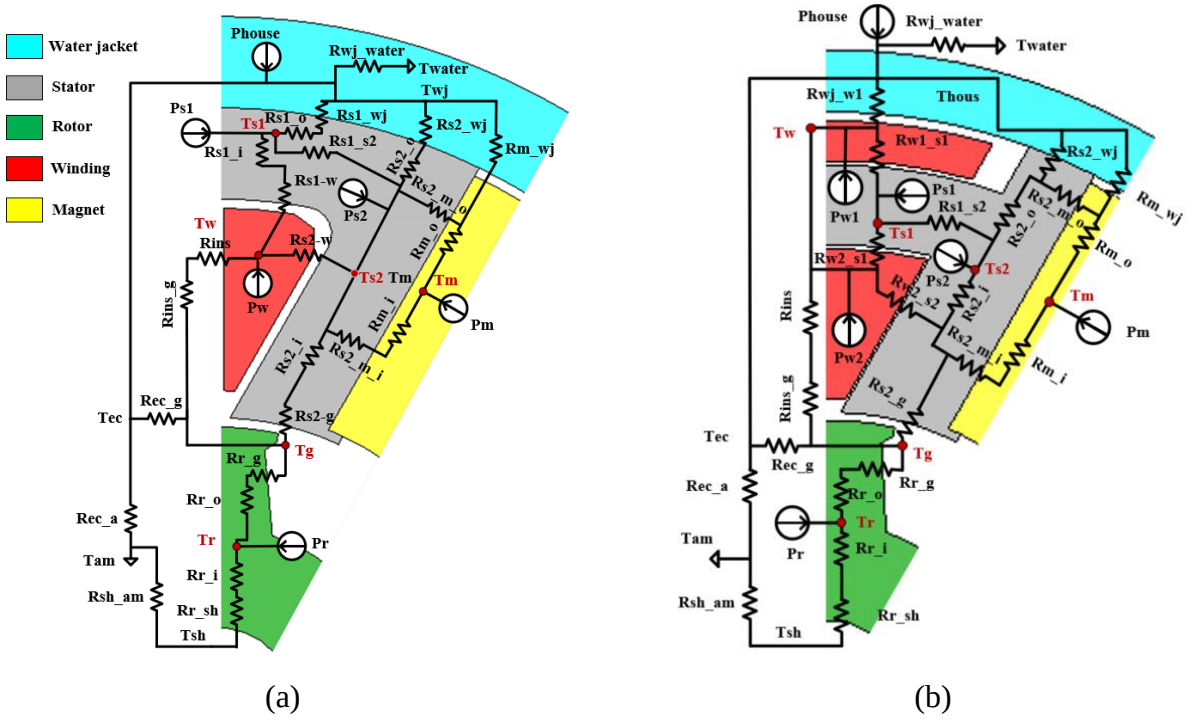

Figure 4.2-2. Steady-state lumped-parameter thermal network (LPTN) model for dual-stator 6/4 FSPM machine with (a) Circumferential winding and (b) Toroidal winding

copper, and the heat can be dissipated to the air region inside the housing through the end winding. The corresponding thermal resistance is modelled in Figure 4.2-2. The thermal conductivities of the machine components are given in TABLE 4-5. As can be seen, the thermal conductivities of the stator and rotor core are anisotropic due to the laminated structure. The heat transfer in the radial direction is dominant. Therefore, it is reasonable to simplify the heat transfer in the stator and rotor into a 2D study.

The values for heat sources are from the electromagnetic simulation described in Chapter 3, including the copper loss, iron loss, magnet eddy current loss, and the housing loss. Besides the different winding topologies (DLCW vs. SLTW), influence brought by the different encapsulation materials are also investigated. In the following part, two design cases are compared: DLCW 6/4 FSPM machine encapsulated with CC-1105 (noted as M1 material) and SLTW 6/4 FSPM machine encapsulated with EFI-108 (noted as M2 material).

The thermal networks for the two winding topologies share many thermal resistances in common, especially related to the rotor. The thermal resistance values for the two LPTNs are shown separately in TABLE 4-7 and TABLE 4-8. The geometry of the machine is not regular, and the thermal resistance of each component cannot be directly calculated with (Equation 4-3) - (Equation 4-5). Reasonable simplifications and assumptions are necessary to model the heat transfer in the 6/4 FSPM machines. The derivations of critical thermal resistances and the simplification used in the thermal modelling are shown in the following sections.

A. Equivalent Rotor Modeling

The FSPM machine has a salient shape rotor, as can be seen in Figure 4.1-1, the air gap length is non-uniform along the arc. In addition, the number of rotor poles is different from the stator slot number, which makes it difficult to form a partial thermal network model using the symmetry of the machine structure. In order to apply (Equation 4-4) to calculate the conduction

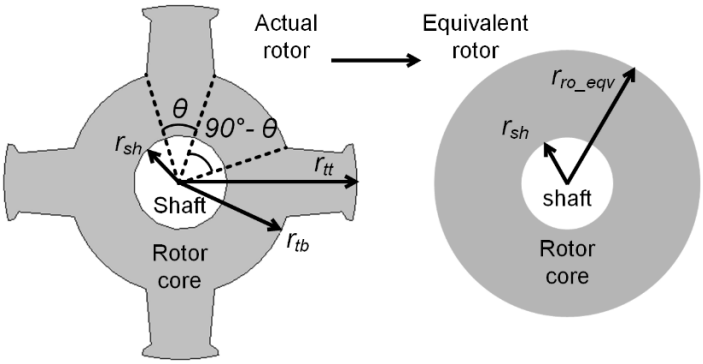

Figure 4.2-3. Equivalent rotor model transformation from salient rotor structure to cylindrical structure.

thermal resistance in the rotor core, the salient rotor needs to be reshape into a cylindrical form. Therefore, an equivalent cylindrical rotor is modelled as shown in Figure 4.2-3. Due to the salient rotor pole, the distance from the rotor inner surface to the rotor outer surface is not uniform in the azimuthal direction. An equivalent length of the conduction heat transfer in the rotor can be calculated using (Equation 4-6), where the geometry variables are given in Figure 4.2-3. Note that

$$r_{ro,equ} = r_{tt}\frac{\theta}{90°} + r_{tb}\frac{90° - \theta}{90°} \qquad \text{(Equation 4-6)}$$

the angle is in the unit of degree and the equivalent rotor has the same shaft radius (r_{sh}) as the actual rotor. The equivalent rotor has a hallow cylindrical shape and the conduction heat transfer can be modelled by (Equation 4-4). The rotor thermal resistance values are given in TABLE 4-7 and TABLE 4-8, respectively.

B. Air gap heat transfer

The heat transfer between the stator/rotor iron surface and the air gap is convective and can be characterized by (Equation 4-5). For a regular and smooth interface, analytical equations based on Taylor-Couette theory have been developed [152]. However, due to the salient rotor structure, the flow in the air gap of the FSPM machine is highly turbulent and can only be characterized by

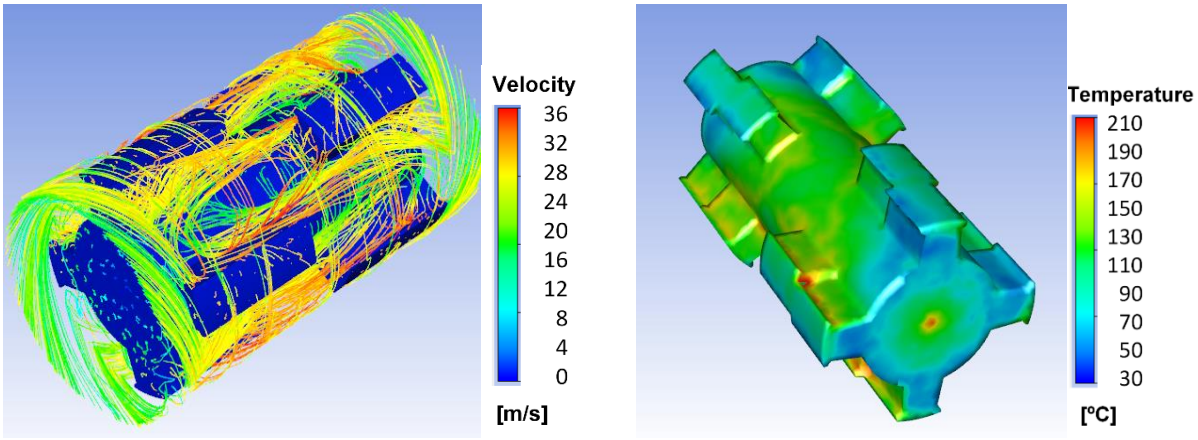

(a) (b)

Figure 4.2-4. Characterization of air flow in the air gap region (a) Air flow velocity stream line plot (b) Rotor surface temperature

empirical equations or CFD simulation [153]. In reference [154], the connective heat transfer coefficient is correlated to the rotor tip speed based on CFD simulation. It has taken the salient rotor pole structure of FSPM machine into account. Due to the dual-stator configuration of the machine under investigation and the complex flow characteristics in the air gap, the results from [155] cannot be apply directly to the 6/4 FSPM machine. Therefore, similar to the determination of heat transfer coefficient of the water jacket, ANSYS Fluent is used as the CFD tool to simulate the heat transfer in the air gap region. A 5000 W/m^2 surface heat flux is assigned to the rotor, and by putting the resulting area weighted average temperature from the simulation into (Equation 4-2), the average heat transfer coefficient can be derived.

The air flow path lines around the rotor at 4800 rpm and the temperature on the rotor wall are shown in Figure 4.2-4 (a) and Figure 4.2-4 (b), respectively. The salient rotor pole causes significant turbulence in the air gap, which is beneficial for heat transfer. On the other hand, the turbulence causes higher dragging force and makes the windage loss high. The discussion on the windage loss of FSPM machine is shown in Chapter 5, where rotor shrouds are added to the end

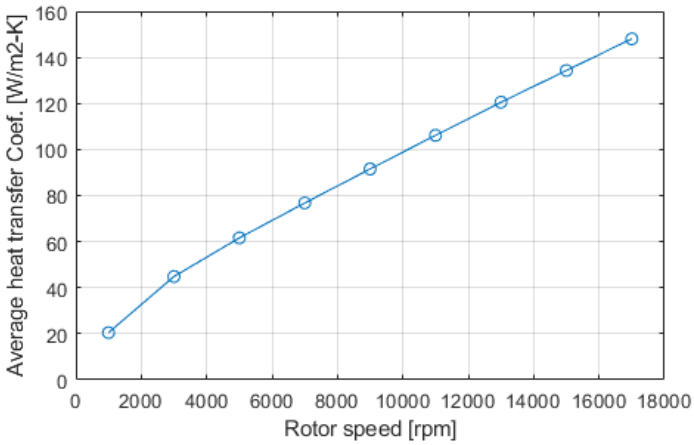

Figure 4.2-5. Rotor surface average heat transfer coefficient at different rotation speed

of the rotor to reduce the axial air flow. Trade-off are made between the windage loss and the rotor heat dissipation.

The average heat transfer coefficient is calculated for a series of velocities from 1000 rpm to 17000 rpm. The average heat transfer coefficient versus rotation speed is given in Figure 4.2-5. As can be seen, the heat transfer coefficient increases as the rotation speed goes up. Note that for the DLCW and SLTW 6/4 FSPM machine, the rotor structures are identical. Therefore, the results here are applicable to both machines. In the thermal analysis in the following part, the rotor speed is chosen to be 4800 rpm.

C. Winding Equivalent Thermal Resistance Model

The winding is an important component in the thermal analysis as it is usually the hot spot inside the motor. The thermal modeling of the winding is more complicated than the stator and rotor. The winding volume is made up of multiple turns, and is a composite of insulation material, conductor, and air. In the literature, researchers use empirical correlation equations [155], or model the winding by breaking it into several layers of copper and insulation [156]. Depends on the slot filling factor and insulating material, the in-slot thermal conductivity varies in a large range. Since

(a) (b)

Figure 4.2-6. Equivalent stator slot model for heat transfer from winding to stator
(a) Real slot occupation (b) Equivalent slot model.

the thermal resistance of the copper and the insulation layer are in series, s simple way of modeling the thermal behavior within the stator slot is to group the components into two parts, i.e. copper and insulation layer [157], as shown in Figure 4.2-6. Certainly, this method cannot predict the detailed temperature distribution inside the stator slot. But it can easily estimate the highest temperature of the winding, which is the most important information. The thickness of the insulation layer can be calculated from the circumference length of the inner slot and the area of insulation material by (Equation 4-7).

$$d_{insul} = \frac{S_{slot}(1-k_{fill})}{L_{slot}} \qquad \text{(Equation 4-7)}$$

With the single insulation layer model, two thermal resistances, for the heat transfer in copper and insulation layer respectively, are used to estimate the highest temperature of the winding. The winding of the machine under study is made up of 8 strands of AWG #22 wire, which has a diameter of 0.644 mm. The copper area inside one stator slot can then be calculated based on the known slot area and the slot filling factor. A slot liner is usually used in electric machine and just adds one more thermal resistance next to the equivalent insulation layer. The slot liner (Nomex 410) has a thickness of 0.18 mm and 0.12 W/m-K thermal conductivity. As

mentioned previously, to facilitate the heat transfer, the windings of the two machines are encapsulated with two different materials. The total thermal resistance between the winding and the stator iron is the sum of the resistance from the encapsulation material and the slot liner, assuming no air is left in the stator slot volume. The thermal resistances associated with the stator slot and winding for the two machines are given in Figure 4.2-2.

D. Contact Resistance Between Surfaces

Due to the manufacturing tolerance and the roughness of the material surface, the interface between two adjacent parts cannot be perfectly flat, as shown in Figure 4.2-7 [158]. The small gaps between the two surfaces impede the heat transfer and this effect can be modelled by the contact thermal resistance. The geometry of the gaps is usually irregular and is hard or impossible to know precisely. One method to model the contact thermal resistance is using an equivalent air gap, which is usually derived from experimental testing and empirical equations. The manufacturing process and material types significantly affect the length of the equivalent gap. Applying pressure to the assembly or using a tight tolerance will help to reduce the equivalent gap between two parts and enhance the heat transfer. In this paper, no special pressurized assembly is used. Therefore, the equivalent gap distances used to calculate the contact

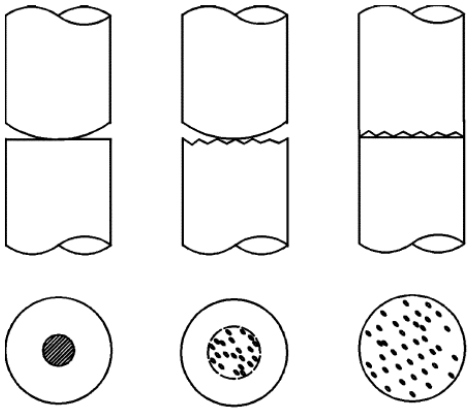

Figure 4.2-7. Different types of interface gap [157]

TABLE 4-6. EQUIVALENT INTERFACE GAPS FOR CONTACT THERMAL RESISTANCE

Contact interface	Gap (mm)
Housing-Stator	0.074
Stator-Magnet	0.048
Shaft-Rotor	0.074

thermal resistance are from reference [159], and the numbers are shown in TABLE 4-6. The associated thermal resistance are given in TABLE 4-7 and TABLE 4-8, respectively.

TABLE 4-7. THERMAL RESISTANCES FOR THE DLCW MACHINE WITH M1 ENCAPSULATION

Description	Resistance Type	Symbol	(K/W)
water jacket and water	Convection	Rwj_water	0.004
stator core 1 and water jacket	Contact	Rs1_wj	0.152
inner part of stator core 1	Conduction	Rs1_o	0.007
outer part of stator core 1	Conduction	Rs1_i	0.007
winding to stator core 1	Conduction	Rs1_w	0.381
stator core 2 and water jacket	Contact	Rs2_wj	0.295
outer part of stator core 2	Conduction	Rs2_o	0.071
inner part of stator core 2	Conduction	Rs2_i	0.071
stator core 2 and magnet	Contact	Rs2_m_o	0.116
stator core 2 and magnet	Contact	Rs2_m_i	0.116
winding to stator core 2	Conduction	Rs2_w	0.514
stator core 2 and air gap	Convection	Rs2_g	4.051
stator core 1 and core 2	Conduction	Rs1_s2	0.041
outer part of magnet	Conduction	Rm_o	0.518
inner part of magnet	Conduction	Rm_i	0.518
magnet to water jacket	Conduction	Rm_wj	23.15
inside to surface of end winding	Conduction	Rins	0.819
ending winding and air gap	Convection	Rins_g	6.883
rotor surface and air gap	Convection	Rr_g	0.715
outer part of rotor core	Conduction	Rr_o	0.011
inner part of rotor core	Conduction	Rr_i	0.019
rotor core and shaft	Contact	Rr_sh	0.517
shaft and ambient	Convection	Rsh_am	8.841
end cap and ambient	Convection	Rec_a	2.964
end cap and air gap	Convection	Rec_g	3.767

TABLE 4-8. THERMAL RESISTANCES FOR THE SLTW MACHINE WITH M2 ENCAPSULATION

Description	Resistance Type	Symbol	(K/W)
water jacket and water	Convection	Rwj_water	0.004
stator core 2 and water jacket	Contact	Rs2_wj	0.307
inner part of stator core 2	Conduction	Rs2_o	0.029
outer part of stator core 2	Conduction	Rs2_i	0.029
stator core 1 and core 2	Conduction	Rs1_s2	0.041
stator core 2 and magnet	Contact	Rs2_m_o	0.116
stator core 2 and magnet	Contact	Rs2_m_i	0.116
stator core 2 and air gap	Convection	Rs2_g	2.327
outer part of magnet	Conduction	Rm_o	0.582
inner part of magnet	Conduction	Rm_i	0.582
magnet to water jacket	Conduction	Rm_wj	26.04
inside to surface of end winding	Conduction	Rins	0.145
ending winding and air gap	Convection	Rins_g	6.883
winding 1 to stator core 1	Conduction	Rw1_s1	0.038
winding 1 to water jacket	Conduction	Rwj_w1	0.038
winding 2 to stator core 1	Conduction	Rw2_s1	0.077
winding 2 to stator core 2	Conduction	Rw2_s2	0.040
rotor surface and air gap	Convection	Rr_g	0.715
outer part of rotor core	Conduction	Rr_o	0.011
inner part of rotor core	Conduction	Rr_i	0.019
rotor core and shaft	Contact	Rr_sh	0.517
shaft and ambient	Convection	Rsh_am	8.841
end cap and ambient	Convection	Rec_a	2.964
end cap and air gap	Convection	Rec_g	3.767

E. Machine losses characterization

The heat sources shown in the thermal network model are associated with the losses in the machine. The accuracy of loss estimation strongly influences the temperature estimation. In this part, the machine iron loss, magnet loss and housing loss are from the electromagnetic FEA simulation shown in Chapter 3. The copper loss is from the analytical calculation shown in Chapter 2. The machine losses associated with different levels of current densities are shown in Figure 4.2-8. Note that the machine losses and performance are temperature dependent. A two-way

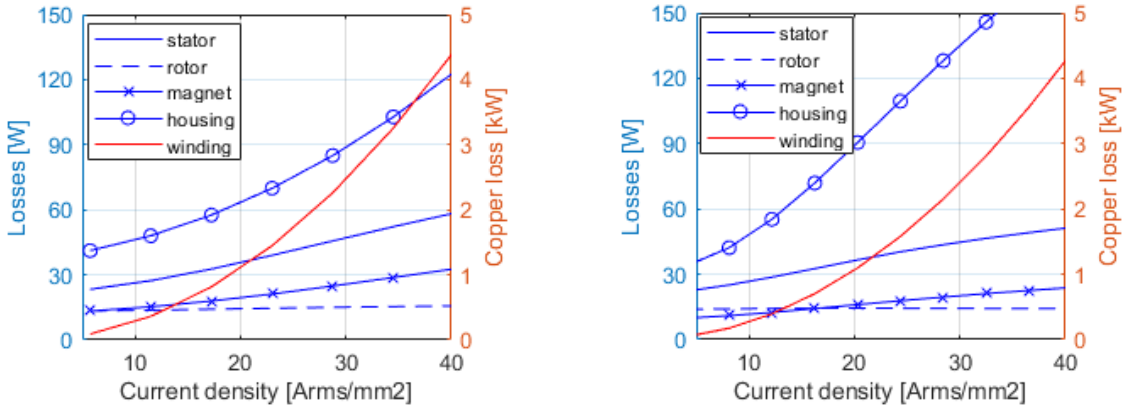

Figure 4.2-8. Loss segregation as a function of current density for (a) Circumferential winding machine and (b) Toroidal winding machine.

coupled FEA simulation is needed to take this into consideration, which requires tremendous computation time. The most temperature sensitive loss would be the copper loss, since the winding resistance is strongly temperature dependent, as shown in (Equation 4-8). where $R_{s,ref}$ is the

$$R_s = R_{s,ref}[1 + \alpha_{Cu}(T - T_{ref})] \qquad \text{(Equation 4-8)}$$

winding resistance (Ω) at the reference temperature T_{ref} (°C), α_{Cu} is the temperature coefficient of the resistivity ($°C^{-1}$) of copper. The iteration shown in Figure 4.2-9 is used to ensure that the temperature dependent resistance is accounted for correctly in the modelling. The copper losses

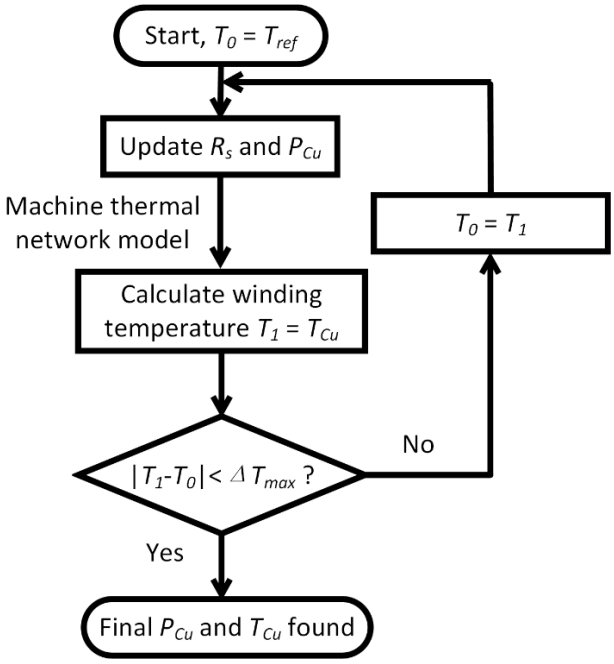

Figure 4.2-9. Flow chart for determining temperature dependent copper loss.

shown in Figure 4.2-8 correspond to a reference winding temperature of 100 ºC and are used as the initial temperature in the iteration process. However, in the rest of this paper the temperature-dependent copper loss is used.

4.2.3. Thermal performance evaluation for 6/4 FSPM machine

With the LPTN model, the thermal performance of the dual-stator 6/4 FSPM machine can be evaluated. Based on the winding topology and the choice of encapsulation material, four comparison cases are modelled, i.e. concentrated winding with encapsulation material 1 (CW-M1), concentrated winding with encapsulation material 2 (CW-M2), toroidal winding with encapsulation material 1 (TW-M1), and toroidal winding with encapsulation material 2 (TW-M2). The thermal models for the four cases are developed in the previous section. It is intuitive that the motors using higher thermal conductivity encapsulation material should have better thermal

performance, and the toroidal winding topology should have a lower temperature. This section will quantify the thermal performance difference and illustrate which modification brings more impact to the machine's thermal performance.

A. Current density limit with fixed coolant flow

Water jacket is used as the cooling method for the four design cases. In this part, the flow rate of the coolant is kept constant, which means the thermal resistance of the water jacket is kept the same. The temperatures of the armature winding, permanent magnet, stator core, and rotor core of the four designs are estimated with the thermal models at different current density levels. The temperature variations of each component as a function of the current density are shown in Figure 4.2-10. Note that because the magnets are tightly sandwiched between two stator cores, the stator temperature is very close to the magnet temperature and their temperatures are shown in the same plot. As can be seen in Figure 4.2-10 (a), regardless of the winding topologies, the machines with M2 encapsulation material has a significantly lower temperature than the machine with M1 encapsulation. For machines with the same encapsulation material, the use of toroidal winding topology leads to a lower temperature than the circumferential winding, because the outer winding is very close to the heat sink.

The choice of encapsulation material does not significantly influence the stator/magnet temperature for the circumferential winding topology because the stator core is directly attached to the heat sink. However, for the toroidal winding topology, as can be seen in Figure 4.2-10 (b), the encapsulation material makes a significant difference. The design with M1 encapsulation has a high stator/magnet temperature because the contact area between the stator and the water jacket is limited. The heat from the stator and magnet needs to travel through the slot area. Therefore, encapsulation material with high thermal conductivity is preferred in toroidal winding topology.

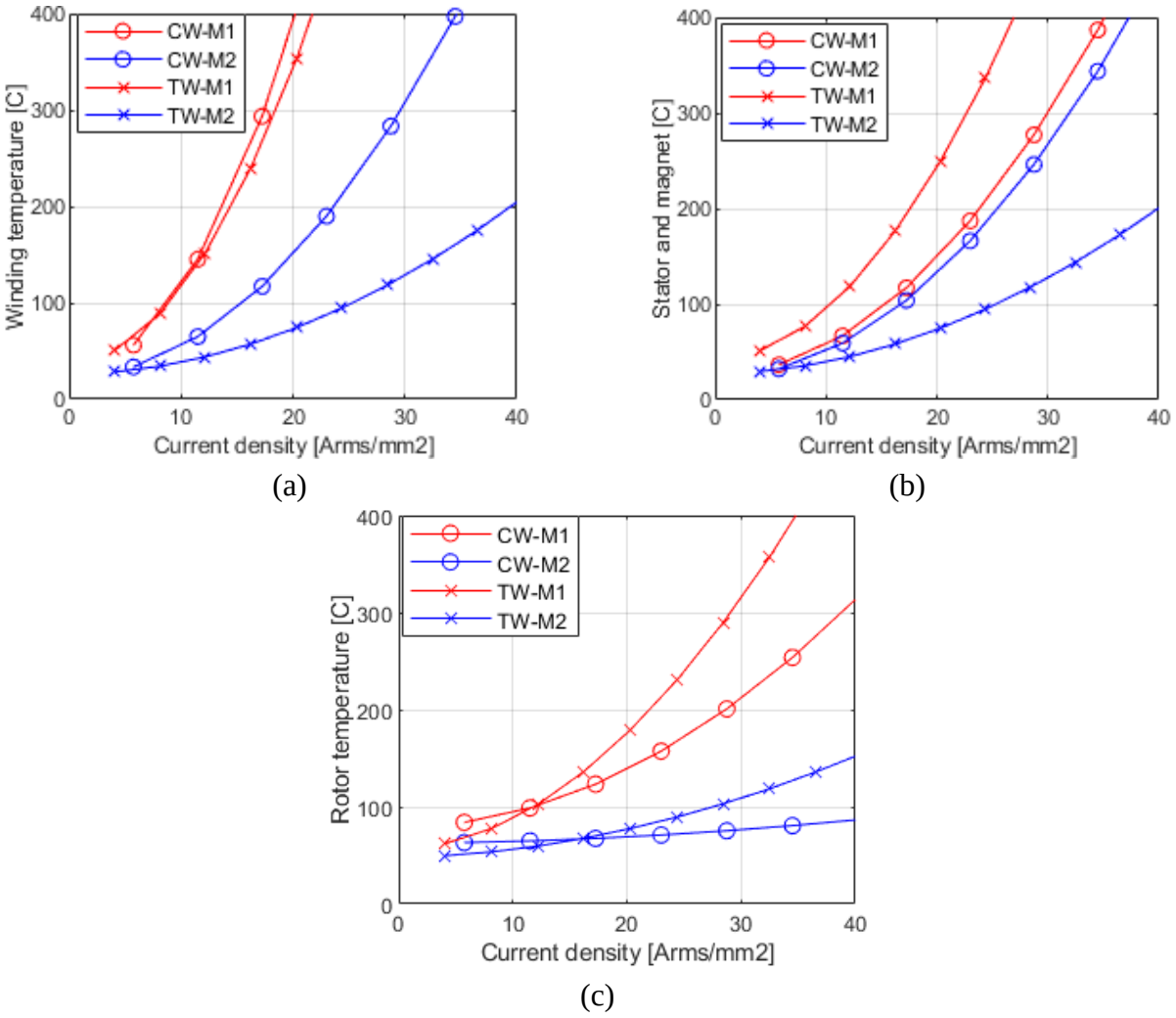

Figure 4.2-10. Dual-stator 6/4 FSPM machines temperatures versus stator slot current density at (a) Stator winding (b) Stator and magnet (c) Rotor

The rotor temperatures for machines with M2 encapsulation is lower than M1 encapsulation because of the more effective heat transfer to the water jacket. As shown in Figure 4.2-10 (c), below 20 Arms/mm^2, the rotor temperatures for CW and TW topologies are similar because there is no direct contact between the stator assembly and the rotor.

The temperature limit in the electrical machine is determined by the class of winding insulation and the grade of the permanent magnet. Taking an example of Class H winding insulation (180 °C continuous) and Type H NdFeB magnet (120 °C continuous), the corresponding

current density limit of each machine component can be found. Note that the machine component with the lowest current density limit determines the overall machine limit. The current density limit of the CW-M1 design is 11.5 Arms/mm^2, which is almost at the lower bound of the typical current density range for liquid-cooled machine [160]. The current density limit of the CW machine could be improved to 20 Arms/mm^2 with M2 encapsulation material, and the limiting factor changes to the magnet temperature. The TW-M1 machine is limited at 12 Arms/mm^2 due to the insufficient magnet cooling. The TW machine current density limit can be significantly improved to 30 Arms/mm^2 with M2 encapsulation.

B. Temperature limit with high coolant flow rate and thermal conductivity encapsulation

The cooling capability of the water jacket depends on the coolant flow characteristics in the channel. As shown in Section for water jacket design, a high flow rate leads to a high heat transfer coefficient. However, significant pumping power might be required to push the coolant to a high velocity and compromise the system efficiency. The current density limits based on the constant fluid flow and fixed temperature limits derived in the previous part could be further generalized by varying the coolant flow rate and parameterizing the thermal conductivity of the encapsulation

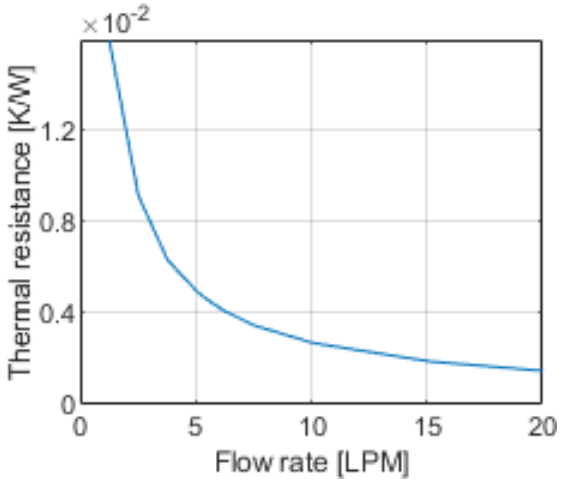

Figure 4.2-11. Thermal resistance of the water jacket as a function of coolant flow rate.

material. As it is known, the convective heat transfer coefficient increases almost linearly with the flow rate. (Equation 4-5) shows that the convective thermal resistance is proportional to the inverse of the heat transfer coefficient, which indicates that the thermal resistance has a hyperbolic relation versus the flow rate, as can be seen in Figure 4.2-11. Therefore, having a very high coolant flow rate will not provide much benefit in the cooling performance, but will consume a large amount of pumping power.

The extreme case of using a high flow rate would be there is no temperature increase from the inlet to the outlet of the coolant channel, and the water jacket temperature equals the coolant temperature, i.e. R_{wj_water} in the thermal network equals 0 K/W. In this case, the machine thermal performance depends mainly on the conductivity of the encapsulation material. With the same winding and magnet temperature limits mentioned previously, the current density limits correspond to different thermal conductivities of the encapsulation material are shown in Figure 4.2-12. Note that Figure 4.2-12 only considers the thermal constraints of the motor and assumes an infinite coolant flow rate. It serves to give the reader an idea of how the thermal conductivity of the encapsulation material affects the thermal performance of the machine. The actual

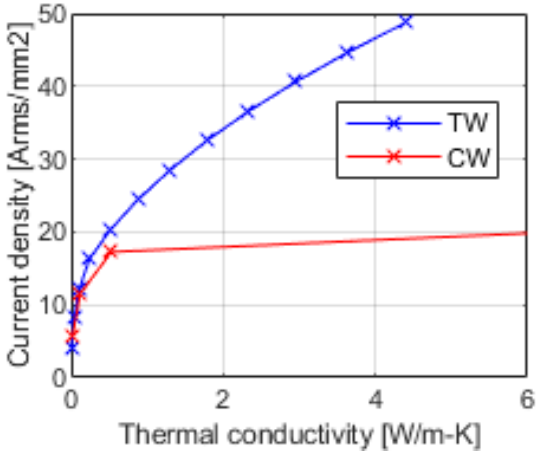

Figure 4.2-12. Current density limit of the machines with different encapsulation thermal conductivities

achievable current density depends on lots of other factors such as the machine topology, the cooling technology used, the saturation of the core material, etc. As can be seen in Figure 4.2-12, the TW topology benefits more from the improvement of encapsulation material since the encapsulation and insulation layers are the only thermal resistance between the winding and the water jacket. With the development of encapsulation material, the x-axis range of Figure 4.2-12 could certainly be extended.

C. Thermal performance with natural convection cooling

As shown in part A of this section, with water jacket cooling, the current density limit of the TW-M2 design is 30 Arms/mm^2. Such high current density is not always required for conventional application. Considering the current density at rated condition is around 10 Arms/mm^2, the 30 Arms/mm^2 capability seems to be overwhelming. Water jacket cooling is a type of active cooling, which require extra pumping power to circulate the coolant. The water jacket and the associated pump add the cost and complexity of the system. Therefore, passive cooling with natural air convection is usually used for low-cost application. Since the TW-M2 design has the best thermal

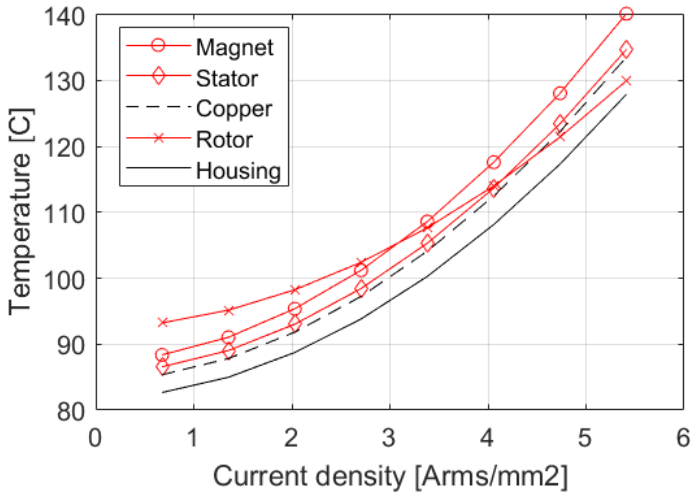

Figure 4.2-13. Component temperature of SLTW 6/4 FSPM machine with M2 encapsulation and natural convection cooling

performance among the four designs, it is used to evaluate the thermal performance of the 6/4 FSPM machine with natural convection cooling.

By replacing the heat transfer coefficient for the water jacket with the natural air convection coefficient, the LPTN model for the TW-M2 design with natural cooling is ready to use. Following the same procedure as presented in part A, the temperatures of each machine component are shown in Figure 4.2-13. Because of the stator mounted permanent magnet, the eddy current loss in the permanent magnet exists even at low load condition. If the machine only has passive cooling, the current density is limited to around 4 Arms/mm^2 for steady state operation.

4.3. Machine transient thermal behavior

Overloading capability is appreciated in many applications such as electric vehicle. The overloading performance is usually limited by the machine thermal constraint. In electric machines, different components are made of different materials and have different thermal conductivity and thermal capacity. During overloading operation, the copper loss could be several times higher than during rated operation. It is necessary to ensure the temperature of each machine component is below the limit. Thermal capacitance is needed in the LPTN model, however, due to the complexity of the machine geometry, accurate modelling of the thermal capacitance is difficult. Therefore, thermal finite element analysis (FEA) is used to study the transient thermal behavior.

4.3.1. Thermal finite element analysis

A. Thermal FEA modeling

The thermal FEA is similar to the electromagnetic FEA, where the geometry of the machine is drawn and imported to the FEA solver. By using the 3D structure, the FEA can consider the heat transfer in the axial and planar direction, which provides a more accurate result. In addition, the FEA simulation is able to couple the electromagnetic simulation with the thermal simulation.

Losses from each part of the machine could be accurately assigned to the elements in the simulation. However, FEA simulation is more time consuming compared to solving a thermal network, because of the large number of elements in the model.

After importing the machine geometry into the FEA solver, component materials and thermal conditions need to be assigned properly. The thermal properties of the materials used in the 6/4 FSPM machine are shown in TABLE 4-5. Note that the anisotropic thermal conductively of the lamination need to be entered by defining the first and second axis direction. In addition, the heat transfer in the winding is also anisotropic because of the non-unity slot filling factor. The direction of the windings must be specified (defined as the first direction) as shown in Figure 4.3-1.

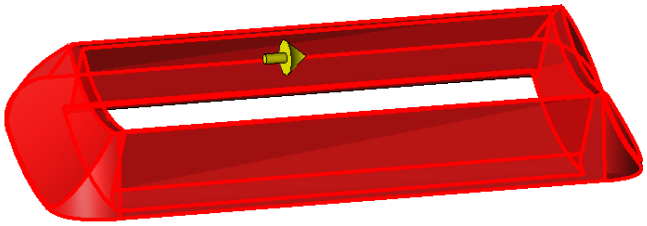

Figure 4.3-1. Defining current flow direction in coils

Heat can flow more easily in the first direction compared to the second direction. The thermal conductivity of the first axis can be calculated as $k_{Cu}k_{fill}$, where k_{Cu} is the thermal conductivity of copper and k_{fill} is the slot filling factor. The thermal conductivity of the second axis is dependent on the property of the encapsulation material and can be calculated with (Equation 4-3) and (Equation 4-7).

The thermal conditions include the heat sources and heat transfer models for the boundaries. The heat transfer within one solid body is conduction heat transfer and can be accurately simulated giving a fine enough mesh. As mentioned previously, the heat sources are the loss information from the electromagnetic simulation. The most accurate two-coupling is not used for the sake of

time saving. The copper loss is calibrated with temperature variation, as shown in the previous section. The boundary conditions include the convective heat transfer and the contact thermal resistance. The convective heat transfer condition is defined for solid-fluid interface such as the rotor surface, stator surface, and water jacket wall. Similar to the LPTN model, the convective heat transfer in thermal FEA is also characterized by the heat transfer coefficient from CFD simulation. The contact thermal resistance is the same as in the LPTN. For two components adjacent to each other, if the contact thermal condition is not set, the heat transfer is considered perfect and no temperature gradient exists between the two surfaces, which is usually not true.

As mentioned above, thermal FEA explicitly models the details associated with conduction heat transfer, the convective coefficient must be assigned for each surface between solid and fluid. The convective heat transfer is linked with the machine solid model through the simulation circuit, as shown in Figure 4.3-2. In addition, the mechanical loss is cannot be simulation in electromagnetic FEA and is mapped into the thermal simulation with thermal circuit. Parts that are not drawn in the 3D structure such as the shaft, housing end cap also need to be represented by

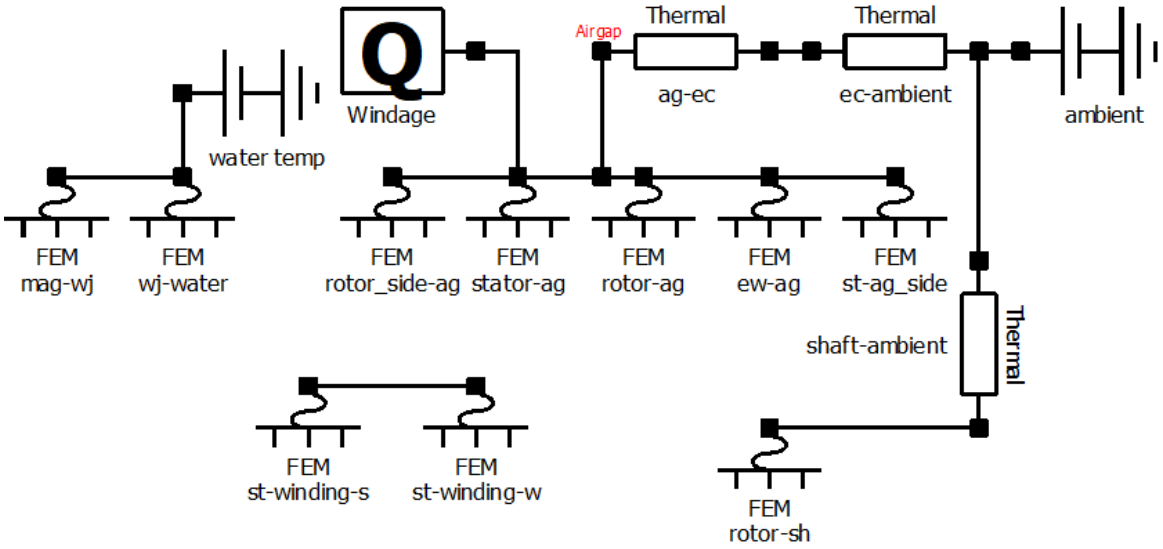

Figure 4.3-2. Thermal circuit in FEA tool

equivalent thermal boundary conditions. The ambient temperature is set to 23 °C which is measured in the testing room.

B. Result comparison between FEA and LPTN

In order to verify the consistency of the thermal FEA simulation and the LPTN model, the steady state thermal performance is first compared with the DLCW 6/4 FSPM machine at rated condition. The machine losses and thermal parameters are given in the previous part and are not repeated here.

The temperature distribution contour plots for each part of the machine are shown in Figure 4.3-3, which gives a more clear and straight forward information about the thermal behavior of the machine than the LPTN model. The average temperatures for each part of the machine are

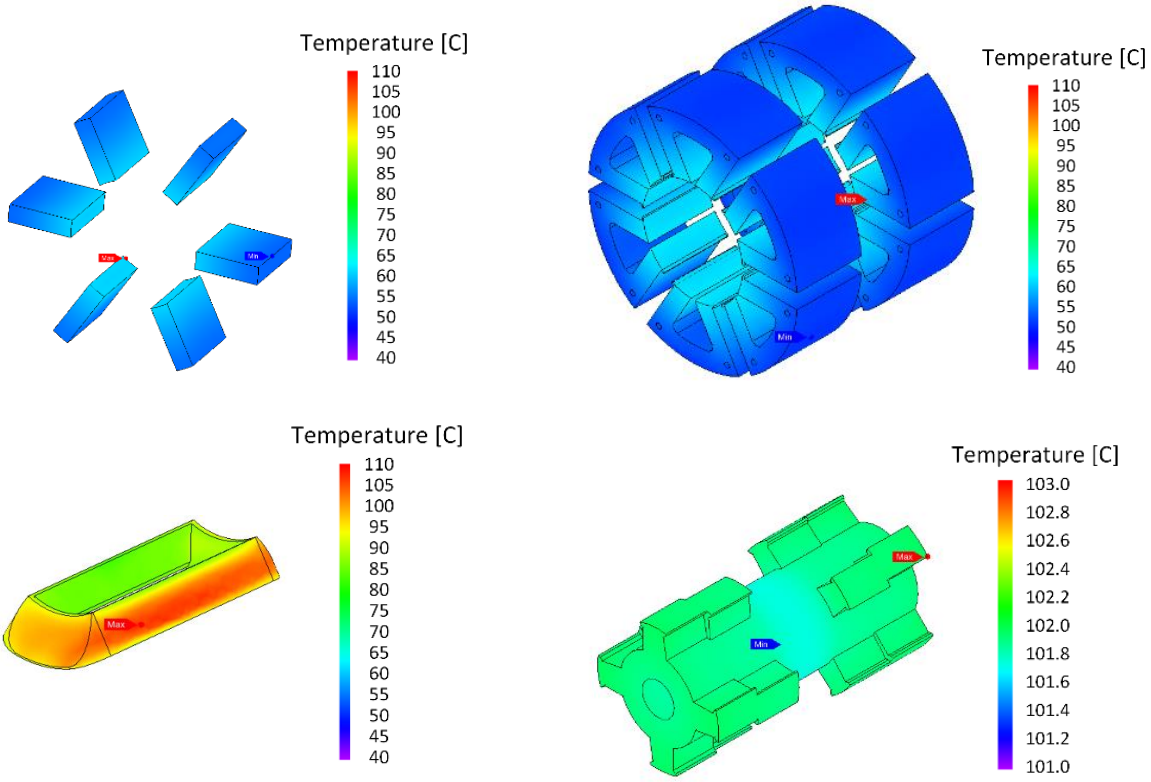

Figure 4.3-3. Temperature distribution of dual-stator 6/4 FSPM machine at 4800 rpm from FEA simulation.

TABLE 4-9. TEMPERATURE OF 6/4 FSPM MACHINE COMPONENTS FROM FEA SIMULATION AND LPTN MODEL

Node	LPTN (°C)	FEA (°C)
Stator	56.6	58.7 (+3.6%)
Magnet	56.3	56.0 (-0.5%)
Winding	115.1	105.0 (-8.8%)
Rotor	103.2	102.1 (-1.1%)

summarized in TABLE 4-9, together with the results from LPTN. Since the thermal FEA simulation and the LPTN model share many parameters in common such as the material properties and the convective heat transfer coefficient, it is not surprising that the results from the two methods match well. The temperature calculated by LPTN agrees with FEA simulation results within 10%.

4.3.2. 6/4 FSPM machine transient thermal behavior

In order to simulate the transient thermal behavior, the thermal capacitances of the machine materials need to be included and are shown in TABLE 4-10. The thermal capacitances for the two windings with different encapsulation materials are the same because the thermal capacitance of the copper is much larger than the encapsulation material. The transient thermal behavior of the two machines are studied for overloading conditions up to 2.0 p.u. armature current at 4800 rpm.

TABLE 4-10. 6/4 FSPM MACHINE PARAMETERS AND MATERIAL PROPERTIES

Parameters	DLCW	SLTW
Permanent magnet	k_{mag} = 8.9 W/m-K C_p = 502 J/kg-K	
Water jacket material	Aluminium, k_{alu} = 205 W/m-K, C_p = 900 J/kg-K	
Lamination steel	Arnon 5, thickness = 0.127mm k_{ax} = 0.7 W/m-K, k_{pl} = 22.4 W/m-K, C_p = 491 J/kg-K	
Winding/Encapsulation	C_p = 180 J/kg-K k_1 = 114 W/m-K, k_2 = 0.2	C_p = 180 J/kg-K k_1 = 115 W/m-K, k_2 = 2.3

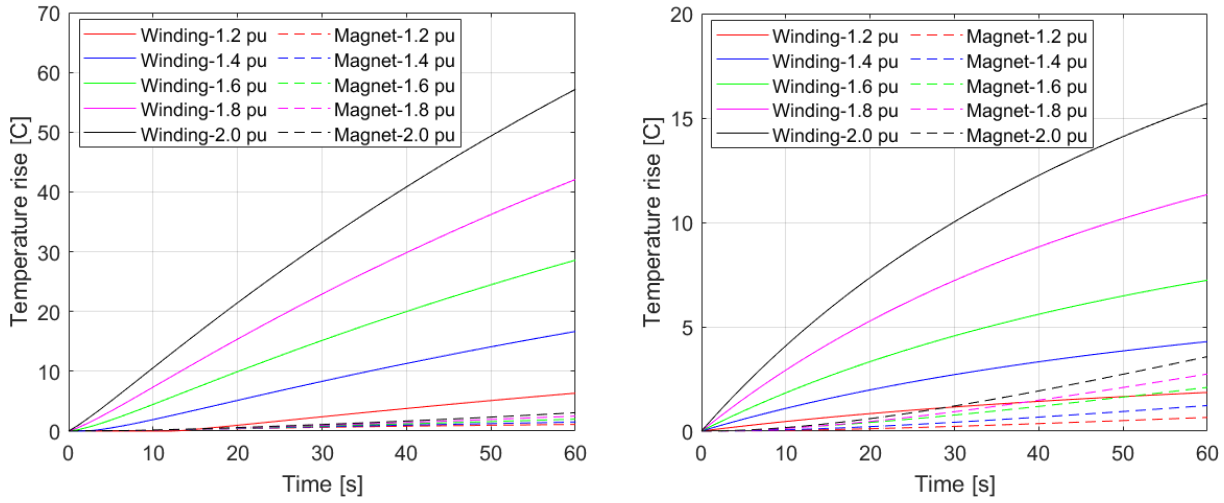

Figure 4.3-4. Transient temperature rises during overloading operations for (a) DLCW 6/4 FSPM machine with M1 encapsulation and (b) SLTW 6/4 FSPM machine with M2 encapsulation.

The increase of armature current not only affects the winding copper loss, but also has impact on the stator/rotor iron loss, magnet loss, and housing loss. The losses variation at different loading conditions can be found in Figure 4.2-8.

The thermal steady state at rated armature current (1.0 p.u.) is first reached, and the steady state temperatures for each component are assigned as the initial temperatures in the overloading simulation. The overloading losses for each part are given and the transient thermal simulations are run for 60 seconds. The temperatures of the winding and the magnet are the most critical ones since the temperature limits of the winding insulation and the permanent magnet are the thermal constraints of the machine.

The transient temperature rises of the winding and magnet for the two machines during overloading operation up to 2.0 p.u. armature current are shown in Figure 4.3-4 (a) and Figure 4.3-4 (b), respectively. As can be seen, the increase of the machine loading has a much faster impact on the winding temperature than on the magnet temperature. Especially for the case of the DLCW 6/4 FSPM machine, where the winding does not have close contact with the water jacket,

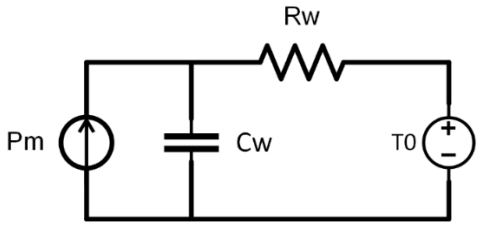

Figure 4.3-5. Thermal network for short-time transient overloading

the temperature rise for the winding is 10 times faster than that for the magnet. For the SLTW 6/4 FSPM machine, the winding temperature rise is about 5 times faster over the 60 second period. Therefore, for short-time transient thermal analysis, the machine thermal behavior can be approximated by a first-order system as shown in Figure 4.3-5, where *Pm* is the additional machine loss (mostly winding copper loss) at overloading condition with respect to the rated condition. While the magnet temperature rise can be neglected during the short-time transient, the winding temperature rise ΔT (°C) can be approximately calculated with (Equation 4-9), where ΔT_{final} is the

$$\Delta T(t) = \Delta T_{final}(1 - e^{-t/\tau_w}) \quad \text{(Equation 4-9)}$$

$$\tau_w = R_w C_w \quad \text{(Equation 4-10)}$$

final temperature rise with specific overloading current after a sufficient long time. The thermal time constant τ_w (second) can be derived as (Equation 4-10), where R_w and C_w are the thermal resistance and thermal capacitance of the winding, respectively.

Taking the DLCW 6/4 FSPM machine with a 2.0 p.u overloading as an example, the temperature rise during the short-time transient is simulated with the thermal FEA model. The temperature rises and the governing first-order equation is shown in Figure 4.3-6. As can be seen, the temperature rise of the stator winding is much faster than the other components of the machine.

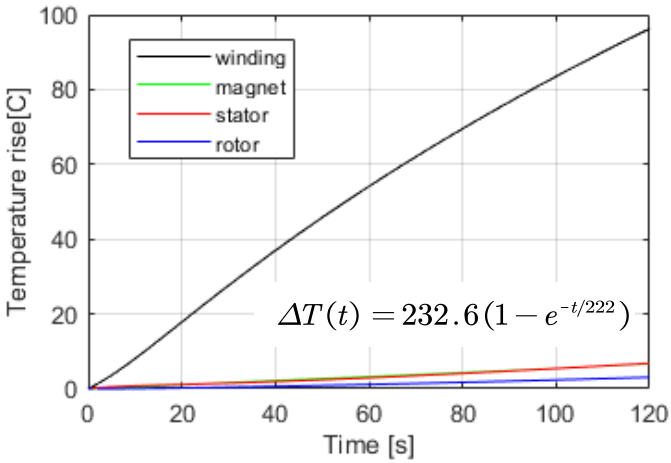

Figure 4.3-6. Winding temperature variation with first-order approximation

Transient thermal experiments have been conducted to verify the thermal FEA simulation as well as the first-order approximation. The time constant of the winding temperature rise is 222 seconds, which is approximately 4 minutes.

4.4. Summary

This chapter first presents the cooling design of the dual-stator 6/4 FSPM machine. Because the majority of the heat sources such as the armature winding, stator core, and permanent magnet are in the stator, water jacket is an appropriate choice to cool the FSPM machine. Two types of water jacket, with spiral channel water jacket and axial channel water jacket, are investigated and compared. It is shown that the spiral channel water jacket has lower turbulence and less pressure drop compared to the axial channel water jacket. Therefore, spiral channel water jacket requires less pumping power for the same coolant flow rate. However, axial channel water jacket has the benefit of a more flexible design. Without influencing the fluid characteristics, the location of the inlet/outlet of the channel can be easily modified.

Having the temperature-sensitive permanent magnet in the stator assembly, the thermal analysis of the FSPM machine need to be carefully investigated. For steady state thermal analysis, lumped-parameter thermal network (LPTN) is chosen for its fast computation. The LPTN model

for the both DLCW and SLTW 6/4 FSPM machines are established. In addition to the different winding topologies, two different types of winding encapsulation materials are considered, and their impact on the thermal performance are investigated. It is shown that the SLTW 6/4 FSPM machine with advanced encapsulation material can achieve three times higher current density than the DLCW 6/4 FSPM machine with conventional encapsulation.

The transient thermal performance of the 6/4 FSPM machine under overloading condition is investigated with thermal finite element analysis (FEA). It is shown that the winding temperature reacts 5-10 times faster than the other machine component and can be approximated with a first-order equation.

Chapter 5 Special Design Consideration in FSPM Machine

Unlike the interior permanent magnet (IPM) and surface permanent magnet (SPM) machines that have been widely used in the practice, flux-switching permanent machine (FSPM) machine has not been commonly seen in the industry and commercialized product, despite the fact that FSPM machine possesses many benefits such as robust rotor structure and easy thermal management. This is because FSPM machine has certain disadvantages that prevent it from commercialization. Disadvantages of FSPM machine include high torque ripple and the vibration/noise issue comes with it, high fundamental frequency due to the large pole pair number, housing loss because of the stator mounted permanent magnets, and high windage loss due to the salient rotor structure. Having the aforementioned issues solved is important and inevitable for using FSPM machines in real world applications.

As presented in the first and second chapter, the high fundamental frequency issue could be alleviated by using low pole FSPM topology, i.e. dual-stator 6/4 FSPM machine. It is shown that the dual-stator 6/4 FSPM machine can reduce the fundamental frequency by 60% compared to the most commonly seen 12/10 structure under the same speed. The fundamental frequency reduction brings a significant decrease in the iron loss. The torque ripple issue for FSPM machine has been addressed in many research papers [32], [115], [161], [162], which involve machine geometry modification such as rotor tooth shaping and rotor skewing as well as different control strategy such as harmonics injection. Torque ripple reduction for dual-stator 6/4 FSPM machine with step skewed rotor has been investigated in [115]. With a two-step skewed rotor of 5° span angle, the torque ripple could be reduced by 62% while maintaining 98% of the average torque.

This chapter focuses on the investigation of housing loss and the windage friction loss of the 6/4 FSPM machine. Few literatures can be found on the study of the housing loss of FSPM machine, which is a non-negligible aspect especially for high-speed application. Researches on the reduction of windage loss for switch reluctance machine (SRM), which also has salient rotor structure, can be found in the literature [133], [135], [136]. However, the windage loss reduction structure would bring different impact on the electromagnetic performance of FSPM machine. Especially for the dual-stator 6/4 FSPM machine under study, which has a three-part rotor. Therefore, the windage loss characterization is different from SRM and conventional 12/10 FSPM machine and is worth investigating. The objective of this chapter is to investigate the two aforementioned design aspects that have not been investigated enough. The results will contribute to the popularization of FSPM machine into practical use.

5.1. Housing loss

The housing loss of the dual-stator 6/4 FSPM machine has been briefly discussed in Chapter 3, where the housing eddy current circulation is plotted and the housing loss of the single-layer

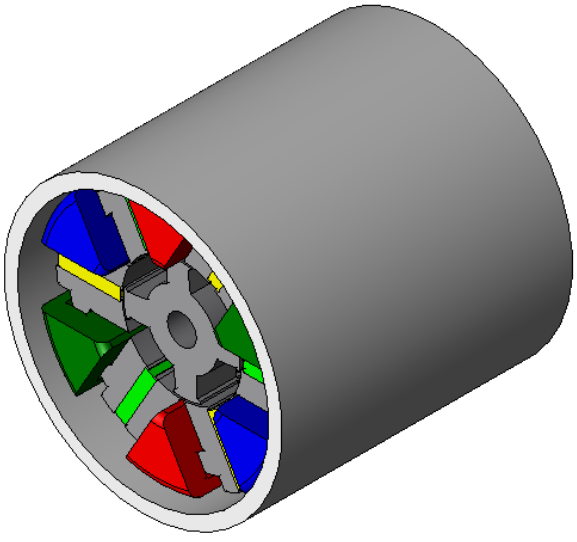

Figure 5.1-1. Geometry of the dual-stator 6/4 FSPM machine with single-layer toroidal winding

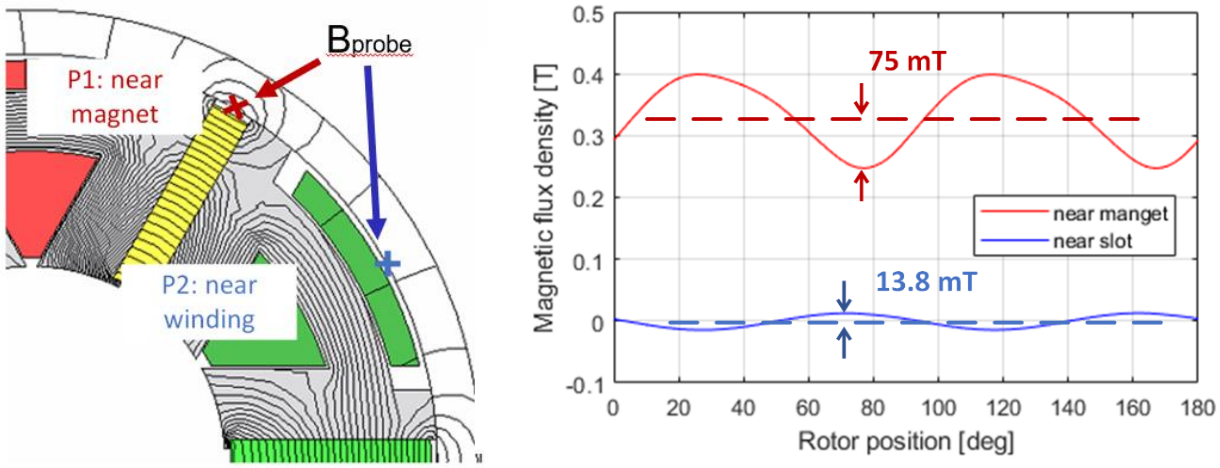

(a) (b)

Figure 5.1-2. (a) Magnetic flux penetration into aluminum housing and the placement of B field probe (b) Magnetic flux density variation near magnet and winding slot

machine and the double layer machine is given. In this chapter, a more detailed study on housing loss and methods to reduce the housing loss is presented. Without the loss of generality, the single-layer toroidal winding machine shown in Figure 5.1-1 is used to study the housing loss. As the returning coil of the toroidal winding is close to the housing, its influence on the housing needs to be studied separately with the magnet.

The machine housing is made of Aluminum, which is a non-magnetic material. However, as can be seen in Figure 5.1-2 (a), although most of the magnetic flux is confined mostly in the stator and rotor iron, there are still a certain amount of leakage magnetic flux as shown. To observe the magnetic flux variation in the housing, two magnetic flux density probes are placed near the magnet and the stator winding slot. The magnetic flux density variation is shown in Figure 5.1-2 (b). As can be seen, the magnetic flux variation near the permanent magnet is about 5.4 times larger than that near the winding slot. The eddy current loss density in conductor can be calculated by (Equation 5-1). According to the previous equation, the eddy current loss due to the stator-

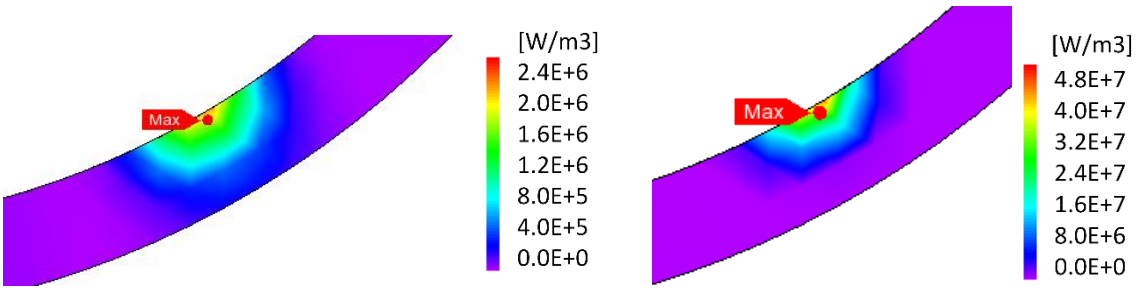

(a) (b)

Figure 5.1-3. Housing eddy current loss density (a) at 1500 rpm (100 Hz) and (b) at 15000 rpm (1000 Hz)

$$p_{ec} = \frac{\pi^2 B_p^2 d_2 f^2}{6\rho_e} \qquad \text{(Equation 5-1)}$$

mounted permanent magnet is about 30 times higher than due to the toroidal winding. Therefore, in this report, the magnet related housing loss is the focus.

From the eddy current loss density given in (Equation 5-1), volume integration is needed to calculate the total housing loss. However, the eddy current loss distribution is non-linear. Therefore, finite element analysis tool is used to estimate the total housing eddy current loss. The eddy current loss density of the 6/4 FSPM machine at 1500 rpm (100 Hz) and 15000 rpm (1000 Hz) are shown, respectively. As can be seen, at lower speed (frequency), the eddy current loss penetration is much deeper than at higher speed (frequency). This is due to the frequency dependent nature of the eddy current, as shown in (Equation 5-2). As a result, with the volume

$$\delta_{penetration} = \sqrt{\frac{\rho}{2\pi f \mu}} \qquad \text{(Equation 5-2)}$$

integration, the housing eddy current loss is not proportional to the square of the frequency. The housing loss of the 6/4 FSPM machine at different speed is shown in Figure 5.1-4.

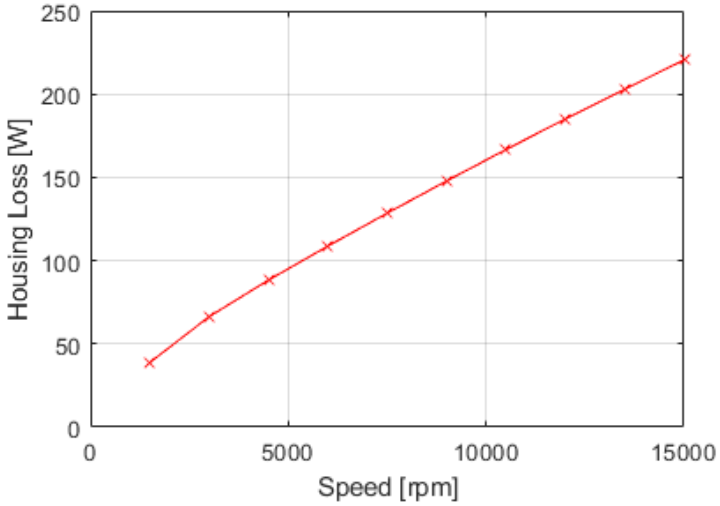

Figure 5.1-4. Housing eddy current loss of 6/4 FSPM machine at different speed

There are two obvious solutions to the housing loss issue: adding iron bridge outside the stator-mounted permanent magnet to shunt the leakage magnetic flux or leave cavities in the housing near the magnet. With the first solution, the leakage flux is shunt by the magnet bridge, as well as the useful magnetic flux. Therefore, trade-off study is needed between the reduction of housing loss and the loss of output power. From the structural perspective, the iron bridge allows the stator iron to use a single piece lamination, which makes the stator tolerance control easier and reduces the stator assembly complexity. The contact surface area between the housing and the stator is also increased, which improves the cooling of the stator. The second solution is straight forward and does not have impact on the electromagnetic performance of the machine. However, the cavities need to be axially grooved into the housing, which introduce extra machining work and increase the manufacturing cost. With the cavities in the housing, the thickness of the housing is no longer uniform, and the contact area is reduced, which could cause mechanical issue when putting the stator into the housing by shrink fit or press fit. In addition, the non-uniform housing thickness brings problem for grooving spiral water jacket channel. To avoid intersecting with the cavities, axially grooved channel can be used as shown in Figure 4.1-2 (b). However, as shown in

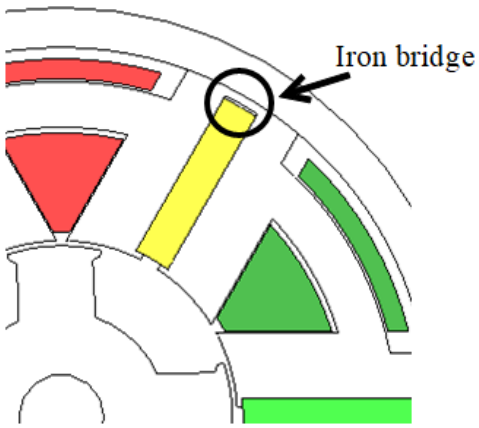

Figure 5.1-5. Magnet iron bridge structure for shunting the flux leakage in the housing

chapter 4, the axially groove channel has higher pressure drop and more flow turbulence than the spiral channel.

5.1.1. Magnet iron bridge

The illustration of the magnet iron bridge is shown in Figure 5.1-5. As the permeability of silicon steel is much larger than the aluminum, the magnetic flux will be shunt by the iron bridge instead of penetrating into the housing. However, as the iron bridge should not be too thick to avoid losing too much magnetic flux that is producing torque, the iron bridge would be heavily saturated. Parametric study on the iron bridge thickness is done to find the optimal thickness for the trade-off between high housing eddy current loss and low output torque. The output torque and housing loss of the machine with different iron bridge is shown in Figure 5.1-6. Note that 1.5 mm is thinnest bridge allowed due to manufacturing concern. As can be seen, with a 3.5 mm iron bridge, although the housing loss is reduced by 40%, the torque is also reduced by 11%. In addition, because of the reduction of magnetic flux density in the tooth and the air gap, the stator and rotor core iron loss and magnet eddy current loss are also reduced. The total improvement of efficiency is 1%. With 1.5 mm iron bridge, the torque is reduced by 4%, and the housing loss is reduced by

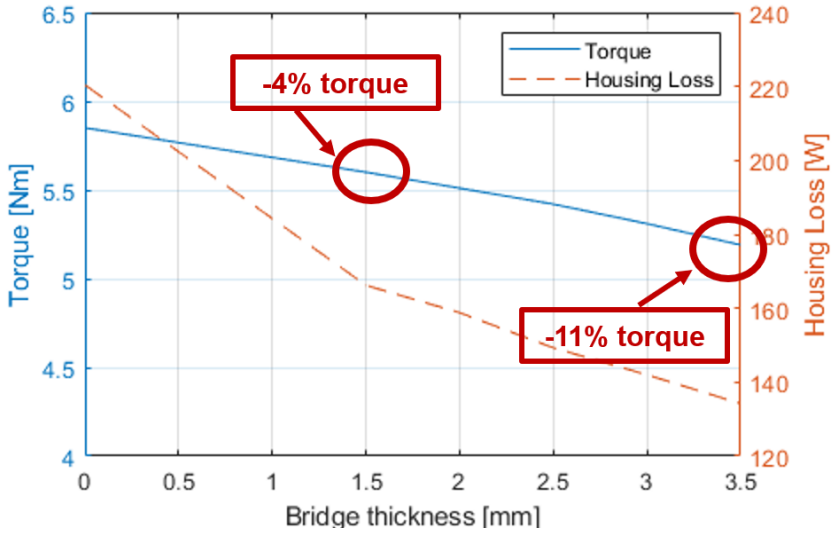

Figure 5.1-6. Housing loss reduction and output torque variation with different magnet iron bridge thickness.

TABLE 5-1. LOSSES AND EFFICIENCIES OF 6/4 FSPM MACHINE WITH DIFFERENT MAGNET IRON BRIDGE THICKNESS

	No bridge	1.5 mm	2 mm	2.5 mm	3 mm	3.5 mm
Torque [Nm]	5.85	5.60	5.51	5.42	5.31	5.19
Output power [kW]	9.19	8.80	8.66	8.51	8.34	8.15
Iron loss [W]	225.4	224.7	207.3	200.5	193.7	186.4
Magnet loss [W]	57.3	54.3	44.6	41.6	38.5	35.6
Copper loss [W]	307.6	307.6	307.6	307.6	307.6	307.6
Housing loss [W]	102.4	76.8 (-25%)	73.8	69.4	66.0	62.4
Efficiency [%]	93.0	93.0	93.2	93.2	93.2	93.2

25%. The losses of each part and the efficiency of 6/4 FSPM machine with different iron bridge thickness is captured in TABLE 5-1.

5.1.2. Housing cavities

As can be seen, the housing eddy current loss is concentrated near the magnet. Therefore, the second way of reducing housing eddy current loss would be removing the lossy volume in the housing, as can be seen in Figure 5.1-7. The benefit of this method is that the output torque will

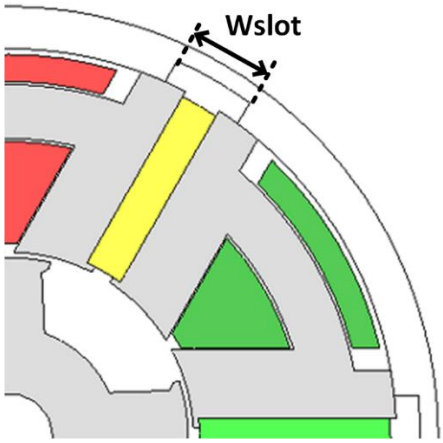

Figure 5.1-7. Cavity in the machine housing near permanent magnet for reducing eddy current loss.

not be affected since the aluminum is non-magnetic material. The width of the slot in the housing is studied as a design parameter. The housing loss and the machine efficiency is plotted against the variation of the slot width, as shown in Figure 5.1-8. As can be seen, the housing loss is significantly reduced by removing the lossy volume in the housing. With larger housing slot, the eddy current loss is reduced slightly. The improvement of the total efficiency is not significant. In

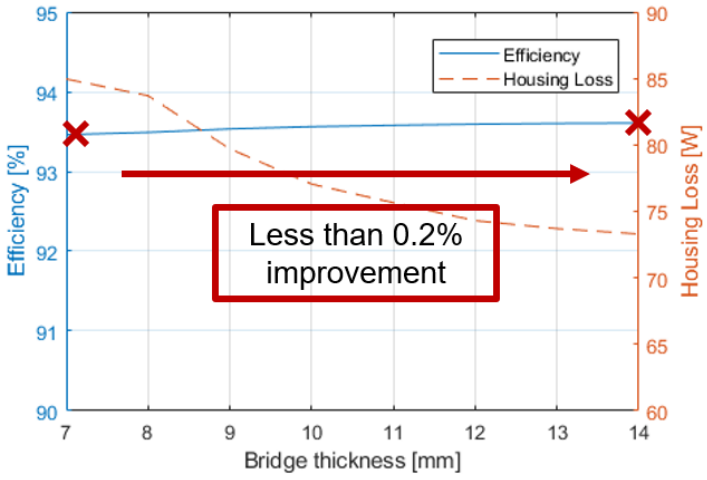

Figure 5.1-8. Housing loss reduction and efficiencies with different housing slot width.

TABLE 5-2. LOSSES AND EFFICIENCIES OF 6/4 FSPM MACHINE WITH OR WITHOUT SLOT NEAR MAGNET IN THE HOUSING

	No slot	With slot
Torque [Nm]	5.85	5.85
Output power [kW]	9.19	9.19
Iron loss [W]	225.4	227.6
Magnet loss [W]	57.3	58.1
Copper loss [W]	307.6	307.6
Housing loss [W]	102.4	41.0
Efficiency [%]	93.0	93.5

addition, if the slot is too large, the contact surface between the housing and the stator core might be too small and cause mechanical issue while shrink fitting. Therefore, 7 mm wide slot is chosen here. The losses of each part of the machine is shown in TABLE 5-2.

5.2. Windage loss

As has been mentioned previously, one of the advantages of FSPM machine is the simple and robust rotor structure because of the absence of permanent magnet in the rotor. The robust rotor is preferable for high-speed application. However, the FSPM machine has a salient rotor pole, which cause more dragging force than round shape rotor due to the addition of axial air flow [132]. The excessive windage loss acts against the high-speed application compared to the surface permanent magnet and interior permanent magnet machine with round shape rotor. It has been shown that the windage loss could be as high as 44% of the total machine loss for high-speed applications [133]. Therefore, the windage loss of FSPM machine needs to be carefully evaluated and windage loss reduction should be applied for high-speed application.

In literature, discussions about the windage loss for salient shape rotor have been carried out for switched reluctance machines (SRM) [135][136] and FSPM machines [163] with conventional 12/10 topology. Several windage loss reduction topologies have been proposed and their influence on the machine performance have been investigated as well. However, the low-pole FSPM

machine investigated in this report has a dual-structure. Therefore, the conclusions for the single stage salient rotor cannot be directly applied. In addition, the influence of the modified rotor structure on the electromagnetic performance also need to be investigated.

5.2.1. Machine sizing and windage loss reduction rotor structure

The machine windage loss becomes non-negligible for high rotor tip speed. The geometry parameters of the machine studied in given in TABLE 5-3. The rotor tip speed of a dual-stator 6/4 FSPM machine with rotor OD of 122 mm running at 15,000 rpm is 96 m/s. Several windage loss reduction rotor structure has been proposed for switch reluctance machine such as ribs between two adjacent rotor poles, shrouds attached to the end of the rotor, or combining both to form a cylindrical shape. The rib introduced between the rotor poles would cause undesired flux leakage, which influences the performance of the motor. The rotor shrouds also influence the magnetic flux distribution. To avoid changes in the electromagnetic performance, non-magnetic composite materials are considered to give the salient rotor a smooth profile [164]. However, the manufacturing process becomes more complicated, and furthermore, retainment and tolerance

TABLE 5-3. DESGIN PARAMETERS OF 70 KW 6/4 FSPM MACHINE

Parameter	Value
Stator OD [mm]	260
Rotor OD [mm]	122
Stack length [mm]	220
Gap between stator [mm]	60
Airgap length [mm]	1
Rotor Pole height [mm]	22
Output power [kW]	70
Top speed [RPM]	15,000
Torque at top speed [Nm]	45

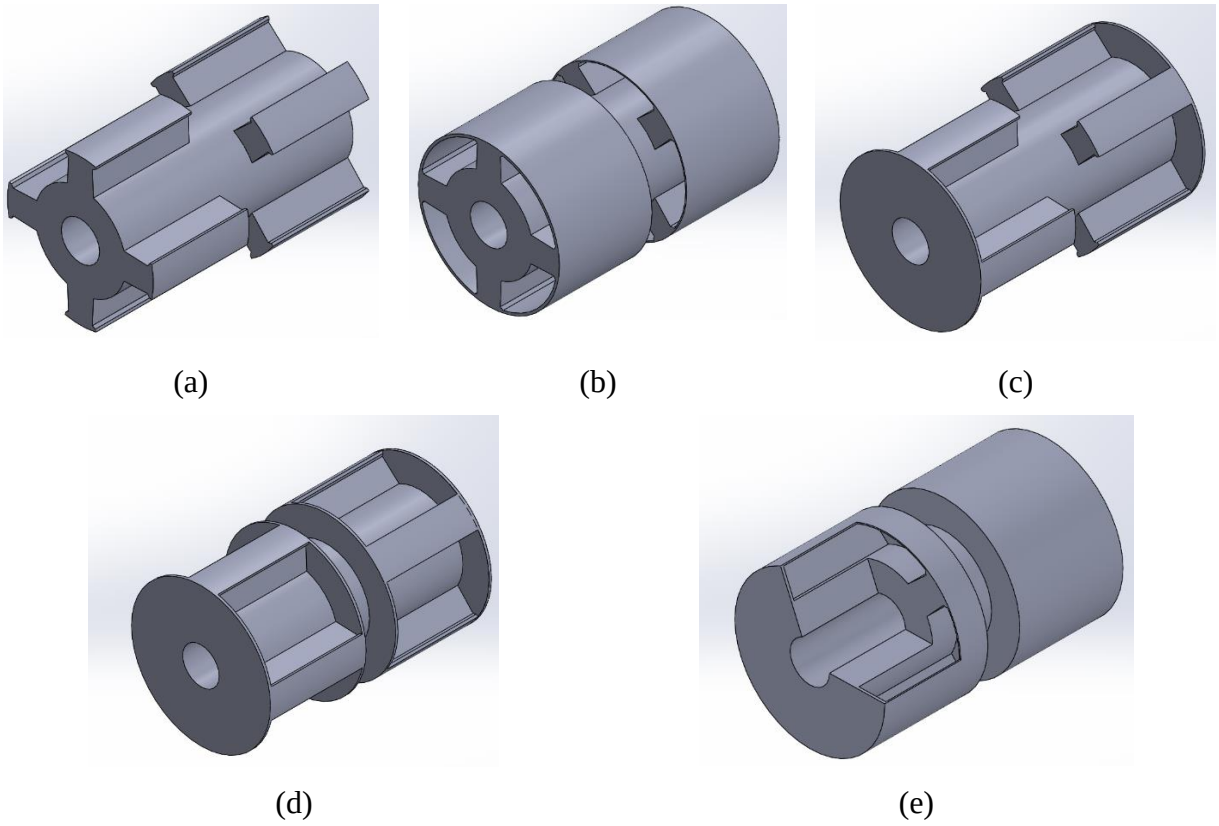

Figure 5.2-1. Original and modified rotor structure for windage loss (a) Original dual-stator 6/4 FSPM rotor (b) Rotor with ribs (c) Rotor with two end shrouds (d) Rotor with four end shrouds (e) Cylindrical rootor

issues could be critical, especially for high-speed applications. The modified rotor structure discussed in this paper only involves changing the lamination geometry. The original and modified rotor structures for the dual-stator 6/4 FSPM machine are shown in Figure 5.2-1. The cut view of the cylindrical rotor is shown to illustrate the inner structure. Note that the stator of the machines is identical. In Figure 5.2-1 (c) and Figure 5.2-1 (d), rotor shrouds are added to prevent the axial air flow. By intuition, similar outcome can be achieved by enclosing the end cap of the machine. In the following part, the windage loss of 6/4 FSPM machines with rotor structure modifications and enclosed end cap is evaluated and compared.

5.2.2. Windage loss estimation and structural analysis

Windage loss is the power dissipated due to the aerodynamic drag from the rotating rotor. It not only degrades machine efficiency, but also introduces extra heat. Therefore, quantifying windage loss is an important aspect of high-speed machine design. Windage loss of FSPM machines can be estimated by referring to known windage loss from similar machines [132]. There are two main categories in terms of rotor structure: cylindrical rotor and salient pole rotor. The cylindrical rotor is often used in interior PM machines, surface PM machines, synchronous reluctance machines and induction machines. The airgap between the stator and rotor is usually thin and uniform and it has a smaller Reynolds number per (Equation 5-3), where r is the rotor

$$Re = \frac{r\omega\rho t}{\mu} \qquad \text{(Equation 5-3)}$$

outer radius (m), ω is the angular speed (rad/s), t is the airgap length (m), ρ and μ are the density (kg/m^3) and viscosity (Pa-s) of the fluid in the airgap. Low Reynolds number means that the fluid flow within the airgap is more likely to be laminar. Whereas airgap of the salient pole rotor is not uniform, and easily causes turbulence, which causes higher windage loss.

The machine under study is a 70 kW 6/4 dual-stator FSPM machine. The geometry parameters and operating condition are given in TABLE 5-3. FSPM machine has a salient pole rotor similar to the SRM. As mentioned previously, the non-uniform airgap and axial air flow cause the high windage loss. Four modified rotor structures are proposed for windage loss reduction, as shown in Figure 5.2-1. Analytical equations have been developed to calculate the windage loss of rotor with cylindrical rotor shape and salient pole shape. Transient air flow characteristics and more detailed air flow distribution can be simulated with computational fluid dynamics (CFD).

A. Windage loss estimation by empirical method

Windage loss for concentric cylinders is usually calculated by Taylor-Couette flow theory [165]. However, this analytical approach works for low surface speed, where laminar flow dominates in the airgap. The machine under investigation rotates at 15,000 RPM, and the rotor tip speed reaches 97 m/s. Random turbulence occurs in the airgap and the analytical equation is no longer valid. Empirical estimation of windage loss for high-speed machine is provided in [132], where the windage loss of machine with a cylindrical rotor and salient pole rotor is discussed. However, the conclusion in [132] cannot be easily extended to the machine under study here, since as shown in Figure 5.2-1 (a), the rotor of the dual-stator 6/4 FSPM machine consists of three parts: two salient-pole and one cylinder. But for the full-cylindrical case, we could use the empirical equations to estimate the windage loss of the rotor. For the original salient rotor structure, superposition could be applied, where the total windage loss is the sum of the windage loss for individual rotor part.

In reference [132], to obtain the windage power loss, the Reynolds number is first calculated using (Equation 5-3) for a given machine geometry and working environment. The skin friction

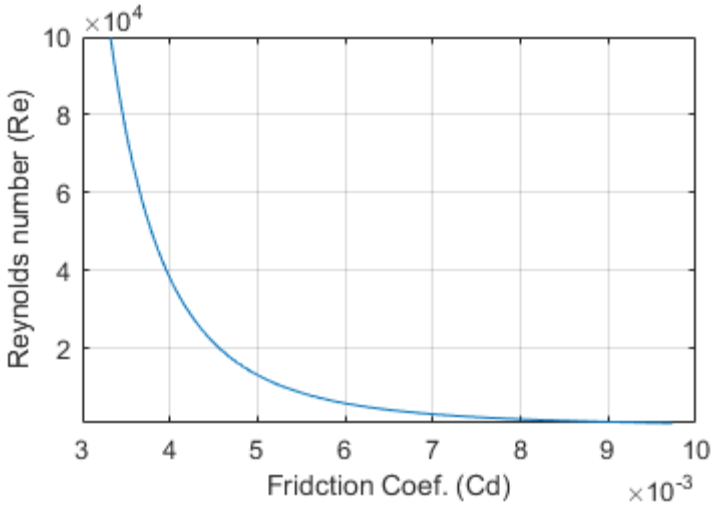

Figure 5.2-2. Friction coefficient – Reynolds number empirical relation for turbulence flow

coefficient C_d can be calculated with the Reynolds number by(Equation 5-4), which is valid for the turbulent Reynolds number in the high-speed machine. Notice that there is no available analytical solution for friction coefficient that involves turbulence. (Equation 5-4) is derived from

$$\frac{1}{\sqrt{C_d}} = 2.04 + 1.768 ln(Re\sqrt{C_d}) \quad \text{(Equation 5-4)}$$

$$P_{w,cyl} = \pi C_d \rho r^4 \omega^3 L \quad \text{(Equation 5-5)}$$

$$K = 8.5\frac{H}{R} + 2.2 \quad \text{(Equation 5-6)}$$

empirical data. The curve described by (Equation 5-4) is plotted in Figure 5.2-2. The windage loss of a cylindrical rotor can then be estimated by (Equation 5-5), where L is the machine stack length (m). The rotor saliency introduces for sure extra loss and could be calibrated with factor K calculated in (Equation 5-6), where H and R are the pole depth (m) and radius (m) of the rotor.

The windage loss of the full cylindrical dual-stator 6/4 FSPM machine can be calculated as the sum of two large cylinders and one smaller cylinder. The windage loss the original rotor can be calculated as the sum of two salient rotor and one cylindrical rotor.

B. Windage loss estimated with CFD tool

Nowadays, computational fluid dynamics (CFD) tools such as ANSYS Fluent provides a more accurate estimation of windage loss for complex geometries. For the dual-stator 6/4 FSPM machine under study, the three segments-rotor makes it skeptical to apply the analytical or empirical equations directly, where CFD tool becomes handy. The rotor geometries are imported into the CFD software as a fluid volume with an inner rotating wall boundary condition. Mesh number of the solid are chosen to have a convergeable CFD simulation. The *k-ω* SST turbulence

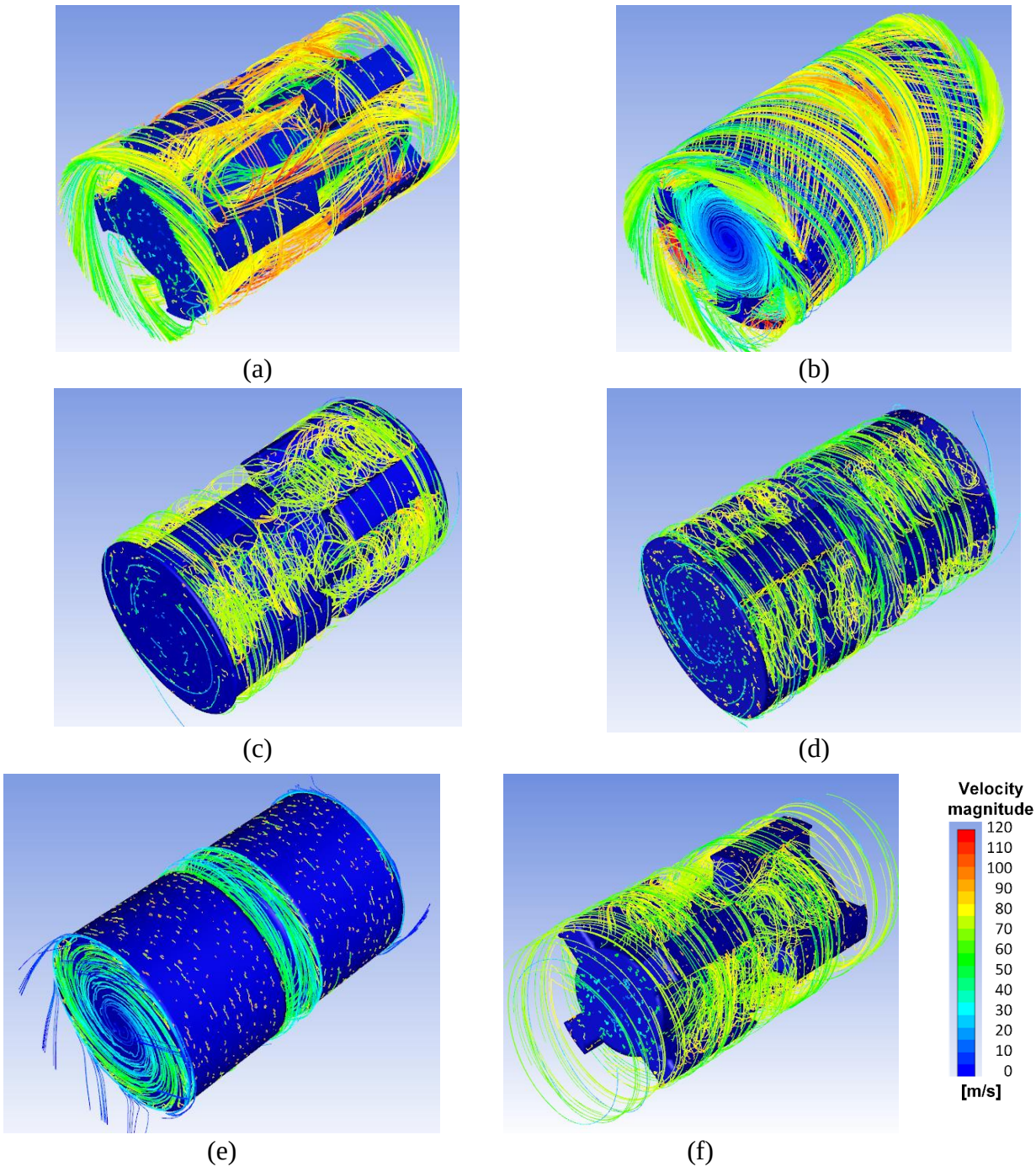

Figure 5.2-3. Air flow velocity stream line plot of dual-stator 6/4 FSPM machine at 15,000 rpm with (a) Original rotor (b) Rotor with rib (c) Rotor with two shrouds (d) Rotor with four shrouds (e) Rotor with cylindrical shape (f) Enclosed machine end cap

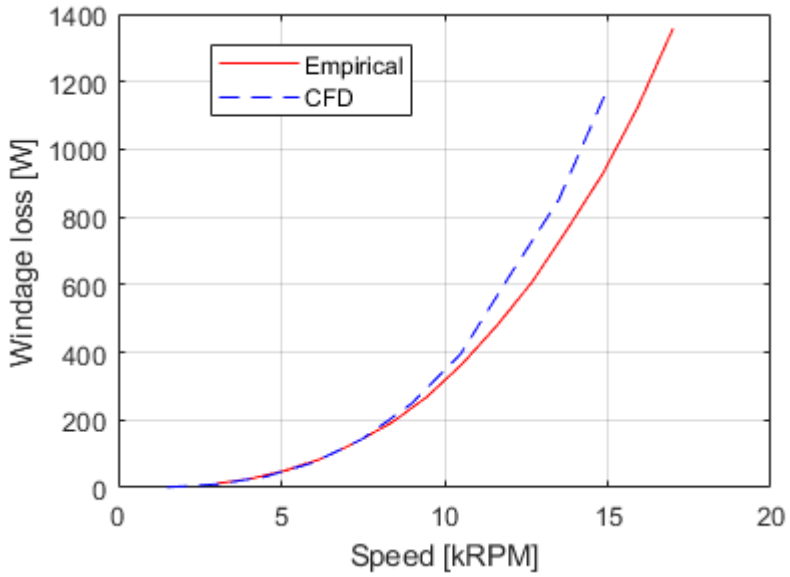

Figure 5.2-4. Comparison of empirical windage loss and CFD windage loss for dual-stator 6/4 FSPM machine

model is used to better capture the drag in the airgap. Fine mesh is preferred for having accurate and better convergent results but takes longer simulation time.

Figure 5.2-3 shows the plot of air flow velocity streamline inside the airgap of the machine for all the rotor structure mentioned previously. It can be seen that due to high rotational speed and the salient rotor structure, the surface speed of air is large, which causes considerable windage loss. As can be seen, there are significant axial air flow in the original rotor structure. The rotors with two shrouds and four shrouds are able to effectively reduce the axial air flow. The air flow for the cylindrical shape rotor is significantly reduced. With the enclosed machine end cap, the axial flow is considerably reduced, as can be seen in Figure 5.2-3 (f). However, because of the end winding region, the axial flow blocking with the end cap is not as effective as with the rotor shroud. As can be seen in Figure 5.2-3 (f). The windage loss from the previously given empirical equations and superposition is compared with the windage loss from CFD simulation in Figure 5.2-4. As can be seen, at two curves match good with a difference less than 5% up to 10 krpm. After 10 krpm, the empirical result becomes lower than the CFD result.

TABLE 5-4. WINDAGE LOSS ESTIMATED WITH ANALYTICAL EQUATIONS AND CFD SIMULATION OF DIFFERENT ROTOR STRUCTURE

Rotor structure	Drag torque [Nm]	Loss [W]
Original rotor	0.750	1177.5
Rib rotor	0.654	1026.8
2-shroud	0.164	257.5
4-shroud	0.152	238.6
Cylindrical (CFD)	0.037	58.1
Cylindrical (Empirical)	0.035	55.6
Enclosed end cap	0.31	486.7

Dragging torque on the rotor surface can be output from the CFD simulation. The value of windage loss is calculated as the product of dragging torque and the rotation speed which is fixed at 15,000 RPM (1570 rad/s). As can be seen in TABLE 5-4, the windage loss for the cylindrical shape rotor from the empirical equations is close to the one estimated by CFD simulation. From windage losses in TABLE 5-4, it can be seen that the windage loss of rotor rib design is still very high, whereas the rotor shroud structures manage to reduce the windage loss significantly. This means that the rotor shroud is a more effective way for reducing the windage loss, and the 4-shroud design is even better than the 2-shroud one. The enclosed machine end cap is able to reduce the windage drag but not as effective as the rotor shroud. The opened end cap allows a better rotor cooling since it allows air exchange between the air gap region and the ambient. The final choice of rotor structure depends on the machine overall efficiency, structural stability, and manufacturability.

C. Structural analysis of windage reduction rotor structures

The added rotor ribs and shrouds are under stress when the machine rotates. Since rotor ribs and shrouds are thinner than the other parts, they are more vulnerable and is more likely to cause structural issue. Structural analysis is needed to verify the windage loss reduction topologies'

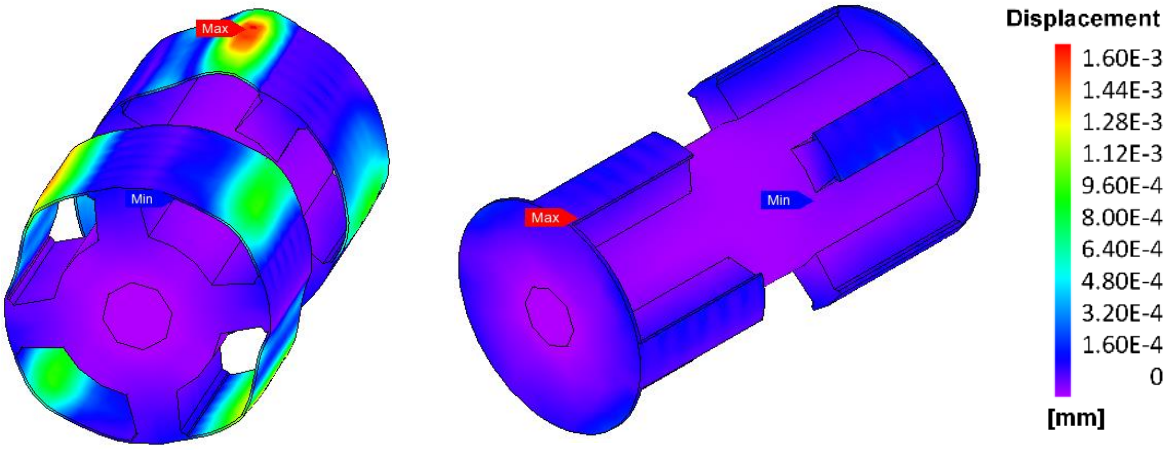

(a) (b)

Figure 5.2-5. Amplitude of displacement of rotor under rated condition with (a) 1 mm rib and (b) Rotor with two shroud.

integrity. Figure 5.2-5 shows the displacement of the rib rotor and the 2-shroud rotor under rated condition. It can be seen that for rotor with 1 mm rib, the maximum displacement is less than 0.002 mm. Note that the air gap is set to 1 mm. Therefore, there is no interference issue between the rotor and the stator even at worst scenario. The displacement for rotor with shroud is one order of amplitude less than the displacement of rib structure. That is to say, the end shroud is more robust than the rib between rotor poles.

Figure 5.2-6 shows the Von Mises stress distribution on the rib rotor and the 2-shroud rotor. For the 1 mm rotor rib structure, the maximum stress occurs on the rib between two rotor poles. The value of the maximum stress is around 5 MPa, which is far less than the tensile strength of normal electrical steel which is around 500 MPa. For rotor with shrouds, the maximum stress occurs at the rotor pole and is also far less than the tensile strength of the material. The thickness of rotor shroud is assumed to be 2 mm for the structural analysis. The actual thickness of the shroud depends on the thickness of the steel lamination. Discussion about the influence of the shroud thickness on the electromagnetic performance is done in the next section.

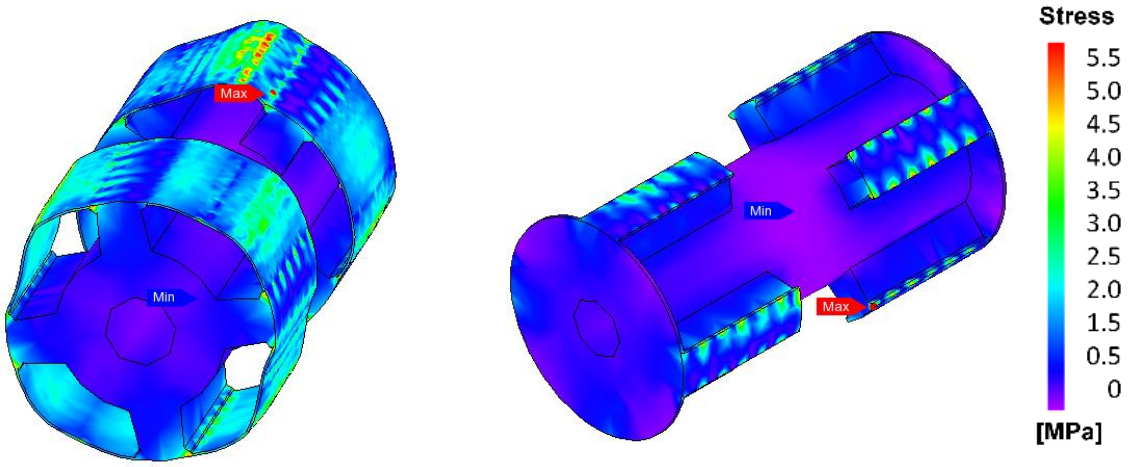

(a) (b)

Figure 5.2-6. Von Mises stress of rotor under rated condition with (a) 1 mm rib and (b) Rotor with two shroud.

TABLE 5-5. MODAL ANALYSIS FOR DIFFERENT ROTOR STRUCTURE

Rotor structure	1st mode frequency [Hz]
Original rotor	11165.8
Rotor with rib	7805.2
Rotor with 2 shrouds	6005.4
Rotor with 4 shrouds	6183.8
Cylindrical rotor	8502.6

Modal vibration analysis for each rotor structure is conducted with structural FEA simulation to ensure the 1st mode frequency is away from the maximum speed of the machine to avoid severe vibration and noise. TABLE 5-5 gives the 1st mode frequency of different rotor structures. The lowest frequency is 6,000 Hz, whereas for 15,000 RPM operation, the rotor frequency is 250 Hz, which is far less than 6,000 Hz. Therefore, resonance is not an issue for all the rotor structures discussed here.

5.2.3. Electromagnetic properties of windage loss reduction structure

A. No-load flux linkage and back EMF

Because of the existence of rotor rib and rotor shroud, the flux path is modified. Flux leakage occurs between the two adjacent rotor poles. Consequently, the torque production and efficiency will be affected. Figure 5.2-7 shows the magnetic flux density for the original rotor and rotor with rib, respectively. It can be observed that the rotor tips and rotor ribs are highly saturated (around 2.0 T). The influence of rotor rib is not significant. The rotor shroud added to the end of the rotor is very thin comparing to the stack length, and the axial magnetic flux is negligible comparing to radial flux. Therefore, the influence is limited, but still need to be verified. The 3D FEA is used to estimate the flux linkage and the back EMF of each case.

Figure 5.2-8 (a) shows the waveform of the flux linkage for the different rotor structures. To illustrate the differences more clearly, Fourier transformation is done to give the harmonic components, as shown in Figure 5.2-8 (b). Note that the even harmonics in the flux linkage are negligible due to the dual-stator structure. It can be observed that the 2-shroud and 4-shroud structure have the highest fundamental component and minimal distortion, whereas the cylindrical

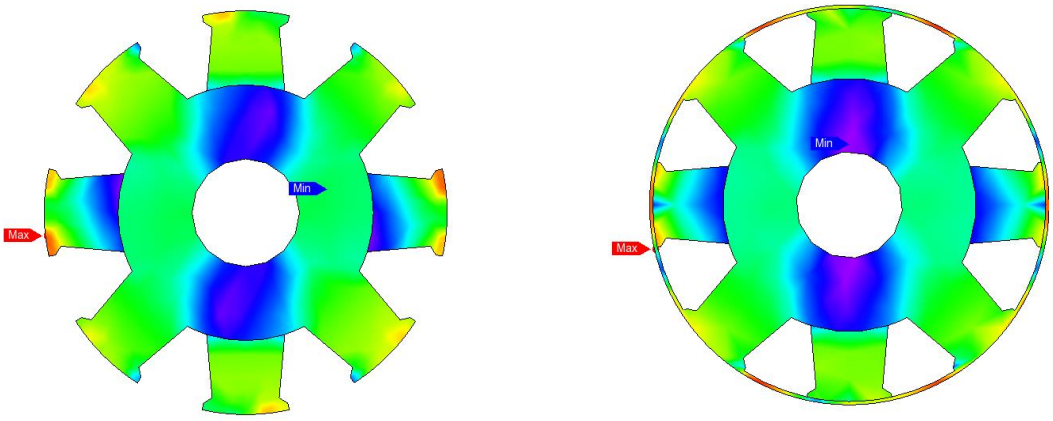

(a) (b)

Figure 5.2-7. Magnetic flux density of rotor (a) Original rotor (b) Rotor with rib

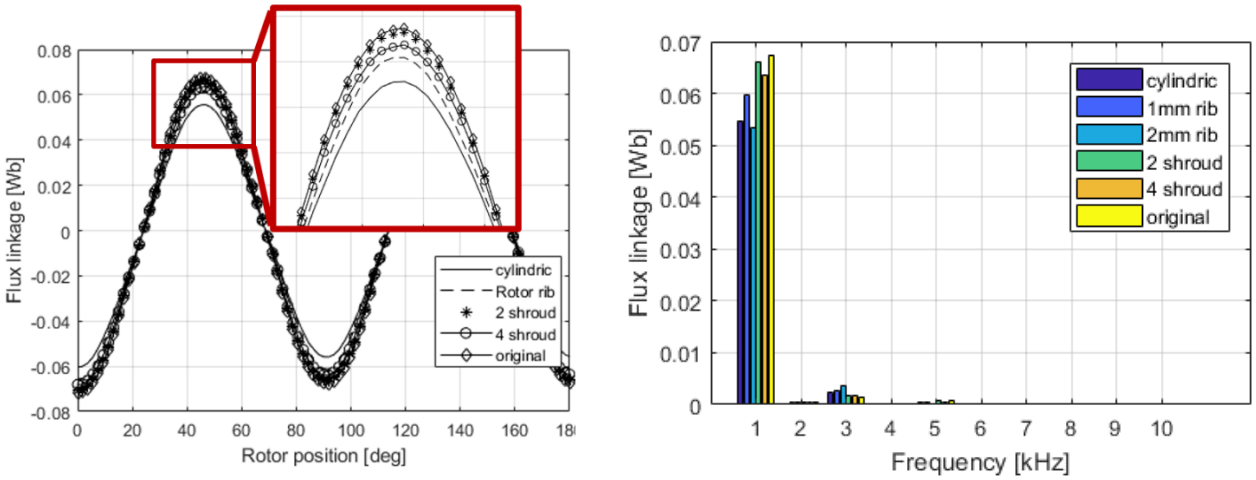

(a) (b)

Figure 5.2-8. Flux linage of dual-stator 6/4 FSPM machine with different type of rotor for windage loss reduction (a) Flux linkage waveform (b) Flux linkage harmonic component

and rib rotor introduce a large number of high order harmonics. It can be concluded that topologies with shrouds added to the ends of rotor have the minimum influence on the electromagnetic performance.

Although the thickness of the shroud is less than 1% of the stack length and the shroud is placed outside of the stator laminations, it is still required to quantify the impact of shroud

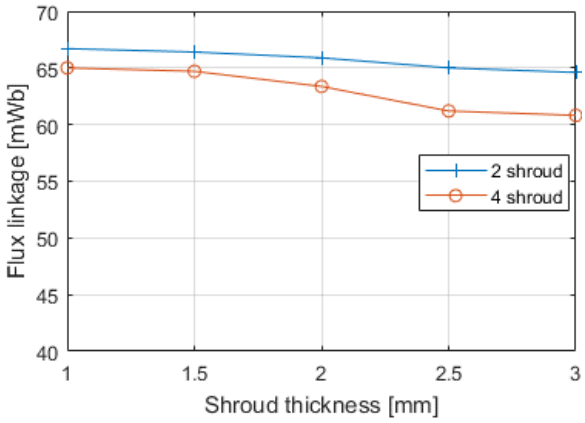

Figure 5.2-9. Flux linkage variation for different shroud thickness

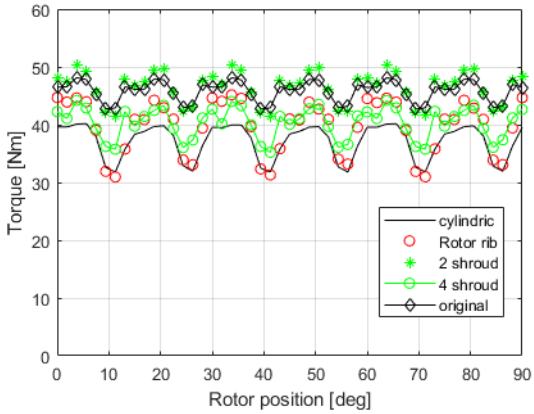

Figure 5.2-10. Output torque of different rotor structure

TABLE 5-6. AVERAGE TORQUE AND TORQUE RIPPLE FOR DIFFERENT ROTOR STRUCTURES

Rotor structure	Average [Nm]	Ripple [Nm P-P]
Original rotor	45.8	5.6
Rotor with rib	39.6	11.4
2 shrouds	46.6	6.5
4 shrouds	45.18	6.8
Cylindrical	37.1	7.6

thickness on flux linkage. Figure 5.2-9 shows the amplitude of flux linkage for different shroud thickness. It can be seen that in both 2-shroud and 4-shroud case, the reductions of flux linkage are less than 1% for 1.5 mm shroud thickness. Whereas starting from 2 mm, the flux linkage drop is larger than 3%. Therefore, a balanced approach is taken between the flux linkage and structural robustness. The shroud thickness is fixed to be 1.5 mm. From the structural analysis done in the previous section, it is shown that a 1 mm shroud is robust enough to hold the structure, which means that the 1.5 mm shroud will not cause any structural issue. Note that the shroud thickness must be a multiple of the lamination thickness. Lamination thicknesses of 0.15 mm to 0.20 mm are under consideration for this machine design.

B. Torque production

As shown in the previous part, the modified rotor structure has introduced distortion in the flux linkage and back EMF waveform. As a result, the average torque is compromised, and larger torque ripple is expected. Figure 5.2-10 shows the torque variation along the rotor position for different rotor structures. To give a clear comparison, TABLE 5-6 summarizes the average torque and torque ripple for each structure. Similar to the result from the previous part, the 2-shroud rotor has the highest average torque among the modified structures. The result shows that with a 1.5 mm thick shroud, the resultant torque is even higher than the original structure. The reason for this

increase is the shrouds are placed outside the stator stack, as a consequence, the rotor stack length is increased. As mentioned previously, the high-order harmonic components in the flux linkage cause torque ripple. Figure 5.2-8 shows that the 4-shroud rotor has the lowest harmonic distortion whereas the rib rotor has a very high harmonic distortion. Torque ripple can also be observed from Figure 5.2-10, where it can be seen that the rotor rib structures have higher torque ripple compared to the rotor shroud and original structure.

C. Overall efficiency comparison

The previous two sections present the windage loss estimation for a 70-kW dual-stator 6/4 FSPM machine with different types of rotor structure and their influence on the electromagnetic performance. It is shown that the windage loss could be significantly reduced by employing shrouds at the end of rotor stack or use a cylindrical shape rotor. However, changing the rotor structure influences the electromagnetic performance. Some of the modified rotor structures significantly compromise the machine electromagnetic performance. TABLE 5-7 summarizes the losses and efficiency of each type of rotor. It can be seen from the table that the 4-shroud rotor has the highest efficiency, and the low windage loss indicates that it is more promising in high-speed

TABLE 5-7. LOSSES AND EFFICIENCIES OF 70 KW DUAL-STATOR 6/4 FSPM MACHINE WITH DIFFERENT ROTOR STRUCTURES

Power [W]	Original	2-shroud	4-shroud	Rib rotor	Cylindrical
Stator Loss	4231.2	4101.0	3883.9	3923.7	3490.6
Rotor Loss	785.1	835.1	866.1	901.0	1062.4
Windage Loss	1177.5	257.5	238.6	1026.8	58.1
Output Power	69676.1	70736.6	69045.0	61123.3	57985.5
Total Loss	6193.8	5193.6	4988.6	5851.5	4611.1
Efficiency [%]	91.83	93.16	93.26	91.26	92.63

region. However, from the perspective of torque density, the 2-shroud rotor is the best choice, and the efficiency is only slightly lower than the 4-shroud design.

Notice that the material of the rotor shroud is chosen to be the silicon steel, the same as the rotor core, for the sake of easy manufacturing. However, the shroud could be fabricated with non-magnetic and non-conductive material. The windage loss and be reduced without sacrifice the output torque. But on the other hand, the manufacturing cost could potentially increase, and the structural strength of the shroud material need to be investigated carefully.

5.2.4. Windage reduction structure and rotor heat transfer

As shown in the previous section, the rotor shroud can effectively prevent the axial air flow in the rotor region and reduce the windage loss. On the other hand, the reduced air flow over the surface of the rotor compromise the convective heat transfer of the rotor. The 6/4 FSPM machines with the original salient teeth rotor and with 2 rotor shrouds are simulated in the CFD simulation software. The corresponding average convective heat transfer coefficients on the rotor surface for the two machines are shown in Figure 5.2-11. As can be seen, the heat transfer coefficient of the 2-shroud rotor is 40% less than the original rotor.

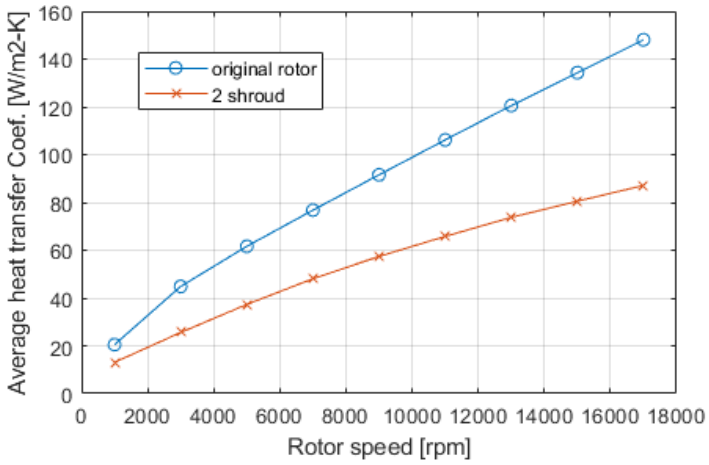

Figure 5.2-11. Convective heat transfer coefficient of the rotor surface for 6/4 FSPM machine with original rotor and with rotor shroud.

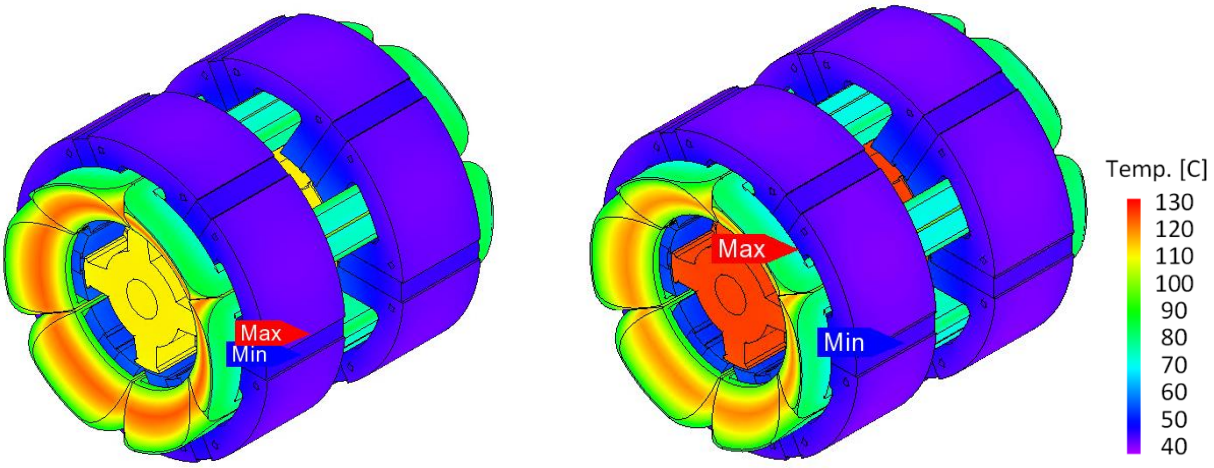

(a) (b)

Figure 5.2-12. Temperature contour of dual-stator 6/4 FSPM machine with original rotor and with shrouded rotor.

TABLE 5-8. TEMPERATURE OF 6/4 FSPM MACHINE COMPONENTS FROM FEA SIMULATION AND LPTN MODEL

Node	Original (°C)	2-shroud (°C)
Stator	56.6	55.8
Magnet	56.3	56.0
Winding (avg)	115.1	108.2 (-5.9%)
Rotor	103.2	127.1 (+23.1%)

The new air gap heat transfer coefficient is used in the new thermal FEA simulation. The updated machine temperature contour plot is shown in Figure 5.2-12. The temperatures of each machine component are shown in TABLE 5-8. As can be seen, the reduced air gap heat transfer coefficient leads to a higher machine rotor temperature and does not have significant influence of the other machine components. As one of the advantages of FSPM machine, the FSPM machine rotor structure is simple and robust. Iron losses are the only heat generated in the rotor. In addition, the rotor laminations are not as temperature sensitive as permanent magnets. Therefore, the reduction in rotor cooling has no significant impact on the machine thermal design.

5.3. Summary

This chapter investigates two special design aspects for FSPM machine, housing loss and windage loss. Focus has been given to the 6/4 FSPM machine for high-speed application. It is shown that due to the stator-mounted permanent magnet and the flux modulation principle, the magnetic field variation in the housing is large, especially the housing volume near the magnet. Therefore, the eddy current loss in the housing is not negligible. For the FSPM machine with single-layer toroidal winding, the returning coil is close to the housing, which is another source of varying magnetic field. However, it is shown that the eddy current loss due to the returning coil is much less than the housing loss caused by the magnet. According the electromagnetic FEA simulation, the housing loss due to the toroidal winding is less than 3% (at rated condition). The housing loss can be reduced with the use of iron bridge over the permanent magnet. However, the iron bridge causes significant flux leakage and compromises the machine performance. Leaving cavities in the housing near the magnet can reduce the housing loss by 60% without compromising the output power. However, the housing slot will increase the manufacturing complexity for the housing and potentially makes the water jacket design complicated.

Due to the salient rotor structure, windage loss in FSPM machine greatly influence the overall efficiency at high-speed. The rotor structure has a major influence on the windage loss of the machine and affects the electromagnetic performance. Finite element analysis (FEA) and computational fluid dynamics (CFD) results show that adding shrouds at the axial ends of the rotor reduce the windage loss by about 78% without compromising the torque. For the dual-stator FSPM machine, there is a choice of two or four shrouds. 2-shroud structure has a higher average torque, whereas 4-shroud structure has lower windage loss and higher efficiency. The rotor rib is shown to be less effective than the shrouds for reducing windage loss and has a decreases torque by 10%. It is also shown that the shroud structure is more robust in terms of structural strength and has less

deformation. Therefore, the shroud structures are recommended over the rib design as an improvement in high-speed FSPM machines. The 2 shrouds at the end of the rotor prevent the axial air flow, which not only reduce the windage loss but also compromise the rotor convective cooling. CFD simulation results suggest that the convective heat transfer on the rotor surface is reduced by 44% with the 2-shroud rotor. The 2-shrond rotor 6/4 FSPM machine has 24°C higher rotor temperature than the original rotor, which is not a problem for FSPM machine. The temperature of the rest of the machine is almost not affected.

Chapter 6 Experiment Verification

To verify the performance and characteristics of the dual-stator 6/4 FSPM machine estimated by the analytical calculation and finite element analysis simulation, prototype motors are built and installed on dynamometer test bench for experimental testing. In this chapter, the prototype machine manufacturing, the test equipment, and the testing procedure for both electromagnetic and thermal testing are presented. The measured results are compared with the calculation and simulation results to validate the electromagnetic and thermal model of the machine.

6.1. Prototype motor fabrication

The double-layer concentrated winding (DLCW) and single-layer toroidal winding (SLTW) 6/4 FSPM machine have been prototyped. The mechanical prints for each machine part are drawn

TABLE 6-1. GEOMETRY AND OPERATING PARAMETERS OF THE PROTOTYPE DUAL-STATOR 6/4 FSPM MACHINE

Parameter	Values
Rated power [kW]	10
Rated speed [rpm]	15 000
Operation frequency, f [Hz]	1000
Rated voltage [Vrms]	158.2
Rated current [Arms]	24
Stator outer diameter, D_{os} [mm]	130
Stator inner diameter, D_{is} [mm]	62
Total lamination stack length, L_e [mm]	80
Rotor outer diameter, D_{ir} [mm]	30
Airgap length, g [mm]	1
Gap between stators, d_{gap} [mm]	30
NdFeB magnet remanence [T]	1.2

and the tolerances are assigned with the help of engineers from Arnold Technologies. The two prototype motors have the same power and total volume. The basic machine sizing and operation parameters are given in TABLE 6-1. The stator core, water jacket channel, and the winding topology of the DLCW and SLTW 6/4 FSPM machines are different, which is specified in this section.

6.1.1. Double-layer concentrated winding 6/4 FSPM machine prototype

The 6/4 FSPM machine has 8 poles from the control aspect, which requires 1000 Hz fundamental frequency at the speed of 15000 rpm. Thin laminations of electric steel are needed to avoid high iron loss. Arnon 5 from Arnold technology with a thickness of 0.127 mm is chosen. A whole list of machine parts is given in the bill of material (BOM) given in the Annex A. The assembled machine and the CAD drawing are shown in Figure 6.1-1.

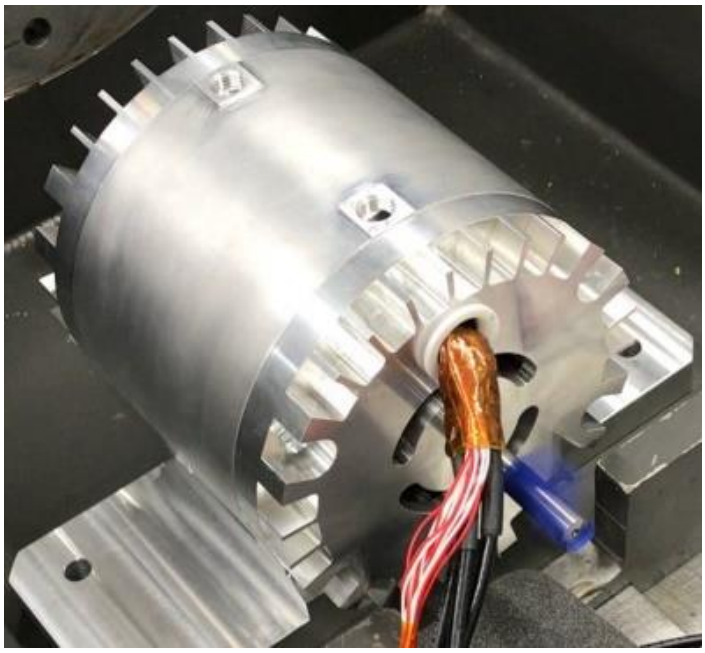

Figure 6.1-1. Photo of the assembled prototype DLCW 6/4 FSPM prototype motor

A. DLCW 6/4 FSPM machine stator assembly

The prototype motor has a modular stator design, the front and rear stator are made of 6 U-shape stator units, respectively. In order to hold the 6 stator units together, circular rings with threaded holes are used, as shown in Figure 6.1-2. The keys on the circular ring are to fix the azimuthal position of the stator relative to the housing. The magnets are sandwiched between the two stator units, fixed by a thin layer of glue. The stator cores have through holes to accommodate the bolts that attach the circular ring. The stators are shrunk fit to the housing before wound with coil because the axial distance between the two stators need to be fixed first. The winding is randomly hand wound, with a slot filling factor of approximately 40%. The copper section area for each turn is about 3.5 mm^2, which corresponds to the AWG #12 wire. To alleviate the winding skin effect and make the multi-turns coil easier to wound, 8 strands of AWG# 22 wire is used. The Nomex 410 is used as the slot liner to guarantee the insulation between the winding and the stator.

To monitor the temperatures of the machine winding and magnet, resistive temperature detectors are embedded in the coil while winding the machine and are attached to the surface of

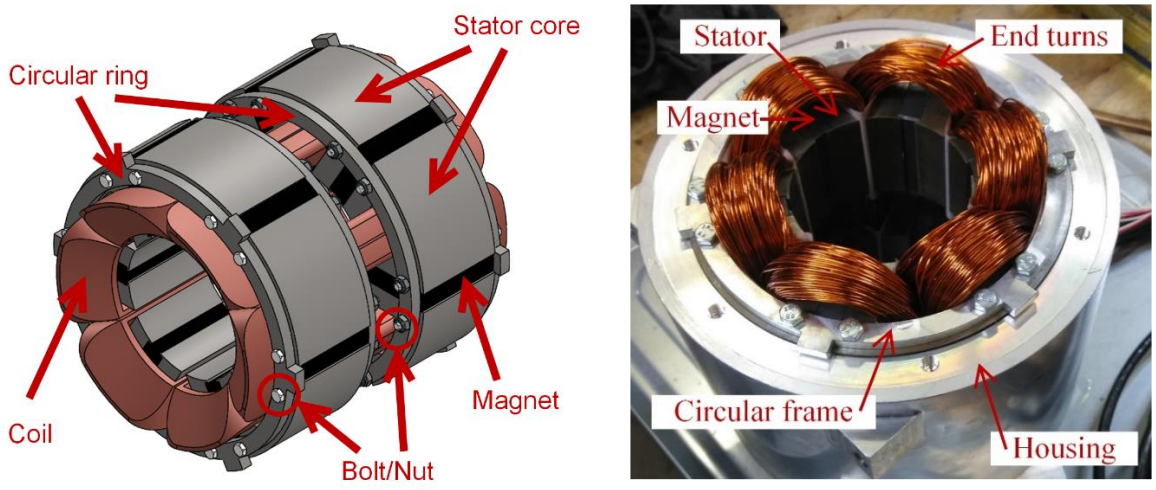

(a) (b)

Figure 6.1-2. Stator assembly of the DLCW 6/4 FSPM machine (a) CAD drawing and (b) Actual stator assembly photo

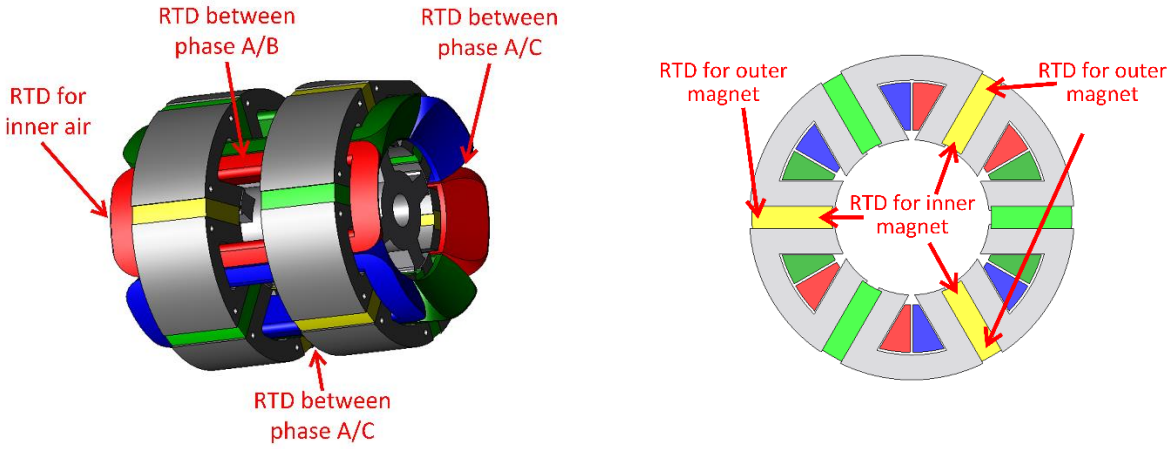

(a) (b)

Figure 6.1-3. Placement of 10 RTD temperature sensors in the DLCW 6/4 FSPM machine prototype

the magnets, as illustrated in Figure 6.1-3. The stator slots are encapsulated with epoxy to make the winding cooling better. As mentioned in Chapter 4, the Dolphon CC-1105 is used as the encapsulation material.

B. DLCW 6/4 FSPM machine rotor assembly

The rotor of FSPM machine only contains laminations of electrical steel. As shown in Figure 6.1-4, the DLCW 6/4 FSPM machine rotor has 4 rotor poles for each of the two torque-producing section. The cylindrical shape middle part of the rotor corresponds to the 30 mm gap between the

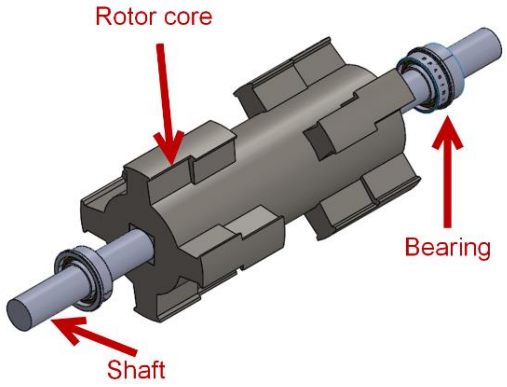

Figure 6.1-4. Rotor assembly CAD drawing

two stators. The whole rotor is made of the same material to simplify the manufacturing. Each rotor pole is step skewed by 5° to reduce the cogging torque [117]. The rotor core is also made of Arnon 5 laminations, which are glued together.

The shaft is shrunk fit into the rotor. The shaft hole in the rotor is made to be square shape to better transfer the torque from the rotor to the shaft and no key is needed. High-speed bearings (AST-F63801) are used in the prototype to meet the 15000-rpm target speed. It is impossible to put RTD onto the rotor. The rotor temperature is monitored by thermal camera through openings on the housing, as described in the following part.

C. DLCW 6/4 FSPM motor housing

The housing of the motor also serves as the water jacket to cool the machine. For the DLCW 6/4 FSPM machine, spiral channel water jacket is used. The water jacket consists of two part, an inner part and an outer part. The channel of the water jacket is carved on the inner housing, while the outer housing is a hallow cylinder. The outer housing is shrink fitted to the inner housing to guarantee the water tightness, as shown in Figure 6.1-5 (a). Two through holes are drilled on the outer housing as the inlet and outlet for the water jacket.

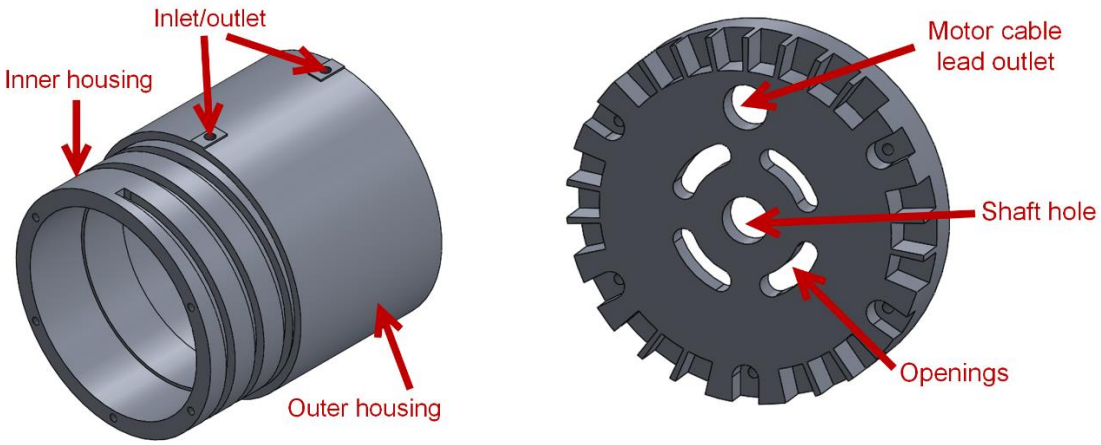

(a) (b)

Figure 6.1-5. DLCW 6/4 FSPM machine housing (a) Water jacket (b) End cap.

The housing has a front and a rear end cap, which are mandatory for high rotation speed machine for the safety consideration. As can be seen in Figure 6.1-5 (b), fins are created on the end cap to facilitate the convective heat transfer. In addition, four openings are left on each end cap. The openings serve as windows to inspect the inside of the machine. The rotor temperature is monitored by a thermal camera through the openings.

6.1.2. Single-layer toroidal winding 6/4 FSPM machine prototype

The single-layer toroidal winding (SLTW) 6/4 FSPM machine has the same power rating and the same outer diameter and stack length as the double-layer concentrated winding machine shown in the previous section. The stator/rotor core, permanent magnet, and the housing use the same material as well. The BOM for the SLTW 6/4 FSPM machine is given in the Annex B. The assembled prototype motor is shown in Figure 6.1-6. The prototype design of the DLCW machine has been through several engineering iterations to make the motor easier to manufacture. The prototyping experience of the DLCW 6/4 FSPM motor prototyping is useful for the manufacture of the SLTW 6/4 FSPM motor prototype.

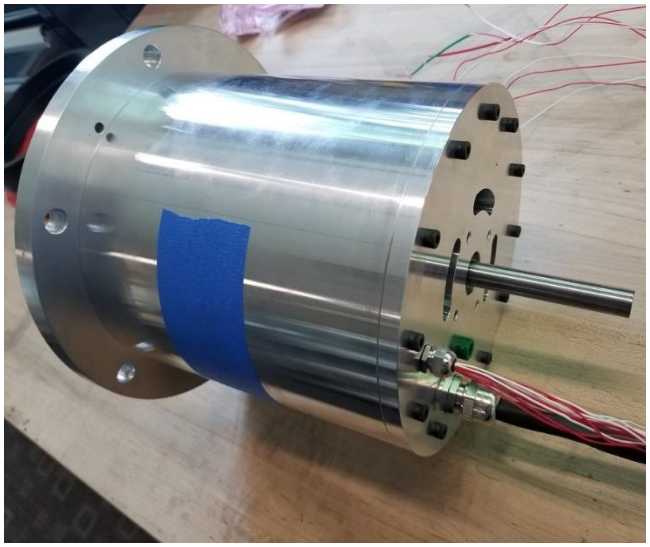

Figure 6.1-6. Photo of the assembled prototype SLTW 6/4 FSPM prototype motor

A. SLTW 6/4 FSPM machine stator assembly

Because of the toroidal winding topology, the stator unit of the SLTW 6/4 FSPM machine has an H-shape to accommodate the returning coil. Instead of having a totally modular stator design, the stator lamination of the SLTW 6/4 FSPM machine is designed to be one piece, as shown in Figure 6.1-7, to make the stator assembling process easy. The stator units are connected by a 1 mm iron bridge at the outside of the permanent magnet. As can be seen, the circular ring is no longer needed, which simplify the assembling process of the stator. The magnets are inserted between the two stator cores. A keyway is carved in the stator core to lock the relative position of the stator core and the housing.

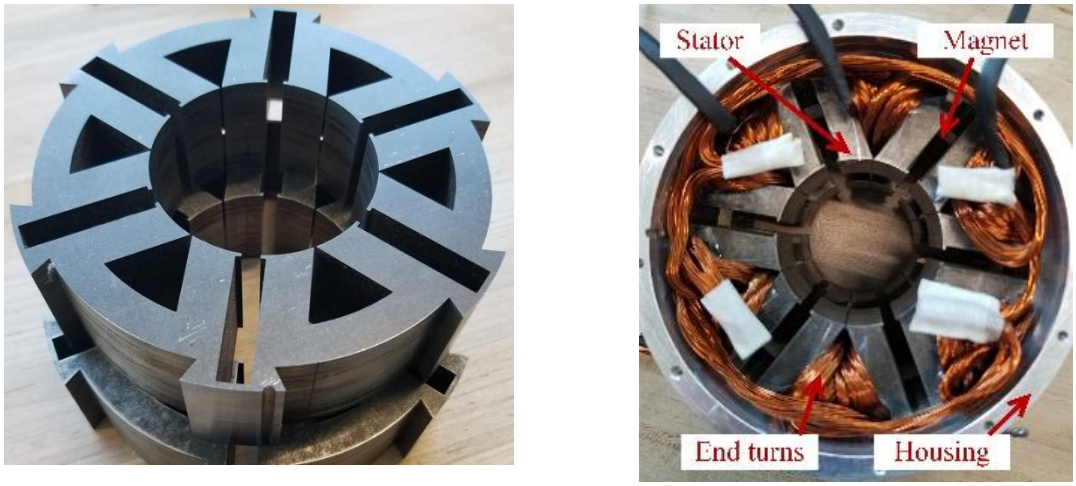

(a) (b)

Figure 6.1-7. Photos of the stator of the SLTW 6/4 FSPM machine (a) Stator core and (b) Stator assembly.

Same as the DLCW 6/4 FSPM machine, the stators are put into the housing before the machine is wound. 9 strands of AWG # 23 wire are used to form the coil. Note that the strands are transposed in order to reduce the proximity effect. Because of the single-layer design, there is no need for phase-phase insulation. Therefore, the slot filling factor is able to achieve about 45%.

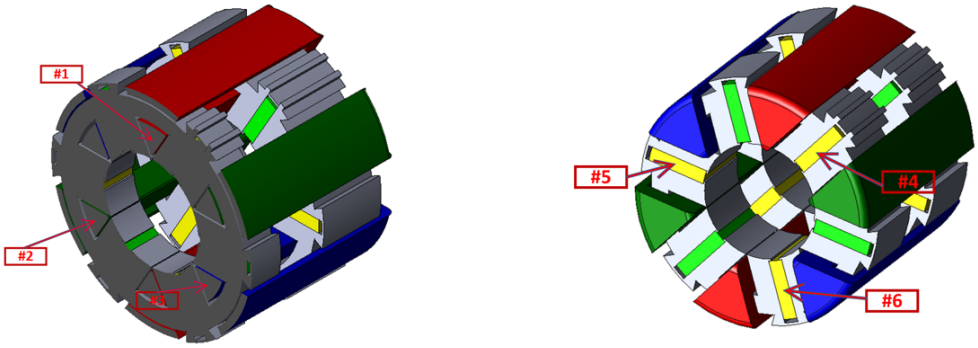

RTD. a RTD. b

RTD placement

Figure No.	RTD	Description
RTD. a	#1	Middle of slot winding of phase A1
RTD. a	#2	Middle of slot winding of phase B1
RTD. a	#3	Middle of slot winding of phase C1
RTD. b	#4	Side surface of magnet in front stator, between phase A and B
RTD. b	#5	Side surface of magnet in front stator, between phase B and C
RTD. b	#6	Side surface of magnet in front stator, between phase A and C

Figure 6.1-8. RTD temperature sensors placement of the SLTW 6/4 FSPM machine

Nomex 410 slot liner is used to ensure the insulation between the coil and the stator. RTDs are inserted among the coils and are attached to the magnet to monitor the components temperature, as shown in Figure 6.1-8. The stator slots are encapsulated with EFI-108 epoxy, which has a thermal conductivity of 1.9 W/m-K.

B. SLTW 6/4 FSPM machine rotor assembly

The rotor of the SLTW 6/4 FSPM machine is almost identical to the rotor of the DLCW 6/4 FSPM prototype and only consists of the lamination steel. The three-part design of the rotor with step skew of 5° is preserved, as shown in Figure 6.1-9. As can be seen, in order to reduce the windage loss of the machine, shrouds are added to the end of the rotor. The same silicon steel laminations are used for the shrouds to reduce the manufacturing complexity.

Instead of using a square shaft as in the DLCW 6/4 FSPM prototype, the SLTW 6/4 FSPM prototype uses conventional keyway design, as shown in Figure 6.1-9. Using the shaft key allows

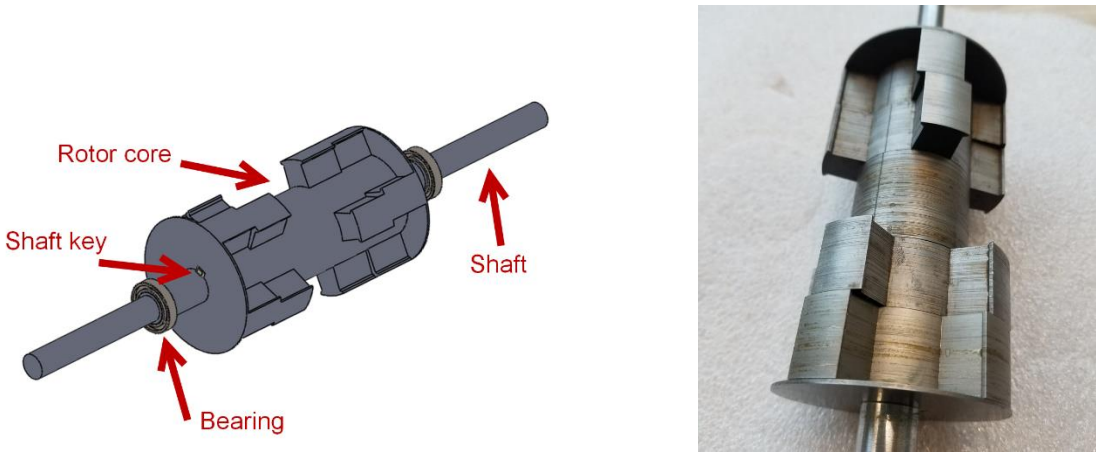

(a) (b)

Figure 6.1-9. Rotor assembly of the SLTW 6/4 FSPM machine (a) CAD drawing and (b) Rotor photo.

the shaft being easily shrink fitted into the rotor core. A pair of high-speed ball bearings (NSK-6802-VV) are used to fulfill the rotation speed requirement.

C. SLTW 6/4 FSPM motor housing

The water jacket housing of the SLTW 6/4 FSPM prototype is also made of two part, which are shrink fit together. The channel has an axial zig-zag shape as can be seen in Figure 6.1-10.

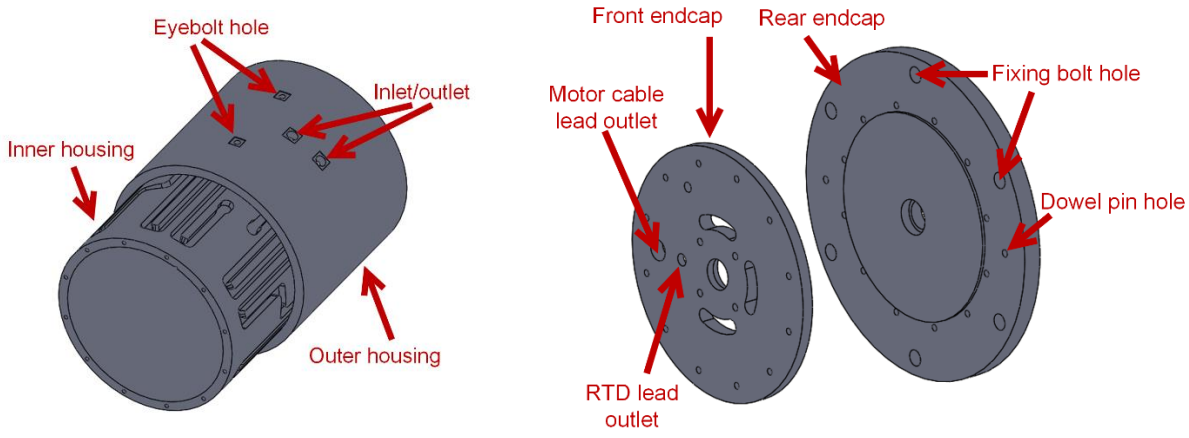

(a) (b)

Figure 6.1-10. CAD drawing of the housing (a) Water jacket and (b) Front and rear end caps

With the axial channel, the positions of the inlet outlet can be placed with more degrees of freedom than the spiral channel water jacket. In this design, the inlet and outlet are placed at the middle of the water jacket. Two eyebolt holes are left on the housing so that the machine can be easily lifted by crane when installing.

The SLTW 6/4 FSPM machine is designed to be able to attach directly to the mounting plate of the dyno test bench. Therefore, six M10 fixing bolt holes are left on the rear end cap, as can be seen in Figure 6.1-10. Two dowel pin holes are created on the end cap to control the position of the machine relative to the dyno bench mounting plate. Two wire lead outlets are left in the front end cap for the motor phase cable and RTD leads, respectively. Cable glands are used to prevent the stress of the cable. Although the test motor drive can use the encoder signal from the dyno motor and does not need a separate encoder, four holes are left on the front end cap to install encoder if necessary.

Hi-potential tests up to 2kV are done for the two prototype machines to ensure the phase-phase and phase-ground insulation. Preliminary impedance and back EMF measuring are done to ensure the balance of the three phases.

6.2. Prototype motor test setup

6.2.1. Test equipment and configurations

In order to test the electromagnetic and the thermal performance of the DLCW and SLTW 6/4 FSPM prototype motors (referred as test motor in the following paragraph), they are mounted on the dynamometer test setup. An induction motor controlled by an inverter and a bi-directional DC power supply is used as the prime mover machine during no-loading test and as the load machine during loaded test (referred as load motor in the following paragraph). The test motor is controlled by a commercial 3-phase ac drive from Rockwell. A power analyzer is used to record the electrical input and mechanical output power of the test motor. The motor voltage is read via

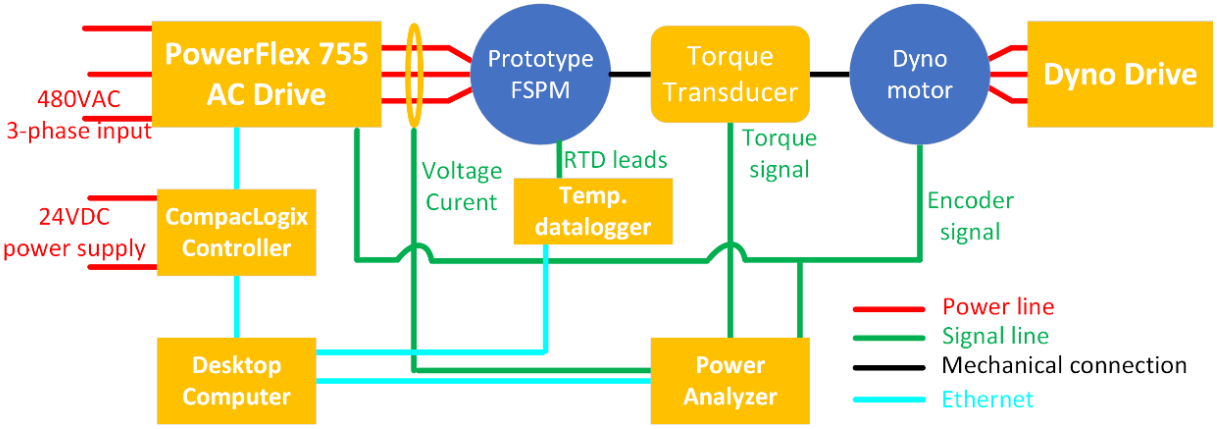

Figure 6.2-1. Schematics of the dynamometer test bench setup (Add temperature data logger, electric power measurement).

a high voltage differential probe, and the current is measured by a current transducer. A torque transducer is coupled between the load motor and the test motor, the torque signal is read by the power analyzer. The motor speed and position information are from the encoder mounted on the load motor. The voltage and current applied to the test motor are also recorded by the power analyzer to calculate the electrical input power. As mentioned in the previous section, resistive temperature detectors (RTDs) are embedded in the prototype motors to monitor the temperatures of the critical machine component such as the armature winding and the permanent magnet. A multi-channel datalogger is used to read and record the temperature variation of the test motor during operation. All the communications among the motor drive, power analyzer, datalogger, and the control desktop are realized by ethernet cable. The control of the test motor is done in a separate room for the safety consideration. A schematic drawing of the dynamometer test bench setup is shown in Figure 6.2-1. Photo of the DLCW and SLTW 6/4 FSPM machine test bench set up are shown in Figure 6.2-2 (a) and Figure 6.2-2 (b), respectively. For the safety consideration, the coupler between the shaft of the load motor and the test motor and the torque transducer, are covered by a steel dome. PWM inverter is used to control the prototype motors which could potentially cause radiated and conducted EMI. A Copper braid shielding is used to cover the motor

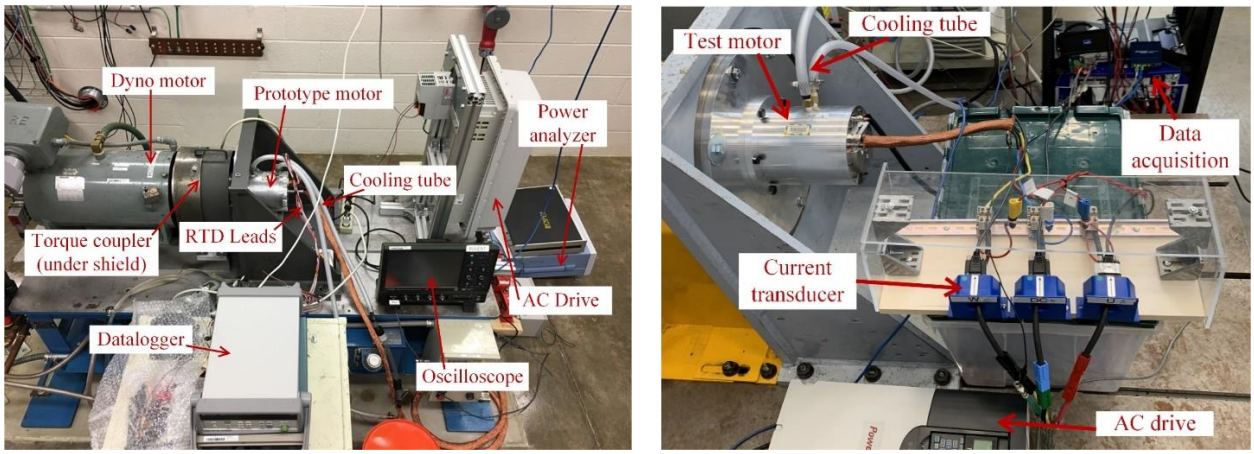

(a) (b)

Figure 6.2-2. Photo of dynamometer test bench setup for (a) DLCW 6/4 FSPM prototype motor and (b) SLTW 6/4 FSPM prototype motor

input cables. The copper shield is connected to the protective earth of the drive as well as motor housing to create a low impedance path for the common mode current.

Both DLCW and SLTW 6/4 FSPM prototype motors equip with water jacket cooling system. A temperature-controlled bath circulator is used as the cooling pump and heat exchanger for the cooling fluid of the motors. Deionized water is used as the coolant because of the low cost and safety. The inlet/outlet temperature and the flow rate of the coolant are measured, and the inlet temperature is controlled to be 23°C. The inlet and outlet of the water jacket are connected to the tube of the bath circulator via NPT 1/8 threaded holes.

The prototype motors are installed on the dynamometer testing bench from built by Anderson Electric and Control. Inc. The dyno bench is equipped with an oil-cooled induction machine with incremental encoder, accelerometer to monitor the vibration, inverter with output filter, and bi-directional DC power supply. A list of the control, measuring, and recording equipment is given in TABLE 6-2. The DLCW and SLTW 6/4 FSPM machine are tested sequentially, and some of the measurement are done with different equipment. All measurements

are done within the range and bandwidth of the equipment. Therefore, the change of measurement tool does not affect the validity of the results.

TABLE 6-2. DESCRIPTION OF PROTOTYPE MOTOR TESTING EQUIPMENT

Equipment	Description
Prototype motor	Dual-stator 6/4 FSPM motor with DLCW and SLTW
	10 RTDs embedded for temperature monitoring
	10 ft phase cable shielded with copper braid
Drive/Controller	PowerFlex 755, up to 12 kHz switching, Imax = 65 A
	Compact Logix 5370 controller
	Ethernet interface between drive/controller/desktop
Power analyzer	WT 1800 with Motor option module
	5A current input limit, current measured by current transducer with ratio of 1750:1. Voltage directly measured
	Ethernet interface with desktop
Torque transducer	T10FS-500 from HBM
	Analogue and digital output, ± 500 Nm, with 0.1% accuracy
Dynamometer (Dyno 5) Dynamometer (Dyno 6)	15000 rpm induction machine
	Dual-output incremental encoder with 512 PPR
Cooling pump	NESLAB RTE-7 series
	500 W cooling capacity, 15 LPM max flow rate
	Maximum 16’ pump head
Temperature datalogger	Keysight 37492A Datalogger, 20 analogue multi-function channels
	Ethernet interface with desktop

6.2.2. Switching current ripple and choose of output filter

As shown previously, a commercial AC drive is used to drive the prototype FSPM machine. As a matter of fact, the DC bus voltage of the drive is 10 times higher than the rated voltage of the motor, which is not a preferable match in terms of minimizing current ripple. To mitigate the current ripple, an output filter could be added to the drive, as illustrated in Figure 6.2-3, where the

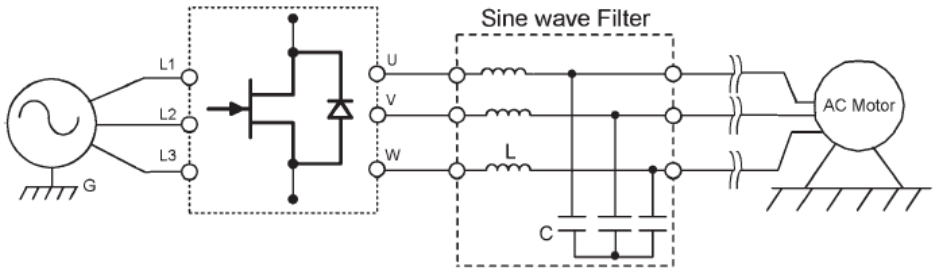

Figure 6.2-3. Electric motor drive system with output filter.

sine wave filter could also be replaced be three inductors for simple design. To decide on the choice of output filter, simulations based on MathWorks® Simulink have been done. The schematic of the system is shown in Figure 6.2-4.

The current ripple without filter is first investigated. The simulated and measured current waveforms at 1200 rpm are shown in Figure 6.2-5. As can be seen, the measured data matches well with the simulated results. It is shown that the current ripple reaches 73.7% of the amplitude without filter. Such large ripple will cause extra copper loss in the winding as well as iron loss in the stator and rotor. Therefore, output filter is needed for the test setup. Two filter options have been considered, i.e. LC sine wave filter and inductor. The design principle of the output filter is

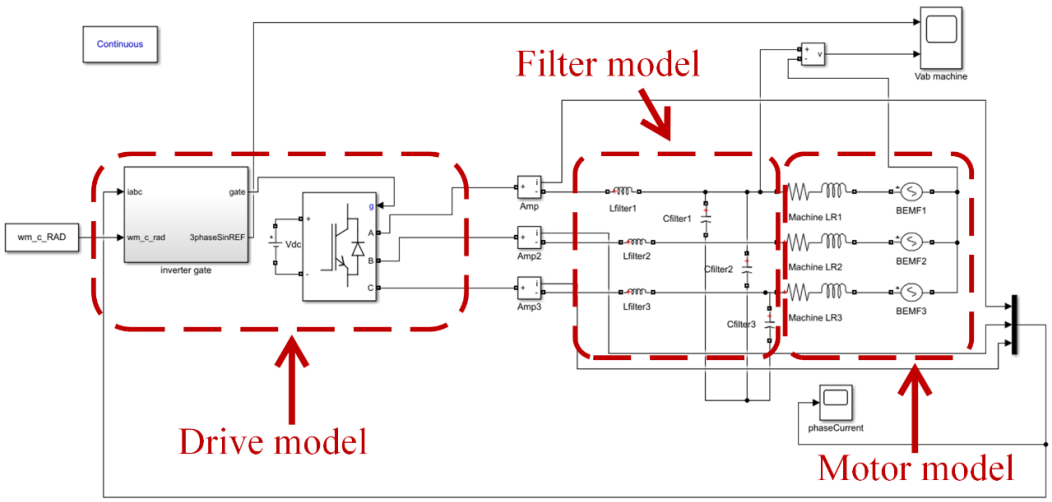

Figure 6.2-4. Simulink model of the drive system.

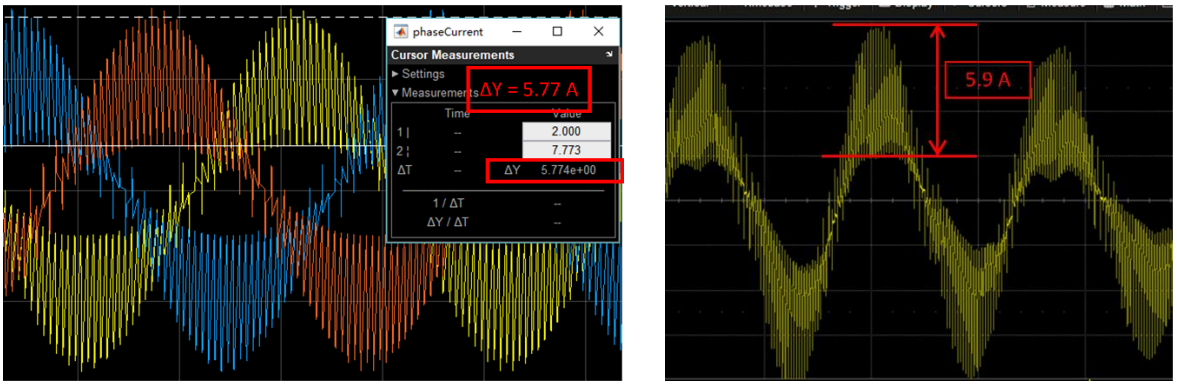

(a) (b)

Figure 6.2-5. Motor phase current waveforms without filter (a) Simulated (b) Measured

well explained in [166]. The filter impedance usually should be close to the motor impedance, which is 2.25 Ohm. Filter impedance could be calculated by (Equation 6-1), where L_f and C_f are the filter inductance and filter capacitance respectively. The fundamental frequency of the motor is between 20 Hz to 320 Hz, the switching frequency is 4 kHz. The desired break frequency is set

$$Z_{filter} = \sqrt{\frac{L_f}{C_f}} \qquad \text{(Equation 6-1)}$$

$$f_{break} = \sqrt{\frac{1}{L_f C_f}} \qquad \text{(Equation 6-2)}$$

to 1.2 kHz. The break frequency of a LC filter could be calculated by (Equation 6-2). Three inductors of 0.5 mH and three capacitors of 20uF are chosen as the filter component, which provide a break frequency of 1.5 kHz according to (Equation 6-1) and (Equation 6-2).

For the inductor filter case, the inductance is chosen to be the similar as the motor winding inductance, i.e. 0.5 mH. The simulated current waveforms for the LC filter and inductor filter are given in Figure 6.2-7. As can be seen, the current ripple is significantly reduced compared to the no-filter case. It is shown that the inductor filter gives lower current ripple than the LC filter.

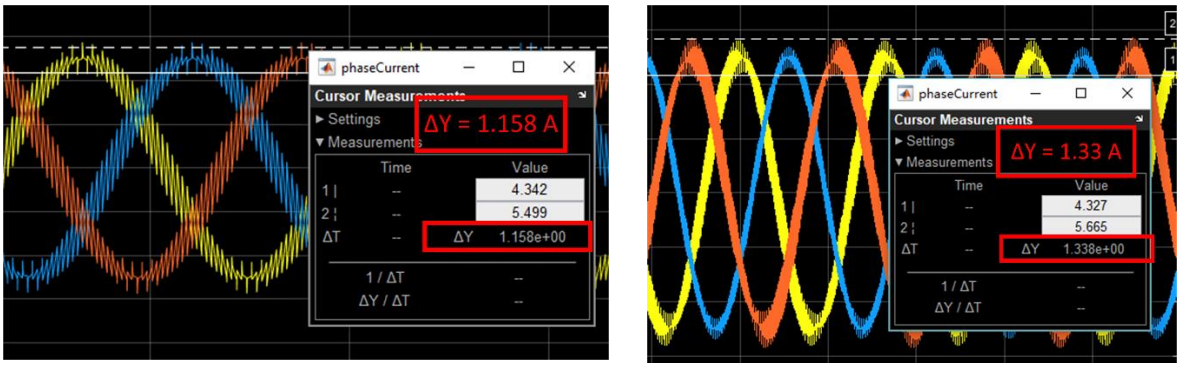

(a) (b)

Figure 6.2-7. Motor phase current waveform with filter (a) LC sine-wave fileter (b) Inductor

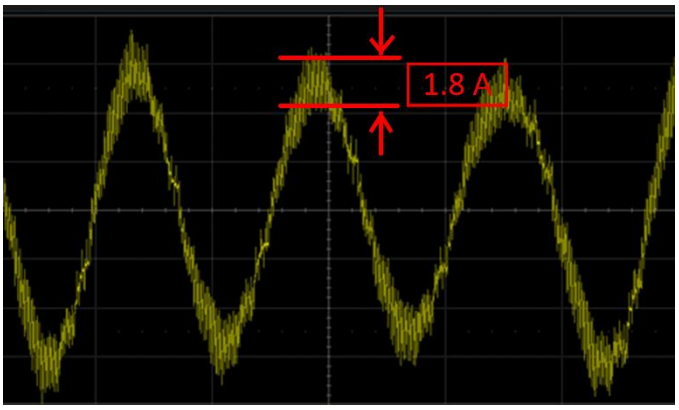

Figure 6.2-6. Motor current waveform with inductor filter

Therefore, three 0.5 mH inductors are added between the drive output and the motor, and the current waveform is measured as shown in Figure 6.2-6.

6.3. Electromagnetic performance tests

6.3.1. Prototype motors parameters

Up on receiving the prototype motor, static machine parameters such as the winding resistances and winding inductances are measured as a sanity check. Since the machine dynamic performance is not the focus, rotor inertia is not measured. The prototype motors have only the three phase leads without access to the neutral point. Therefore, line-to-line resistance and reactance are measured with an impedance analyzer with a sweep of frequency from 20 Hz to 1000

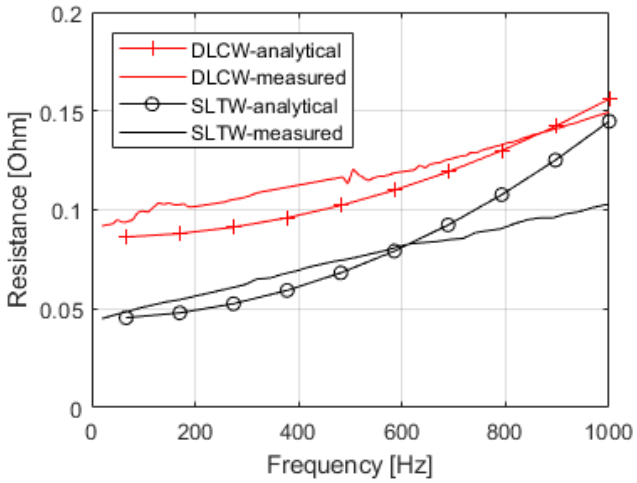

Figure 6.3-1. Measured variation of prototype motors stator winding resistance considering the ac resistance.

Hz. The measured machine static parameters at 100 Hz and 1kHz are shown in TABLE 6-3. The three phases of the prototype motors are well balanced, and the line-neutral resistances and inductances are shown. As can be seen, most of the measured parameters match with the calculated parameters shown in Chapter 2, except for the SLTW 6/4 FSPM machine winding resistance at 1 kHz. The measured winding resistance at 1 kHz is 41% smaller than the calculated value, as can be seen in Figure 6.3-1. This is because one turn of the SLTW 6/4 FSPM machine is made of 9 strands of AWG #23 wires, and they are transposed to reduce the proximity effect. The transposed effect is not considered in the calculated value because it is complicated to model and can be calibrated by the measurement. The electromagnetic and thermal performance of the machines are

TABLE 6-3. MEASURED PARAMETERS OF THE DUAL-STATOR 6/4 FSPM MACHINE

Parameter		**@ 100 Hz**		**@ 1 kHz**	
		Calculate	Measured	Calculate	Measured
DLCW	Rs [mΩ]	98	105.5 (+7.1%)	159	150 (-5.7%)
	Ls [uH]	530	485 (-8.5%)	-	-
SLTW	Rs [mΩ]	47	50 (+6%)	147	104 (-41%)
	Ls [uH]	470	450 (-4.3%)	-	-

evaluated in Chapter 3 and Chapter 4 with the calibrated winding resistance. The measured prototype motors' inductances match well with the calculated values within 9%.

6.3.2. Open circuit test

Before connecting the test motor to the drive, open circuit test is done to verify that the test motor has a balanced back EMF and reasonable cogging torque [167].

A. Back EMF of the prototype motors

Same as other permanent magnet machines such IPM and SPM, unbalanced back EMF is usually due to either the miscounting of the number of turns per phase, or internal short circuit. Such fault should be able to be detected from the static machine parameters measurement. Asymmetric machine stator geometry due to the manufacturing tolerance could also lead to unbalanced back EMF. Specifically, for the FSPM machine, the magnets are in the stator. Un unbalanced back EMF could be observed if one of the magnets has a different remnant flux density or sizing from the others.

The open circuit test is done by spinning the test motor with the test motor. The three-phase line-to-line voltages are measured by an oscilloscope via high-voltage differential probes. The three-phase voltage waveforms for the DLCW and SLTW 6/4 FSPM prototype motors are shown in Figure 6.3-2 (a) and Figure 6.3-2 (c), respectively. As can be seen, the three-phase back EMFs for the two prototypes are well balanced and are close to the sinusoidal waveform. The amplitudes of the measured back EMF of the two prototype motors match very well with the simulated back EMF waveform. To have a better quantitative comparison, the harmonic components of the back EMF are given in Figure 6.3-2 (b) and Figure 6.3-2 (d), respectively. The difference between the measured data and the simulation results of the fundamental component of the back EMF is less than 4%, which means the manufacturing of the prototype motors is well done, and the magnet characteristics meet well with the datasheet numbers. The back EMF of the two prototypes is

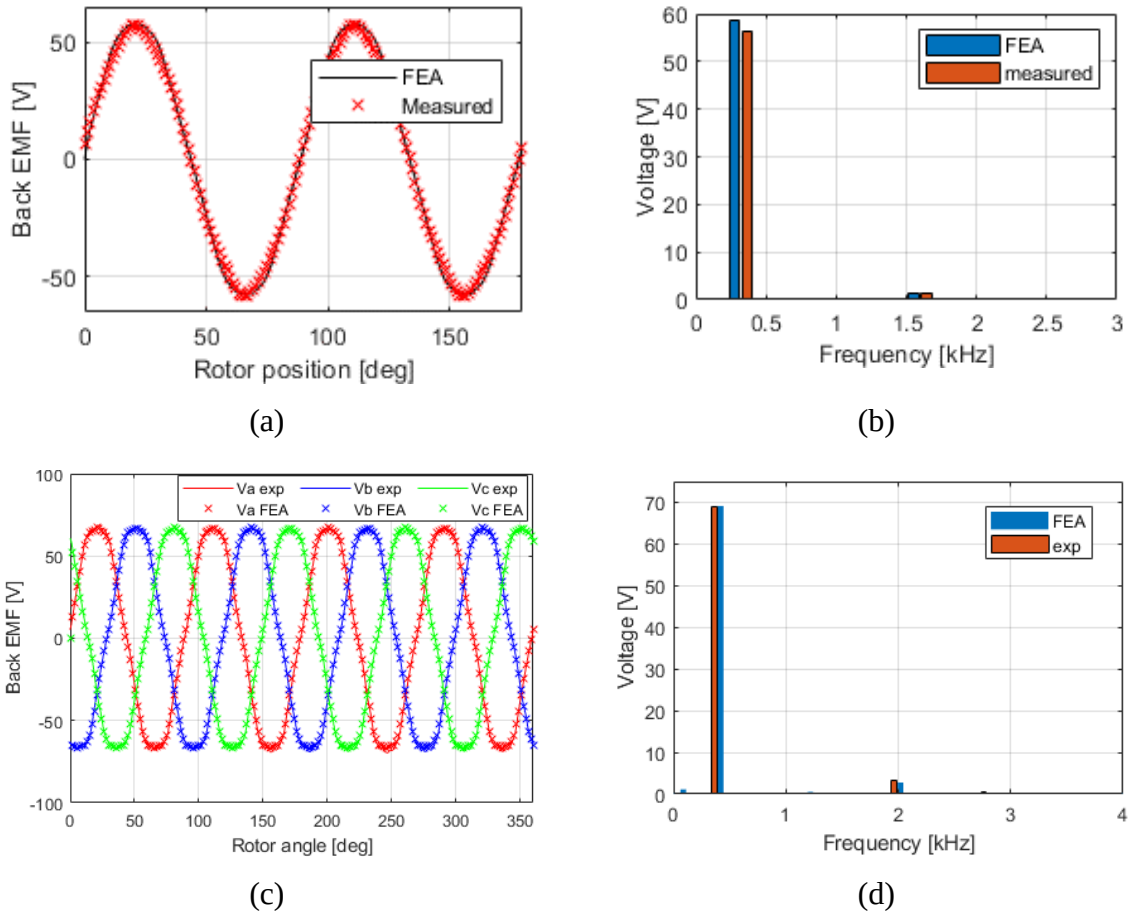

Figure 6.3-2. Measured three-phase back EMF of the prototype dual-stator 6/4 FSPM machine at 4800 rpm.

measured at different speed. As can be seen in Figure 6.3-3, the back EMF of both prototypes increase linearly with the speed.

B. Cogging torque of the prototype motors

The FSPM machine has a permanent magnet machine with double saliency structure. The cogging torque is produced while the rotor is sweeping across the stator teeth without armature current. The rotor poles tend to get aligned with the stator tooth and get away from the slot opening and magnet opening because the aligned position provides the least reluctance path. The cogging torque of FSPM machine is usually large because of the double saliency structure. The reluctance

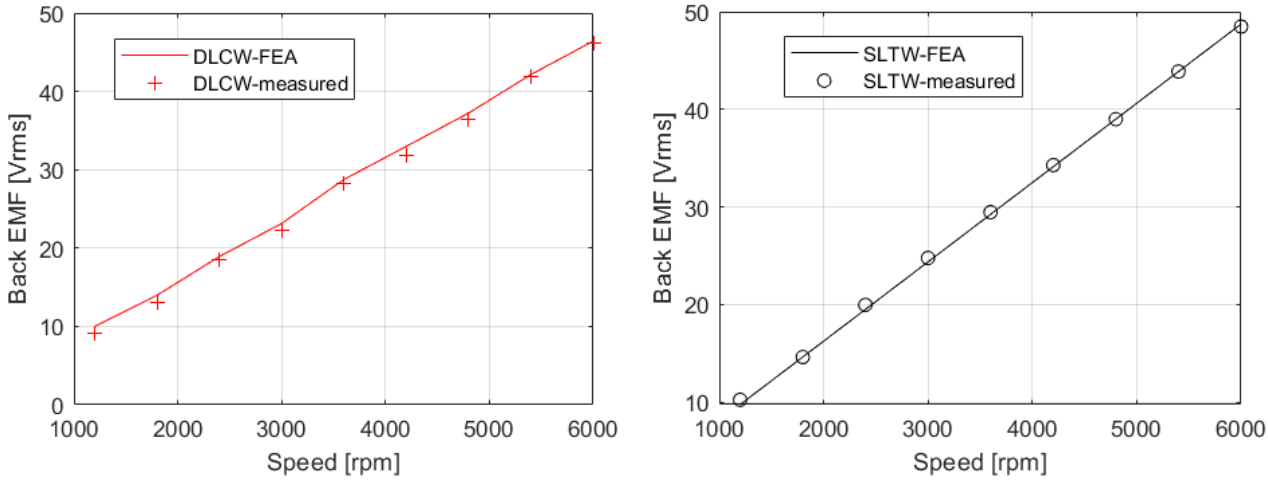

(a) (b)

Figure 6.3-3. Back EMF of prototype 6/4 FSPM motors at different speeds.

variation has been analyzed in Chapter 2. The two prototype 6/4 FSPM machines under test have step skewed rotors as shown in Figure 6.3-4 to reduce the cogging torque as well as the torque ripple [115]. The DLCW and SLTW 6/4 FSPM prototypes are designed to have the same sizing and power, and the different winding topologies do not affect the cogging torque. Therefore, the two prototype FSPM motors have the similar level of cogging torque.

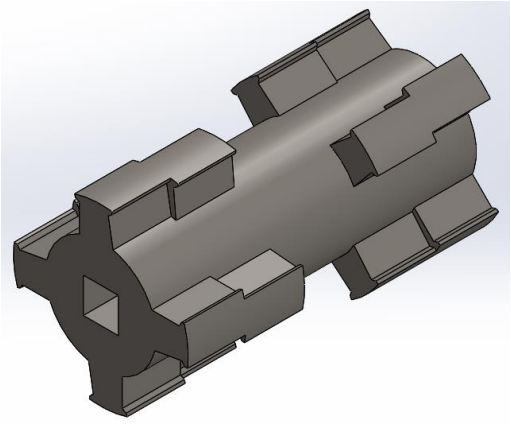

Figure 6.3-4. 3D view of the step skewed rotor for torque ripple reduction.

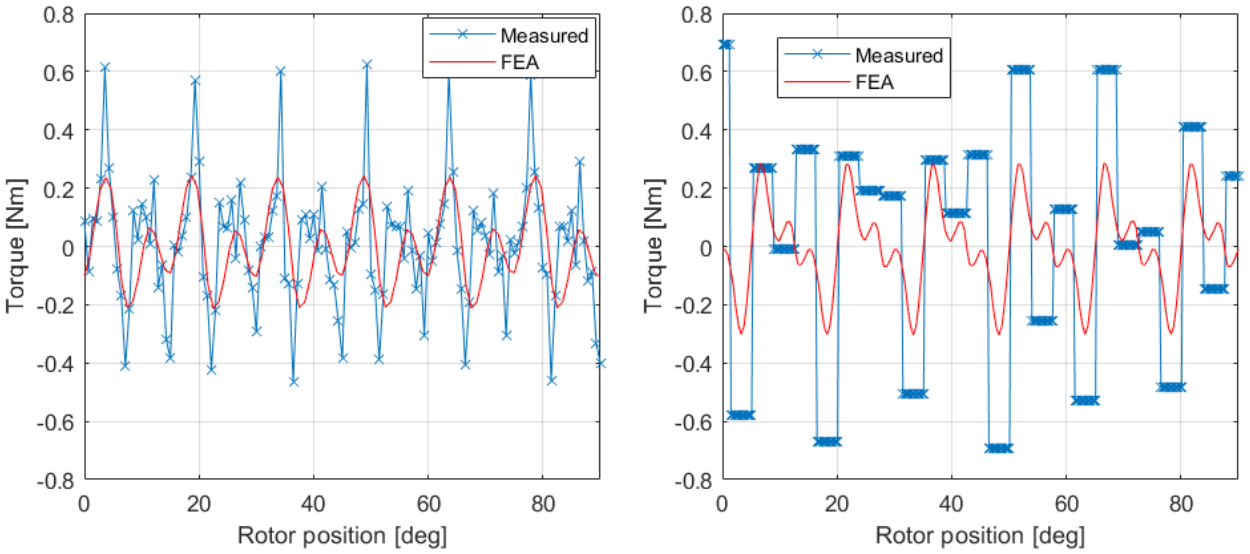

(a) (b)

Figure 6.3-5. Cogging torque waveform for the dual-stator 6/4 FSPM machine.

The cogging torque waveforms from the experimental measurement and FEA simulation for the DLCW and SLTW 6/4 FSPM prototypes are shown in Figure 6.3-5 (a) and Figure 6.3-5 (b), respectively. It can be seen that the period of cogging torque from FEA and experimental test matches well. For conventional FSPM machine, the number of cogging torque period per rotation equals to the least common multiplier (LCM) of the stator slot number and rotor pole number. Since the machine under study has a dual-stator structure, the cogging period per rotation is doubled. Therefore, there are 24 cogging periods per revolution. The torque of the two prototype motors are recorded by the same torque transducer, which has an accuracy of 0.5 Nm. In addition, the dyno motor also has a certain level of torque ripple that will influence the cogging torque measurement for the prototype motor. Therefore, the cogging torque difference between the measured data and the FEA result is in an acceptable range. For the SLTW prototype, the torque information is recorded by a faster data acquisition system. Therefore, the resolution of the SLTW prototype cogging torque waveform is higher than the DLCW prototype.

C. Mechanical loss and no-load iron loss

Note that during no-load test, the recorded torque has a non-zero average offset in the range of 0.1 Nm to 0.4 Nm depending on the rotation speed. The non-zero torque is caused by the mechanical loss and the no-load iron loss. The mechanical loss is from the bearing friction and the windage drag, which cannot be modeled with the FEA simulation. There is varying magnetic field in the stator/rotor core even no armature current is applied and causes no-load iron loss. The no-load dragging torque and loss are recorded at different speeds, as shown in Figure 6.3-6 (a) and Figure 6.3-6 (b), respectively. The no-load iron losses are simulated with FEA tool. The mechanical losses are compensated in the experimental results of the electromagnetic performance. The mechanical dragging power is interpolated with a third order polynomial as (Equation 6-3), where n is the rotation speed in rpm.

$$P_{mech\ loss} = 5.043n - 1.744n^2 + 0.789n^3 \qquad \text{(Equation 6-3)}$$

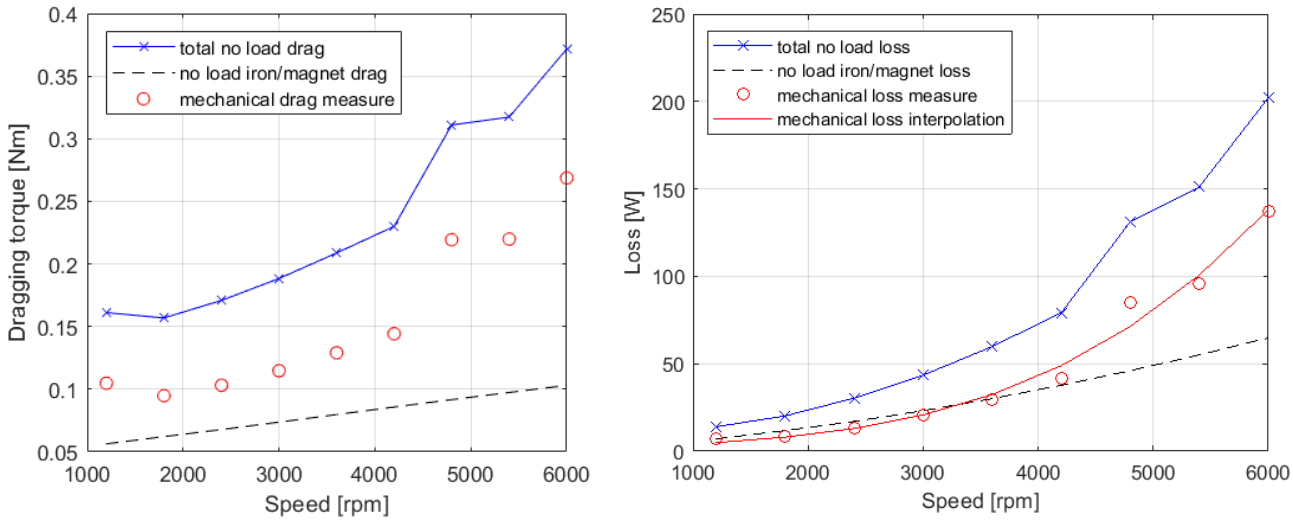

(a) (b)

Figure 6.3-6. Mechanical dragging powr and no-load iron loss (a) Torque and (b) Loss

6.3.3. Loaded test

A. Torque production characteristics

From the control prospective, FSPM machine has negligible saliency because both *d*-axis and *q*-axis flux pass through the permanent magnets in the stator, and the permanent magnet has almost the same permeability as air. Therefore, the FSPM machine can be controlled in the same

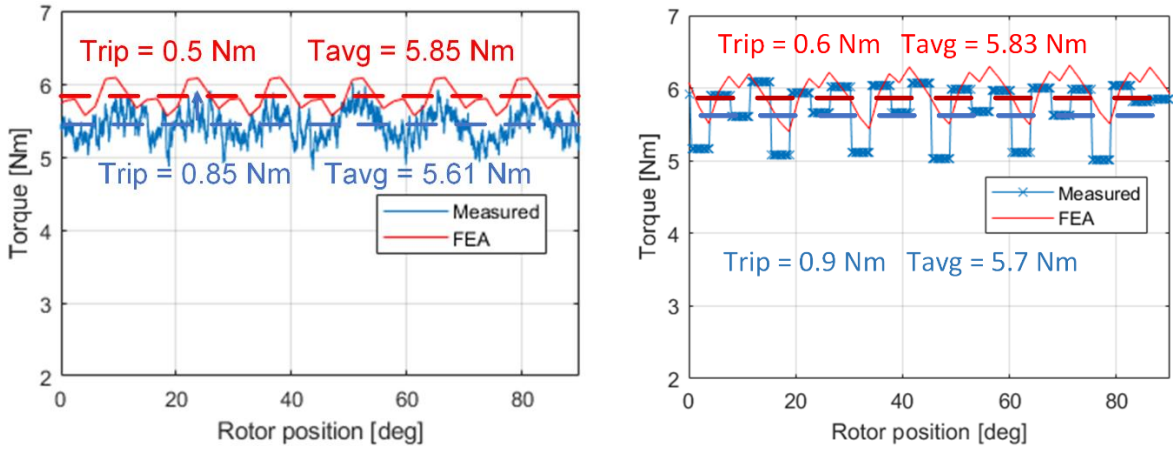

(a) (b)

Figure 6.3-7. Rated output torque waveform of (a) DLCW 6/4 FSPM machine and (b) SLTW 6/4 FSPM machine.

way as for the SPM machine, i.e. zero *d*-axis current control. Without considering the saturation, the output torque should be proportional to the armature current amplitude, which is also the *q*-axis current. The waveforms of the rated output torque of the DLCW and SLTW 6/4 FSPM prototype motors are shown in Figure 6.3-7 (a) and Figure 6.3-8 (b), respectively. Although the resolutions of the data are different for the two prototypes testing because different dataloggers are used, the torque ripples from the two machines can be clearly observed. The two prototype machines have the similar rated output torque and the same torque ripple periodicity. For both prototype machines, the measured torque match with the FEA simulation within 5%. Note that the

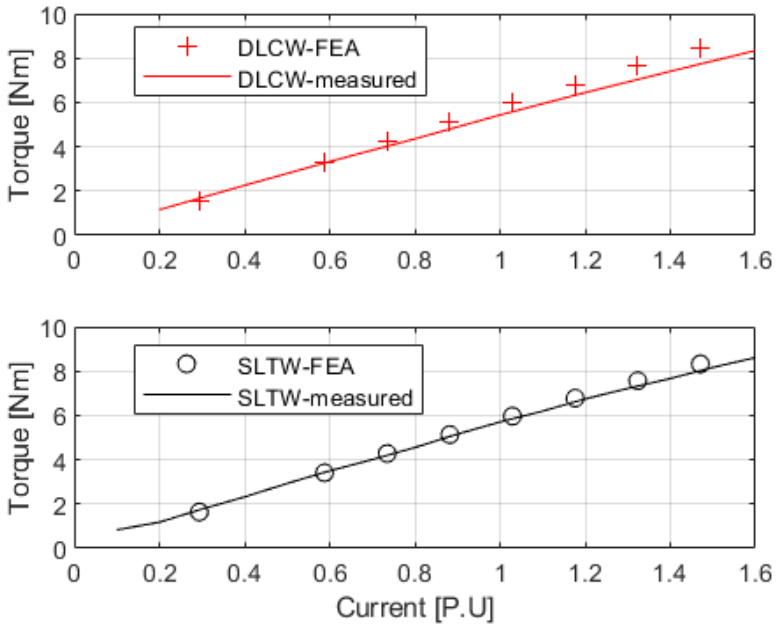

Figure 6.3-8. Output torque characteristics of the dual-stator 6/4 FSPM machine (a) Torque-current curve (b) Output torque waveform

mechanical losses of the two machines are not simulated in the FEA and are compensated as shown in the previous section.

The FSPM machine has a spoke-type magnet in the stators, and the flux-focusing effect allows the FSPM machine has a high flux density in the air gap and stator teeth. Therefore, the overload capability of FSPM machine is limited. Different levels of armature current are injected to investigate the torque-current relation. The current command is changed from 0 p.u. up to 1.6 p.u. The torque-current curves of the DLCW and SLTW dual-stator 6/4 FSPM machine from experimental measurement and FEA simulation are shown in Figure 6.3-8. The measured torque matches well with the simulated value within 5% under or at the rated operating point. Beyond the rated operating point, the measured torque is less than the simulated torque. It is probably because at overloading condition, the magnets are getting hot and the remnant flux is reduced, which causes the reduction of output torque.

As mentioned in chapter 2, FSPM machine has negligible saliency, i.e. inductances in *d*-axis and *q*-axis are almost identical. Therefore, zero *d*-axis control is applied at and before rated speed. The output torque can be expressed by (Equation 6-4). To verify the claim, the output torque

$$T_{out} = \frac{3P}{2}\lambda_{PM} I_q \cos\gamma \qquad \text{(Equation 6-4)}$$

is measured at different current angle γ. The current angles are varied from 0° to 90° in a stair step fashion. The current angles are controlled by varying the PM machine offset angle in the drive parameters list. As shown in Figure 6.3-9, the torque is maximum at the zero current angle and become zero when γ = 90°, which indicates a zero *q*-axis current.

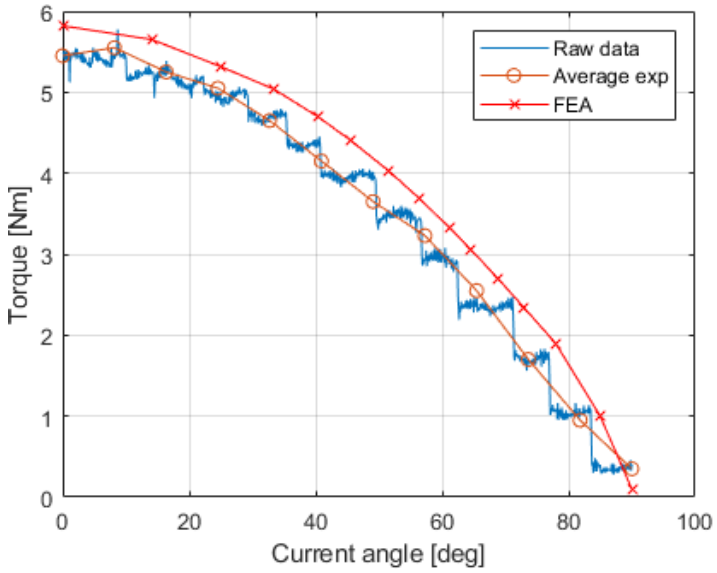

Figure 6.3-9. Torque versus current angle in dual-stator 6/4 FSPM machine

B. Prototype motors losses and efficiencies

As mentioned previously, the electrical input power and the mechanical output power are measured and recorded by the power analyzer. The total machine operating loss includes the

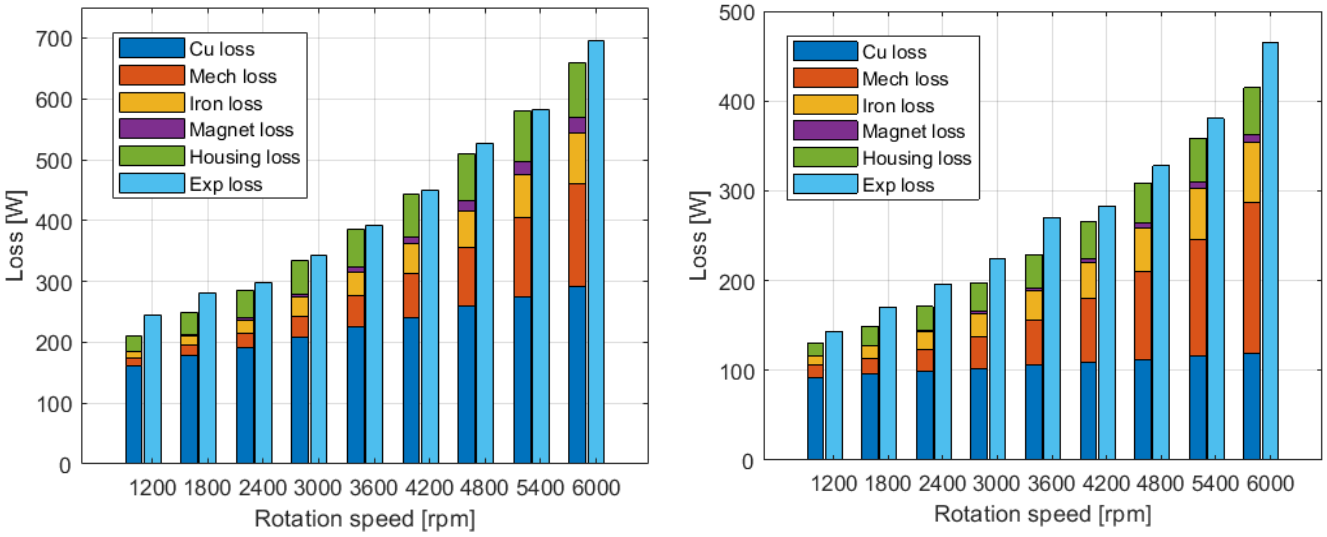

(a) (b)

Figure 6.3-10. Loss comparison between measured data and simulation results

copper loss, stator/rotor iron loss, magnet eddy current loss, housing eddy current loss, and mechanical loss. The copper loss can be calculated based on the measured winding impedance calibrated by the winding temperature, and the mechanical loss can be estimated by subtracting no-load iron loss from the total no-load dragging power. However, the iron loss and the magnet/housing loss cannot be easily segregated.

TABLE 6-4. COMPARISON OF OPERATING PARAMETERS BETWEEN TESTING AND FEA SIMULATION

Parameters	DLCW		SLTW	
	FEA	Exp	FEA	Exp
Output torque (Nm)	5.85	5.61 (-4.1%)	5.83	5.70 (-2.2%)
Speed (rpm)	3000		3000	
Output power (W)	1837.8	1762.4 (-4.1%)	1831.5	1790.7 (-2.2%)
Voltage (Vrms)	29.2	31.1 (+6.5%)	30.2	31.9 (+5.6%)
Current (Arms)	24		24	
Copper loss (W)	221.7	221.7	102.2	102.2
Iron/Mag/House loss	54.8	64.4 (+17.5%)	55.6	66.4 (+19%)
Efficiency (%)	86.9	86.0 (-0.9%)	92.0	91.4 (-0.6%)

The estimated losses are compared with measured losses at different speeds for the two prototype motors, as shown in Figure 6.3-10. It can be seen that the copper losses are increasing with speed because of the ac winding resistance shown previously. The iron loss and the magnet and housing eddy current loss are also increasing as the speed goes up. The difference between the FEA simulated loss and the measured loss is around 10% for the test speed range. Higher speed testing cannot be achieved because of the limitation of the test bench. A detailed machine loss comparison is done at the speed of 3000 rpm for both prototype motors, as shown in TABLE 6-4. The discrepancy of the predicted and measured data for the iron loss and the magnet/housing loss comes from the PWM induced iron loss. The PWM induced iron loss is not considered in the FEA simulation because a sinusoidal current source is used to power the machine.

C. Power factor

Power factor is an important characteristic of electric machines. To deliver the same output power, low power factor machine requires high VA rating of the drive, which either has a high voltage stress or has larger current that introduce extra loss. The power factor of electric machine can be calculated with (Equation 6-5), where E is the back EMF of the machine, R_s and X_q are the

$$PF = \cos\delta = \frac{E + R_s I_q}{\sqrt{(E + R_s I_q)^2 + (X_q I_q)^2}} \qquad \text{(Equation 6-5)}$$

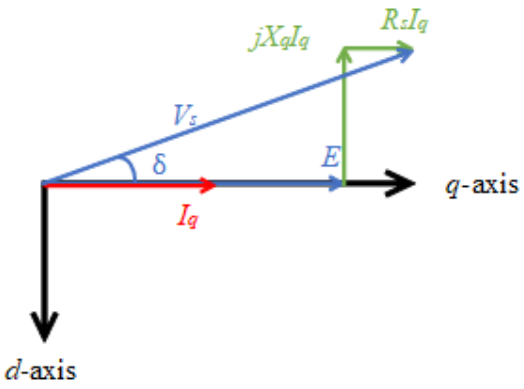

Figure 6.3-11. Phasor diagram of 6/4 FSPM machine with zero *d*-axis current control

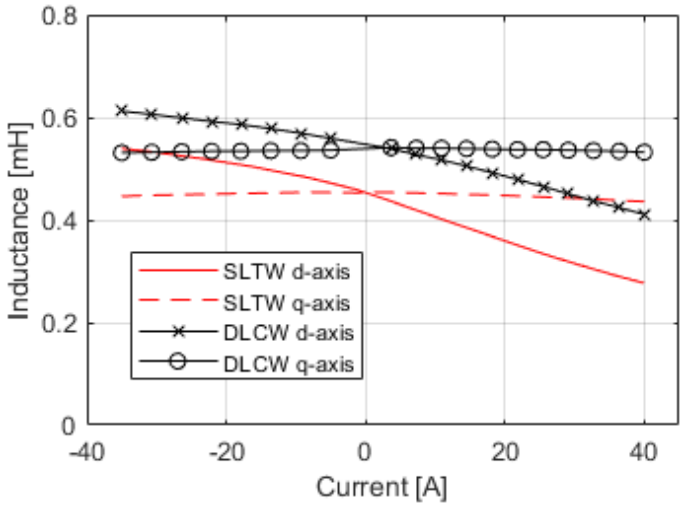

Figure 6.3-12. *d*-axis and *q*-axis inductance variation due to iron saturation

winding resistance and the *q*-axis reactance, respectively, I_q is the *q*-axis current value. The phasor diagram shown in Figure 6.3-11 helps to understand how the non-unity power factor occurs. The power factor is the cos value of the angle δ. The DLCW and SLTW 6/4 FSPM machine inductances are shown in Figure 6.3-12. The derivation of FSPM machine inductance can be found in Chapter 2 and is not repeated here.

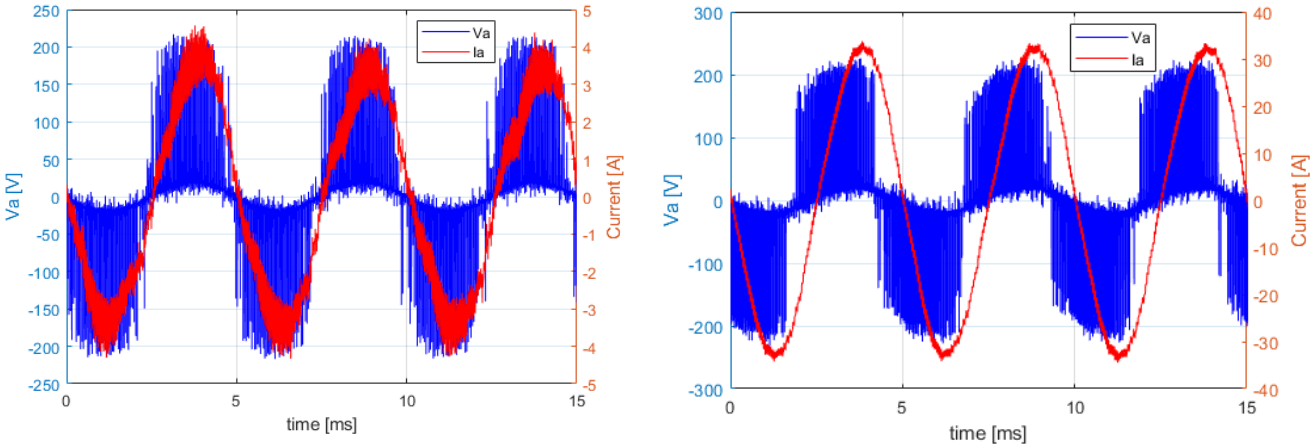

(a) (b)

Figure 6.3-13. Phase A current and voltage waveform at (a) Light load (b) Full-load

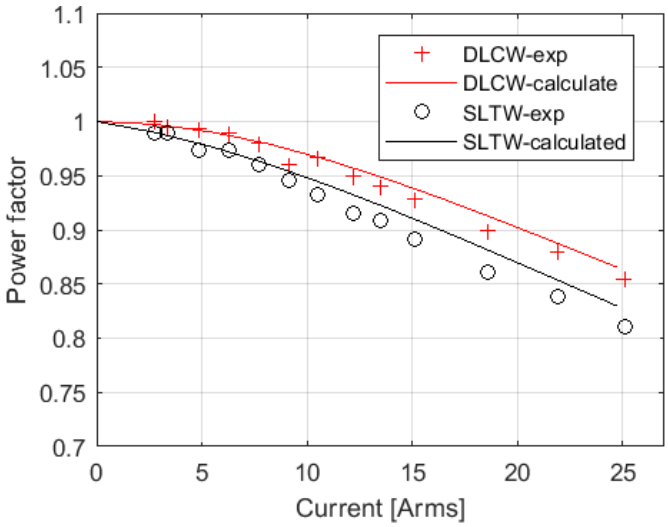

Figure 6.3-14. Power factor of dual-stator 6/4 FSPM machine

The angle δ shown in (Equation 6-5) is the angle between the phase of the motor terminal voltage and the armature current. As shown in Figure 6.3-13 (a), the armature current is almost in-phase with the terminal voltage at light load condition, which means the power factor is close to one. In Figure 6.3-13 (b), the current has a larger phase shift versus the voltage at the rated load condition, which leads to a lower power factor.

The SLTW 6/4 FSPM machine has a slightly lower inductance but also a smaller winding resistance than the DLCW 6/4 FSPM machine. At lower speed, where the reactance of the machine is not as large, the DLCW machine has a higher power factor. However, at high-speed, where the machine reactance dominant, the SLTW machine has the higher power factor. The relation between the power factor and the current are shown in Figure 6.3-14 for both machines at 3000 rpm. As can be seen, at this speed, the SLTW machine has a slightly lower power factor than the DLCW machine. The measured power factor matches well with the calculated value. The power factor decreases with the current increases as predicted in the previous part.

6.4. Thermal testing of dual-stator 6/4 FSPM machine

To verify the thermal performance of the 6/4 FSPM machine and to validate the thermal analysis for the DLCW and SLTW 6/4 FSPM machine conducted in Chapter 4, experimental thermal testing is carried out for the two 6/4 FSPM machine prototypes. The thermal test equipment and test setup have been introduced in Section 6.2. The motor temperatures are monitored with embedded RTD sensors. A 20-channel data logger is used to read and record the signals from the RTDs, as shown in Figure 6.4-1. The reference zero temperature resistance and

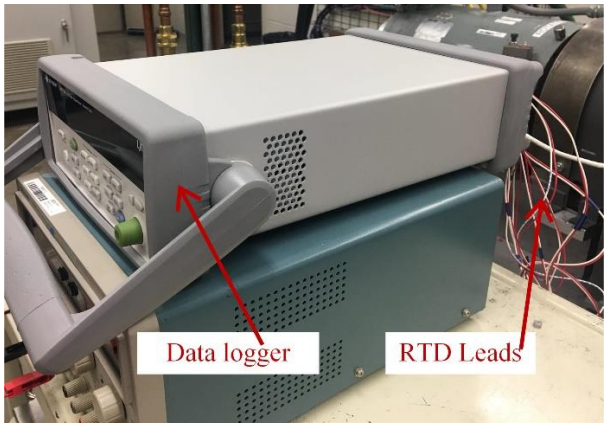

Figure 6.4-1. Data logger for temperature recording.

the temperature gain should be set correctly to get an accurate measured temperature. The updating rate of the data logger is 1.67 s, which is enough to show the dynamics of temperature variation. The data logger is connected to the desktop computer via Ethernet cable. Temperature data are recorded simultaneously as the test is going on. The cooling device such as the water jacket and cooling pump is introduced in the previous section and is not repeated here.

To monitor the temperature of the prototype machine rotor, an Infrared thermal camera is used to measure the rotor surface temperature through the opening on the motor end cap, as shown

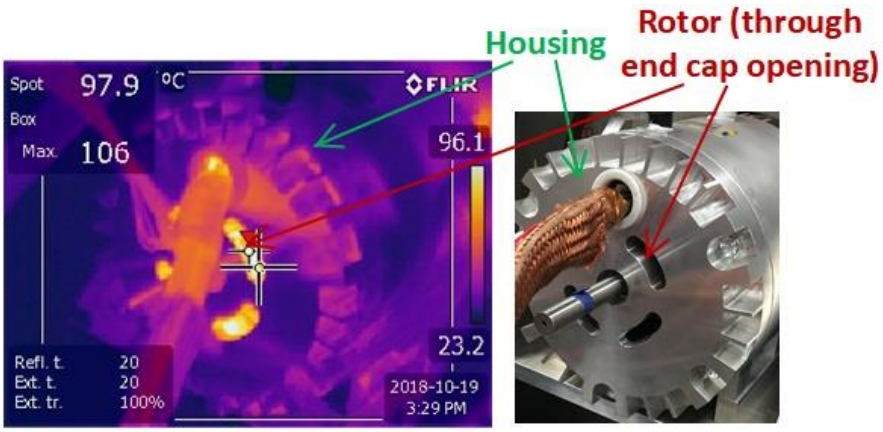

Figure 6.4-2. IR image of the dual-stator 6/4 FSPM motor at thermal steady state.

in Figure 6.4-2. Note that no person is allowed staying in the dyno room while the testing is going on and the thermal camera is not on throughout the whole test. Therefore, the temperature of the rotor is taken quickly after the motor is turn off, and only steady state rotor temperature is captured.

6.4.1. Steady state thermal testing and comparison

The cooling design and the thermal performance of the DLCW and SLTW dual-stator 6/4 FSPM machine have been analyzed in Chapter 4. The steady state thermal behavior has been investigated with lumped parameter thermal network (LPTN), and it is shown that the SLTW 6/4 FSPM machine encapsulated with EFI-108 resin have a much lower steady state temperature than the DLCW 6/4 FSPM machine with the same slot current density.

To validate the LPTN models for the steady state rated operation, the DLCW and SLTW 6/4 FSPM prototype motor are run at 4800 rpm with rated torque command. The test starts from the room temperature (23°C) until thermal steady state. The cooling channel inlet temperature is controlled to be 23 °C as well. The cooling channel outlet temperature is measured to be 27 °C, and the flow rate is 5.5 LPM. Note that at rated torque condition, the slot current density of the two machines are 9.2 A_{rms}/mm^2.

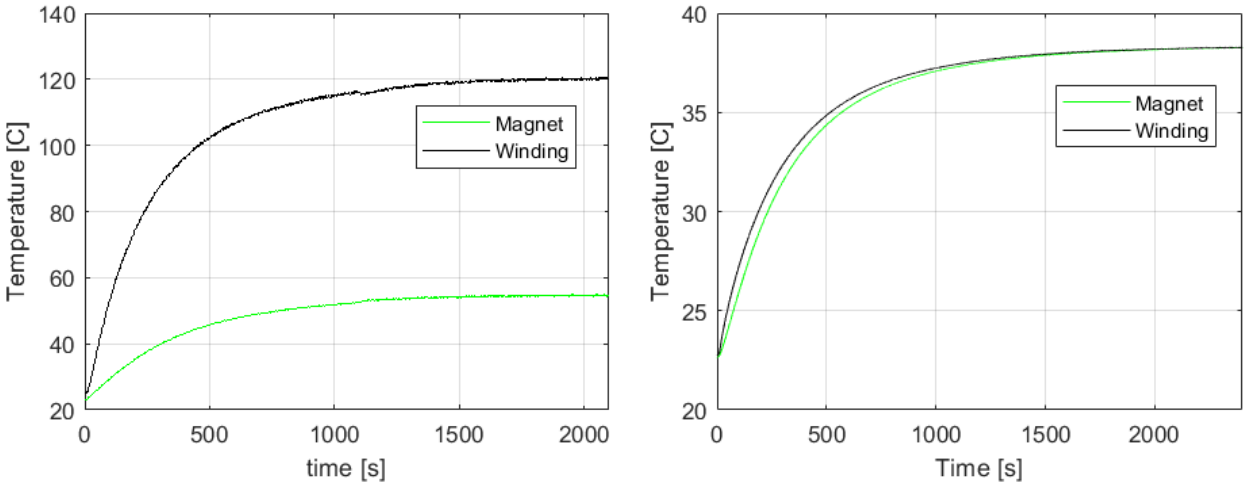

(a) (b)

Figure 6.4-3. Temperature rise of different parts of the prototype motor till steady state (a) DLCW 6/4 FSPM machine, (b) SLTW 6/4 FSPM machine

The temperature variations of the machine winding and the permanent magnet for the two prototypes are shown in Figure 6.4-3 (a) and Figure 6.4-3 (b), respectively. As can be seen, with the same stator slot current density, the temperature of the SLTW 6/4 FSPM machine with EFI-108 encapsulation is much lower than the DLCW 6/4 FSPM machine with CC-1105 encapsulation. In addition, the DLCW 6/4 FSPM prototype motor reaches thermal steady state after about 30 minutes, while the temperature of the SLTW 6/4 FSPM prototype takes about 20 minutes to stabilize. The SLTW 6/4 FSPM machine reaches steady state faster because its winding thermal resistance is smaller than that of the DLCW machine, as shown in Chapter 4. Therefore, the thermal time constant with the unit of second, which calculated as $\tau = RC$, of the SLTW 6/4 FSPM machine is smaller than the DLCW machine.

The temperature gradient among the machine components of SLTW machine is smaller than the DLCW machine. This is because the encapsulation material used for the SLTW machine has

ten times higher thermal conductivity, and the toroidal winding topology allows a better cooling for the winding coil.

Many factors during the experiment can affect the machine temperature during the test. The LTPN model only provides the results of the thermal steady state. Therefore, in order to validate the LTPN model, two slot current density level are tested for each topology. According to the thermal analysis shown in Chapter 4, the current density limit of the DLCW machine is 11.2 Arms/mm^2. Therefore, the DLCW machine is tested with 5 Arms/mm^2 and 9.2 Arms/mm^2. The SLTW machine has a much higher current density limit and is tested with 7.2 Arms/mm^2 and 10.8 Arms/mm^2. The steady state temperatures of the two machines from the experimental testing are compared with the results from the LPTN models, as shown in TABLE 6-5 and TABLE 6-6, respectively. As can be seen from the table, for the two operating points of each prototype, the

TABLE 6-5 TEMPERATURE DISTRIBUTION (°C) OF THE DLCW 6/4 FSPM MACHINE AT DIFFERENT CURRENT DENSITIES

	Temp. (°C) 5 Arms/mm^2			**Temp. (°C) 9.2 Arms/mm^2**		
	LPTN	Exp	Error	LPTN	Exp	Error
Stator	38.1	41.1	(+7.3%)	52.7	56.3	(+6.8%)
Coil	58.7	57.5	(-2.1%)	121.5	115.1	(-5.3%)
Rotor	83.9	87.3	(+3.9%)	91.4	97.9	(+6.6%)

TABLE 6-6 TEMPERATURE DISTRIBUTION (°C) OF THE SLTW 6/4 FSPM MACHINE AT DIFFERENT CURRENT DENSITIES

	Temp. (°C) 7.2 Arms/mm^2			**Temp. (°C) 10.8 Arms/mm^2**		
	LPTN	Exp	Error	LPTN	Exp	Error
Stator	37.0	36.6	(-1.1%)	43.2	44.1	(+2.0%)
Coil	37.1	33.5	(-9.7%)	48.7	46.6	(-4.5%)
Rotor	63.1	65.9	(+4.2%)	82.7	84.3	(+1.9%)

steady state temperatures estimated by the LPTN model match well with respect to the measured temperature within 10%. The errors come from the loss estimation and the convective heat transfer coefficients which are derived from CFD simulation.

6.4.2. Transient thermal testing

The transient thermal performance of the 6/4 FSPM machine has been analyzed in Chapter 4. It is shown that the winding of the machine together with the encapsulation, has a much slower thermal dynamics than the core and the magnet of the machine. In a time span of 60 seconds, the winding temperature rise is 5-10 times faster than the core and magnet temperature. This conclusion means that during a short period overloading operation, the winding is more likely to cause over-heating problem than the permanent magnet.

The transient thermal performance has been investigated with the thermal FEA simulation in Chapter 4. The long-time thermal transient behavior of the 6/4 FSPM machine is compared with the measured temperature variation, as shown in Figure 6.4-4 (a). It can be seen that the

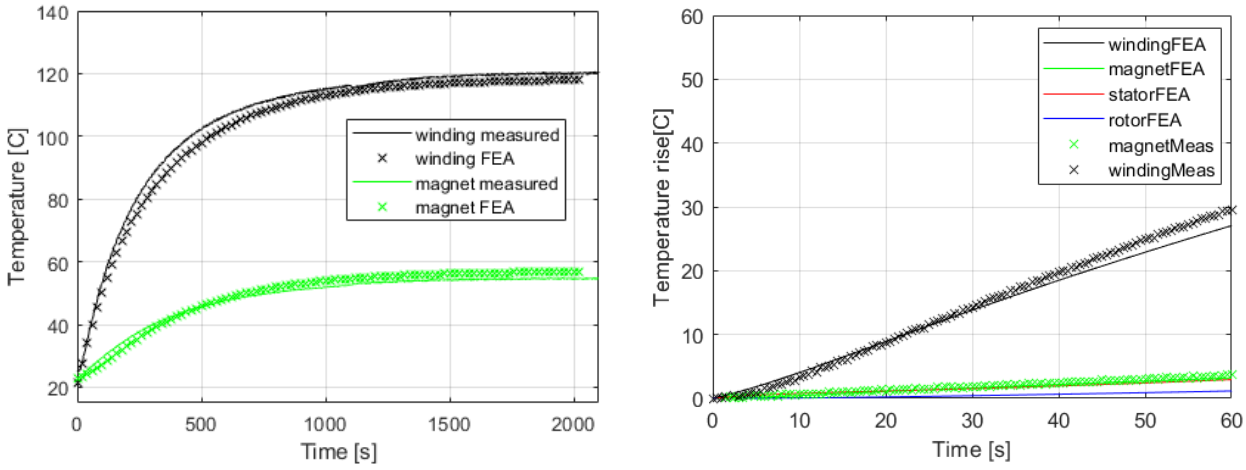

(a) (b)

Figure 6.4-4. Temperature rise of different parts of the prototype motor till steady state of different component inside the motor

temperature from FEA simulation matches well with measured value. To validate the short-time transient thermal behavior, the 6/4 FSPM machine is first run with rated current until thermal steady state. Then a 1.5 p.u. current is given for 60 second. The short-time transient temperature rise of the winding and the core/magnet are shown in Figure 6.4-4 (b). As can be seen, the measured temperature rise is slightly faster than the estimated temperature rise, but the error between the two is within 7%.

6.5. Summary

In this chapter, the prototyping, installing and testing of the prototypes of the DLCW and SLTW 6/4 FSPM motor are presented. Practices to reduce the manufacturing tolerance such as using single-piece stator lamination are developed. Features facilitating the installation such as the use of eyebolts and cable glands are added to the SLTW FSPM prototype, according to the experience from the DLCW FSPM prototype.

The testing equipment information is given to ensure the repeatability of the testing. The machine static parameters are first measured and shows good agreement with the design thanks to the manufacturer's expertise in machine prototyping. The electromagnetic and thermal characteristics predicted by the analytical calculation and FEA simulation shown in the previous chapters are verified by the experimental testing. The results from the no-load and loaded tests show good agreement with the FEA simulation with explanation error. The thermal testing verifies the steady state LPTN model and the transient thermal FEA model.

Chapter 7 Conclusion and Future Work

7.1. Research conclusions

The main conclusions of this research are summarized in this section. Low-pole (6/4) FSPM machine is identified as the research focus because of its robust rotor structure, easy thermal management, and relatively low fundamental frequency. The operation principle and popular slot/pole combinations of FSPM machine are reviewed. The second-order harmonic in the flux linkage of the 6/4 FSPM machine is explained and the harmonic cancellation achieved by the dual-stator structure is illustrated. The winding factor calculation for the 6/4 FSPM machine with EMF vector graph is presented. It is shown that the use of single-layer winding could significantly increase the winding factor of the 6/4 FSPM machine. The proposed single-layer toroidal winding (SLTW) 6/4 FSPM topology is shown to be able to achieve higher efficiency and better thermal performance than the original design. Multi-physics design for the 6/4 FSPM machine has been carried out, including the electromagnetic design, cooling system design, thermal analysis, and windage loss reduction.

Low-pole (6/4) FSPM machine

- FSPM machine is a promising candidate for high-speed applications due to the robust rotor structure and easy thermal management. However, the majority of existing FSPM machines have high pole-count which is not appropriate for high-speed operation from the loss minimization perspective.
- There are many possible slot/pole combinations for FSPM machine, and most of the FSPM machines employ non-overlapping concentrated winding. It is shown that high-pole FSPM machines usually have high winding factor because the slot-pole

ratio is close to 1. The double-layer concentrated winding 6/4 FSPM has only a winding factor of 0.5, which requires higher electric/magnetic loading to achieve the same output power.

- The winding factor of the 6/4 FSPM machine could be increased to unity by using single-layer winding. In addition, the single-layer topology can achieve higher slot filling factor compared to double-layer topology because no phase-phase insulation is need.
- Conventional circumferentially wound winding is not feasible for single-layer 6/4 configuration due to long end turn and thick overlapping between phases. As an alternative, toroidal winding is easy to assemble and makes the single-layer 6/4 FSPM machine possible for manufacture.

Comparison between single and double-layer 6/4 FSPM machine

- The change of winding topology causes variation of the stator core geometry (from U-shape to H-shape). Optimization study suggests a wider stator and rotor tooth than the DLCW 6/4 FSPM machine to obtain the best performance.
- The optimized single-layer toroidal winding (SLTW) and the double-layer concentrated winding (DLCW) dual-stator 6/4 FSPM machines are compared. The machines are designed to have the same back EMF, same power, and same speed. The SLTW topology require lower electric loading due to the high winding factor. Therefore, the copper loss of the SLTW machine is significantly reduced and has 5% higher efficiency than the DLCW machine at 3000 rpm.
- The SLTW 6/4 FSPM machine has a lower inductance and resistance. The power factor of the two machine depends on the speed and load level. The DLCW machine

has higher power factor at low speed region, and the SLTW machine has higher power factor at high speed region.

Cooling system and thermal analysis of FSPM machine

- Having both permanent magnet and armature winding in the stator, FSPM machine can be effectively cooled by water jacket cooling. Meanwhile, having the temperature sensitive component and the major heat source together requires careful thermal analysis.
- Steady state thermal analysis has been done with lumped-parameter thermal network (LPTN) based on the geometry of the machine. Thermal finite element analysis (FEA) can be used to investigate the transient thermal behavior. Convective heat transfer needs to be characterized with computational fluid dynamics (CFD).
- Water jackets with spiral and axial cooling channel have been investigated. The spiral channel has lower pressure drop and less turbulence than the axial channel. But the inlet/outlet position is not as flexible as the axial channel.
- The winding topology and the winding encapsulation material have significant impact on the thermal performance of the machine, especially the winding temperature. When only consider the thermal constraint, with the same temperature limit, the SLTW FSPM machine with a good encapsulation material can achieve three times higher slot current density than the DLCW FSPM machine with conventional encapsulation material.
- The winding/encapsulation has a much faster thermal dynamic than the stator core and magnet. For a 60s short-time overloading operation, the winding temperature increase is 5 – 10 times larger than the temperature increase of the stator/magnet.

- The DLCW and SLTW 6/4 FSPM prototype motors with temperature sensors embedded are built. The thermal steady state and thermal transient testing have been conducted. The experimental results are compared with the simulation and show good agreement.

Housing loss and windage loss of FSPM machine

- Housing loss for FSPM machine is investigated with 3D FEA simulation to make sure whether the use of toroidal winding has introduced unacceptable extra housing loss. It is shown that the magnetic flux density variation is much larger near the magnet than near the returning coil of the toroidal winding. Therefore, the stator-mounted permanent magnet is the main cause of high eddy current loss.
- The housing loss due to the stator-mounted permanent magnet could be reduced by having a thin iron bridge outside the magnet or leaving cavity in the housing at the vicinity of permanent magnet. Housing cavity can reduce the housing loss by 60% without compromising the output power. However, axial channel water jacket is needed if the cavity is employed.
- Windage loss is not negligible for FSPM machine at high-speed operation because of the axial air flow due to the salient rotor. Windage loss could be effectively reduced by adding shrouds to the end of the rotor. The shrouded rotor can reduce the windage loss by 80%, with no torque reduction. The use of shrouded rotor reduces the air gap convective heat transfer. But the rotor only consists lamination steel and is not sensitive to temperature variation.

7.2. Research contributions

The major contributions of the research are summarized as follow

Proposed No Middle End-Turn Dual-Stator 6/4 FSPM Machine

- The origin of the second-order harmonic in the flux linkage of the 6/4 FSPM machine is analyzed. The second-order harmonic cancellation realized by two shifted stators with no middle end-turn coil is proposed.
- Compare the performance of original dual-stator 6/4 FSPM machine and the no middle end-turn design. The benefit of the no middle end-turn design is illustrated with FEA simulation.

Proposed single-layer toroidal winding dual-stator 6/4 FSPM machine

- The winding factor of 6/4 FSPM machine is calculated and the realization of high winding factor design with single-layer structure is illustrated. The sizing equation for 6/4 FSPM machine is derived. Manufacturing difficulties of the single-layer winding topology are identified.
- Single-layer toroidal winding 6/4 FSPM machine is proposed to solve the manufacturing challenges of the single-layer winding design. Machine parameters of the single-layer and double-layer winding designs are calculated.

Compared the performance of the proposed 6/4 FSPM machines

- The sizing parameters of the single-layer toroidal winding 6/4 FSPM machine are optimized. Single-layer and double-layer winding dual-stator 6/4 FSPM machines with the same volume and output power are designed and compared to illustrate the benefit of the proposed single-layer winding design.
- Finite element analysis models are built to simulate the electromagnetic performance of the single-layer and double-layer winding dual-stator 6/4 FSPM machine.

Designed the cooling system and conducted thermal analysis for 6/4 FSPM machine with single-layer and double-layer winding

- Water jacket with spiral and axial cooling channel have been designed. The cooling performance is investigated with computational fluid dynamics simulation. The benefits and drawbacks of each type are identified.
- Thermal analysis of the single-layer and double-layer winding dual-stator 6/4 FSPM machine is conducted. Different winding encapsulation materials are investigated. The influence brought by the winding topology and encapsulation material are investigated.

Investigated the special design consideration for FSPM machine

- Housing loss of the FSPM machine is investigated. The housing loss of the toroidal winding design is investigated. The major source of housing loss is identified and modified machine structures to reduce the housing loss are proposed.
- Windage loss of the dual-stator 6/4 FSPM machine at high-speed operation is studied. Impacts on the electromagnetic performance brought by the modified rotor structures for windage loss reduction have been investigated.

Built prototype motor and conduct experimental tests

- The design of the single-layer and double-layer winding dual-stator 6/4 FSPM machines are prototyped. The prototype motors are equipped with cooling jacket and temperature sensors to conduct thermal testing.
- The prototype motors are installed on the dynamometer test bench. Open-circuit and loaded tests are conducted to validate the analytical calculation and finite element simulation results.

- Steady state and transient thermal testing are conducted to validate the LPTN and FEA thermal models built for the single-layer and double-layer dual-stator 6/4 FSPM machines.

7.3. Remaining work

Investigation of 6/4 FSPM machine with ferrite magnet

Rare-earth permanent magnet with high remnant flux density is usually used in electric machine to achieve high power density. FSPM machine has the potential to have high air gap flux density due to the flux-focusing effect even with low-cost ferrite magnet. In addition, the FSPM machine is less vulnerable to demagnetization compared to SPM or IPM machine. Therefore, the trade-off between the cost and the performance for the FSPM machine with rare-earth permanent magnet or ferrite magnet would be different for SPM or IPM machines. Considering the low magnet eddy current loss due to the high electrical resistivity, the ferrite 6/4 FSPM Machine could be a good candidate for high-speed or low-cost application.

Fault tolerance analysis of 6/4 FSPM design

Fault-tolerant capability is an important aspect of the electrical machine designs, especially in the applications related to aerospace, transportation, and industry, etc. Investigations on the fault-tolerance characteristics of 6/4 FSPM machine with different winding topologies are meaningful. Identify the advantages and disadvantages and compare them with respect to the electric machines that are used currently would help the improvement of the industry.

Acoustic noise and structural stress analysis of 6/4 FSPM machine

For applications such as home appliance and electric vehicle, the acoustic noise of electric machine is very important and affects the user experience. According to the literature, one of the major sources of the acoustic noise of electric machines including the FSPM machine is the

ovalization of the stator core due to the radial/tangential force. It is valuable to investigate possible acoustic noise reduction in FSPM machine. In addition, as mentioned in the prototype manufacturing section, iron bridges could be used to reduce the machine manufacturing complexity. The structural stress on the thin bridge needs to be investigated to avoid excessive shear stress that break the iron bridge connection.

Magnet in the stator gap

As shown in the thesis, certain gap between the two stators in the dual-stator 6/4 FSPM machine is needed to avoid magnetic flux leakage. On the other hand, the gap between the stators increase the machine volume without contributing to the output power. It is possible to reduce the length of the gap while preventing the magnetic flux leakage by inserting a permanent magnet between the two stators. The material, thickness, and the remnant flux of the magnet need to be investigated and optimized.

Dual-rotor SLTW 6/4 FSPM machine

In the single-layer toroidal winding 6/4 FSPM machine design, the returning coil placed outside the stator does not contribute the torque production. Dual-rotor design with toroidal winding have been investigated in some special applications such as in-wheel drive motor. The use of dual-rotor structure for the single-layer toroidal winding is particularly interesting because the second-order harmonic cancellation can be realized without using a dual-stator structure. As has been shown, the dual-stator structure requires gaps between the stator to avoid flux leakage. Therefore, the dual-rotor design can potentially further increase the power density and efficiency of the 6/4 FSPM machine.

Chapter 8 Reference

[1] D. Gerada, A. Mebarki, N. L. Brown, C. Gerada, A. Cavagnino, and A. Boglietti, "High-speed electrical machines: technologies, trends, and developments," *IEEE Trans. Ind. Electron.*, vol. 61, no. 6, pp. 2946–2959, Jun. 2014, doi: 10.1109/TIE.2013.2286777.

[2] M. T. Caprio, V. Lelos, J. D. Herbst, and J. Upshaw, "Advanced induction motor endring design features for high speed applications," in *IEEE International Conference on Electric Machines and Drives, 2005.*, 2005, pp. 993–998, doi: 10.1109/IEMDC.2005.195843.

[3] Z. Kolondzovski, A. Arkkio, J. Larjola, and P. Sallinen, "Power limits of high-speed permanent-magnet electrical machines for compressor applications," *IEEE Trans. Energy Convers.*, vol. 26, no. 1, pp. 73–82, Mar. 2011, doi: 10.1109/TEC.2010.2089459.

[4] E. Schubert and B. Sarlioglu, "Mechanical design method for a high-speed surface permanent magnet rotor," in *2016 IEEE Energy Conversion Congress and Exposition (ECCE)*, 2016, pp. 1–6, doi: 10.1109/ECCE.2016.7855239.

[5] L. Weili, L. Lin, L. Jinyang, S. Jiafeng, C. Junci, and L. Dong, "Influence of Sleeve Material on Electromagnetic Field Based on Multi-Physical Field for Permanent Magnet Synchronous Motor," in *2018 IEEE International Magnetic Conference (INTERMAG)*, 2018, pp. 1–6, doi: 10.1109/INTMAG.2018.8508607.

[6] S. S. Nair, J. Wang, L. Chen, R. Chin, and M. Beniakar, "Prediction of 3D eddy current loss in retaining sleeve of surface mounted permanent magnet machines," in *2017 IEEE International Electric Machines and Drives Conference (IEMDC)*, 2017, pp. 1–7, doi: 10.1109/IEMDC.2017.8002070.

[7] C. A.G., C. I.M., and H. G., "The stability of NdFeB magnets," in *IEE Colloquium on New Permanent Magnet Materials and their Applications*, 1989, pp. 4/1-4/2.

[8] D. Fernandez, D. Reigosa, A. B. Diez, J. M. Guerrero, and F. Briz, "Magnet Thermal and Magnetization State Monitoring in PMSMs Based on Magnet Resistivity Estimation," in *2018 IEEE 9th International Symposium on Sensorless Control for Electrical Drives (SLED)*, 2018, pp. 54–59, doi: 10.1109/SLED.2018.8486070.

[9] K. R. Rajagopal, B. Singh, B. P. Singh, and N. Vedachalam, "Novel methods of temperature compensation for permanent magnet sensors and actuators," *IEEE Trans. Magn.*, vol. 37, no. 4, pp. 1995–1997, Jul. 2001, doi: 10.1109/20.951032.

[10] A. Boglietti, A. Cavagnino, D. Staton, M. Shanel, M. Mueller, and C. Mejuto, "Evolution and Modern Approaches for Thermal Analysis of Electrical Machines," *IEEE Trans. Ind. Electron.*, vol. 56, no. 3, pp. 871–882, Mar. 2009, doi: 10.1109/TIE.2008.2011622.

[11] M. Roffi, F. J. T. E. Ferreira, and A. T. De Almeida, "Comparison of different cooling fan designs for electric motors," in *2017 IEEE International Electric Machines and Drives Conference (IEMDC)*, 2017, pp. 1–7, doi: 10.1109/IEMDC.2017.8002270.

[12] Y. Hou, X. Liu, J. Liu, M. Li, and L. Pu, "Experimental study on phase change spray cooling," *Exp. Therm. Fluid Sci.*, vol. 46, pp. 84–88, Apr. 2013, doi: 10.1016/J.EXPTHERMFLUSCI.2012.11.023.

[13] D. H. Lim and S. C. Kim, "Thermal performance of oil spray cooling system for in-wheel motor in electric vehicles," *Appl. Therm. Eng.*, vol. 63, no. 2, pp. 577–587, Feb. 2014, doi: 10.1016/J.APPLTHERMALENG.2013.11.057.

[14] W. Sixel, M. Liu, and B. Sarlioglu, "Rotor Thermal Design for Electric Machines: Challenges and Opportunities," in *2018 IEEE Transportation Electrification Conference and Expo (ITEC)*, 2018, pp. 821–826, doi: 10.1109/ITEC.2018.8450185.

[15] S. A. McElhinney, T. M. Jahns, and T. A. Shedd, "Centrifugally pumped thermosiphons for motor rotor cooling," in *Volume 3: Advanced Fabrication and Manufacturing; Emerging Technology Frontiers; Energy, Health and Water- Applications of Nano-, Micro- and Mini-Scale Devices; MEMS and NEMS; Technology Update Talks; Thermal Management Using Micro Channels, Jets, Sprays*, 2015, p. V003T04A011, doi: 10.1115/IPACK2015-48516.

[16] J. Rao, R. Qu, J. Ma, and W. Xu, "Investigate the influence of magnetic bridge design on mechanical strength and electromagnetic characteristics in high speed IPM machines," in *2014 17th International Conference on Electrical Machines and Systems (ICEMS)*, 2014, pp. 22–27, doi: 10.1109/ICEMS.2014.7013444.

[17] R. Lin, S. D. Sudhoff, and C. Krousgrill, "Analytical method to compute bridge stresses in V-shape IPMs," *IET Electr. Power Appl.*, vol. 12, no. 7, pp. 938–945, Aug. 2018, doi: 10.1049/iet-epa.2018.0053.

[18] M. Cheng, W. Hua, J. Zhang, and W. Zhao, "Overview of stator-permanent magnet brushless machines," *IEEE Trans. Ind. Electron.*, vol. 58, no. 11, pp. 5087–5101, Nov. 2011, doi: 10.1109/TIE.2011.2123853.

[19] Chunhua Liu, K. T. Chau, J. Z. Jiang, and Shuangxia Niu, "Comparison of Stator-Permanent-Magnet Brushless Machines," *IEEE Trans. Magn.*, vol. 44, no. 11, pp. 4405–4408, Nov. 2008, doi: 10.1109/TMAG.2008.2002632.

[20] B. Sarlioglu, Yifan Zhao, and T. A. Lipo, "A novel doubly salient single phase permanent magnet generator," in *Proceedings of 1994 IEEE Industry Applications Society Annual Meeting*, pp. 9–15, doi: 10.1109/IAS.1994.345505.

[21] Yongbin Li and Chunting Chris Mi, "Doubly Salient Permanent-Magnet Machine With Skewed Rotor and Six-State Commutating Mode," *IEEE Trans. Magn.*, vol. 43, no. 9, pp. 3623–3629, Sep. 2007, doi: 10.1109/TMAG.2007.901949.

[22] X. Zhu, L. Quan, D. Chen, M. Cheng, Z. Wang, and W. Li, "Design and Analysis of a New Flux Memory Doubly Salient Motor Capable of Online Flux Control," *IEEE Trans. Magn.*, vol. 47, no. 10, pp. 3220–3223, Oct. 2011, doi: 10.1109/TMAG.2011.2154358.

[23] X. Zhu, L. Wang, Y. Chen, L. Chen, and L. Quan, "A Non-Rare-Earth Doubly Salient Flux Controllable Motor Capable of Fault-Tolerant Control," *IEEE Trans. Magn.*, vol. 51, no. 11, pp. 1–4, Nov. 2015, doi: 10.1109/TMAG.2015.2443137.

[24] M. Lin, M. Cheng, and E. Zhou, "Design and performance analysis of new 12/8-pole doubly salient permanent-magnet motor," in *Sixth International Conference on Electrical Machines and Systems*, 2003, pp. 21–25.

[25] L. Zhang, L. J. Wu, X. Huang, and Y. Fang, "A Novel Structure of Doubly Salient Permanent Magnet Machine," in *2018 XIII International Conference on Electrical Machines (ICEM)*, 2018, pp. 2009–2015, doi: 10.1109/ICELMACH.2018.8506712.

[26] T. H. Kim and J. Lee, "A Study of the Design for the Flux Reversal Machine," *IEEE Trans. Magn.*, vol. 40, no. 4, pp. 2053–2055, Jul. 2004, doi: 10.1109/TMAG.2004.832488.

[27] Tae Heoung Kim, Sung Hong Wo, Ki Bong, and Ju Lee, "Reduction of cogging torque in flux-reversal machine by rotor teeth pairing," *IEEE Trans. Magn.*, vol. 41, no. 10, pp. 3964–3966, Oct. 2005, doi: 10.1109/TMAG.2005.855182.

[28] R. P. Deodhar, S. Andersson, I. Boldea, and T. J. E. Miller, "The flux-reversal machine: a new brushless doubly-salient permanent-magnet machine," *IEEE Trans. Ind. Appl.*, vol. 33, no. 4, pp. 925–934, 1997, doi: 10.1109/28.605734.

[29] Tae Heoung Kim, "A Study on the Design of an Inset-Permanent-Magnet-Type Flux-Reversal Machine," *IEEE Trans. Magn.*, vol. 45, no. 6, pp. 2859–2862, Jun. 2009, doi: 10.1109/TMAG.2009.2018776.

[30] Y. Gao, R. Qu, D. Li, J. Li, and G. Zhou, "Consequent-Pole Flux-Reversal Permanent-Magnet Machine for Electric Vehicle Propulsion," *IEEE Trans. Appl. Supercond.*, vol. 26, no. 4, pp. 1–5, Jun. 2016, doi: 10.1109/TASC.2016.2514345.

[31] S. E. Rauch and L. J. Johnson, "Design principles of flux-switch alternators," *Trans. Am. Inst. Electr. Eng. Part III Power Appar. Syst.*, vol. 74, no. 3, Jan. 1955, doi: 10.1109/AIEEPAS.1955.4499226.

[32] W. Fei, P. C. K. Luk, B. Xia, Y. Wang, and J. X. Shen, "Permanent magnet flux switching integrated-starter-generator with different rotor configurations for cogging torque and torque ripple mitigations," in *Proc. IEEE Energy Convers. Congr. Expo (ECCE)*, 2010, pp. 1715–1722, doi: 10.1109/ECCE.2010.5618119.

[33] Z. Q. Zhu, Y. Pang, D. Howe, S. Iwasaki, R. Deodhar, and A. Pride, "Analysis of electromagnetic performance of flux-switching permanent-magnet Machines by nonlinear adaptive lumped parameter magnetic circuit model," *IEEE Trans. Magn.*, vol. 41, no. 11, pp. 4277–4287, Nov. 2005, doi: 10.1109/TMAG.2005.854441.

[34] J. T. Chen and Z. Q. Zhu, "Winding configurations and optimal stator and rotor pole combination of flux-switching PM brushless AC machines," *IEEE Trans. Energy Convers.*, vol. 25, no. 2, pp. 293–302, Jun. 2010, doi: 10.1109/TEC.2009.2032633.

[35] A. S. Thomas, Z. Q. Zhu, and G. W. Jewell, "Comparison of flux switching and surface mounted permanent magnet generators for high-speed applications," *IET Electr. Syst. Transp.*, vol. 1, no. 3, p. 111, 2011, doi: 10.1049/iet-est.2010.0049.

[36] J. D. McFarland, T. M. Jahns, and A. M. EL-Refaie, "Analysis of the torque production mechanism for flux-switching permanent-magnet machines," *IEEE Trans. Ind. Appl.*, vol. 51, no. 4, pp. 3041–3049, Jul. 2015, doi: 10.1109/TIA.2015.2411655.

[37] Z. Q. Zhu and J. T. Chen, "Advanced flux-switching permanent magnet brushless machines," *IEEE Trans. Magn.*, vol. 46, no. 6, pp. 1447–1453, Jun. 2010, doi: 10.1109/TMAG.2010.2044481.

[38] Wei Hua, Ming Cheng, Z. Q. Zhu, and D. Howe, "Analysis and optimization of back EMF waveform of a flux-switching permanent magnet motor," *IEEE Trans. Energy Convers.*, vol. 23, no. 3, pp. 727–733, Sep. 2008, doi: 10.1109/TEC.2008.918612.

[39] R. Leuzzi, Y. Li, and B. Sarlioglu, “Performance evaluation of a hybrid-excited flux-switching PM motor for traction applications,” in *IECON 2016 - 42nd Annual Conference of the IEEE Industrial Electronics Society*, 2016, pp. 1846–1851, doi: 10.1109/IECON.2016.7793742.

[40] C. Sanabria-Walter, H. Polinder, and J. A. Ferreira, “High-Torque-Density High-Efficiency Flux-Switching PM Machine for Aerospace Applications,” *IEEE J. Emerg. Sel. Top. Power Electron.*, vol. 1, no. 4, pp. 327–336, Dec. 2013, doi: 10.1109/JESTPE.2013.2280183.

[41] B. Sarlioglu, J. H. Kim, and Y. Li, “Axial flux switching permanent magnet machine.” Google Patents, 2016.

[42] H. Zhou, L. Quan, X. Zhu, and Y. Du, “Thermal analysis of a V-shape sandwiched flux switching permanent magnet machine for electric vehicles,” in *2015 18th International Conference on Electrical Machines and Systems (ICEMS)*, 2015, pp. 790–794, doi: 10.1109/ICEMS.2015.7385141.

[43] W. Fei, P. C. K. Luk, and J. Shen, “Torque analysis of permanent-magnet flux switching machines with rotor step skewing,” *IEEE Trans. Magn.*, vol. 48, no. 10, pp. 2664–2673, Oct. 2012, doi: 10.1109/TMAG.2012.2198223.

[44] W. Hua, Z. Q. Zhu, M. Cheng, Y. Pang, and D. Howe, “Comparison of flux-switching and doubly-salient permanent magnet brushless machines,” in *Proc. Int. Conf. Elect. Mach. Syst., Nanjing, China*, 2005, pp. 165–170, doi: 10.1109/ICEMS.2005.202506.

[45] Y. Li, “Flux-coupling low pole flux-switching permanent magnet machines,” University of Wisconsin-Madison, 2017.

[46] D. Li, R. Qu, and J. Li, “Topologies and analysis of flux-modulation machines,” in *2015 IEEE Energy Conversion Congress and Exposition (ECCE)*, 2015, pp. 2153–2160, doi: 10.1109/ECCE.2015.7309964.

[47] T. Zou, D. Li, R. Qu, and D. Jiang, “Performance Comparison of Surface and Spoke-Type Flux-Modulation Machines With Different Pole Ratios,” *IEEE Trans. Magn.*, vol. 53, no. 6, pp. 1–5, Jun. 2017, doi: 10.1109/TMAG.2017.2662081.

[48] J. T. Chen, Z. Q. Zhu, A. S. Thomas, and D. Howe, “Optimal combination of stator and rotor pole numbers in flux-switching PM brushless AC machines,” in *International Conference on Electrical Machines and Systems*, 2008, pp. 2905–2910.

[49] G. Verez, G. Barakat, Y. Amara, O. Bennouna, and G. Hoblos, “Impact of pole and slot combination on noise and vibrations of flux-switching PM machines,” in *2014 International Conference on Electrical Machines (ICEM)*, 2014, pp. 182–188, doi: 10.1109/ICELMACH.2014.6960178.

[50] J. T. Chen and Z. Q. Zhu, “Comparison of all- and alternate-poles-wound flux-switching PM machines having different stator and rotor pole numbers,” *IEEE Trans. Ind. Appl.*, vol. 46, no. 4, pp. 1406–1415, Jul. 2010, doi: 10.1109/TIA.2010.2049812.

[51] C. Wang, J. C. S. Lai, and D. W. J. Pulle, “Prediction of acoustic noise from variable-speed induction motors: deterministic versus statistical approaches,” *IEEE Trans. Ind. Appl.*, vol. 38, no. 4, pp. 1037–1044, Jul. 2002, doi: 10.1109/TIA.2002.800567.

[52] Feng Li, Wei Hua, Minghao Tong, Guishu Zhao, and Ming Cheng, “Nine-Phase Flux-Switching Permanent Magnet Brushless Machine for Low-Speed and High-Torque Applications,” *IEEE Trans. Magn.*, vol. 51, no. 3, pp. 1–4, Mar. 2015, doi: 10.1109/TMAG.2014.2364716.

[53] A. S. Thomas, Z. Q. Zhu, R. L. Owen, G. W. Jewell, and D. Howe, “Multiphase Flux-Switching Permanent-Magnet Brushless Machine for Aerospace Application,” *IEEE Trans. Ind. Appl.*, vol. 45, no. 6, pp. 1971–1981, 2009, doi: 10.1109/TIA.2009.2031901.

[54] F. Li, W. Hua, and M. Cheng, “Design and optimization of a nine-phase flux-switching PM generator for wind power systems,” in *2014 17th International Conference on Electrical Machines and Systems (ICEMS)*, 2014, pp. 471–477, doi: 10.1109/ICEMS.2014.7013532.

[55] M. Tong, W. Hua, P. Su, M. Cheng, and J. Meng, “Investigation of a Vector-Controlled Five-Phase Flux-Switching Permanent-Magnet Machine Drive System,” *IEEE Trans. Magn.*, vol. 52, no. 7, pp. 1–5, Jul. 2016, doi: 10.1109/TMAG.2016.2524503.

[56] X. Xue, W. Zhao, J. Zhu, G. Liu, X. Zhu, and M. Cheng, “Design of Five-Phase Modular Flux-Switching Permanent-Magnet Machines for High Reliability Applications,” *IEEE Trans. Magn.*, vol. 49, no. 7, pp. 3941–3944, Jul. 2013, doi: 10.1109/TMAG.2013.2244201.

[57] Y. Li and W. Xu, “Optimization and performance analysis of E-core and C-core flux-switching permanent-magnet machines for electric vehicle applications,” in *2014 17th International Conference on Electrical Machines and Systems (ICEMS)*, 2014, pp. 53–59, doi: 10.1109/ICEMS.2014.7013436.

[58] J. T. Chen, Z. Q. Zhu, and D. Howe, “Stator and Rotor Pole Combinations for Multi-Tooth Flux-Switching Permanent-Magnet Brushless AC Machines,” *IEEE Trans. Magn.*, vol. 44, no. 12, pp. 4659–4667, Dec. 2008, doi: 10.1109/TMAG.2008.2004264.

[59] Z. Q. Zhu, J. T. Chen, Y. Pang, D. Howe, S. Iwasaki, and R. Deodhar, "Analysis of a Novel Multi-Tooth Flux-Switching PM Brushless AC Machine for High Torque Direct-Drive Applications," *IEEE Trans. Magn.*, vol. 44, no. 11, pp. 4313–4316, Nov. 2008, doi: 10.1109/TMAG.2008.2001525.

[60] J. T. Chen, Z. Q. Zhu, and D. Howe, "Optimization of multi-tooth flux-switching PM brushless ac machines," in *2008 18th International Conference on Electrical Machines*, 2008, pp. 1–6, doi: 10.1109/ICELMACH.2008.4799940.

[61] L. Mo, L. Quan, Y. Chen, and H. Qiu, "Sandwiched Flux-Switching Permanent-Magnet Brushless AC Machines Using V-Shape Magnets," in *2013 IEEE Vehicle Power and Propulsion Conference (VPPC)*, 2013, pp. 1–5, doi: 10.1109/VPPC.2013.6671738.

[62] Y. J. Zhou and Z. Q. Zhu, "Torque Density and Magnet Usage Efficiency Enhancement of Sandwiched Switched Flux Permanent Magnet Machines Using V-Shaped Magnets," *IEEE Trans. Magn.*, vol. 49, no. 7, pp. 3834–3837, Jul. 2013, doi: 10.1109/TMAG.2013.2238219.

[63] R. Owen, Z. Q. Zhu, J. B. Wang, D. A. Stone, and I. Urquhart, "Mechanically adjusted variable-flux concept for switched-flux permanent-magnet machines," in *2011 International Conference on Electrical Machines and Systems*, 2011, pp. 1–6, doi: 10.1109/ICEMS.2011.6073502.

[64] Z. Q. Zhu, M. M. J. Al-ani, X. Liu, M. Hasegawa, A. Pride, and R. Deodhar, "Comparison of alternate mechanically adjusted variable flux switched flux permanent magnet machines," in *2012 IEEE Energy Conversion Congress and Exposition (ECCE)*, 2012, pp. 3655–3662, doi: 10.1109/ECCE.2012.6342481.

[65] Z. Q. Zhu, M. M. J. Al-Ani, X. Liu, and B. Lee, "A Mechanical Flux Weakening Method for Switched Flux Permanent Magnet Machines," *IEEE Trans. Energy Convers.*, vol. 30, no. 2, pp. 806–815, Jun. 2015, doi: 10.1109/TEC.2014.2380851.

[66] H. Yang, Z. Q. Zhu, H. Lin, and S. Lyu, "Comparative Study of Hybrid PM Memory Machines Having Single- and Dual-Stator Configurations," *IEEE Trans. Ind. Electron.*, vol. 65, no. 11, pp. 9168–9178, Nov. 2018, doi: 10.1109/TIE.2018.2823703.

[67] H. Hua, Z. Q. Zhu, A. Pride, R. Deodhar, and T. Sasaki, "Comparison of end effect in series and parallel hybrid permanent magnet variable flux memory machines," in *2017 20th International Conference on Electrical Machines and Systems (ICEMS)*, 2017, pp. 1–6, doi: 10.1109/ICEMS.2017.8056389.

[68] N. Li, J. Zhu, M. Lin, G. Yang, and Y. Kong, "Flux-weakening performance of series permanent magnet memory machine," in *2017 20th International Conference on Electrical Machines and Systems (ICEMS)*, 2017, pp. 1–4, doi: 10.1109/ICEMS.2017.8056469.

[69] F. Li, K. T. Chau, C. Liu, and Z. Zhang, "Design Principles of Permanent Magnet Dual-Memory Machines," *IEEE Trans. Magn.*, vol. 48, no. 11, pp. 3234–3237, Nov. 2012, doi: 10.1109/TMAG.2012.2199477.

[70] H. Liu, H. Lin, Z. Q. Zhu, M. Huang, and P. Jin, "Permanent Magnet Remagnetizing Physics of a Variable Flux Memory Motor," *IEEE Trans. Magn.*, vol. 46, no. 6, pp. 1679–1682, Jun. 2010, doi: 10.1109/TMAG.2010.2044638.

[71] V. Ostovic, "Memory motors," *IEEE Ind. Appl. Mag.*, vol. 9, no. 1, pp. 52–61, Jan. 2003, doi: 10.1109/MIA.2003.1176459.

[72] H. Yang, Z. Q. Zhu, H. Lin, S. Fang, and Y. Huang, "Synthesis of Hybrid Magnet Memory Machines Having Separate Stators for Traction Applications," *IEEE Trans. Veh. Technol.*, vol. 67, no. 1, pp. 183–195, Jan. 2018, doi: 10.1109/TVT.2017.2762082.

[73] H. Yang, H. Lin, Z. Q. Zhu, D. Wang, S. Fang, and Y. Huang, "A Variable-Flux Hybrid-PM Switched-Flux Memory Machine for EV/HEV Applications," *IEEE Trans. Ind. Appl.*, vol. 52, no. 3, pp. 2203–2214, May 2016, doi: 10.1109/TIA.2016.2524400.

[74] E. Hoang, M. Lecrivain, S. Hlioui, and M. Gabsi, "Hybrid excitation synchronous permanent magnets synchronous machines optimally designed for hybrid and full electrical vehicle," in *8th International Conference on Power Electronics - ECCE Asia*, 2011, pp. 153–160, doi: 10.1109/ICPE.2011.5944569.

[75] E. Sulaiman, T. Kosaka, and N. Matsui, "A novel hybrid excitation flux switching synchronous machine for a high-speed hybrid electric vehicle applications," in *2011 International Conference on Electrical Machines and Systems*, 2011, pp. 1–6, doi: 10.1109/ICEMS.2011.6073505.

[76] Wei Hua, Ming Cheng, and Gan Zhang, "A Novel Hybrid Excitation Flux-Switching Motor for Hybrid Vehicles," *IEEE Trans. Magn.*, vol. 45, no. 10, pp. 4728–4731, Oct. 2009, doi: 10.1109/TMAG.2009.2022497.

[77] E. Hoang, M. Lecrivain, and M. Gabsi, "A new structure of a switching flux synchronous polyphased machine with hybrid excitation," in *2007 European Conference on Power Electronics and Applications*, 2007, pp. 1–8, doi: 10.1109/EPE.2007.4417204.

[78] Y. Tang, E. Ilhan, J. J. H. Paulides, and E. A. Lomonova, "Design considerations of flux-switching machines with permanent magnet or DC excitation," in *2013 15th European Conference on Power Electronics and*

Applications (EPE), 2013, pp. 1–10, doi: 10.1109/EPE.2013.6634396.

[79] Y. Tang, J. J. H. Paulides, T. E. Motoasca, and E. A. Lomonova, "Flux-Switching Machine With DC Excitation," *IEEE Trans. Magn.*, vol. 48, no. 11, pp. 3583–3586, Nov. 2012, doi: 10.1109/TMAG.2012.2199100.

[80] Y. J. Zhou and Z. Q. Zhu, "Comparison of low-cost wound-field switched-flux machines," in *2013 IEEE Energy Conversion Congress and Exposition*, 2013, pp. 904–911, doi: 10.1109/ECCE.2013.6646799.

[81] A. S. Thomas, Z. Q. Zhu, and L. J. Wu, "Novel Modular-Rotor Switched-Flux Permanent Magnet Machines," *IEEE Trans. Ind. Appl.*, vol. 48, no. 6, pp. 2249–2258, Nov. 2012, doi: 10.1109/TIA.2012.2226860.

[82] D. J. Evans and Z. Q. Zhu, "Novel Partitioned Stator Switched Flux Permanent Magnet Machines," *IEEE Trans. Magn.*, vol. 51, no. 1, pp. 1–14, Jan. 2015, doi: 10.1109/TMAG.2014.2342196.

[83] C. C. Awah *et al.*, "Comparison of Partitioned Stator Switched Flux Permanent Magnet Machines Having Single- or Double-Layer Windings," *IEEE Trans. Magn.*, vol. 52, no. 1, pp. 1–10, Jan. 2016, doi: 10.1109/TMAG.2015.2477679.

[84] H. Hua and Z. Q. Zhu, "Novel Hybrid-Excited Switched-Flux Machine Having Separate Field Winding Stator," *IEEE Trans. Magn.*, vol. 52, no. 7, pp. 1–4, Jul. 2016, doi: 10.1109/TMAG.2016.2522920.

[85] H. Yang, Z. Q. Zhu, H. Lin, S. Fang, Y. Huang, and Z. Xu, "Novel dual stator switched flux hybrid magnet memory machines," in *2016 XXII International Conference on Electrical Machines (ICEM)*, 2016, pp. 830–836, doi: 10.1109/ICELMACH.2016.7732622.

[86] I. Boldea and S. A. Nasar, "Linear electric actuators and generators," *IEEE Trans. Energy Convers.*, vol. 14, no. 3, pp. 712–717, 1999, doi: 10.1109/60.790940.

[87] C. F. Wang, J. X. Shen, L. L. Wang, and K. Wang, "A novel permanent magnet flux-switching linear motor," in *4th IET International Conference on Power Electronics, Machines and Drives (PEMD 2008)*, 2008, pp. 116–119, doi: 10.1049/cp:20080494.

[88] J.-X. Shen and W.-Z. Fei, "Permanent magnet flux switching machines — Topologies, analysis and optimization," in *4th International Conference on Power Engineering, Energy and Electrical Drives*, 2013, pp. 352–366, doi: 10.1109/PowerEng.2013.6635633.

[89] C. F. Wang and J. X. Shen, "A Method to Segregate Detent Force Components in Permanent-Magnet Flux-Switching Linear Machines," *IEEE Trans. Magn.*, vol. 48, no. 5, pp. 1948–1955, May 2012, doi: 10.1109/TMAG.2011.2177852.

[90] Shending Xu, Wenxiang Zhao, Jinghua Ji, Yi Du, Duo Zhang, and Guohai Liu, "Thrust ripple reduction of linear flux-switching PM motor using harmonic injected current," in *2013 International Conference on Electrical Machines and Systems (ICEMS)*, 2013, pp. 1886–1889, doi: 10.1109/ICEMS.2013.6713220.

[91] C.-C. Hwang, P.-L. Li, and C.-T. Liu, "Design and Analysis of a Novel Hybrid Excited Linear Flux Switching Permanent Magnet Motor," *IEEE Trans. Magn.*, vol. 48, no. 11, pp. 2969–2972, Nov. 2012, doi: 10.1109/TMAG.2012.2195716.

[92] R. Cao, M. Cheng, C. Mi, W. Hua, and W. Zhao, "A hybrid excitation flux-switching permanent magnet linear motor for urban rail transit," in *2011 IEEE Vehicle Power and Propulsion Conference*, 2011, pp. 1–5, doi: 10.1109/VPPC.2011.6043076.

[93] R. Cao, M. Cheng, C. Mi, W. Hua, X. Wang, and W. Zhao, "Modeling of a Complementary and Modular Linear Flux-Switching Permanent Magnet Motor for Urban Rail Transit Applications," *IEEE Trans. Energy Convers.*, vol. 27, no. 2, pp. 489–497, Jun. 2012, doi: 10.1109/TEC.2012.2190985.

[94] J. Cai, Q. Lu, Y. Jin, C. Chen, and Y. Ye, "Performance investigation of multi-tooth flux-switching PM linear motor," in *2011 International Conference on Electrical Machines and Systems*, 2011, pp. 1–6, doi: 10.1109/ICEMS.2011.6073745.

[95] Y. Shen, Q. Lu, H. Li, J. Cai, X. Huang, and Y. Fang, "Analysis of a Novel Double-Sided Yokeless Multitooth Linear Switched-Flux PM Motor," *IEEE Trans. Ind. Electron.*, vol. 65, no. 2, pp. 1837–1845, Feb. 2018, doi: 10.1109/TIE.2017.2696492.

[96] L. Huang, H. Yu, M. Hu, J. Zhao, and Z. Cheng, "A Novel Flux-Switching Permanent-Magnet Linear Generator for Wave Energy Extraction Application," *IEEE Trans. Magn.*, vol. 47, no. 5, pp. 1034–1037, May 2011, doi: 10.1109/TMAG.2010.2093509.

[97] W. Zhang, X. Liang, M. Lin, L. Hao, and N. Li, "Design and Analysis of Novel Hybrid-Excited Axial Field Flux-Switching Permanent Magnet Machines," *IEEE Trans. Appl. Supercond.*, pp. 1–1, 2016, doi: 10.1109/TASC.2016.2517662.

[98] N. Li, M. Lin, G. Yang, and L. Xu, "Design and analysis of a hybrid permanent magnet axial field flux-switching memory machine," in *2016 IEEE Conference on Electromagnetic Field Computation (CEFC)*, 2016, pp. 1–1, doi: 10.1109/CEFC.2016.7816318.

[99] J. Zhao, M. Lin, D. Xu, L. Hao, and W. Zhang, "Vector Control of a Hybrid Axial Field Flux-Switching Permanent Magnet Machine Based on Particle Swarm Optimization," *IEEE Trans. Magn.*, vol. 51, no. 11, pp. 1–4, Nov. 2015, doi: 10.1109/TMAG.2015.2435156.

[100] L. Hao, M. Lin, D. Xu, N. Li, and W. Zhang, "Cogging torque reduction of axial field flux-switching permanent magnet machine by rotor tooth notching," in *2015 IEEE Magnetics Conference (INTERMAG)*, 2015, pp. 1–1, doi: 10.1109/INTMAG.2015.7157392.

[101] Y. Ma, W. Zhang, Y. Yang, and H. Bao, "Research on loss of axial field flux-switching permanent magnet machine," in *2014 17th International Conference on Electrical Machines and Systems (ICEMS)*, 2014, pp. 1145–1149, doi: 10.1109/ICEMS.2014.7013643.

[102] M. Dhifli, H. Bali, Y. Laoubi, G. Barakat, and Y. Amara, "Analytical modeling of the magnetic field in axial field flux-switching permanent magnet machines at no-load," in *2013 15th European Conference on Power Electronics and Applications (EPE)*, 2013, pp. 1–10, doi: 10.1109/EPE.2013.6634682.

[103] F. Marignetti, M. A. Darmani, and S. M. Mirimani, "Electromagnetic sizing of axial-field flux switching permanent magnet machine," in *IECON 2016 - 42nd Annual Conference of the IEEE Industrial Electronics Society*, 2016, pp. 1624–1628, doi: 10.1109/IECON.2016.7793175.

[104] W. Zhao, T. A. Lipo, and B.-I. Kwon, "A Novel Dual-Rotor, Axial Field, Fault-Tolerant Flux-Switching Permanent Magnet Machine With High-Torque Performance," *IEEE Trans. Magn.*, vol. 51, no. 11, pp. 1–4, Nov. 2015, doi: 10.1109/TMAG.2015.2445926.

[105] Y. Pang, Z. Q. Zhu, D. Howe, S. Iwasaki, R. Deodhar, and A. Pride, "Comparative study of flux-switching and interior permanent magnet machines," in *Proceeding of International Conference on Electrical Machines and Systems 2007, Oct. 8-11, Seoul, Korea.*, 2007.

[106] A. Fasolo, L. Alberti, and N. Bianchi, "Performance Comparison Between Switching-Flux and IPM Machines With Rare-Earth and Ferrite PMs," *IEEE Trans. Ind. Appl.*, vol. 50, no. 6, pp. 3708–3716, Nov. 2014, doi: 10.1109/TIA.2014.2319592.

[107] A. S. Thomas, Z. Q. Zhu, and G. W. Jewell, "Proximity Loss Study In High Speed Flux-Switching Permanent Magnet Machine," *IEEE Trans. Magn.*, vol. 45, no. 10, pp. 4748–4751, Oct. 2009, doi: 10.1109/TMAG.2009.2021666.

[108] Z. Q. Zhu *et al.*, "Analysis and reduction of magnet Eddy current loss in flux-switching permanent magnet machines," in *4th IET International Conference on Power Electronics, Machines and Drives (PEMD 2008)*, 2008, pp. 120–124, doi: 10.1049/cp:20080495.

[109] Y. Li, S. Li, Y. Yang, and B. Sarlioglu, "Analysis of flux switching permanent magnet machine design for high-speed applications," in *2014 IEEE Energy Conversion Congress and Exposition (ECCE)*, 2014, pp. 302–309, doi: 10.1109/ECCE.2014.6953408.

[110] W. Xu, G. Lei, T. Wang, X. Yu, J. Zhu, and Y. Guo, "Theoretical Research on New Laminated Structure Flux Switching Permanent Magnet Machine for Novel Topologic Plug-In Hybrid Electrical Vehicle," *IEEE Trans. Magn.*, vol. 48, no. 11, pp. 4050–4053, Nov. 2012, doi: 10.1109/TMAG.2012.2195642.

[111] W. Xu, J. Zhu, Y. Zhang, Y. Guo, and G. Lei, "New Axial Laminated-Structure Flux-Switching Permanent Magnet Machine With 6/7 Poles," *IEEE Trans. Magn.*, vol. 47, no. 10, pp. 2823–2826, Oct. 2011, doi: 10.1109/TMAG.2011.2151842.

[112] E. Sulaiman, T. Kosaka, and N. Matsui, "High Power Density Design of 6-Slot–8-Pole Hybrid Excitation Flux Switching Machine for Hybrid Electric Vehicles," *IEEE Trans. Magn.*, vol. 47, no. 10, pp. 4453–4456, Oct. 2011, doi: 10.1109/TMAG.2011.2140315.

[113] W. Z. Fei and J. X. Shen, "Comparative Study and Optimal Design of PM Switching Flux Motors," in *Proceedings of the 41st International Universities Power Engineering Conference*, 2006, pp. 695–699, doi: 10.1109/UPEC.2006.367568.

[114] Y. Li, D. Bobba, and B. Sarlioglu, "A novel dual-stator flux switching permanent magnet machine with six stator slots and four rotor poles configuration," in *2015 IEEE International Electric Machines & Drives Conference (IEMDC)*, 2015, pp. 1566–1572, doi: 10.1109/IEMDC.2015.7409272.

[115] Y. Li, M. Liu, J. H. Kim, and B. Sarlioglu, "Torque ripple reduction and mechanical tolerance analysis of a novel dual-stator 6/4 flux-switching permanent magnet machine," in *2017 IEEE International Electric Machines and Drives Conference (IEMDC)*, 2017, pp. 1–8, doi: 10.1109/IEMDC.2017.8002329.

[116] D. Bobba, G. Bramerdorfer, Y. Li, T. A. Burress, and B. Sarlioglu, "Stator tooth and rotor pole shaping for low pole flux switching permanent magnet machines to reduce even order harmonics in flux linkage," in *Proc. IEEE Energy Convers. Congr. Expo (ECCE)*, 2016, pp. 1–8, doi: 10.1109/ECCE.2016.7855468.

[117] Y. Li, J. H. Kim, R. Leuzzi, M. Liu, and B. Sarlioglu, "Novel 6-slot 4-pole dual-stator flux-switching permanent magnet machine comparison studies for high-speed applications," in *2016 IEEE Energy*

Conversion Congress and Exposition (ECCE), 2016, pp. 1–8, doi: 10.1109/ECCE.2016.7855296.

[118] D. Bobba, Y. Li, and B. Sarlioglu, "Design optimization for reducing harmonic distortion of flux linkage in low pole flux-switching permanent magnet machines," in *Proc. IEEE Transportation Electrification Conference and Expo (ITEC)*, 2016, pp. 1–6, doi: 10.1109/ITEC.2016.7520258.

[119] Y. Li, D. Bobba, and B. Sarlioglu, "Design and Performance Characterization of a Novel Low-Pole Dual-Stator Flux-Switching Permanent Magnet Machine for Traction Application," *IEEE Trans. Ind. Appl.*, vol. 52, no. 5, pp. 4304–4314, Sep. 2016, doi: 10.1109/TIA.2016.2558160.

[120] C. Sikder, I. Husain, and W. Ouyang, "Cogging torque reduction in flux-switching permanent-magnet machines by rotor pole shaping," *IEEE Trans. Ind. Appl.*, vol. 51, no. 5, pp. 3609–3619, Sep. 2015, doi: 10.1109/TIA.2015.2416238.

[121] D. Wang, X. Wang, and S.-Y. Jung, "Reduction on cogging torque in flux-switching permanent magnet machine by teeth notching schemes," *IEEE Trans. Magn.*, vol. 48, no. 11, pp. 4228–4231, Nov. 2012, doi: 10.1109/TMAG.2012.2200237.

[122] D. Xu, M. Lin, X. Fu, L. Hao, W. Zhang, and N. Li, "Cogging torque reduction of a hybrid axial field flux-switching permanent-magnet machine with three methods," *IEEE Trans. Appl. Supercond.*, vol. 26, no. 4, pp. 1–5, Jun. 2016, doi: 10.1109/TASC.2016.2519524.

[123] L. Mo, X. Zhu, T. Zhang, L. Quan, Y. Wang, and J. Huang, "Temperature rise calculation of a flux-switching permanent-magnet double-rotor machine using electromagnetic-thermal coupling analysis," *IEEE Trans. Magn.*, vol. 54, no. 3, pp. 1–4, Mar. 2018, doi: 10.1109/TMAG.2017.2764182.

[124] G. Li, J. Ojeda, E. Hoang, M. Gabsi, and M. Lecrivain, "Thermal–electromagnetic analysis for driving cycles of embedded flux-switching permanent-magnet motors," *IEEE Trans. Veh. Technol.*, vol. 61, no. 1, pp. 140–151, Jan. 2012, doi: 10.1109/TVT.2011.2177283.

[125] M. Cheng, J. Wang, S. Zhu, and W. Wang, "Loss calculation and thermal analysis for nine-phase flux switching permanent magnet machine," *IEEE Trans. Energy Convers.*, pp. 1–1, 2018, doi: 10.1109/TEC.2018.2837910.

[126] D. A. Staton and A. Cavagnino, "Convection Heat Transfer and Flow Calculations Suitable for Electric Machines Thermal Models," *IEEE Trans. Ind. Electron.*, vol. 55, no. 10, pp. 3509–3516, Oct. 2008, doi: 10.1109/TIE.2008.922604.

[127] X. Cai, M. Cheng, S. Zhu, and J. Zhang, "Thermal Modeling of Flux-Switching Permanent-Magnet Machines Considering Anisotropic Conductivity and Thermal Contact Resistance," *IEEE Trans. Ind. Electron.*, vol. 63, no. 6, pp. 3355–3365, Jun. 2016, doi: 10.1109/TIE.2016.2522942.

[128] P. Timar, *Noise and Vibration of Electric Machines*. Oxford, UK: Elsevier, 1989.

[129] S. Yang, *Low-Noise Electrical Motors*. Oxford, UK: Claredon Press, 1981.

[130] R. S. Girgis and S. P. Vermas, "Method for accurate determination of resonant frequencies and vibration behaviour of stators of electrical machines," *IEE Proc. B Electr. Power Appl.*, vol. 128, no. 1, p. 1, 1981, doi: 10.1049/ip-b.1981.0001.

[131] C. Sikder and I. Husain, "Stator vibration and acoustic noise analysis of FSPM for a low-noise design," in *2016 IEEE Energy Conversion Congress and Exposition (ECCE)*, 2016, pp. 1–8, doi: 10.1109/ECCE.2016.7855469.

[132] E. J. Vrancik, "Prediction of windage power loss in alternators," *NASA Tech. Br.*, Apr. 1971.

[133] K. Kiyota, T. Kakishima, and A. Chiba, "Estimation and comparison of the windage loss of a 60 kW Switched Reluctance Motor for hybrid electric vehicles," in *proc. Int. Power Elect. Conf., Hiroshima, Japan*, 2014, pp. 3513–3518, doi: 10.1109/IPEC.2014.6870001.

[134] H. Nakane, Y. Okada, T. Kosaka, and N. Matsui, "Experimental study on windage loss reduction using two types of rotor for hybrid excitation flux switching motor," in *2016 XXII International Conference on Electrical Machines (ICEM)*, 2016, pp. 1707–1713, doi: 10.1109/ICELMACH.2016.7732754.

[135] S. H. Won, J. Choi, and J. Lee, "Windage loss reduction of high-speed SRM using rotor magnetic saturation," *IEEE Trans. Magn.*, vol. 44, no. 11, pp. 4147–4150, Nov. 2008, doi: 10.1109/TMAG.2008.2001660.

[136] K. Kiyota, T. Kakishima, A. Chiba, and M. A. Rahman, "Cylindrical rotor design for acoustic noise and windage loss reduction in switched reluctance motor for HEV applications," *IEEE Trans. Ind. Appl.*, vol. 52, no. 1, pp. 154–162, Jan. 2016, doi: 10.1109/TIA.2015.2466558.

[137] F. Magnussen and C. Sadarangani, "Winding factors and Joule losses of permanent magnet machines with concentrated windings," in *IEMDC 2003 - IEEE International Electric Machines and Drives Conference*, 2003, vol. 1, pp. 333–339, doi: 10.1109/IEMDC.2003.1211284.

[138] Y. Li, J. H. Kim, R. Leuzzi, M. Liu, and B. Sarlioglu, "Novel 6-slot 4-pole dual-stator flux-switching permanent magnet machine comparison studies for high-speed applications," in *2016 IEEE Energy*

Conversion Congress and Exposition (ECCE), 2016, pp. 1–8, doi: 10.1109/ECCE.2016.7855296.
[139] S. D. Sudhoff, *Power magnetic devices - A multi-objective design approach*, Second. IEEE Press, 2014.
[140] T. A. Lipo, *Introduction to AC Machine Design*, 3rd Editio. Madison, 2015.
[141] A. M. EL-Refaie and T. M. Jahns, "Optimal Flux Weakening in Surface PM Machines Using Fractional-Slot Concentrated Windings," *IEEE Trans. Ind. Appl.*, vol. 41, no. 3, pp. 790–800, May 2005, doi: 10.1109/TIA.2005.847312.
[142] W. Hua and M. Cheng, "Inductance characteristics of 3-phase flux-switching permanent magnet machine with doubly-salient structure," *Diangong Jishu Xuebao/Transactions China Electrotech. Soc.*, vol. 22, no. 11, pp. 21–28, Nov. 2007, doi: 10.1109/ipemc.2006.4778302.
[143] R. Wrobel, S. J. Williamson, N. Simpson, S. Ayat, J. Yon, and P. H. Mellor, "Impact of slot shape on loss and thermal behaviour of open-slot modular stator windings," in *2015 IEEE Energy Conversion Congress and Exposition (ECCE)*, 2015, pp. 4433–4440, doi: 10.1109/ECCE.2015.7310286.
[144] Jae-Woo Kim, Byung-Taek Kim, and Byung Il Kwon, "Optimal stator slot design of inverter-fed induction motor in consideration of harmonic losses," *IEEE Trans. Magn.*, vol. 41, no. 5, pp. 2012–2015, May 2005, doi: 10.1109/TMAG.2005.846270.
[145] Y. Pang, Z. Q. Zhu, D. Howe, S. Iwasaki, R. Deodhar, and A. Pride, "Investigation of iron loss in flux-switching PM machines," in *4th IET International Conference on Power Electronics, Machines and Drives (PEMD 2008)*, 2008, pp. 460–464, doi: 10.1049/cp:20080564.
[146] A. Boglietti, A. Cavagnino, M. Lazzari, and M. Pastorelli, "Predicting iron losses in soft magnetic materials with arbitrary voltage supply: an engineering approach," *IEEE Trans. Magn.*, vol. 39, no. 2, pp. 981–989, Mar. 2003, doi: 10.1109/TMAG.2003.808599.
[147] D. M. Ionel, M. Popescu, M. I. McGilp, T. J. E. Miller, S. J. Dellinger, and R. J. Heideman, "Computation of Core Losses in Electrical Machines Using Improved Models for Laminated Steel," *IEEE Trans. Ind. Appl.*, vol. 43, no. 6, pp. 1554–1564, 2007, doi: 10.1109/TIA.2007.908159.
[148] "Hitachi Metals." [Online]. Available: http://www.hitachi-metals.co.jp.
[149] A. Acquaviva, O. Wallmark, E. A. Grunditz, S. T. Lundmark, and T. Thiringer, "Computationally efficient modeling of electrical machines with cooling jacket," *IEEE Trans. Transp. Electrif.*, vol. 5, no. 3, pp. 618–629, Sep. 2019, doi: 10.1109/TTE.2019.2936122.
[150] H. Li and Y. Shen, "Thermal Analysis of the Permanent-Magnet Spherical Motor," *IEEE Trans. Energy Convers.*, vol. 30, no. 3, pp. 991–998, Sep. 2015, doi: 10.1109/TEC.2015.2419636.
[151] S. Nategh, O. Wallmark, M. Leksell, and S. Zhao, "Thermal Analysis of a PMaSRM Using Partial FEA and Lumped Parameter Modeling," *IEEE Trans. Energy Convers.*, vol. 27, no. 2, pp. 477–488, Jun. 2012, doi: 10.1109/TEC.2012.2188295.
[152] M. Fénot, Y. Bertin, E. Dorignac, and G. Lalizel, "A review of heat transfer between concentric rotating cylinders with or without axial flow," *Int. J. Therm. Sci.*, vol. 50, no. 7, pp. 1138–1155, Jul. 2011, doi: 10.1016/J.IJTHERMALSCI.2011.02.013.
[153] P. Asef, R. B. Perpina, and A. C. Lapthorn, "Optimal pole number for magnetic noise reduction in variable-speed permanent magnet synchronous machines with fractional-slot concentrated windings," *IEEE Trans. Transp. Electrif.*, vol. 5, no. 1, pp. 126–134, Mar. 2019, doi: 10.1109/TTE.2018.2886429.
[154] X. Cai, M. Cheng, S. Zhu, and J. Zhang, "Thermal Modeling of Flux-Switching Permanent-Magnet Machines Considering Anisotropic Conductivity and Thermal Contact Resistance," *IEEE Trans. Ind. Electron.*, vol. 63, no. 6, pp. 3355–3365, Jun. 2016, doi: 10.1109/TIE.2016.2522942.
[155] A. Boglietti, A. Cavagnino, D. Staton, M. Shanel, M. Mueller, and C. Mejuto, "Evolution and Modern Approaches for Thermal Analysis of Electrical Machines," *IEEE Trans. Ind. Electron.*, vol. 56, no. 3, pp. 871–882, Mar. 2009, doi: 10.1109/TIE.2008.2011622.
[156] D. Staton, A. Boglietti, and A. Cavagnino, "Solving the More Difficult Aspects of Electric Motor Thermal Analysis in Small and Medium Size Industrial Induction Motors," *IEEE Trans. Energy Convers.*, vol. 20, no. 3, pp. 620–628, Sep. 2005, doi: 10.1109/TEC.2005.847979.
[157] A. Boglietti, E. Carpaneto, M. Cossale, S. Vaschetto, M. Popescu, and D. Staton, "Stator winding thermal conductivity evaluation: An industrial production assessment," in *2015 IEEE Energy Conversion Congress and Exposition (ECCE)*, 2015, pp. 4865–4871, doi: 10.1109/ECCE.2015.7310346.
[158] M. M. Yovanovich, "Four decades of research on thermal contact, gap, and joint resistance in microelectronics," *IEEE Transactions on Components and Packaging Technologies*, vol. 28, no. 2. pp. 182–206, Jun-2005, doi: 10.1109/TCAPT.2005.848483.
[159] X. Cai, M. Cheng, S. Zhu, and J. Zhang, "Thermal modeling of flux-switching permanent-magnet machines considering anisotropic conductivity and thermal contact resistance," *IEEE Trans. Ind. Electron.*, vol. 63, no.

6, pp. 3355–3365, Jun. 2016, doi: 10.1109/TIE.2016.2522942.
[160] Y. Yang *et al.*, "Thermal management of electric machines," *IET Electr. Syst. Transp.*, vol. 7, no. 2, pp. 104–116, Jun. 2017, doi: 10.1049/iet-est.2015.0050.
[161] H. Jia, M. Cheng, W. Hua, W. Zhao, and W. Li, "Torque Ripple Suppression in Flux-Switching PM Motor by Harmonic Current Injection Based on Voltage Space-Vector Modulation," *IEEE Trans. Magn.*, vol. 46, no. 6, pp. 1527–1530, Jun. 2010, doi: 10.1109/TMAG.2010.2040250.
[162] D. Wang, X. Wang, and S.-Y. Jung, "Reduction on Cogging Torque in Flux-Switching Permanent Magnet Machine by Teeth Notching Schemes," *IEEE Trans. Magn.*, vol. 48, no. 11, pp. 4228–4231, Nov. 2012, doi: 10.1109/TMAG.2012.2200237.
[163] Y. Okada, T. Kosaka, and N. Matsui, "Windage loss reduction for hybrid excitation flux switching motors based on rotor structure design," in *proc. Int. Elect. Mach. Dri. Conf., Miami, FL*, 2017, pp. 1–8, doi: 10.1109/IEMDC.2017.8002360.
[164] T. Raminosoa *et al.*, "Reduced rare-earth flux-switching machines for traction applications," *IEEE Trans. Ind. Appl.*, vol. 51, no. 4, pp. 2959–2971, Jul. 2015, doi: 10.1109/TIA.2015.2397173.
[165] G. I. Taylor, "Stability of a viscous liquid contained between two rotating cylinders," *Philos. Trans. R. Soc. London. Ser. A*, vol. 102, no. 718, pp. 541–542, Feb. 1923, doi: 10.1098/rspa.1923.0013.
[166] M. M. Swamy, J.-K. Kang, and K. Shirabe, "Power Loss, System Efficiency, and Leakage Current Comparison Between Si IGBT VFD and SiC FET VFD With Various Filtering Options," *IEEE Trans. Ind. Appl.*, vol. 51, no. 5, pp. 3858–3866, Sep. 2015, doi: 10.1109/TIA.2015.2420616.
[167] *1812-2014 IEEE Trial-Use Guide for Testing Permanent Magnet Machines*. 2014.

Annex

Annex A – Manufacturing guide for DLCW dual-stator 6/4 FSPM machine prototype

Bill of material (BOM)

ITEM NO.	PART NUMBER	DESCRIPTION	QTY.
1	Rotor	Arnon 5 lamination	1
2	Stator unit	Arnon 5 lamination	12
3	Cir. Frame key	Hold stator units - Aluminum	2
4	Magnet	NdFeB magnet, Br = 1.2 T	12
5	coil	Copper, 8 strands of AWG#22	6
6	Bolt-M4-0.7-55	Connect Cir. Frame to stator unit	24
7	Nut-M4-0.7	Connect Cir. Frame to stator unit	24
8	Cir. Frame no key	Hold stator units - Aluminum	2
9	innerHousing	Aluminum	1
10	outerHousing	Aluminum	1
11	B18.3.1M - 6 x 1.0 x 25 Hex	Bolt End cap	10
12	shaft_square	Harden steel	1
13	AST_Bearings_F63801	Highspeed bearing	2
14	machine_base	Machine base - Aluminum	1
15	side_housing_open	Aluminum	1
16	side_housing_closed	Aluminum	1

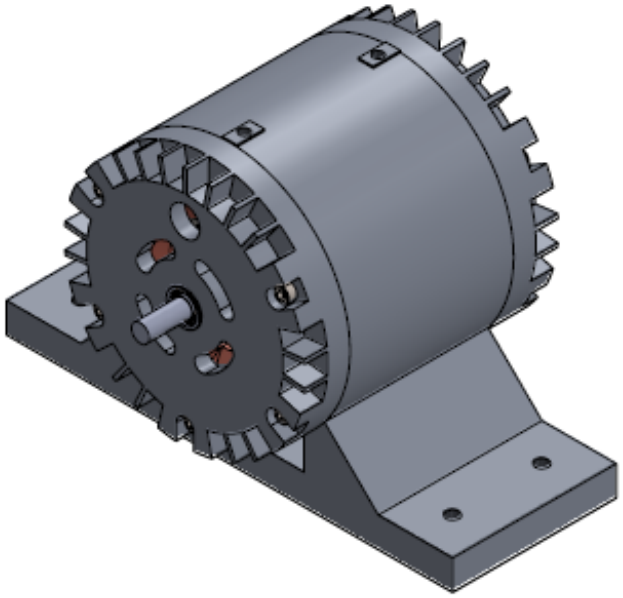

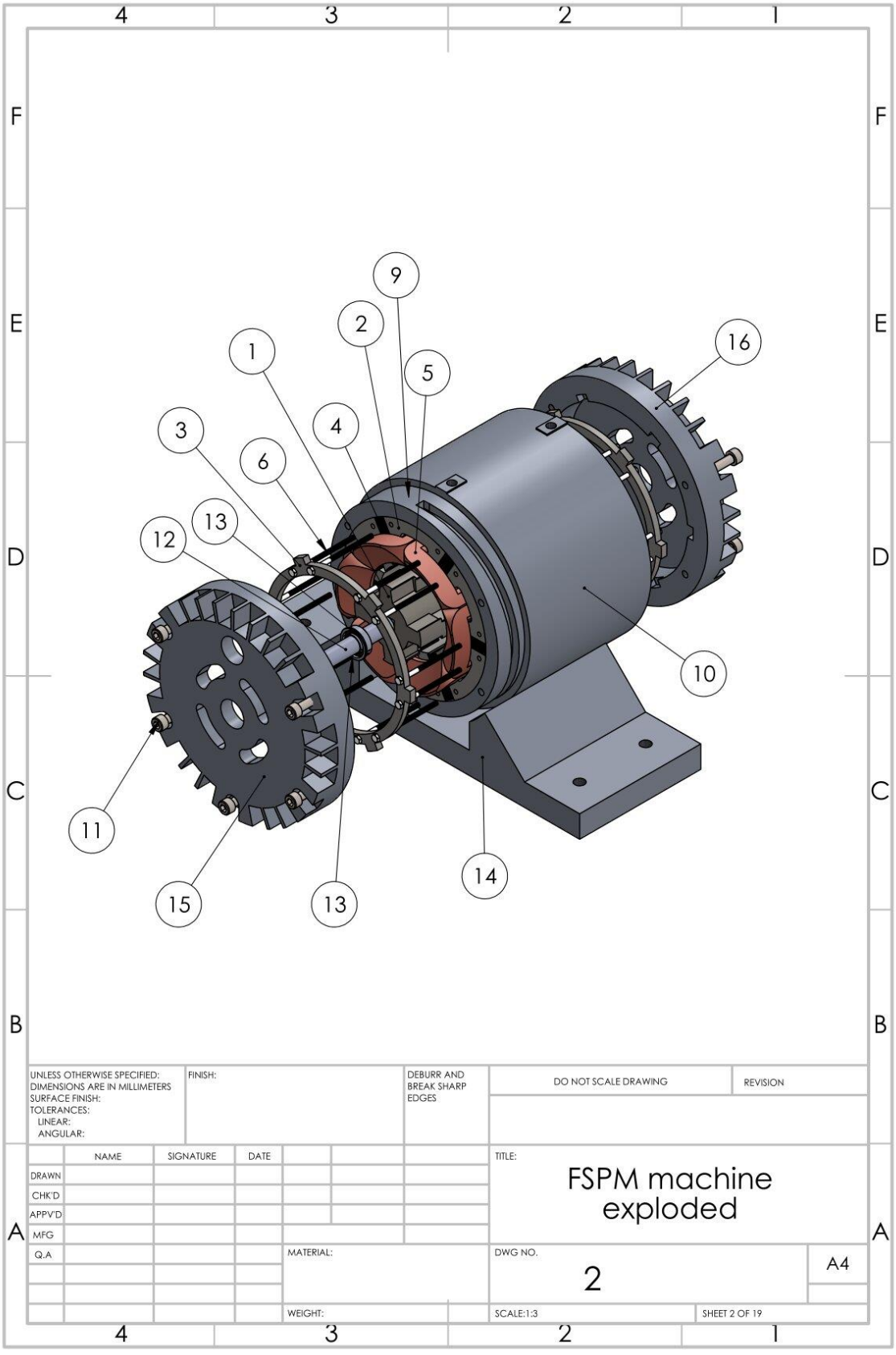
4
3
2
1
F
E
D
C
B
A
9
2
1
5
16
3
4
6
13
12
10
11
15
13
14
UNLESS OTHERWISE SPECIFIED:
DIMENSIONS ARE IN MILLIMETERS
SURFACE FINISH:
TOLERANCES:
LINEAR:
ANGULAR:
FINISH:
DEBURR AND BREAK SHARP EDGES
DO NOT SCALE DRAWING
REVISION
NAME
SIGNATURE
DATE
DRAWN
CHK'D
APPV'D
MFG
Q.A
MATERIAL:
WEIGHT:
TITLE:
FSPM machine exploded
DWG NO.
2
A4
SCALE:1:3
SHEET 2 OF 19

ITEM NO.	PART NUMBER	DESCRIPTION	QTY.
1	Stator unit	Arnon 5 lamination	6
2	Magnet	NdFeB magnet, Br = 1.2 T	6
3	Cir. Frame key	Hold stator units - Aluminum	1
4	Cir. Frame no key	Hold stator units - Aluminum	1
5	Bolt-M4-0.7-55	Connect Cir. Frame to stator unit	12
6	Nut-M4-0.7	Connect Cir. Frame to stator unit	12

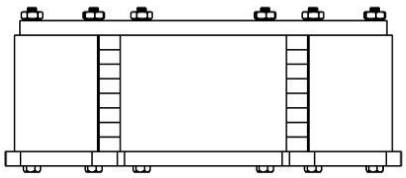

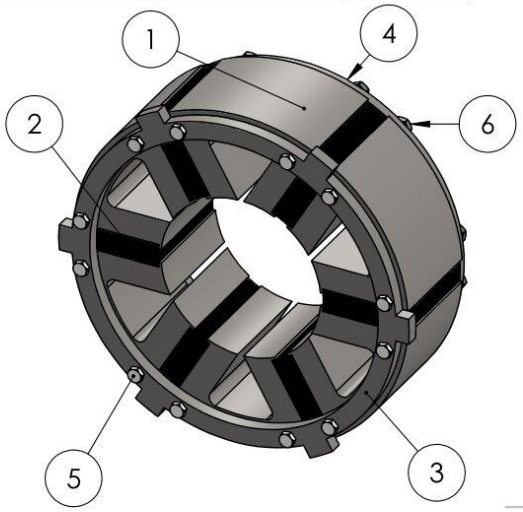

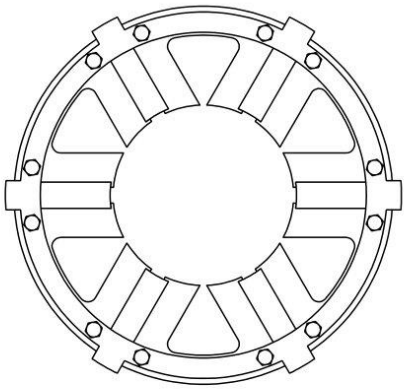

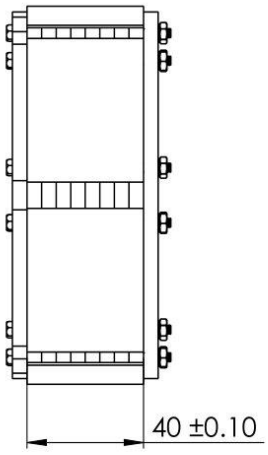

UNLESS OTHERWISE SPECIFIED:
DIMENSIONS ARE IN MILLIMETERS
SURFACE FINISH:
TOLERANCES:
LINEAR:
ANGULAR:

FINISH:

DEBURR AND BREAK SHARP EDGES

DO NOT SCALE DRAWING

REVISION

	NAME	SIGNATURE	DATE
DRAWN			
CHK'D			
APPV'D			
MFG			
Q.A			

TITLE:

Stator assembly

MATERIAL:

DWG NO.

3

A4

WEIGHT:

SCALE:1:2

SHEET 3 OF 19

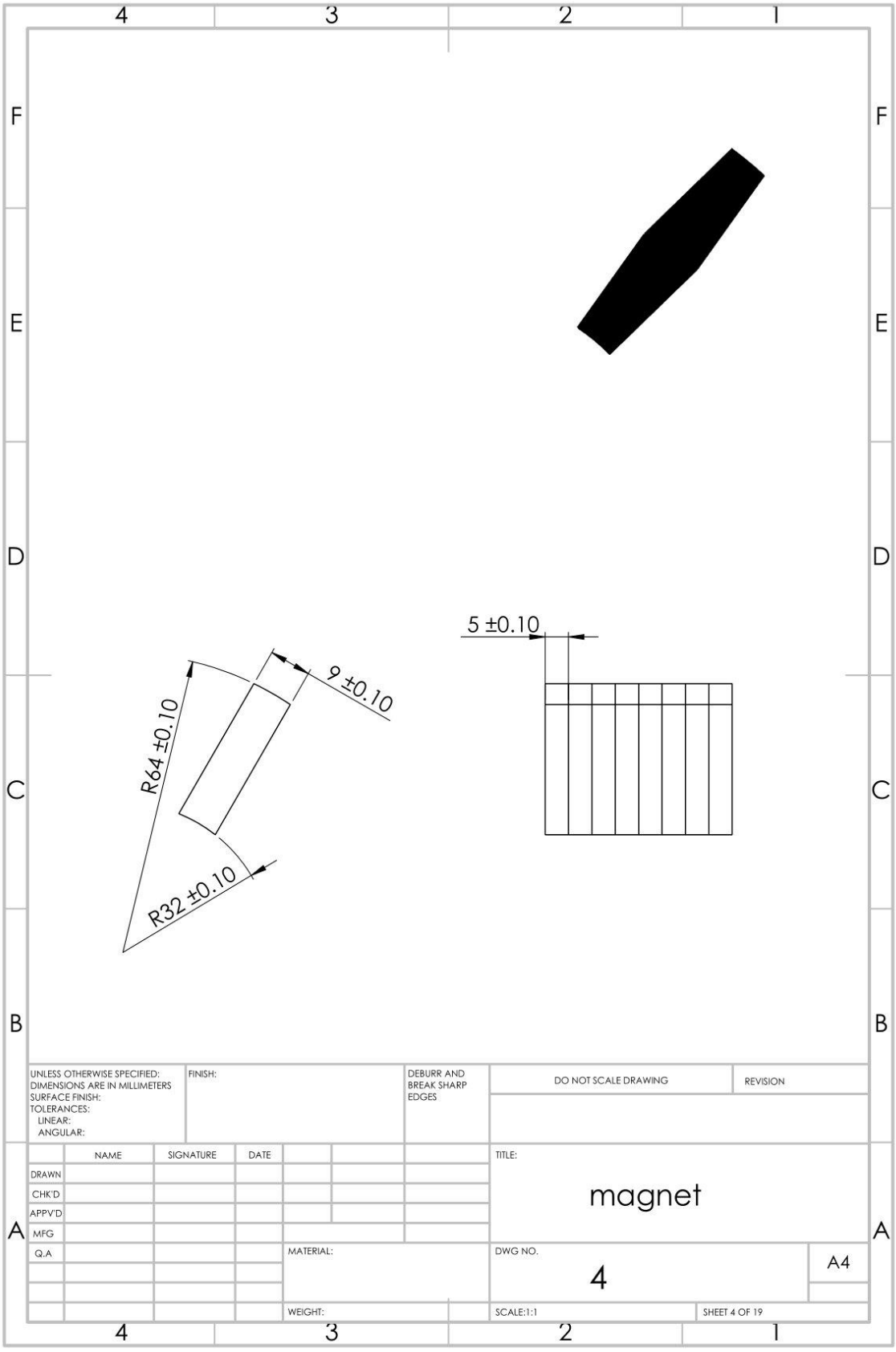
4
3
2
1
F
E
D
C
B
A
5 ±0.10
9 ±0.10
R64 ±0.10
R32 ±0.10
UNLESS OTHERWISE SPECIFIED:
DIMENSIONS ARE IN MILLIMETERS
SURFACE FINISH:
TOLERANCES:
LINEAR:
ANGULAR:
FINISH:
DEBURR AND BREAK SHARP EDGES
DO NOT SCALE DRAWING
REVISION
NAME
SIGNATURE
DATE
DRAWN
CHK'D
APPV'D
MFG
Q.A
TITLE:
magnet
MATERIAL:
DWG NO.
4
A4
WEIGHT:
SCALE:1:1
SHEET 4 OF 19

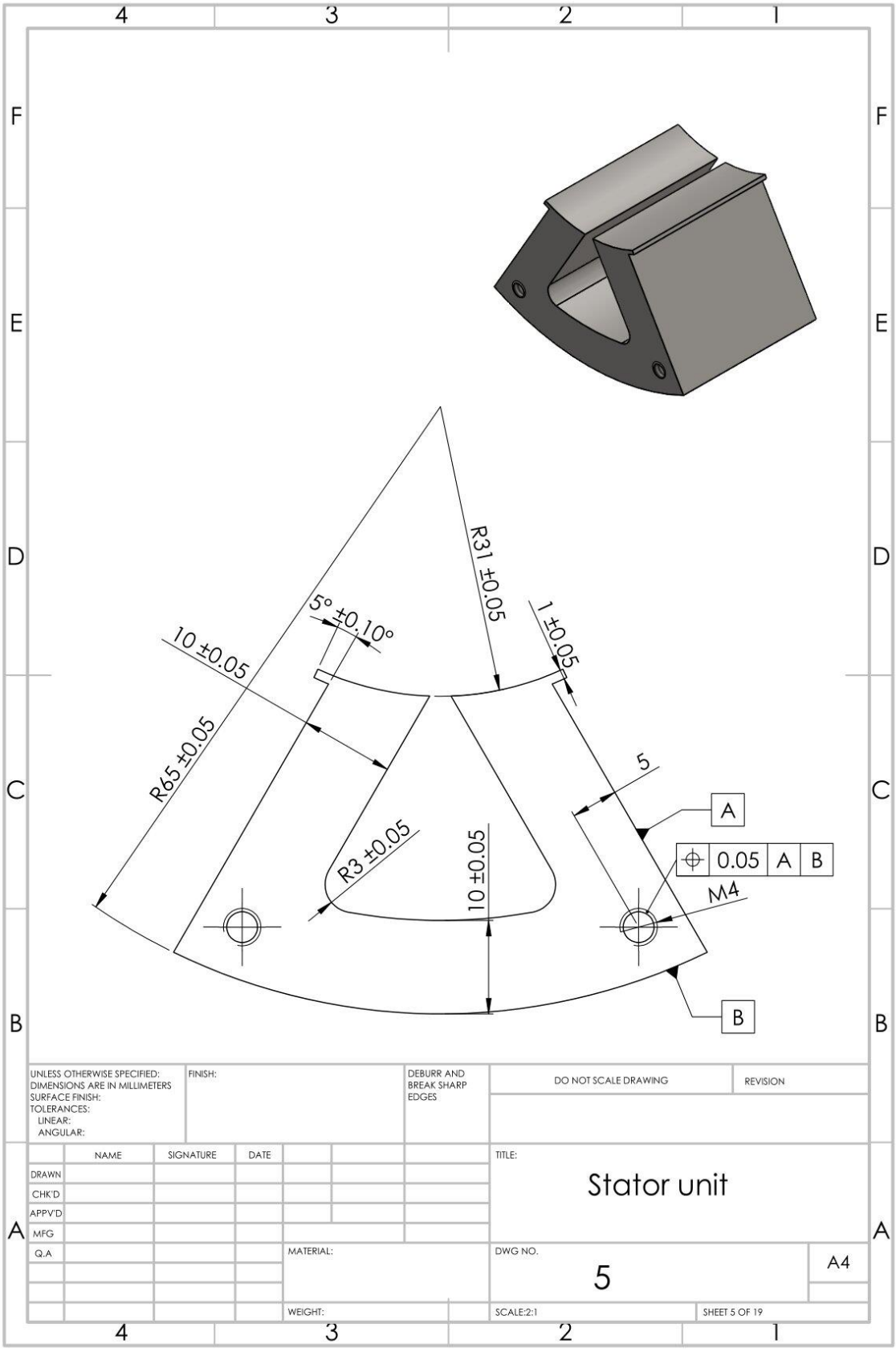
4
3
2
1
F
E
D
C
B
A
R31 ±0.05
5° ±0.10°
1 ±0.05
10 ±0.05
R65 ±0.05
5
A
0.05 A B
M4
R3 ±0.05
10 ±0.05
B
UNLESS OTHERWISE SPECIFIED:
DIMENSIONS ARE IN MILLIMETERS
SURFACE FINISH:
TOLERANCES:
LINEAR:
ANGULAR:
FINISH:
DEBURR AND BREAK SHARP EDGES
DO NOT SCALE DRAWING
REVISION
NAME
SIGNATURE
DATE
DRAWN
CHK'D
APPV'D
MFG
Q.A
TITLE:
Stator unit
MATERIAL:
DWG NO.
5
A4
WEIGHT:
SCALE:2:1
SHEET 5 OF 19

ITEM NO.	PART NUMBER	DESCRIPTION	QTY.
1	Rotor	Arnon 5 lamination	1
2	shaft_square	Harden steel	1
3	AST_Bearings_F63801	Highspeed bearing	2

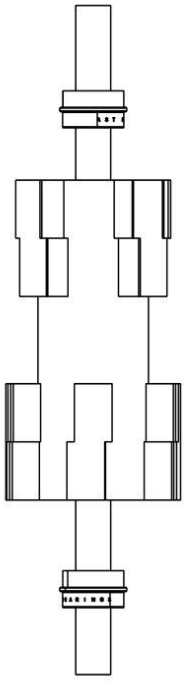

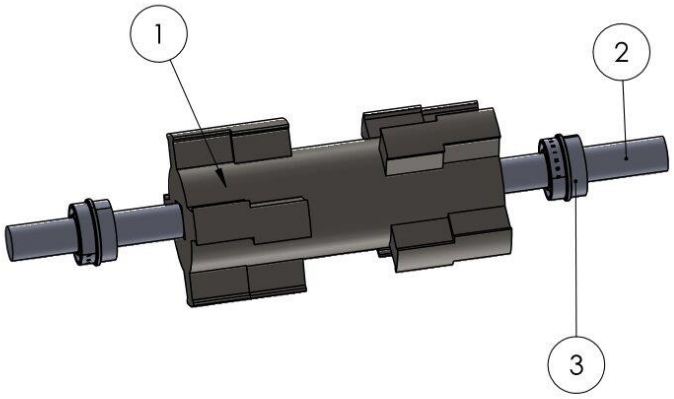

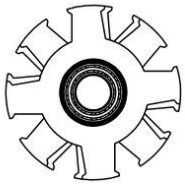

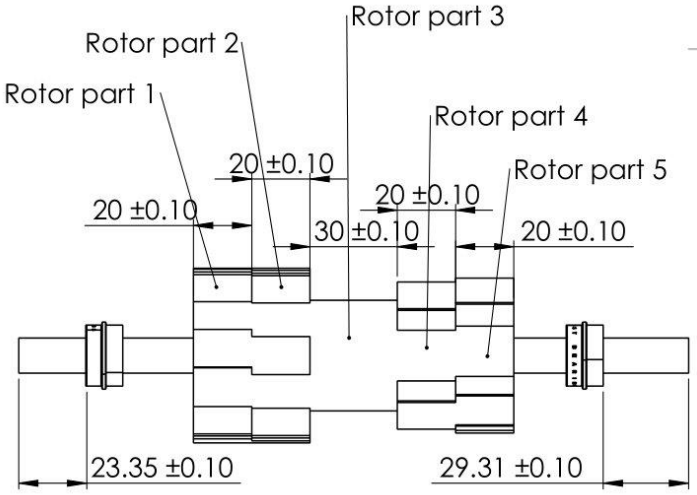

UNLESS OTHERWISE SPECIFIED:
DIMENSIONS ARE IN MILLIMETERS
SURFACE FINISH:
TOLERANCES:
LINEAR:
ANGULAR:

FINISH:

DEBURR AND BREAK SHARP EDGES

DO NOT SCALE DRAWING

REVISION

	NAME	SIGNATURE	DATE
DRAWN			
CHK'D			
APPV'D			
MFG			
Q.A			

TITLE:

Rotor assembly

MATERIAL:

DWG NO.

6

A4

WEIGHT:

SCALE:1:2

SHEET 6 OF 19

Rotor tip dimension can be found in rotor part 2 drawing

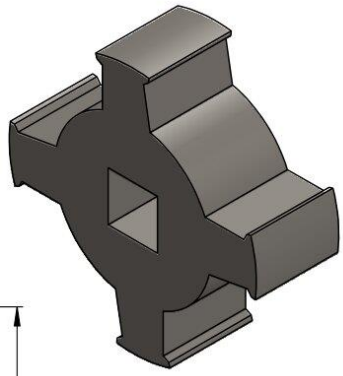

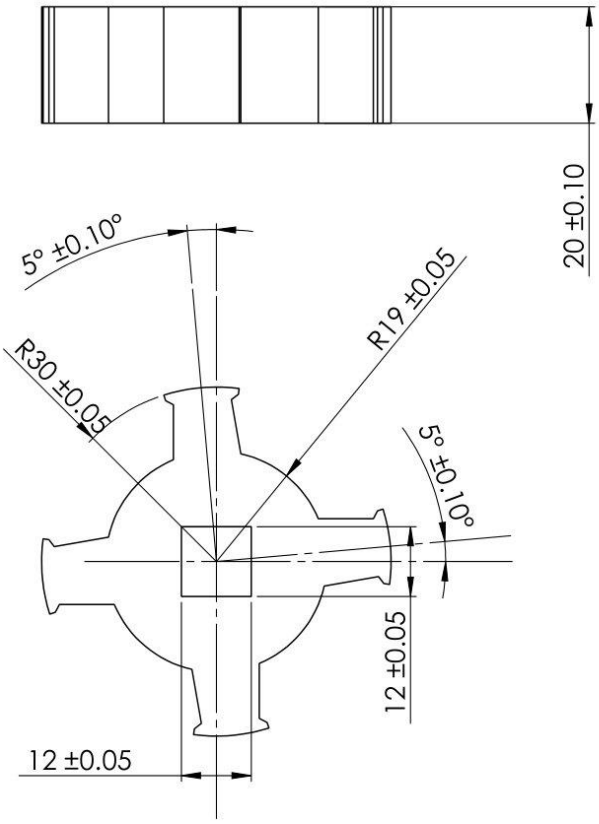

UNLESS OTHERWISE SPECIFIED: DIMENSIONS ARE IN MILLIMETERS SURFACE FINISH: TOLERANCES: LINEAR: ANGULAR:		FINISH:			DEBURR AND BREAK SHARP EDGES		DO NOT SCALE DRAWING	REVISION
	NAME	SIGNATURE	DATE				TITLE:	
DRAWN							Rotor part 1	
CHK'D								
APPV'D								
MFG								
Q.A				MATERIAL:			DWG NO.	A4
							7	
				WEIGHT:			SCALE:1:1	SHEET 7 OF 19

Dimensions not depicted in this page can be found in rotor part 1

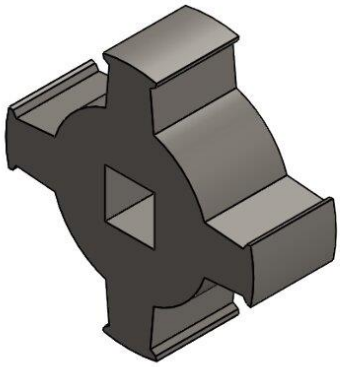

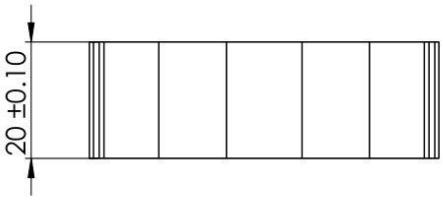

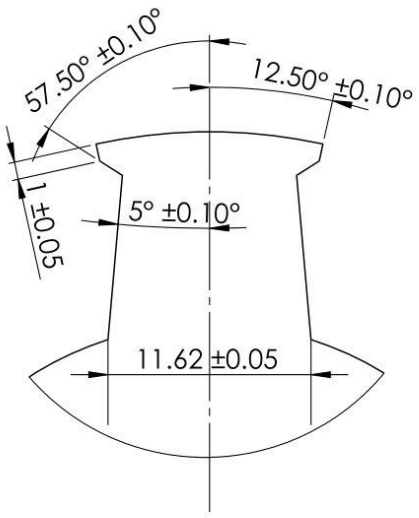

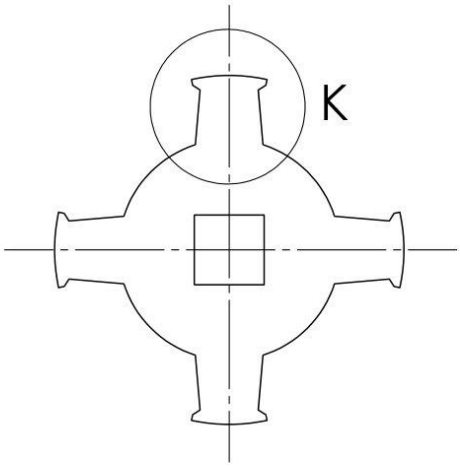

DETAIL K

SCALE 3 : 1

UNLESS OTHERWISE SPECIFIED: DIMENSIONS ARE IN MILLIMETERS SURFACE FINISH: TOLERANCES: LINEAR: ANGULAR:	FINISH:	DEBURR AND BREAK SHARP EDGES	DO NOT SCALE DRAWING / REVISION

	NAME	SIGNATURE	DATE
DRAWN			
CHK'D			
APPV'D			
MFG			
Q.A			

TITLE:	rotor part 2
MATERIAL:	
DWG NO.	8
A4	
WEIGHT:	
SCALE:1:1	SHEET 8 OF 19

Dimensions not depicted in this page can be found in rotor part 1

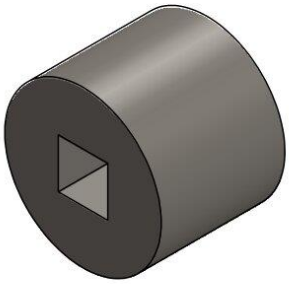

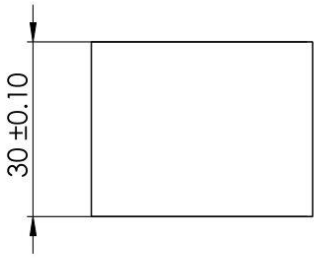

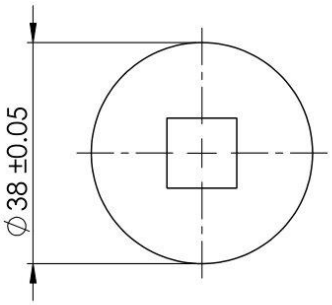

UNLESS OTHERWISE SPECIFIED: DIMENSIONS ARE IN MILLIMETERS SURFACE FINISH: TOLERANCES: LINEAR: ANGULAR:	FINISH:	DEBURR AND BREAK SHARP EDGES	DO NOT SCALE DRAWING / REVISION

	NAME	SIGNATURE	DATE
DRAWN			
CHK'D			
APPV'D			
MFG			
Q.A			

TITLE: rotor part 3

MATERIAL:

DWG NO. 9

A4

WEIGHT:

SCALE:1:1

SHEET 9 OF 19

Dimensions not depicted in this page can be found in rotor part 1

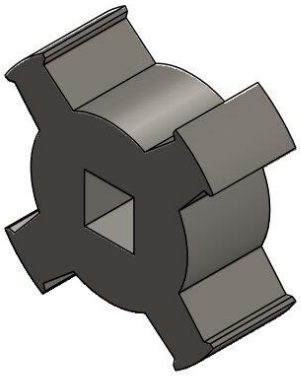

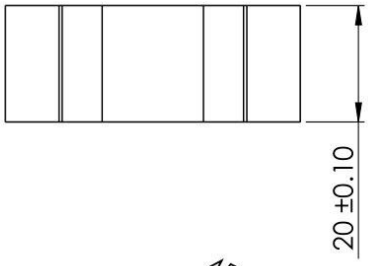

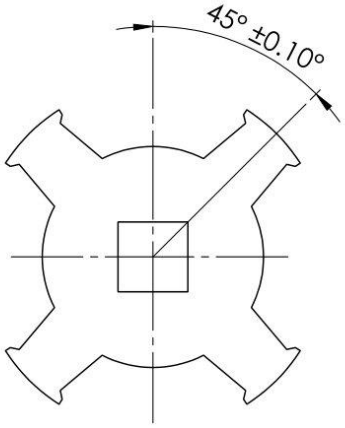

UNLESS OTHERWISE SPECIFIED: DIMENSIONS ARE IN MILLIMETERS SURFACE FINISH: TOLERANCES: LINEAR: ANGULAR:	FINISH:	DEBURR AND BREAK SHARP EDGES	DO NOT SCALE DRAWING / REVISION

	NAME	SIGNATURE	DATE
DRAWN			
CHK'D			
APPV'D			
MFG			
Q.A			

TITLE: rotor part 4

MATERIAL:

DWG NO. 10

A4

WEIGHT:

SCALE:1:1

SHEET 10 OF 19

Dimensions not depicted in this page can be found in rotor part 1

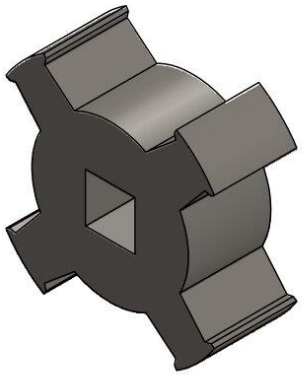

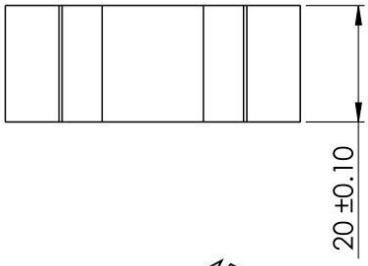

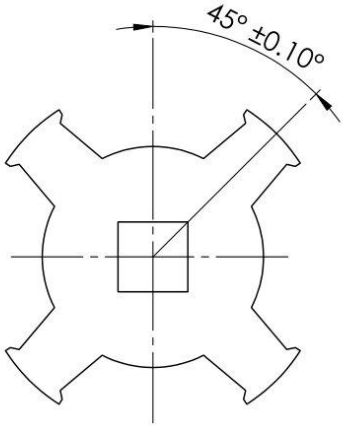

UNLESS OTHERWISE SPECIFIED: DIMENSIONS ARE IN MILLIMETERS SURFACE FINISH: TOLERANCES: LINEAR: ANGULAR:	FINISH:	DEBURR AND BREAK SHARP EDGES	DO NOT SCALE DRAWING / REVISION

	NAME	SIGNATURE	DATE
DRAWN			
CHK'D			
APPV'D			
MFG			
Q.A			

TITLE: rotor part 4

MATERIAL:

DWG NO. 10

A4

WEIGHT:

SCALE:1:1

SHEET 10 OF 19

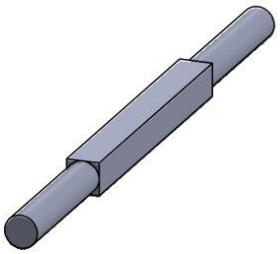

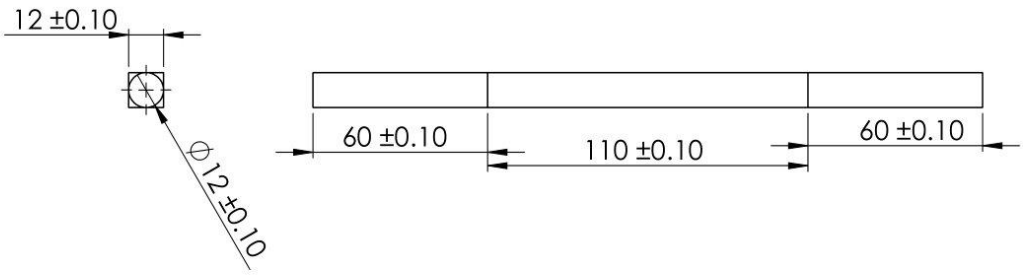

UNLESS OTHERWISE SPECIFIED: DIMENSIONS ARE IN MILLIMETERS SURFACE FINISH: TOLERANCES: LINEAR: ANGULAR:		FINISH:		DEBURR AND BREAK SHARP EDGES		DO NOT SCALE DRAWING	REVISION
	NAME	SIGNATURE	DATE			TITLE:	
DRAWN						Shaft	
CHK'D							
APPV'D							
MFG							
Q.A				MATERIAL:		DWG NO.	A4
						12	
				WEIGHT:		SCALE:1:2	SHEET 12 OF 19

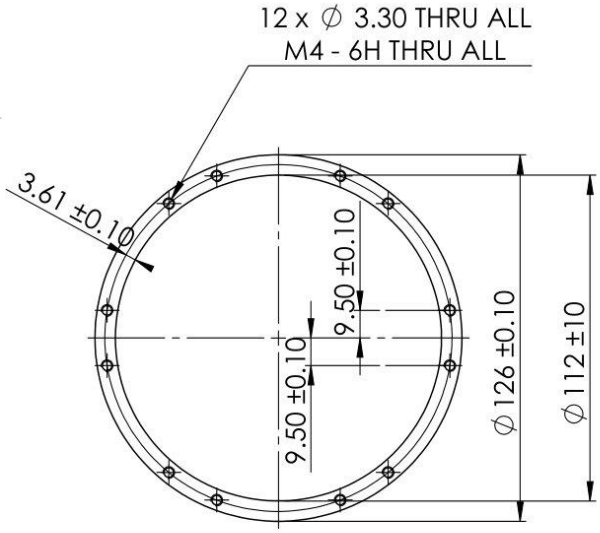

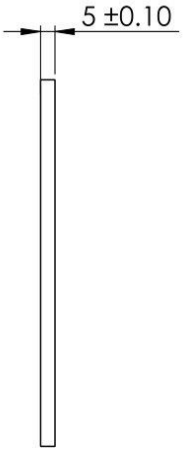

UNLESS OTHERWISE SPECIFIED: DIMENSIONS ARE IN MILLIMETERS SURFACE FINISH: TOLERANCES: LINEAR: ANGULAR:		FINISH:		DEBURR AND BREAK SHARP EDGES		DO NOT SCALE DRAWING	REVISION
	NAME	SIGNATURE	DATE			TITLE:	
DRAWN						Cir. frame no key	
CHK'D							
APPV'D							
MFG							
Q.A				MATERIAL:		DWG NO.	A4
						13	
				WEIGHT:		SCALE:1:2	SHEET 13 OF 19

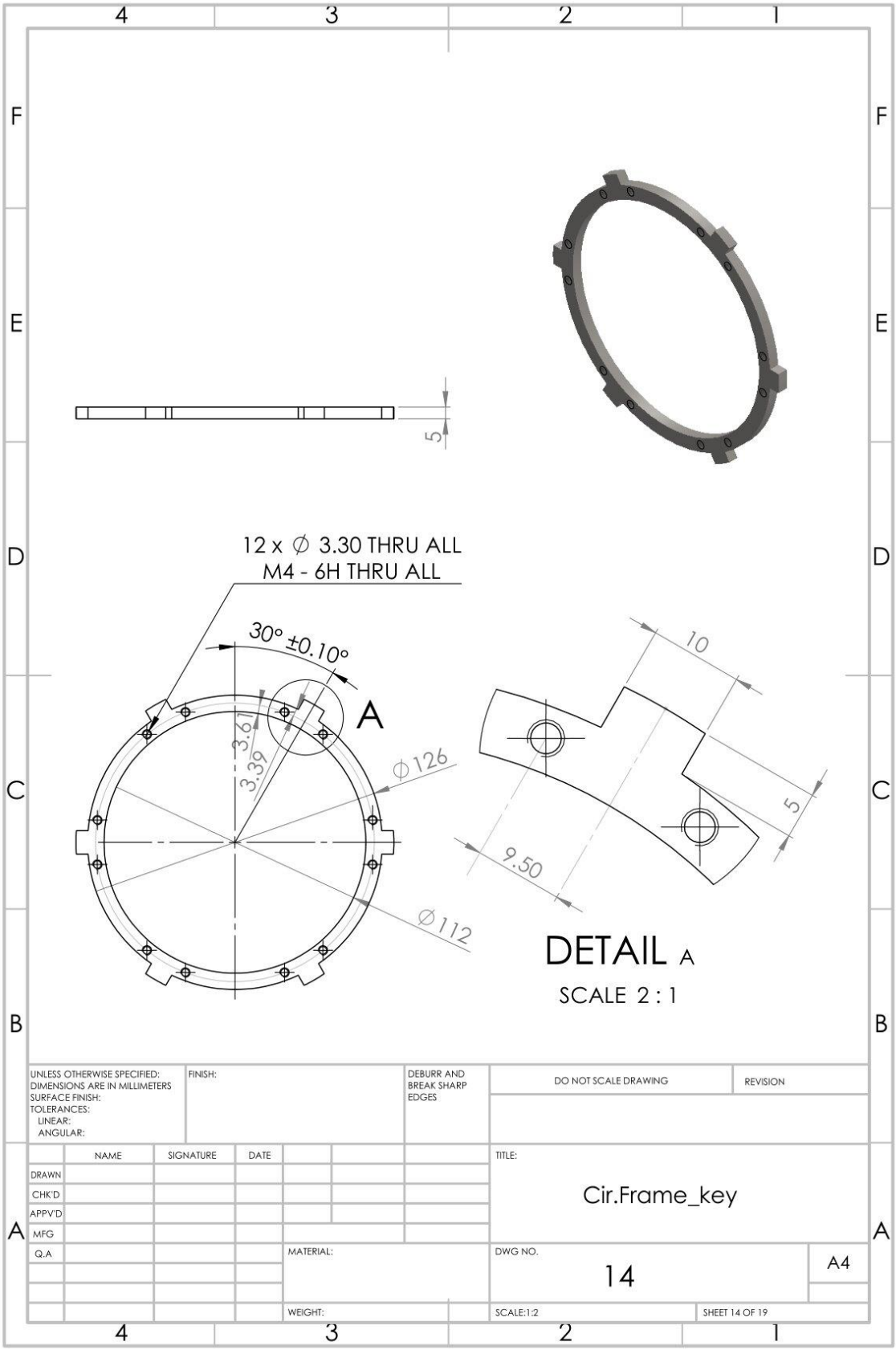
4
3
2
1
F
E
D
C
B
A
5
12 x ∅ 3.30 THRU ALL
M4 - 6H THRU ALL
30° ±0.10°
A
3.6
3.39
∅126
∅112
10
5
9.50
DETAIL A
SCALE 2 : 1
UNLESS OTHERWISE SPECIFIED:
DIMENSIONS ARE IN MILLIMETERS
SURFACE FINISH:
TOLERANCES:
LINEAR:
ANGULAR:
FINISH:
DEBURR AND BREAK SHARP EDGES
DO NOT SCALE DRAWING
REVISION
NAME
SIGNATURE
DATE
DRAWN
CHK'D
APPV'D
MFG
Q.A
MATERIAL:
WEIGHT:
TITLE:
Cir.Frame_key
DWG NO.
14
A4
SCALE:1:2
SHEET 14 OF 19

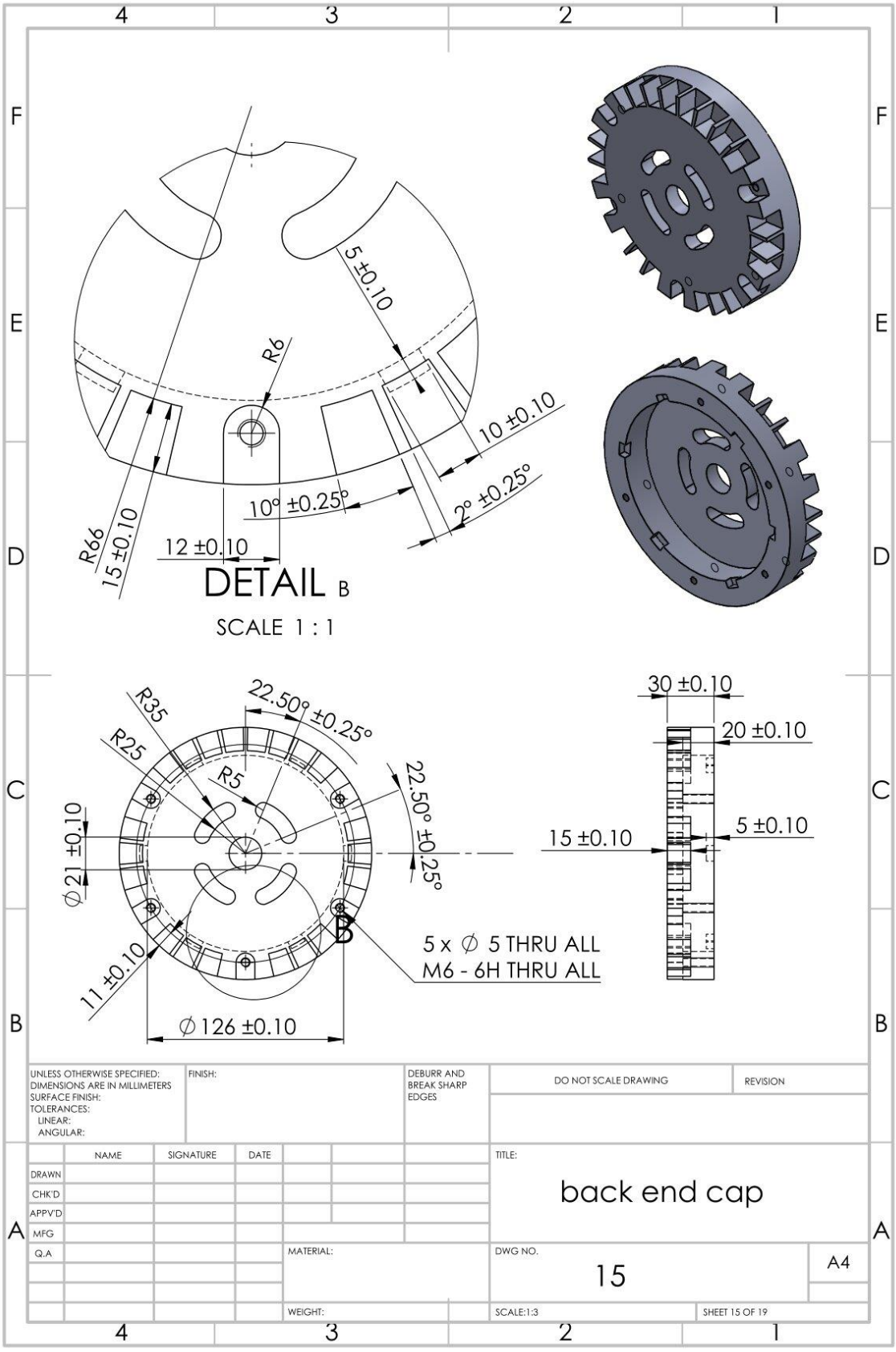
5 ±0.10
R6
10 ±0.10
10° ±0.25°
2° ±0.25°
R66
15 ±0.10
12 ±0.10
DETAIL B
SCALE 1 : 1
R35
R25
22.50° ±0.25°
R5
22.50° ±0.25°
∅21 ±0.10
11 ±0.10
∅126 ±0.10
5 x ∅ 5 THRU ALL
M6 - 6H THRU ALL
30 ±0.10
20 ±0.10
15 ±0.10
5 ±0.10
UNLESS OTHERWISE SPECIFIED:
DIMENSIONS ARE IN MILLIMETERS
SURFACE FINISH:
TOLERANCES:
LINEAR:
ANGULAR:
FINISH:
DEBURR AND BREAK SHARP EDGES
DO NOT SCALE DRAWING
REVISION
NAME
SIGNATURE
DATE
DRAWN
CHK'D
APPV'D
MFG
Q.A
TITLE:
back end cap
MATERIAL:
DWG NO.
15
A4
WEIGHT:
SCALE:1:3
SHEET 15 OF 19

Openings not described are identical as in the back cap

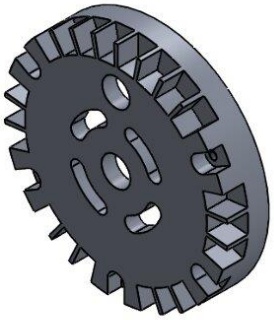

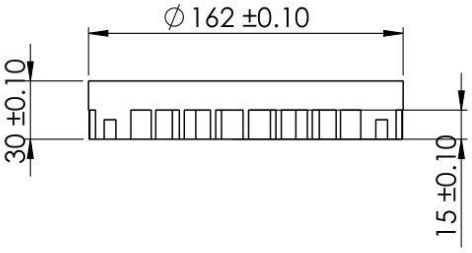

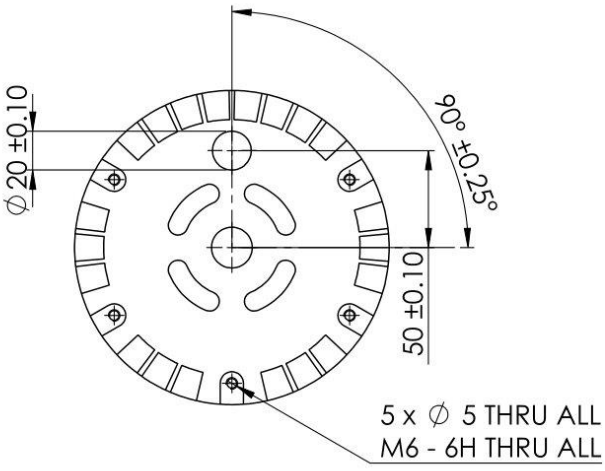

UNLESS OTHERWISE SPECIFIED: DIMENSIONS ARE IN MILLIMETERS SURFACE FINISH: TOLERANCES: LINEAR: ANGULAR:	FINISH:	DEBURR AND BREAK SHARP EDGES	DO NOT SCALE DRAWING / REVISION

	NAME	SIGNATURE	DATE
DRAWN			
CHK'D			
APPV'D			
MFG			
Q.A			

TITLE: Front end cap

MATERIAL:

DWG NO. 16

A4

WEIGHT:

SCALE:1:3

SHEET 16 OF 19

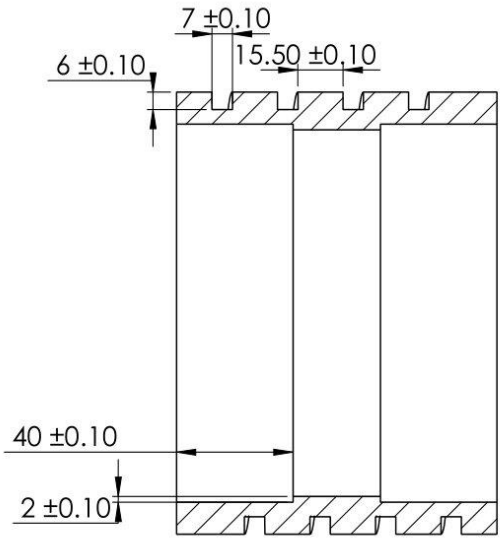

SECTION C-C

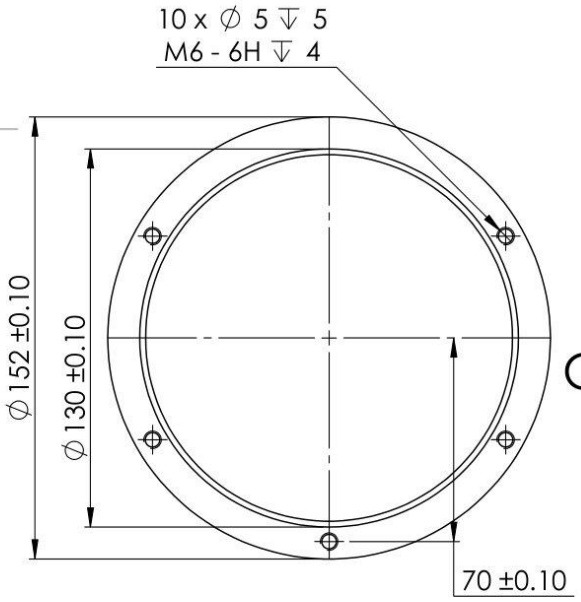

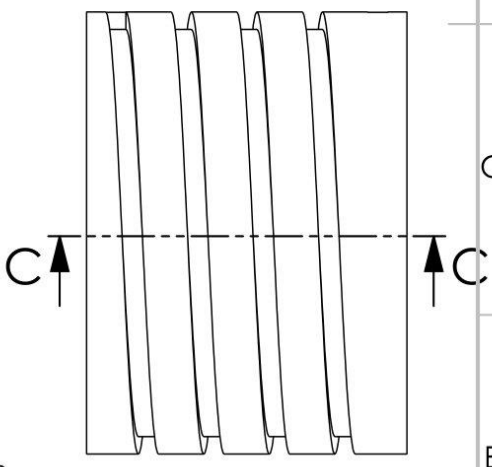

UNLESS OTHERWISE SPECIFIED: DIMENSIONS ARE IN MILLIMETERS SURFACE FINISH: TOLERANCES: LINEAR: ANGULAR:	FINISH:	DEBURR AND BREAK SHARP EDGES	DO NOT SCALE DRAWING	REVISION	
	NAME	SIGNATURE	DATE	TITLE:	
DRAWN				inner housing	
CHK'D					
APPV'D					
MFG					
Q.A			MATERIAL:	DWG NO. 17	A4
			WEIGHT:	SCALE:1:2	SHEET 17 OF 19

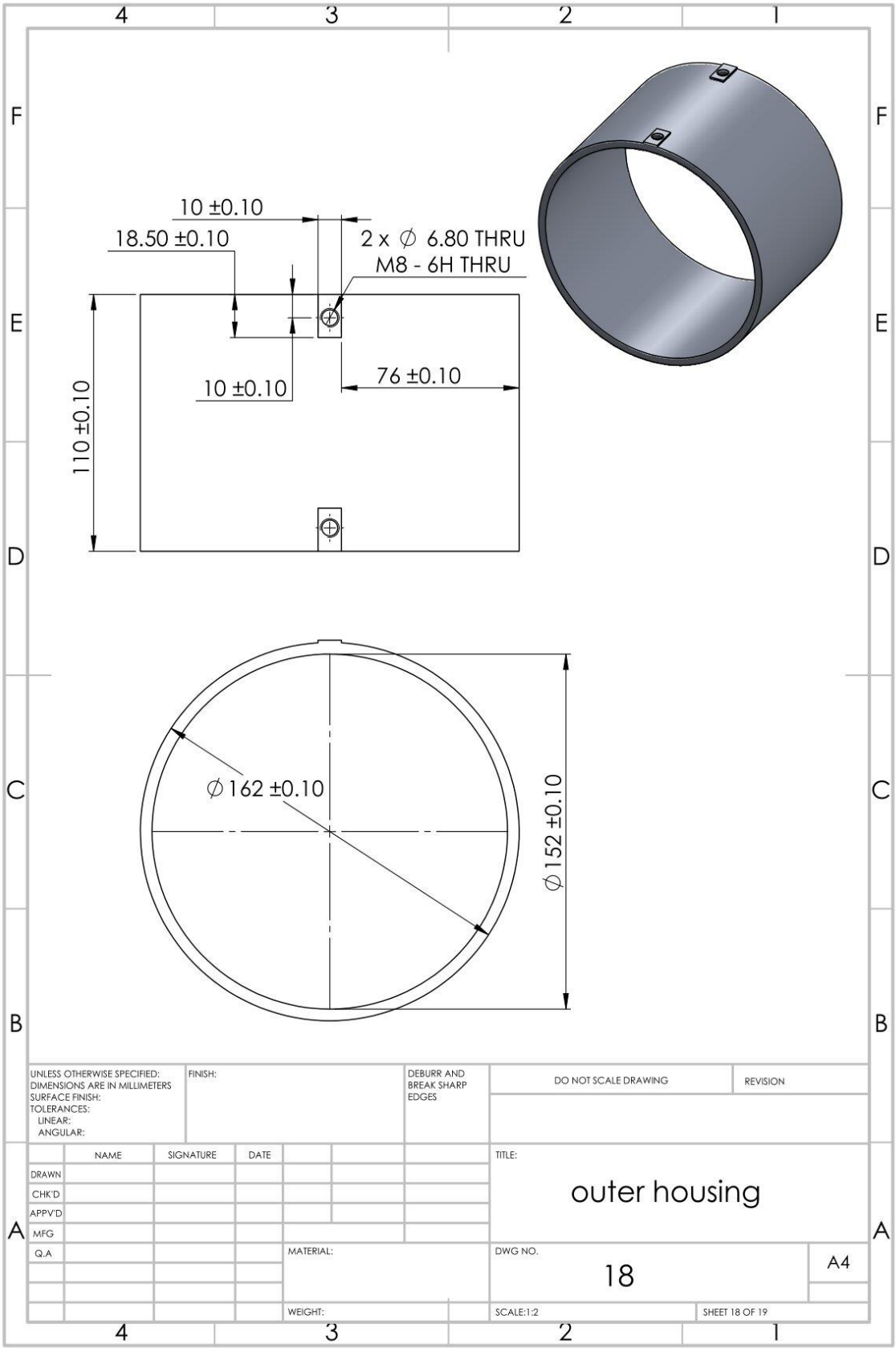
10 ±0.10
18.50 ±0.10
2 x ∅ 6.80 THRU
M8 - 6H THRU
10 ±0.10
76 ±0.10
110 ±0.10
∅162 ±0.10
∅152 ±0.10
UNLESS OTHERWISE SPECIFIED:
DIMENSIONS ARE IN MILLIMETERS
SURFACE FINISH:
TOLERANCES:
LINEAR:
ANGULAR:
FINISH:
DEBURR AND BREAK SHARP EDGES
DO NOT SCALE DRAWING
REVISION
NAME
SIGNATURE
DATE
DRAWN
CHK'D
APPV'D
MFG
Q.A
TITLE:
outer housing
MATERIAL:
DWG NO.
18
A4
WEIGHT:
SCALE:1:2
SHEET 18 OF 19

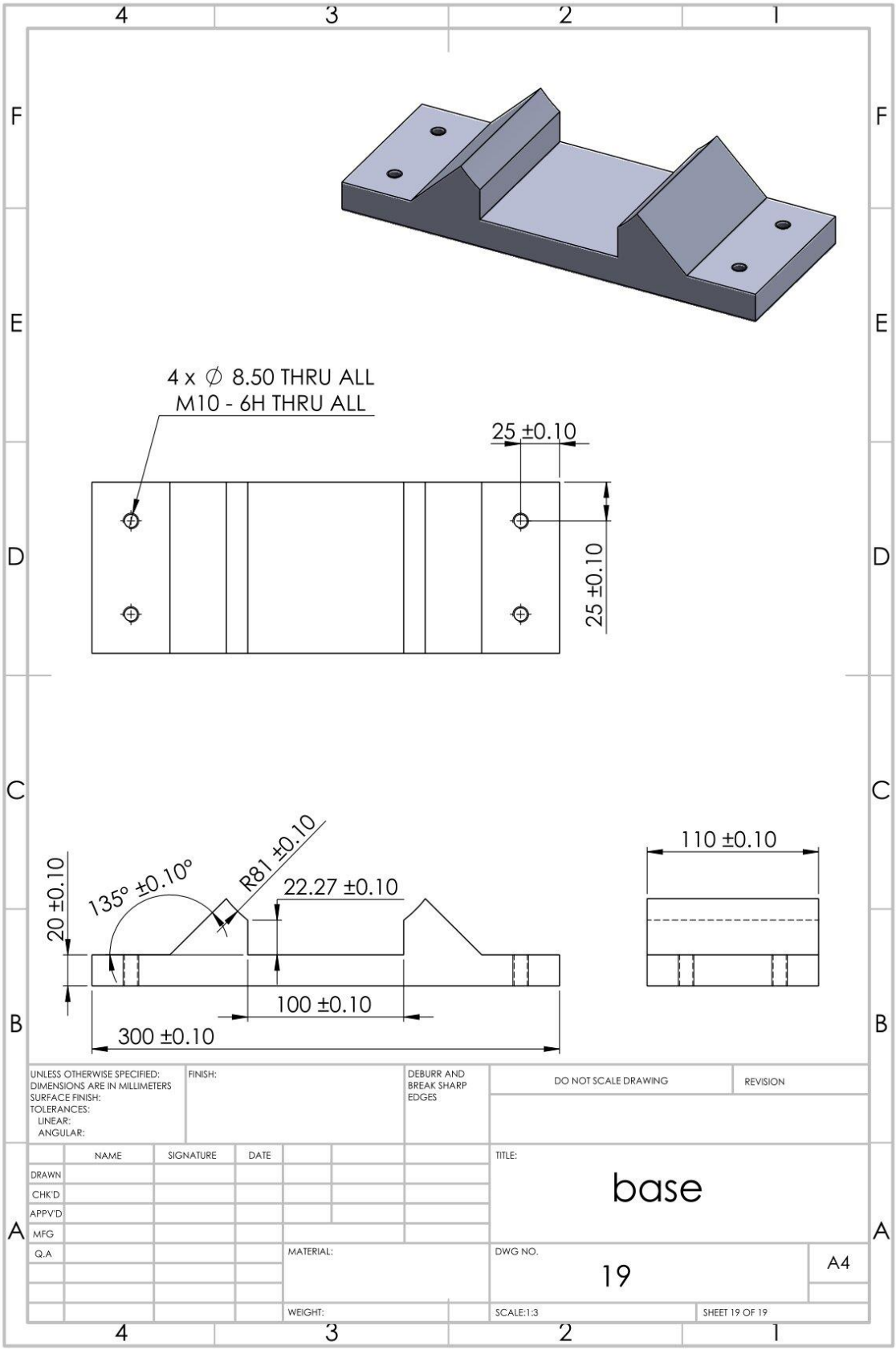
4 x ∅ 8.50 THRU ALL
M10 - 6H THRU ALL
25 ±0.10
25 ±0.10
20 ±0.10
135° ±0.10°
R81 ±0.10
22.27 ±0.10
100 ±0.10
300 ±0.10
110 ±0.10
UNLESS OTHERWISE SPECIFIED:
DIMENSIONS ARE IN MILLIMETERS
SURFACE FINISH:
TOLERANCES:
LINEAR:
ANGULAR:
FINISH:
DEBURR AND BREAK SHARP EDGES
DO NOT SCALE DRAWING
REVISION
NAME
SIGNATURE
DATE
DRAWN
CHK'D
APPV'D
MFG
Q.A
TITLE:
base
MATERIAL:
DWG NO.
19
A4
WEIGHT:
SCALE:1:3
SHEET 19 OF 19

Annex B – Manufacturing guide for SLTW dual-stator 6/4 FSPM machine prototype

Bill of material (BOM)

ITEM NO.	PART NUMBER	DESCRIPTION	QTY.
1	asm_statorLam		2
2	coil		1
3	housing_inner		1
4	housing_outer		1
5	endHousing_fr		1
6	shaft		1
7	endHousing_re		1
8	HEXTS 4x16X14.6-Indented head-D-N		12
9	HEXTS 4x20X18.6-Indented head-D-S		12
10	6802-VV-NSK	Bearing	2
11	shaft_key		1
12	asm_rotorLam		1
13	cable gland	Hylec 111006-Cable Gland	1
14	Green BANANA JACK	ABBATRON-1509-104 Green BananaJack	1
15	motorCable_gland	Hylec K151-1016-00	1
16	M6-1.0 Eyebolt	M6-1.0 Eyebolt	2
17	magnet_rect		12
18	preload_ring	Smalley p/n SSB-0095	1

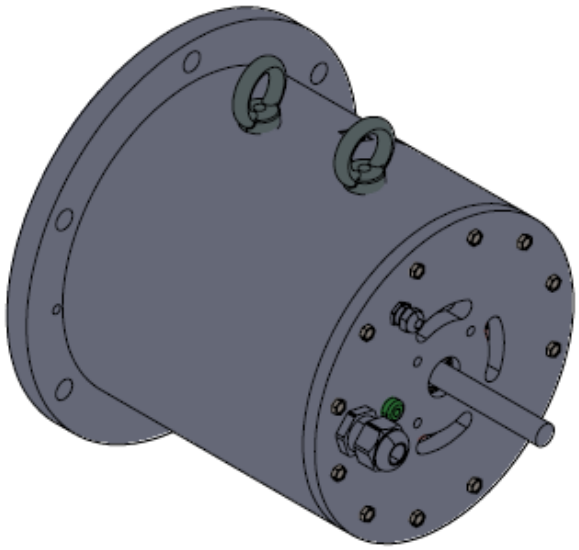

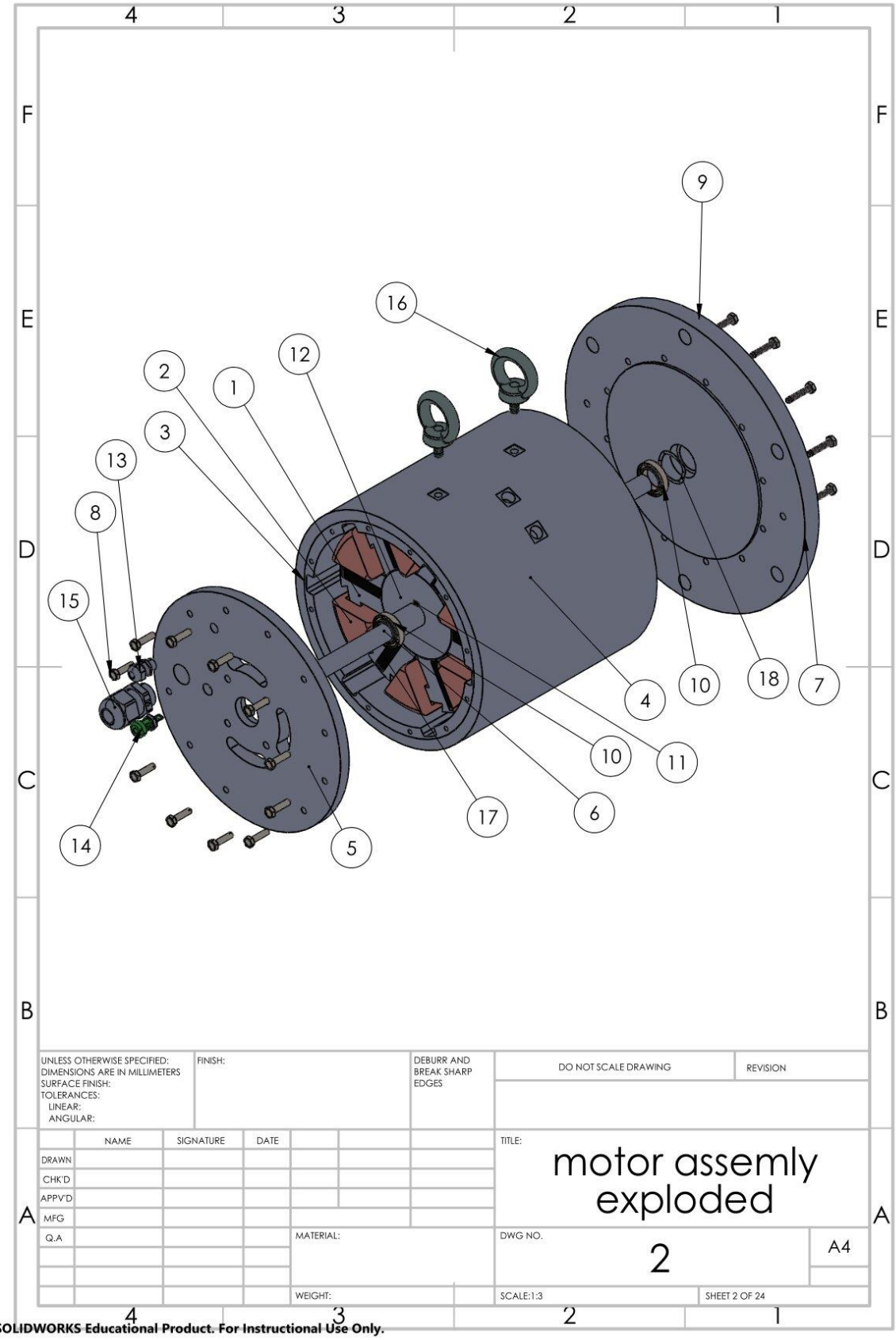

ITEM NO.	PART NUMBER	DESCRIPTION	QTY.
1	asm_statorLam		2
2	housing_inner		1
3	housing_outer		1
4	magnet_rect		12

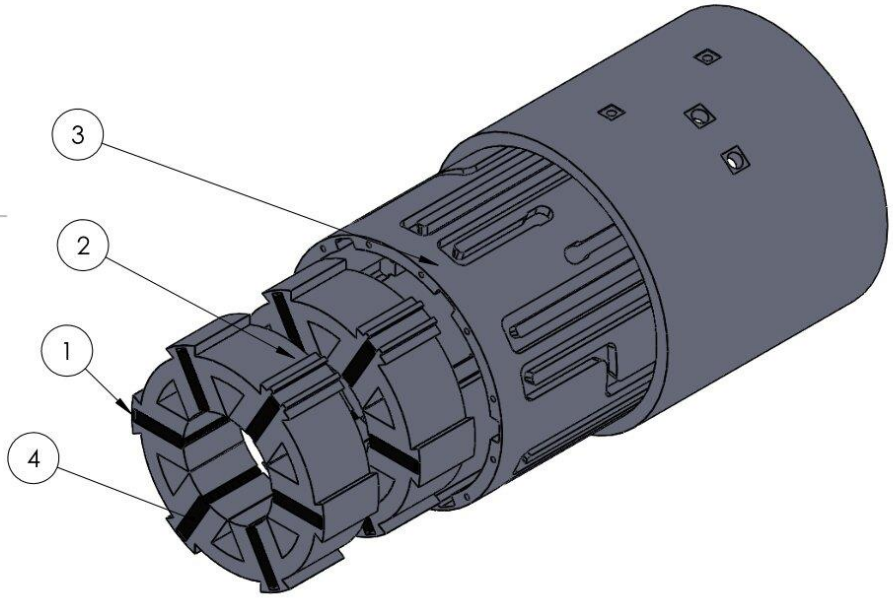

UNLESS OTHERWISE SPECIFIED:
DIMENSIONS ARE IN MILLIMETERS
SURFACE FINISH:
TOLERANCES:
LINEAR:
ANGULAR:

FINISH:

DEBURR AND BREAK SHARP EDGES

DO NOT SCALE DRAWING

REVISION

	NAME	SIGNATURE	DATE
DRAWN			
CHK'D			
APPV'D			
MFG			
Q.A			

TITLE:

stator/housing assembly

MATERIAL:

DWG NO.

3

A4

WEIGHT:

SCALE:1:3

SHEET 3 OF 24

ITEM NO.	PART NUMBER	DESCRIPTION	QTY.
1	stator Lam	Arnon5 stator lamination	315

BREAKALL SHARP EDGES

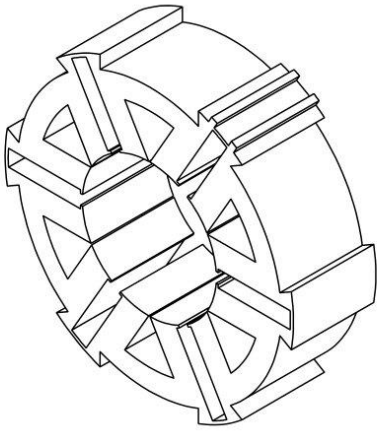

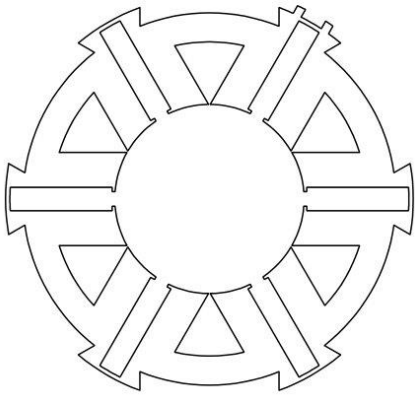

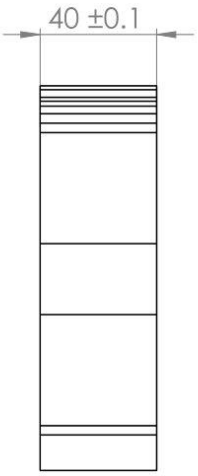

UNLESS OTHERWISE SPECIFIED: DIMENSIONS ARE IN MILLIMETERS SURFACE FINISH: TOLERANCES: LINEAR: ANGULAR:	FINISH:	DEBURR AND BREAK SHARP EDGES	DO NOT SCALE DRAWING / REVISION

	NAME	SIGNATURE	DATE
DRAWN			
CHK'D			
APPV'D			
MFG			
Q.A			

TITLE: asm_statorLam

MATERIAL:

DWG NO. 4

A4

WEIGHT:

SCALE:1:2

SHEET 4 OF 24

ITEM NO.	PART NUMBER	DESCRIPTION	QTY.
1	asm_rotorLam		1
2	shaft		1
3	6802-VV-NSK	ball bearing	2
4	shaft_key		1

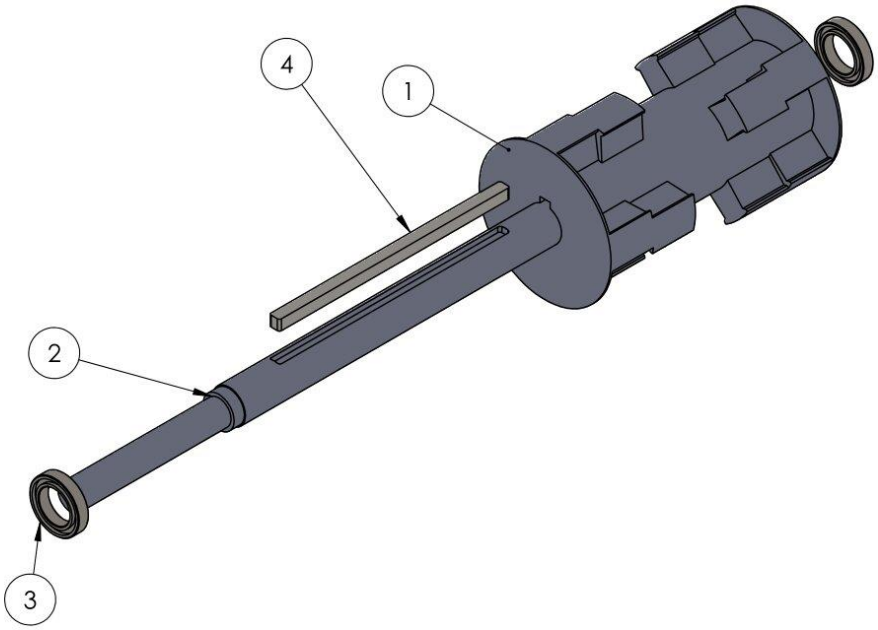

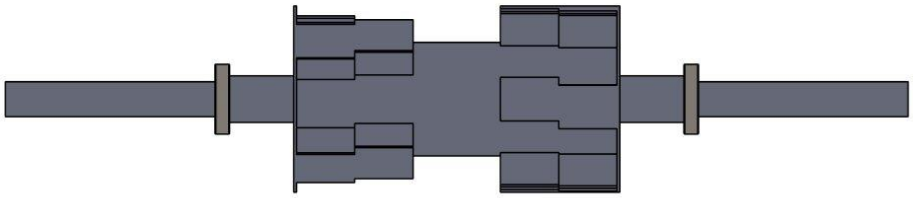

UNLESS OTHERWISE SPECIFIED: DIMENSIONS ARE IN MILLIMETERS SURFACE FINISH: TOLERANCES: LINEAR: ANGULAR:	FINISH:	DEBURR AND BREAK SHARP EDGES	DO NOT SCALE DRAWING / REVISION
NAME / SIGNATURE / DATE			TITLE: rotor shaft assembly
DRAWN			
CHK'D			
APPV'D			
MFG			
Q.A	MATERIAL:		DWG NO. 5 / A4
	WEIGHT:		SCALE:1:2 / SHEET 5 OF 24

ITEM NO.	PART NUMBER	DESCRIPTION	QTY.
1	rotorLam1		16
2	rotorLam2		157
3	rotorLam3		158
4	rotorLam4		236
5	rotorLam5		158
6	rotorLam6		157

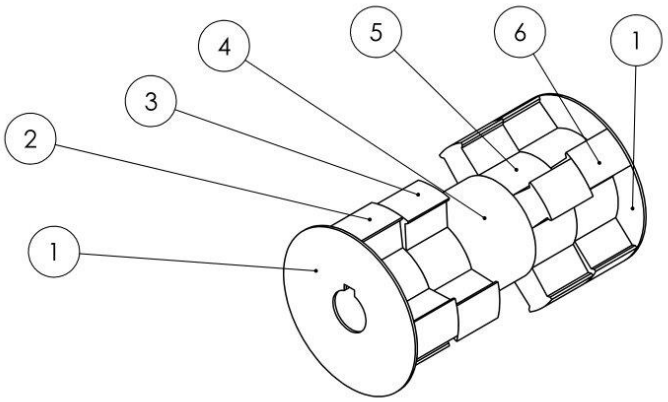

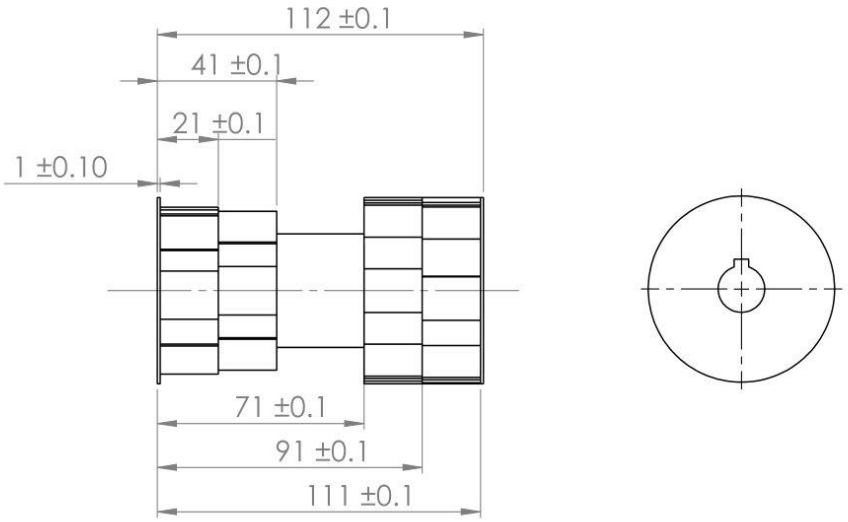

UNLESS OTHERWISE SPECIFIED:
DIMENSIONS ARE IN MILLIMETERS
SURFACE FINISH:
TOLERANCES:
LINEAR:
ANGULAR:

FINISH:

DEBURR AND BREAK SHARP EDGES

DO NOT SCALE DRAWING

REVISION

	NAME	SIGNATURE	DATE
DRAWN			
CHK'D			
APPV'D			
MFG			
Q.A			

TITLE: asm_rotorLam

MATERIAL:

DWG NO. 6

A4

WEIGHT:

SCALE:1:2

SHEET 6 OF 24

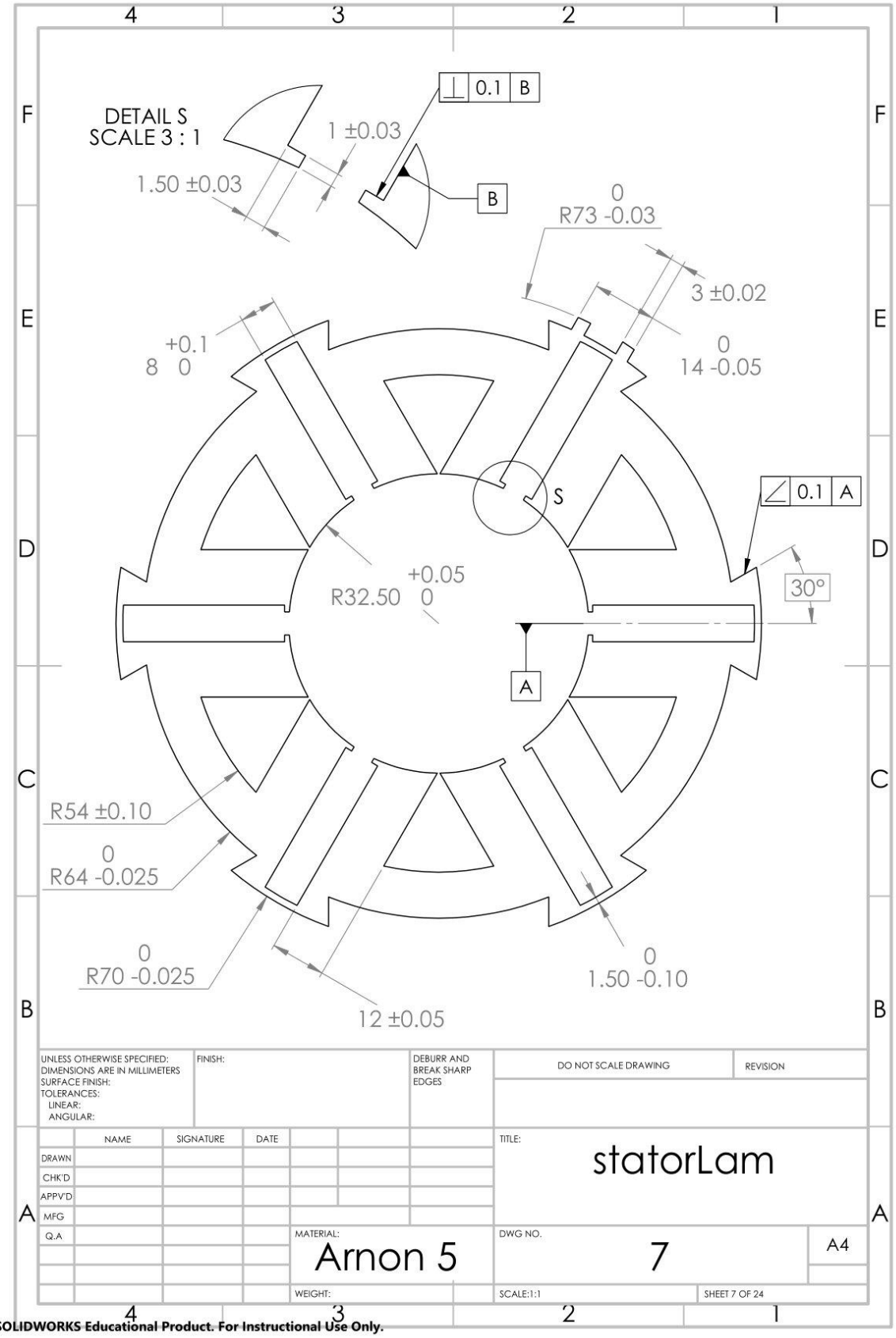

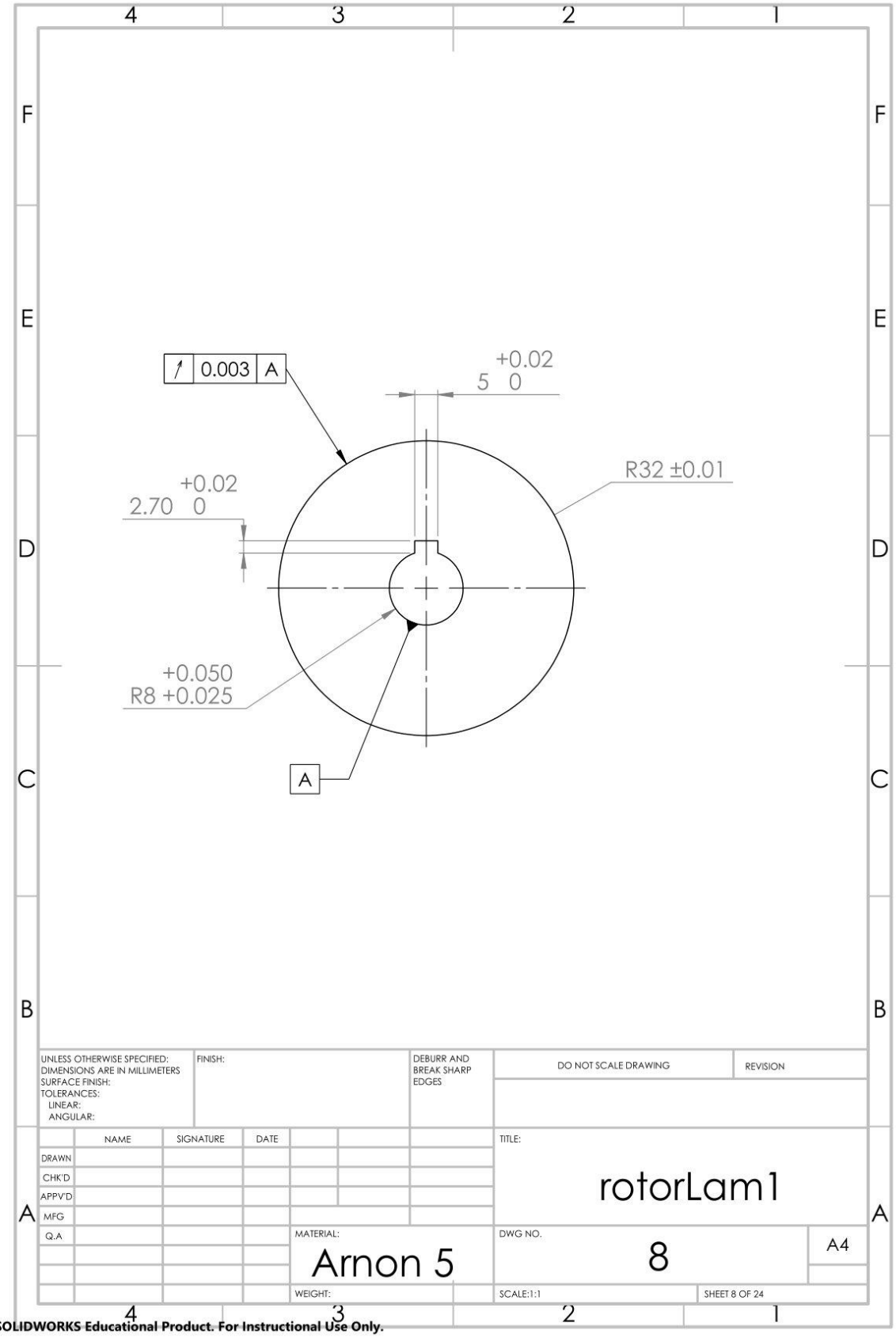

For details about shaft hole, please refer to Drawing No. 8 rotorLam1
For details about rotor pole/tips, please refer to Drawing No. 10. rotorLam3

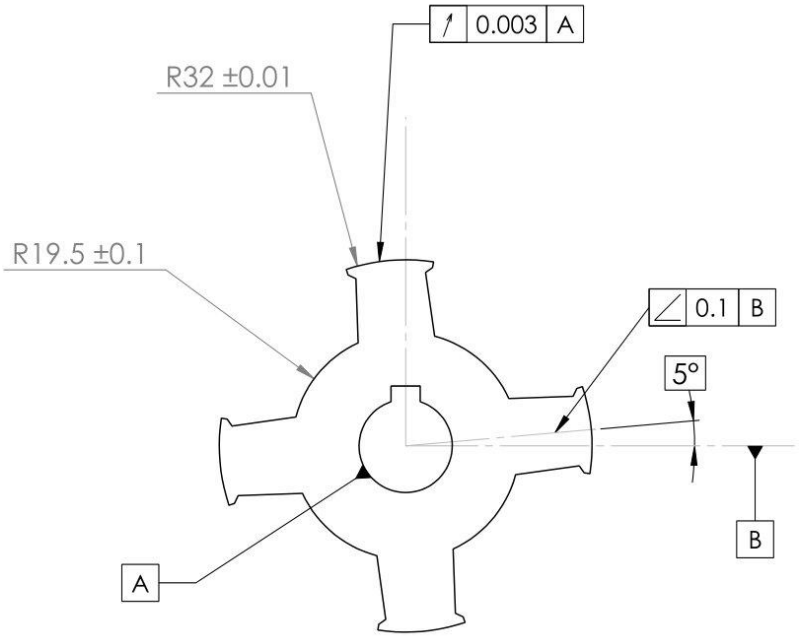

UNLESS OTHERWISE SPECIFIED: DIMENSIONS ARE IN MILLIMETERS SURFACE FINISH: TOLERANCES: LINEAR: ANGULAR:	FINISH:	DEBURR AND BREAK SHARP EDGES	DO NOT SCALE DRAWING / REVISION

	NAME	SIGNATURE	DATE
DRAWN			
CHK'D			
APPV'D			
MFG			
Q.A			

TITLE: rotorLam2

MATERIAL: Arnon 5

DWG NO. 9

A4

WEIGHT:

SCALE:1:1

SHEET 9 OF 24

For details about shaft hole, please refer to Drawing No. 8 rotorLam1

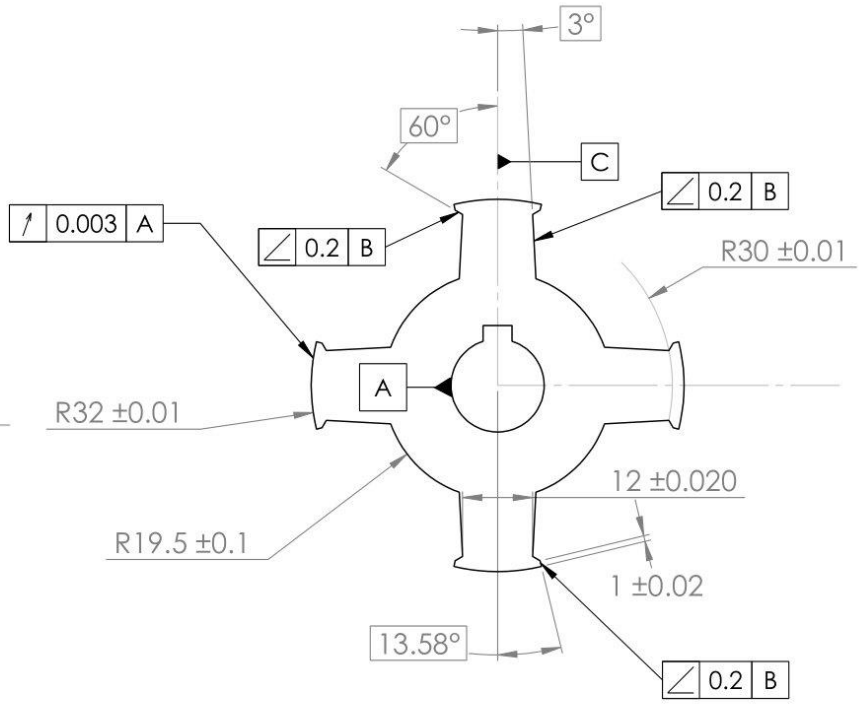

UNLESS OTHERWISE SPECIFIED: DIMENSIONS ARE IN MILLIMETERS SURFACE FINISH: TOLERANCES: LINEAR: ANGULAR:	FINISH:	DEBURR AND BREAK SHARP EDGES	DO NOT SCALE DRAWING / REVISION

	NAME	SIGNATURE	DATE
DRAWN			
CHK'D			
APPV'D			
MFG			
Q.A			

TITLE: rotorLam3

MATERIAL: Arnon 5

DWG NO. 10

A4

WEIGHT:

SCALE:1:1

SHEET 10 OF 24

For details about shaft hole, please refer to drawing No.8 rotorLam1

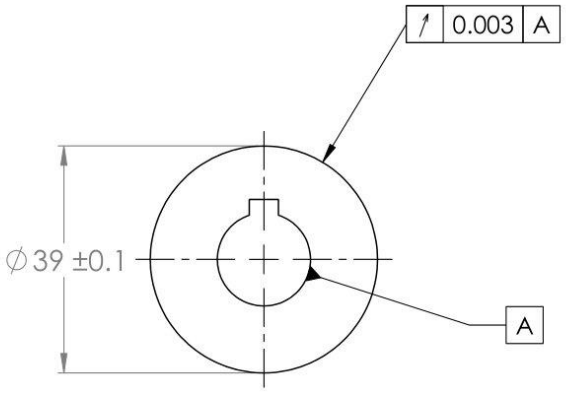

UNLESS OTHERWISE SPECIFIED: DIMENSIONS ARE IN MILLIMETERS SURFACE FINISH: TOLERANCES: LINEAR: ANGULAR:		FINISH:			DEBURR AND BREAK SHARP EDGES		DO NOT SCALE DRAWING	REVISION
	NAME	SIGNATURE	DATE				TITLE: rotorLam4	
DRAWN								
CHK'D								
APPV'D								
MFG								
Q.A				MATERIAL: Arnon 5			DWG NO. 11	A4
				WEIGHT:			SCALE:1:1	SHEET 11 OF 24

For details about shaft hole, please refer to Drawing No. 8 rotorLam1
For details about rotor pole/tip, please refer to Drawing No. 10 rotorLam3

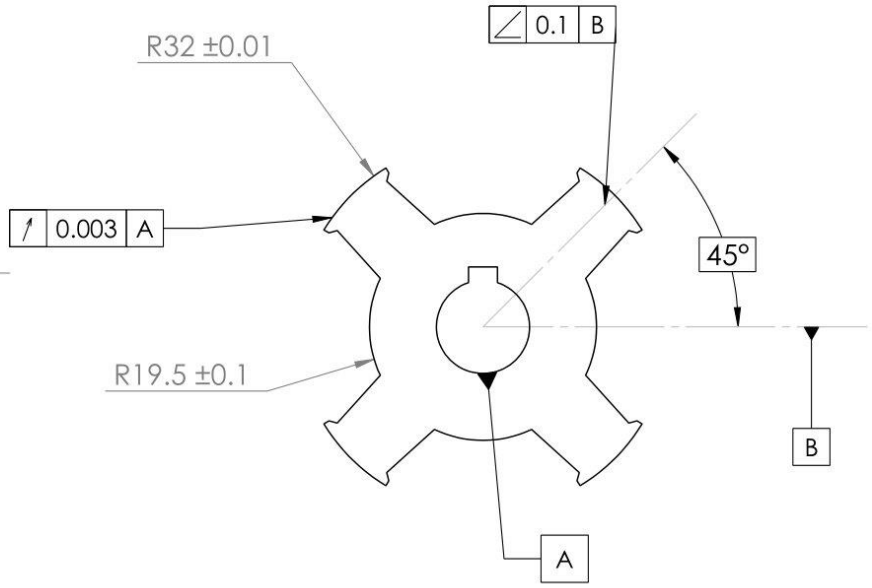

UNLESS OTHERWISE SPECIFIED: DIMENSIONS ARE IN MILLIMETERS SURFACE FINISH: TOLERANCES: LINEAR: ANGULAR:	FINISH:	DEBURR AND BREAK SHARP EDGES	DO NOT SCALE DRAWING / REVISION

	NAME	SIGNATURE	DATE
DRAWN			
CHK'D			
APPV'D			
MFG			
Q.A			

TITLE: rotorLam5

MATERIAL: Arnon 5

DWG NO. 12

A4

WEIGHT:

SCALE:1:1

SHEET 12 OF 24

For details about shaft hole, please refer to Drawing No. 8 rotorLam1
For details about rotor pole/tip, please refer to Drawing No. 10 rotorLam3

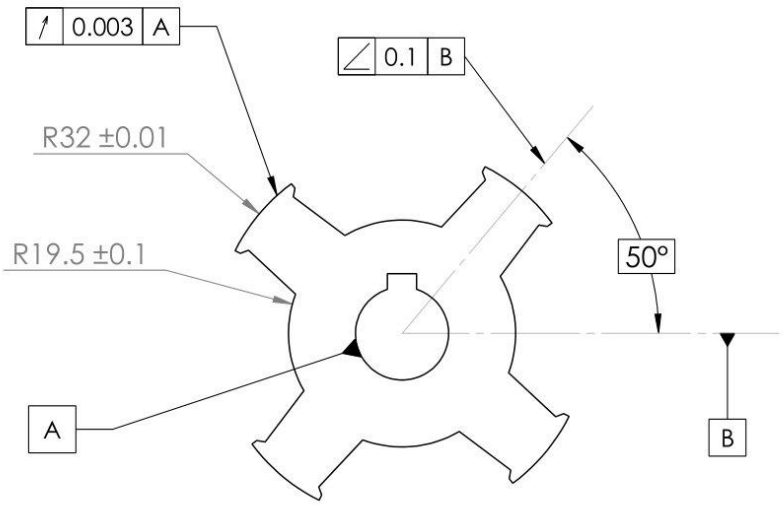

UNLESS OTHERWISE SPECIFIED: DIMENSIONS ARE IN MILLIMETERS SURFACE FINISH: TOLERANCES: LINEAR: ANGULAR:	FINISH:	DEBURR AND BREAK SHARP EDGES	DO NOT SCALE DRAWING / REVISION

	NAME	SIGNATURE	DATE
DRAWN			
CHK'D			
APPV'D			
MFG			
Q.A			

TITLE: rotorLam6

MATERIAL: Arnon 5

DWG NO. 13

A4

WEIGHT:

SCALE:1:1

SHEET 13 OF 24

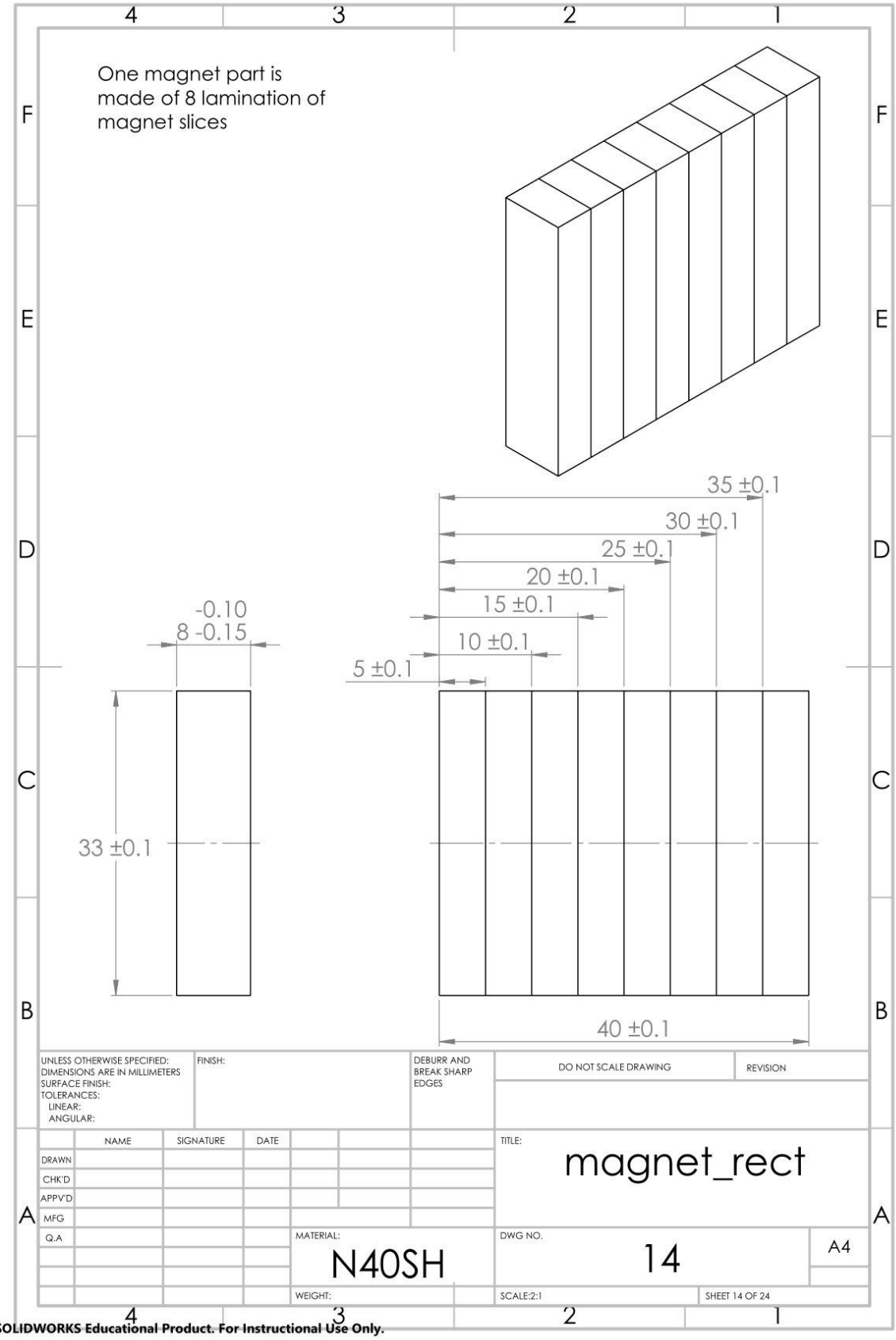

1) BREAK ALL SHARP EDGES

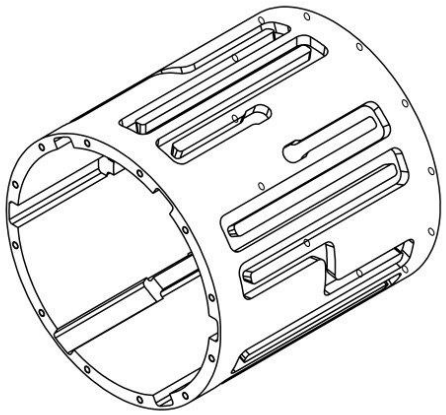

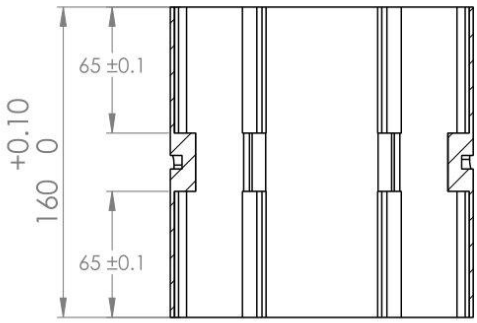

SECTION B-B

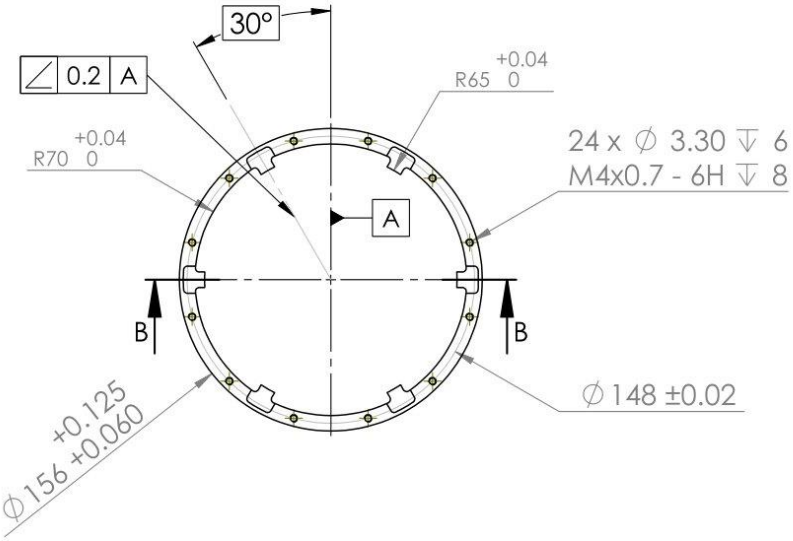

UNLESS OTHERWISE SPECIFIED: DIMENSIONS ARE IN MILLIMETERS SURFACE FINISH: TOLERANCES: LINEAR: ANGULAR:	FINISH:	DEBURR AND BREAK SHARP EDGES	DO NOT SCALE DRAWING / REVISION

	NAME	SIGNATURE	DATE
DRAWN			
CHK'D			
APPV'D			
MFG			
Q.A			

TITLE: housing_inner

MATERIAL: Aluminium

DWG NO. 15

A4

WEIGHT:

SCALE:1:3

SHEET 15 OF 24

1) BREAK ALL SHARP EDGES

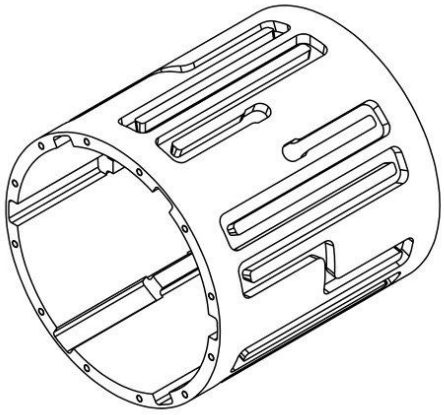

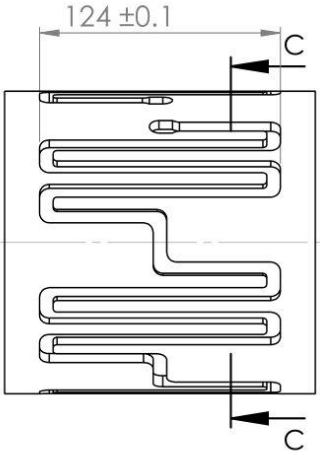

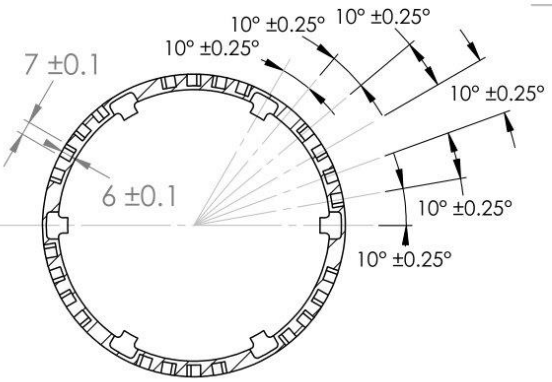

SECTION C-C

UNLESS OTHERWISE SPECIFIED: DIMENSIONS ARE IN MILLIMETERS SURFACE FINISH: TOLERANCES: LINEAR: ANGULAR:		FINISH:		DEBURR AND BREAK SHARP EDGES	DO NOT SCALE DRAWING	REVISION	
	NAME	SIGNATURE	DATE		TITLE: housing_inner		
DRAWN							
CHK'D							
APPV'D							
MFG							
Q.A				MATERIAL: Aluminium	DWG NO. 16		A4
				WEIGHT:	SCALE:1:3	SHEET 16 OF 24	

1) BREAK ALL SHARP EDGES

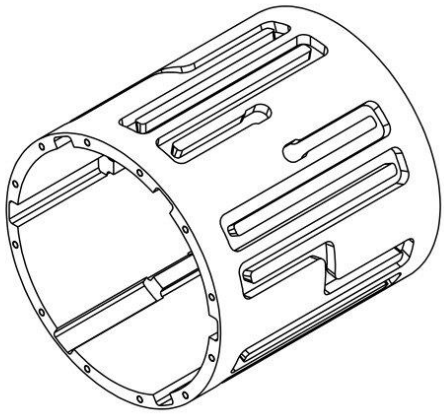

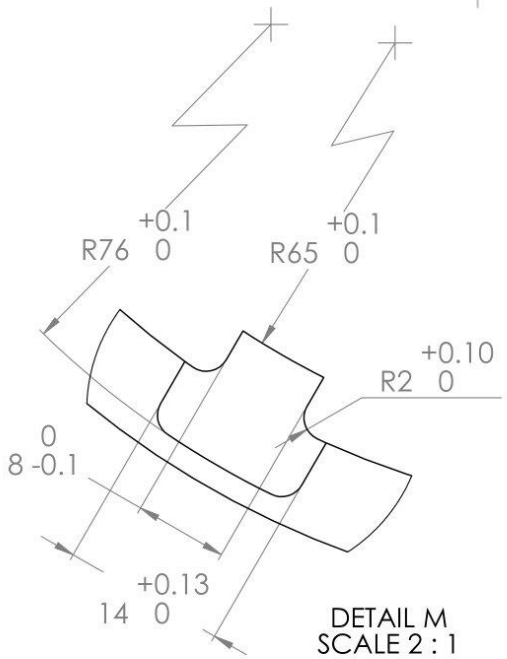

DETAIL M
SCALE 2 : 1

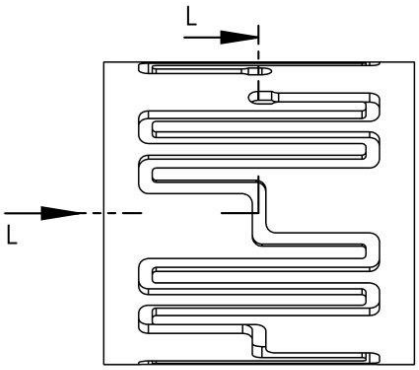

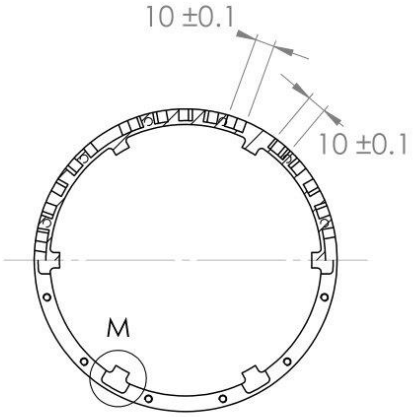

SECTION L-L

UNLESS OTHERWISE SPECIFIED: DIMENSIONS ARE IN MILLIMETERS SURFACE FINISH: TOLERANCES: LINEAR: ANGULAR:	FINISH:	DEBURR AND BREAK SHARP EDGES	DO NOT SCALE DRAWING	REVISION	
	NAME	SIGNATURE	DATE	TITLE: housing_inner	
DRAWN					
CHK'D					
APPV'D					
MFG					
Q.A					
	MATERIAL: Aluminium			DWG NO. 16	A4
	WEIGHT:			SCALE:1:3	SHEET 17 OF 24

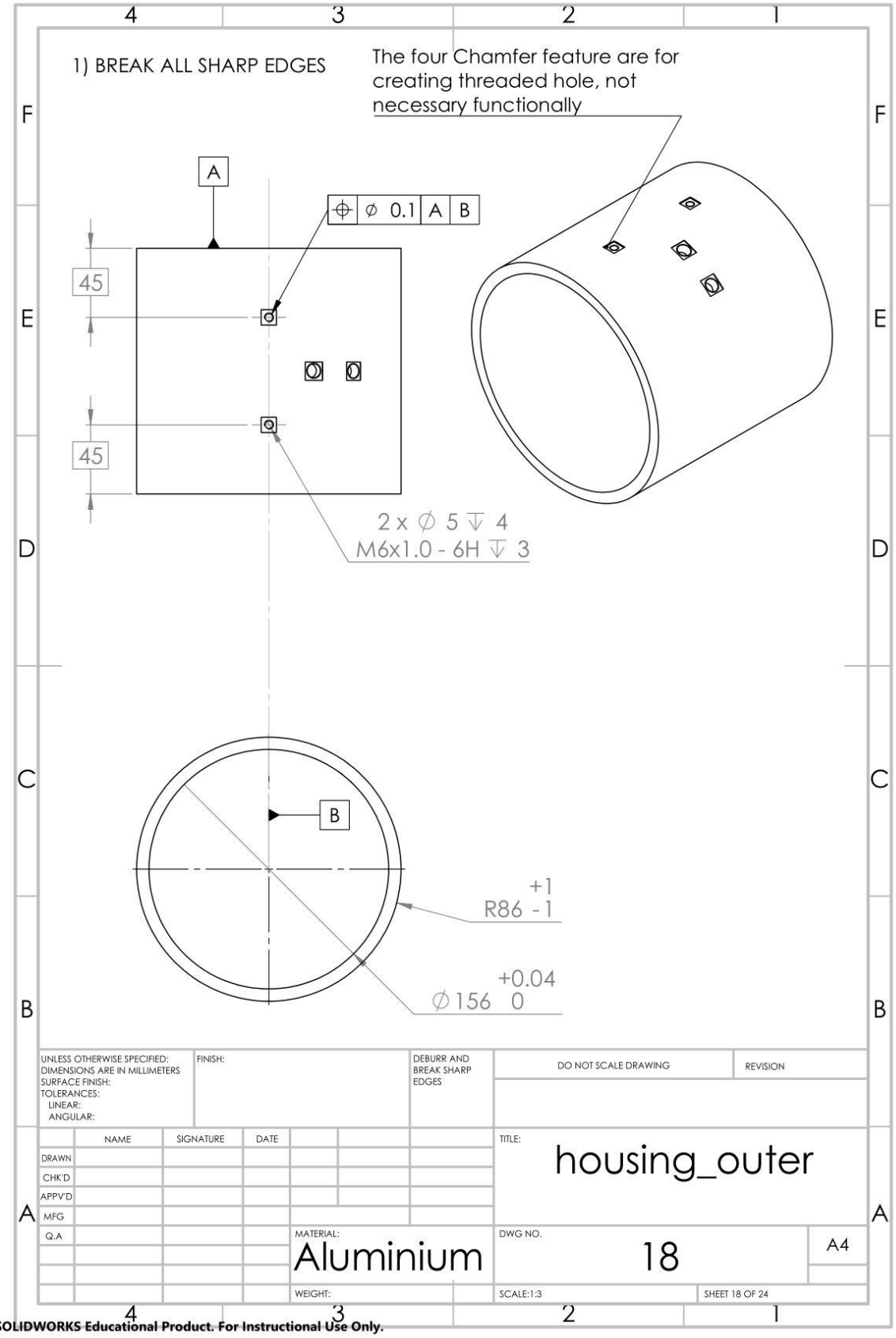

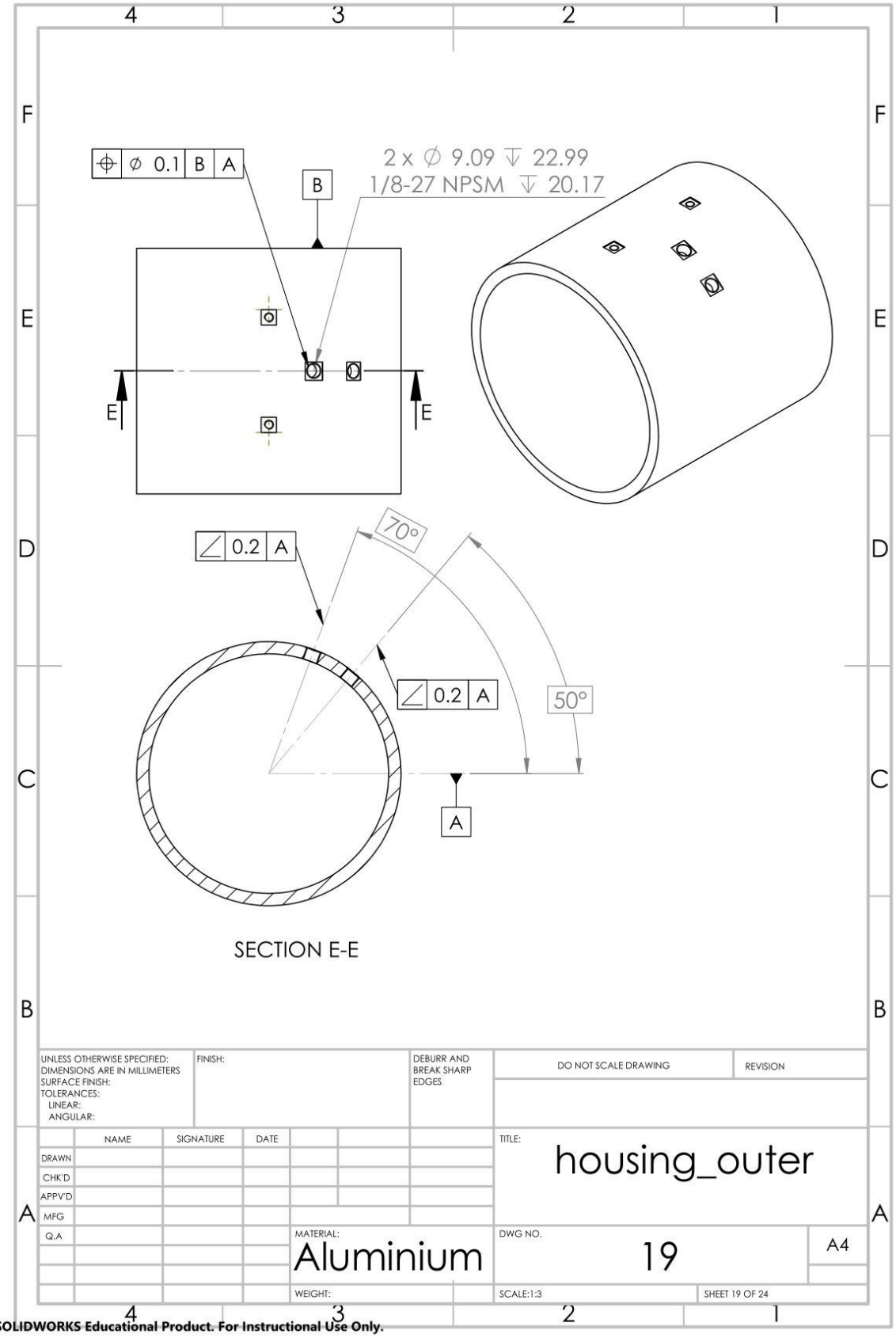

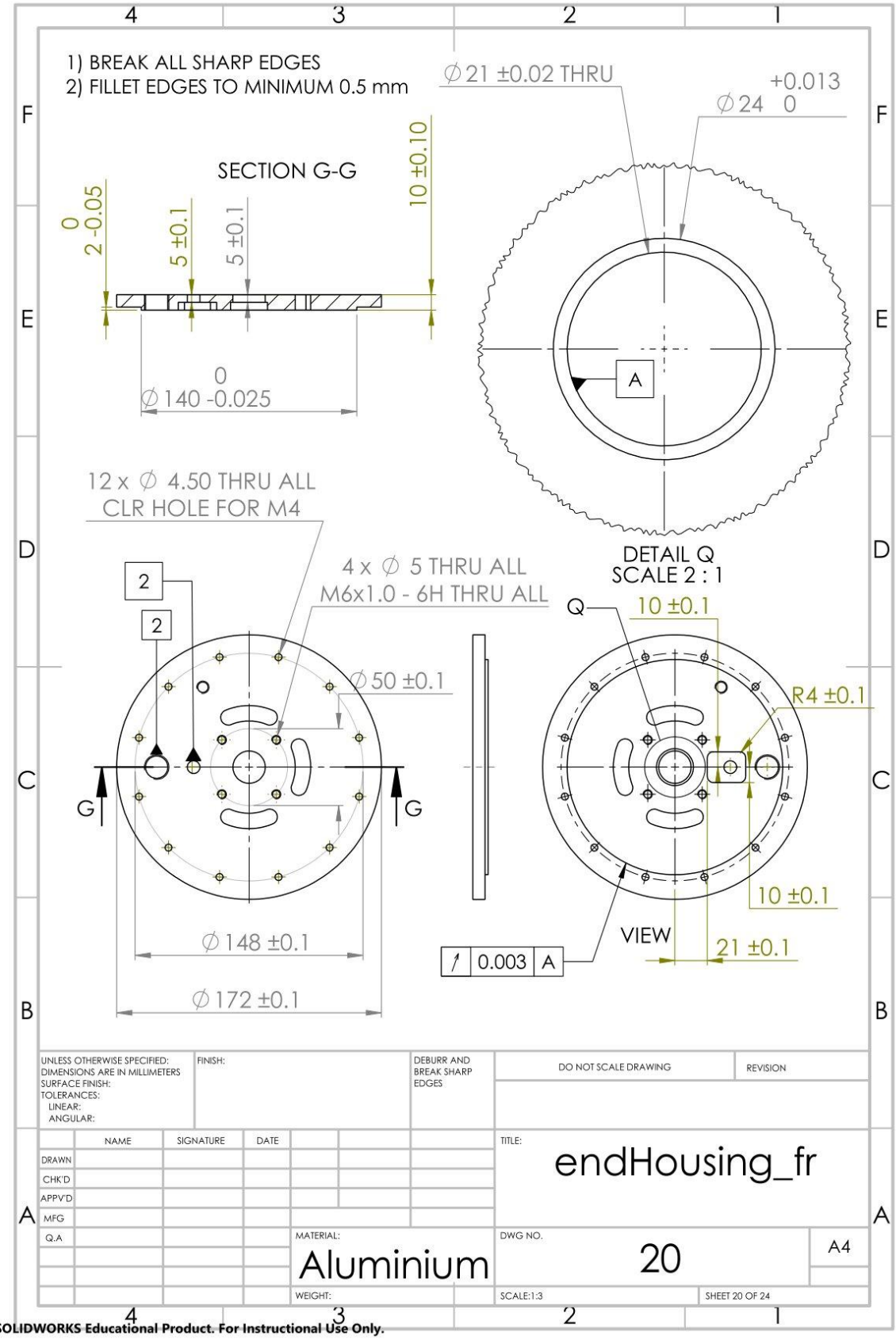

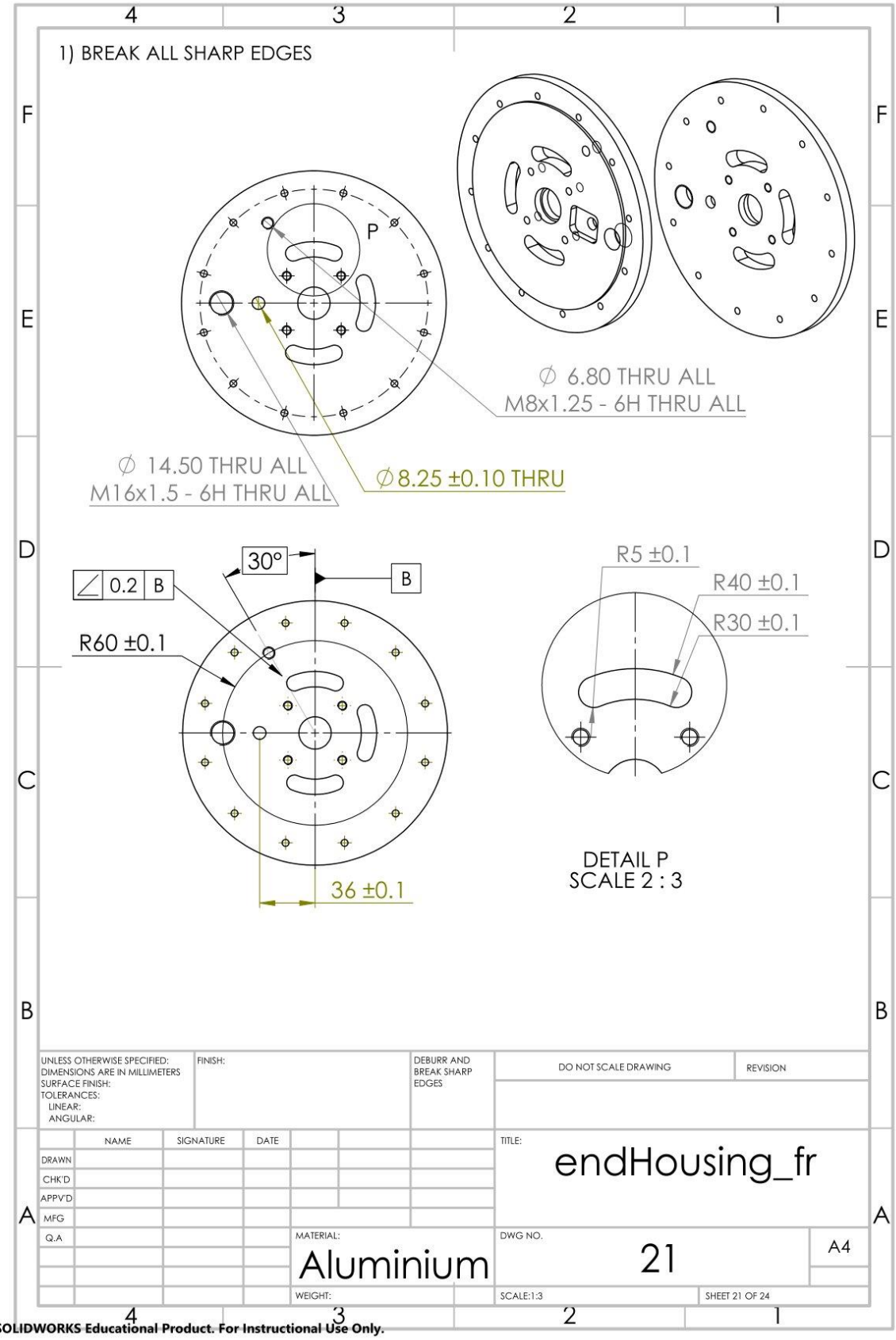

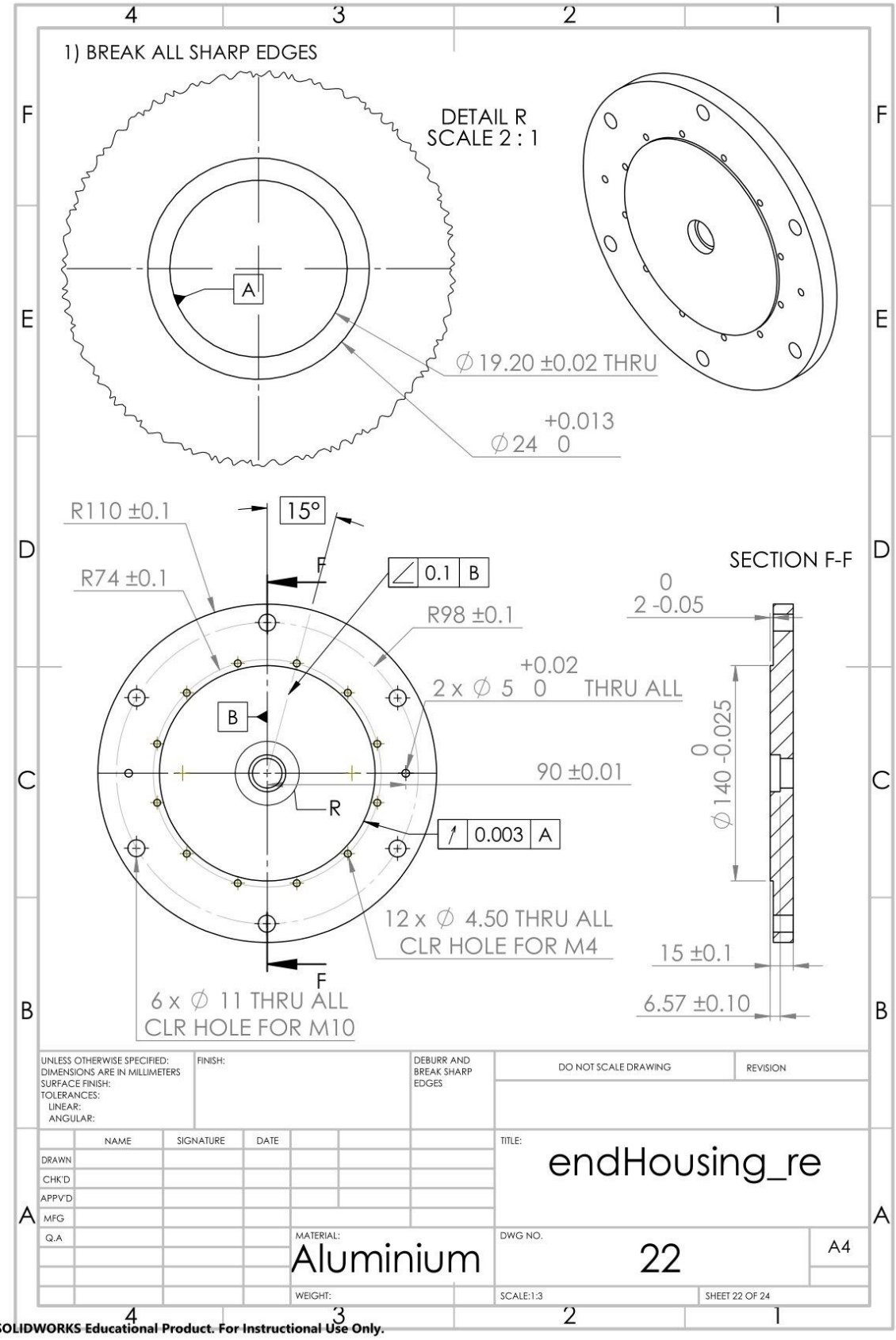

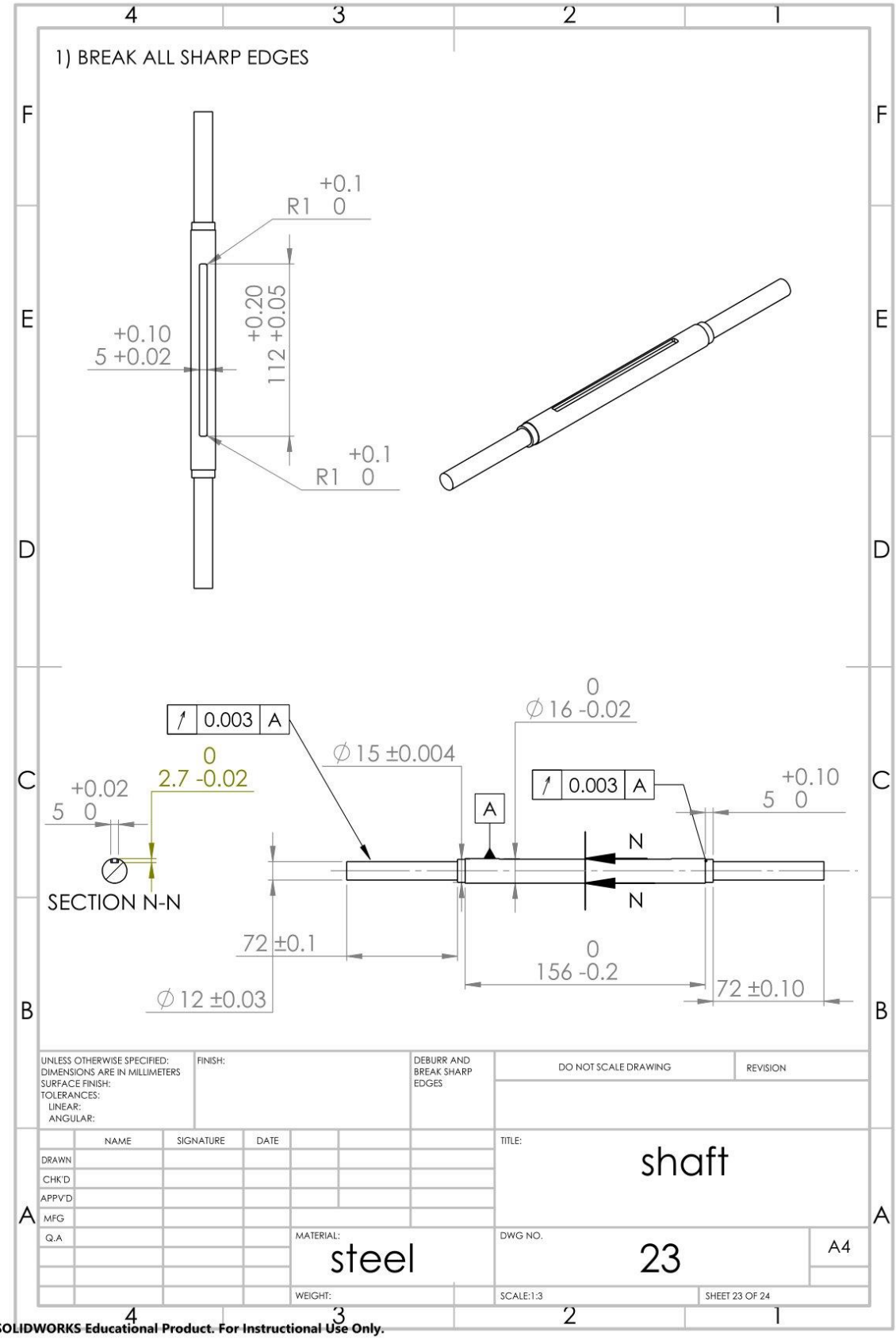

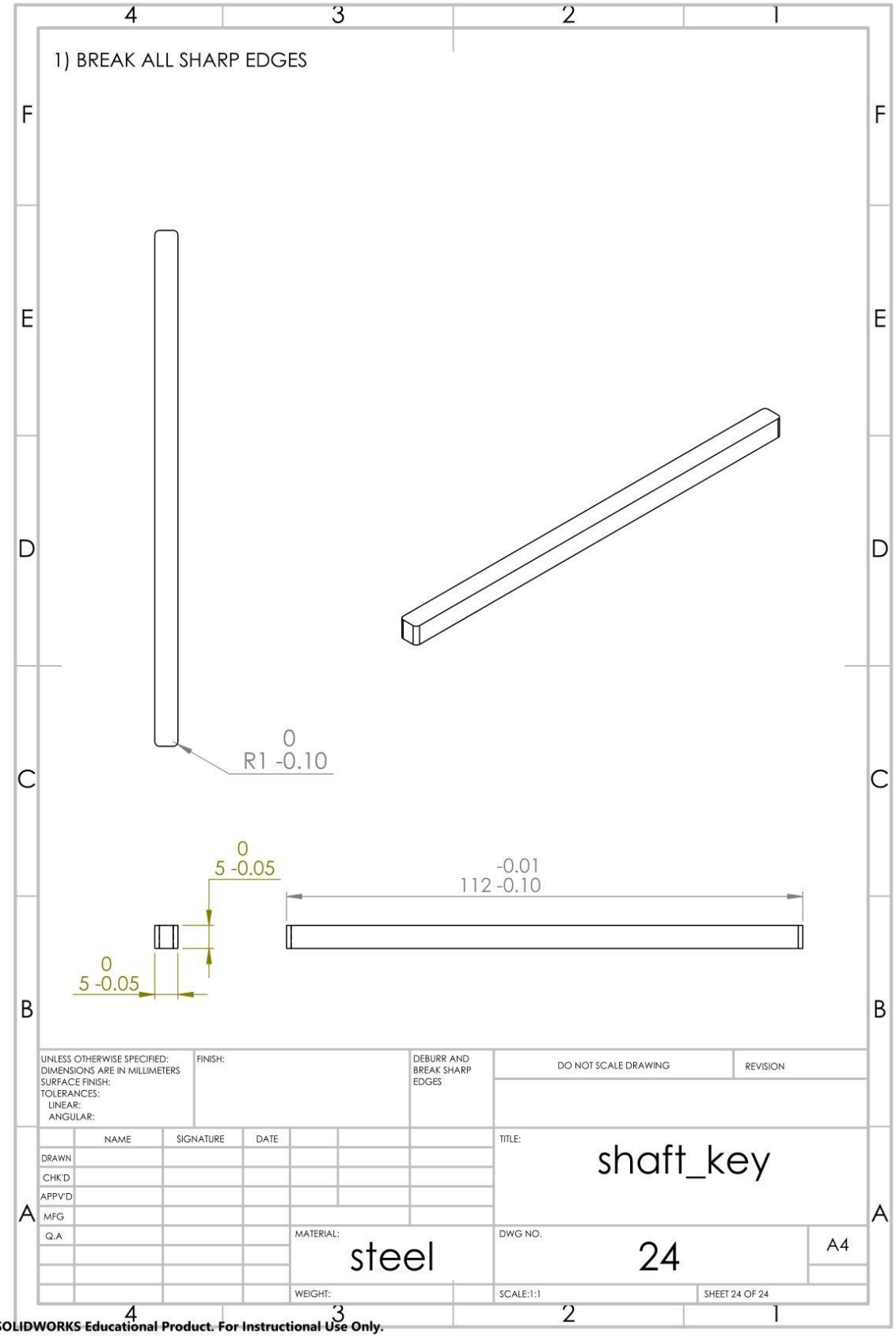
1) BREAK ALL SHARP EDGES
0
R1 -0.10
0
5 -0.05
-0.01
112 -0.10
0
5 -0.05
UNLESS OTHERWISE SPECIFIED:
DIMENSIONS ARE IN MILLIMETERS
SURFACE FINISH:
TOLERANCES:
LINEAR:
ANGULAR:
FINISH:
DEBURR AND BREAK SHARP EDGES
DO NOT SCALE DRAWING
REVISION
NAME
SIGNATURE
DATE
DRAWN
CHK'D
APPV'D
MFG
Q.A
TITLE:
shaft_key
MATERIAL:
steel
DWG NO.
24
A4
WEIGHT:
SCALE:1:1
SHEET 24 OF 24
SOLIDWORKS Educational Product. For Instructional Use Only.